A journey across the X-ray activity of M dwarf stars

Dissertation

der Mathematisch-Naturwissenschaftlichen Fakultät

der Eberhard Karls Universität Tübingen

zur Erlangung des Grades eines

Doktors der Naturwissenschaften

(Dr. rer. nat.)

vorgelegt von

Enza Magaudda

aus Messina/Italien

Tübingen

2022

Gedruckt mit Genehmigung der Mathematisch-Naturwissenschaftlichen Fakultät der Eberhard Karls Universität Tübingen.

Tag der mündlichen Qualifikation:	15.07.2022
Dekan:	Prof. Dr. Thilo Stehle
1. Berichterstatter/-in:	Prof. Dr. Beate Stelzer
2. Berichterstatter/-in:	Prof. Dr. Klaus Werner

To my mom

Zusammenfassung

M Zwergsterne sind die häufigsten Sterne im Universum und zeigen magnetische Aktivität aufgrund eines Dynamomechanismus, der für sehr späte Spektraltypen, die eine vollständig konvektive innere Struktur haben (Übergang $\sim$M3.5), noch nicht verstanden ist. Das Ziel dieser Arbeit ist die Untersuchung der koronalen Röntgenvariabilität von M Zwergen, um indirekt den stellaren Dynamo und seine Abhängigkeit von stellaren Parametern, wie Masse und Rotation, zu untersuchen. Zu diesem Zweck habe ich die Aktivitäts - Rotations - Relation analysiert, die aus zwei verschiedenen Regimen besteht: dem gesättigten Regime für schnell rotierende Sterne und dem ungesättigten Regime für langsam rotierende Sterne, wobei der Übergang zwischen den beiden Bereichen bei einer Periode von $\sim$ 10 Tagen liegt. Das bimodale Verhalten dieser Beziehung hängt nicht nur von der Rotation ab, sondern ist auch mit der Sternmasse und dem Alter des Sterns verbunden. Daher spielt die Sternentwicklung eine wichtige Rolle, wenn es darum geht, zu verstehen, wie sich die magnetische Aktivität während der Lebensdauer eines Sterns ändert.

Die erste Publikation, Magaudda u. a. [39], stellt die Analyse einer Stichprobe von 14 M Zwergen vor, die mit den Röntgen-Satelliten *XMM-Newton* und *Chandra* beobachtet wurden, und deren Rotationsperioden aus Lichtkurven der *Kepler Two-Wheel* (K2) Mission bestimmt wurden. Diese neuen Daten in Kombination mit aktualisierten und homogenisierten Literaturergebnissen liefern die bisher größte einheitliche Stichprobe von M Zwergen (302 Sterne) für Röntgenaktivitäts- und Rotationsstudien. Dies ermöglichte eine detaillierte Untersuchung der Aktivitäts - Masse - Alter - Rotations - Abhängigkeiten. Durch die Analyse der Masseneffekte konnte ich die Abnahme des Röntgenpegels für niedrigere Sternmassen im gesättigten Bereich bestätigen, die zuvor für eine Stichprobe von Sternen mit Spektraltypen von G bis M und mit Massen unter $1.4\,M_{\odot}$ beobachtet wurde. Unter Einbeziehung der Drehimpulsentwicklungsmodelle und der beobachteten Aktivitäts-Rotations-

Relation ($L_\mathrm{x} - P_\mathrm{rot}$), die in meiner Arbeit untersucht wurde, habe ich den Abfall der Röntgenleuchtkraft mit dem Sternalter vorhergesagt und eine gute Übereinstimmung mit der beobachteten L_x von teilweise konvektiven Sternen (SpT<M3.5) mit bekanntem Alter gefunden.

Als Beitrag zur Arbeit von Modirrousta-Galian u. a. [48] bezüglich der Untersuchung des M Zwerges GJ 357 habe ich die mit *XMM-Newton* aufgenommenen Röntgendaten analysiert, die verwendet wurden, um die die Entwicklung der Atmosphäre des Planeten einzuschränken. Insbesondere fanden wir mithilfe der in Magaudda u. a. [39] vorhergesagten $L_\mathrm{x}-$Altersabhängigkeit für M Zwerge eine untere Grenze für das Alter von GJ 357. Wir haben die Entwicklung der Atmosphäre des Planeten untersucht, der GJ 357 umkreist. Unter der Annahme, dass die vom Zentralstern emittierte Strahlung die Planetenatmosphäre zum Verdampfen bringen kann, führten wir eine Rückwärtsrekonstruktion der von GJ 357 emittierten Röntgenstrahlung durch und fanden die Obergrenze der anfänglichen atmosphärischen Masse des Planeten, die sich auf $\sim 38\,\mathrm{M_\oplus}$ beläuft.

Die beiden Arbeiten, Magaudda u. a. [41, 40], präsentieren die ersten Ergebnisse der Analyse neuer Daten, die mit dem *ROentgen Survey with an Imaging Telescope Array (eROSITA)* an Bord der russischen Spektrum-Röntgen-Gamma-Mission (SRG) aufgenommen wurden, kombiniert mit neuen Rotationsperioden, die aus den Lichtkurven des *Transiting Exoplanet Survey Satellite (TESS)* extrahiert wurden. Ich habe nach *eROSITA* und *TESS* Daten gesucht und dabei Sterne aus dem SUPERBLINK Eigenbewegungskatalog der nahen M Zwerge ausgewählt, die mit *Gaia*−DR2 Daten erweitert wurden. Um die Zuordnung zu den eROSITA-Quellen sicherzustellen, habe ich ein sorgfältiges Cross - Match - Verfahren durchgeführt, dessen Ergebnisse mit einem Bayes'schen statistischen Algorithmus (NWAY) bestätigt wurden, der von anderen Mitgliedern des eROSITA-Konsortiums entwickelt wurde. Mit dieser beispiellosen eROSITA-*TESS*-Datenbank für röntgen-emittierende M Zwerge, in Kombination mit meiner Zusammenstellung zuvor untersuchter Röntgen- und Rotationsdaten, untersuchte ich quantitativ die Massenabhängigkeit des gesättigten Bereichs der Aktivitäts - Rotations - Beziehung.

Schließlich habe ich die technischen Möglichkeit von eROSITA in Bezug auf M Zwergsterne untersucht. Zunächst verglich ich die neuen eROSITA - Röntgen-

detektionen mit denen des historischen *ROSAT*-Satelliten (Beobachtungen aus dem Jahr 1991). Dies führte zu einer statistischen Untersuchung der langfristigen Röntgenvariabilität der in Magaudda u. a. [41] vorgestellten M Zwerg-Stichprobe, aus der ich schloss, dass viele leuchtschwache M Zwerge zuvor von *ROSAT* nur entdeckt wurden, weil sie sich in einem hohen Aktivitätszustand befanden.

Später, in Magaudda u. a. [40], untersuchte ich die Rotationsabhängigkeit der Röntgenleuchtkraft im gesättigten Bereich und in drei verschiedenen Massenbereichen und beobachtete einen Mangel an massearmen Sternen mit mittleren Rotationsperioden ($\sim 1 - 10$ Tagen), wahrscheinlich verursacht durch eine schnelle Periodenentwicklung. Durch den Vergleich der von eROSITA entdeckten Sterne mit denen, für die zuverlässige Rotationsperioden aus *TESS*-Lichtkurven vorliegen, habe ich herausgefunden, dass eROSITA empfindlicher ist als *TESS*, d.h. eROSITA kann auch Röntgenstrahlung von langsam rotierenden M Zwergen entdecken, die sich im ungesättigten Bereich mit Perioden befinden, die für *TESS* unzugänglich sind.

Abstract (English)

M dwarfs are the most common stars in the universe and they show magnetic activity due to a dynamo mechanism not yet understood for very late spectral types that appear to have a fully convective internal structure (transition $\sim$M3.5). The purpose of this work is the study of the coronal X-ray variability of M dwarfs in order to indirectly investigate the stellar dynamo and how it depends on stellar parameters, such as mass and rotation. To this end, I analyzed the activity-rotation relation, that is known to consist of two different regimes: the saturated regime for fast-rotating stars and the unsaturated regime for slowly rotating stars, with the transition between the two regimes located at a period of ~ 10 d. The bimodal behavior of this relation not only depends on the rotation but it is also linked to the stellar mass and age. Thus, stellar evolution plays an important role in understanding how magnetic activity changes during the stellar lifetime.

The first paper, Magaudda et al. [39], presents the analysis of a sample of 14 M dwarfs observed with *XMM-Newton* and *Chandra* satellites, and with rotation periods determined from Kepler Two-Wheel (K2) Mission light curves. These new data combined with updated and homogenized literature results provide the largest uniform sample of M dwarfs (302 stars) for X-ray activity and rotation studies to date. This allowed a detailed investigation of the activity-mass-age-rotation dependence. From the analysis of the mass-effects I confirmed the decrease of the X-ray level for lower stellar mass in the saturated regime, previously observed for a sample of stars with spectral types from G to M and with masses lower than $1.4\,M_\odot$. With the joint analysis of angular momentum evolution models and the observed activity-rotation relation ($L_{\rm x} - P_{\rm rot}$) studied in my work, I predicted the decay of the X-ray luminosity with stellar age finding a good agreement with the observed $L_{\rm x}$ of partially convective stars (SpT<M3.5) with known age.

As a contribution to the work of Modirrousta-Galian et al. [48] regarding the study of the M dwarf GJ 357, I analyzed the X-ray data taken with *XMM-Newton*, that were used to put constraints on the atmospheric evolution of the star's planet. In particular, with help of the $L_{\rm x}-$age dependence for M dwarfs I predicted in Magaudda et al. [39] we placed a lower limit on the age of GJ 357. We studied the evolution of the atmosphere of the planet orbiting around GJ 357 performing a backwards reconstruction of the X-ray radiation emitted by GJ 357. In this way, we found the upper limit of the initial primordial atmospheric mass of the planet, amounting to $\sim 38\,{\rm M}_\oplus$, before evaporating caused by the absorption of the stellar X-ray emission by the planet.

The other two papers, Magaudda et al. [41, 40], present the first results from the analysis of new data taken with the *ROentgen Survey with an Imaging Telescope Array (eROSITA)* on board the Russian Spektrum-Roentgen-Gamma mission (SRG) combined with new rotation periods extracted from the *Transiting Exoplanet Survey Satellite (TESS)* light curves. I searched for *eROSITA* and *TESS* data selecting stars from the SUPERBLINK proper motion catalog of nearby M dwarfs, enhanced with *Gaia*-DR2 data. To ensure the correct association between eROSITA X-ray sources and the M dwarfs I performed a meticulous cross-match procedure the results of which were confirmed with a Bayesian statistical algorithm (NWAY) developed by

other members of the eROSITA-DE consortium. With this unprecedented eROSITA-*TESS* data base for X-ray emitting M dwarfs, combined with my compilation of X-ray and rotation data previously studied, I quantitatively investigated the mass dependence of the saturated regime of the activity-rotation relation.

Finally, I investigated the eROSITA capability with respect to M dwarfs. First, I compared the new eROSITA X-ray detections with those from the historical *ROSAT* satellite. This resulted in a statistical investigation of the long-term X-ray variability of the M dwarf sample presented in Magaudda et al. [41], from which I concluded that many faint M dwarfs were previously detected by *ROSAT* only because they happened to be in a higher activity state. Later, in Magaudda et al. [40], I studied the rotation dependence of the X-ray luminosity in the saturated regime for three different mass bins and I observed a paucity of low mass stars with intermediate rotation periods ($\sim 1 - 10\,\mathrm{d}$), probably caused by fast period evolution. By comparing the eROSITA detections for those stars that have also reliable rotation periods from *TESS* light curves, I found that eROSITA is sensitive for detecting slower rotating M dwarfs that are in the unsaturated regime with periods inaccessible to *TESS*.

List of Publications and personal contribution

1. E. Magaudda, B. Stelzer, K. R. Covey, St. Raetz, S. P. Matt, and A. Scholz, *Relation of X-ray activity and rotation in M dwarfs and predicted time-evolution of the X-ray luminosity*, 2020, A&A 638, A20

2. D. Modirrousta-Galian, B. Stelzer, E. Magaudda, J. Maldonado, M. Güdel, J. Sanz-Forcada, B. Edwards, and G. Micela, *GJ 357 b. A super-Earth orbiting an extremely inactive host star*, 2020, A&A 641, A113

3. E. Magaudda, B. Stelzer, St. Raetz, A. Klutsch, M. Salvato, and J. Wolf, *First eROSITA study of nearby M dwarfs and the rotation-activity relation in combination with TESS*, 2022, A&A 661, A29

4. E. Magaudda, B. Stelzer, and St. Raetz, *First eROSITA-TESS results for M dwarfs: Mass dependence of the X-ray activity rotation relation and an assessment of sensitivity limits*, 2022, Astron. Nachr.,343, e220049

No.	Author position (%)	Scientific idea (%)	Data generation (%)	Analysis & interpretation (%)	Paper writing (%)	Status (%)
1	1	40	90	95	80	Published
2	3	10	30	30	30	Published
3	1	40	60	95	50	Published
4	1	40	100	80	80	Published

Contents

Introduction

<div style="text-align: right">1</div>

1.1 Magnetism in late-type stars: convection & rotation

Main-sequence stars of spectral type (SpT) F−L are known to be magnetically active and exhibit sudden and powerful atmospheric events that cause variability in the stellar emission. Multi-wavelength observations allow to study the emitted radiation along the whole electromagnetic spectrum, tracing the physical behavior of the different atmospheric layers of the stars. These emissions are associated with plasma, heated through magnetic processes to temperatures of more than 10^6 K in the outermost and thinnest atmospheric layer, the *corona*. The temperature profile varies non-uniformly through the whole stellar atmosphere (see left panel in Fig. 1.1). Initially, the temperature decreases throughout the photosphere, then an inversion of the gradient occurs in the chromosphere and the temperature increases again first slowly then more abruptly in a thin layer called *transition region* until it approaches 10^6 K in corona. The process responsible for this heating is a major puzzle in solar and stellar physics, in particular two theories are nowadays the most discussed. One is based on a non-radiative mechanism driven by Alfvén waves that causes a magnetic shock that propagates throughout the stellar atmosphere and contributes to the formation of magnetic structures as starspots and active regions [81].

The other theory was first proposed by Parker [60] and it is based on the presence of multiple low energy events called "nanoflares". The rate of occurrence of these events is not yet well established. Nanoflares are variations of the stellar brightness linked to a phenomenon that converts the magnetic energy into kinetic energy and heat. While the energetic flares are powerful and short-term events that suddenly occur in the whole stellar atmosphere (the formation mechanism is explained in Sect. 1.3), nanoflares appear to be a continuous heating source of the quiescent corona [64]. Parker [60] was the first to suggest that a nanoflare is due to the reconfiguration of the magnetic field lines, i.e. magnetic reconnection,

during which the energy stored in the magnetic field is converted into motion of the plasma. In other words, the strong and localized magnetic currents in the solar corona are produced by the twist of the magnetic field lines whose photospheric footpoints, i.e. starspots, are moved by the convective motions [59, 58]. These small length-scale motions are attenuated by turbulences and viscosity, thus the energy is quickly converted into heat and transferred to the point where a nanoflare forms by free electrons that move along the magnetic field lines. From computational models it is known that nanoflares produce a faint and hot component [~ 10 MK, 28] of the emission measure. This quantity informs about the amount of coronal material emitted per unit of volume and at a given temperature [4]. Because of the faint emission provided by nanoflares, it is hard to conduct a reliable and detailed investigation with the instrumentation currently available, thus the model proposed by Parker [60] has not yet been confirmed observationally.

The interior structure of a solar-like star defined here in a broad "sense" as objects with SpT of F to mid$-$M consists of a hot radiative core, where hydrogen is burned into He, surrounded by a convective envelope (see right panel in Fig. 1.1). Between these two regions a thin layer called *tachocline zone* is located [5, 12]. To first approximation, we can consider the inner radiative core as a rigid body, while the plasma inside the convective envelope is subject to differential rotation, i.e. plasma at different latitudes rotates at different periods[1]. The different rotation rate between the inner radiative core and the convective envelope causes a very large shear in the tachocline zone, forming large scale magnetic fields [4, 80]. This is the basis of the so called $\alpha\Omega-$dynamo model (see the scheme in Fig. 1.2) for which the combination of the differential rotation along the poloidal axis with the convective motions along the toroidal axis in the outer envelope continuously powers the magnetic field [29, 80]. Initially, a global dipolar magnetic field (r and θ components) is frozen into the stellar plasma particles. Because of the shear generated between the inner radiative core and the convective envelope the spherical symmetry of the magnetic field breaks and as the star rotates differentially

---

[1]The rate of surface rotation is observed to be the fastest at the equator and to decrease as the latitude increases [81].
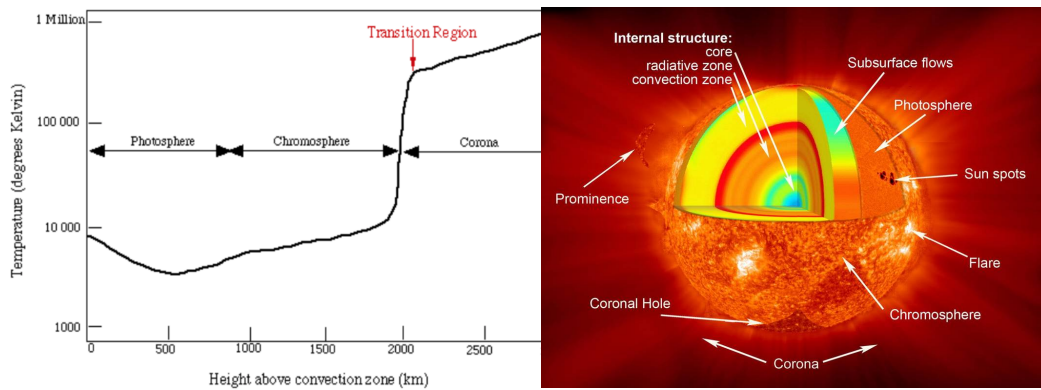
Fig. 1.1: **Left**: Variation of the mean solar temperature as a function of height in the atmosphere. The photosphere shows a negative temperature gradient, that inverts in the chromosphere, causing a sudden transition into the much hotter and thinner outer atmospheric layer that is the corona. Image adopted by M.B. Larson from Sun, Earth, Sky by Kenneth Lang. **Right**: Representation of the solar structure. The inner structure consists of a radiative core where the heat is transferred by radiation, surrounded by an outer envelope where heat is transferred by convection. The inner atmospheric layer is the photosphere where starspots are present, i.e. darker and cooler regions than the surroundings. These are the footpoints from where magnetic field lines rise up into the outer atmospheric layers. Linked to the photospheric starspots, there are the active regions in the above layer called chromosphere, that are brighter and hotter regions than starspots. Finally, the outermost layer is the corona. Here several magnetic structures are shown: eruptive prominence, arch filament formed by the magnetic reconnection of the magnetic field lines and coronal hole, dark and cool areas of open magnetic field lines. The detailed explanation of these features shown in this figure is found i Sect. 1.1,1.2 & 1.3. Credit: NASA Goddard.
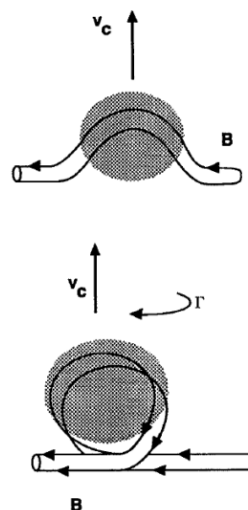
Fig. 1.2: Scheme of the $\alpha - \Omega$ dynamo mechanism. First the magnetic field lines are wrapped by the differential rotation of the star, i.e. $\Omega-$effect. Then, the buoyancy of rising convective cells induces a helical twist in the poloidal field restoring the initial toroidal configuration of the magnetic field [80].

the poloidal field lines get wrapped and generate a toroidal field ($\Omega-$effect). This process defines the first half of a solar activity cycle[2]. To conclude this cycle the initial configuration of the magnetic field needs to be restored. To achieve this, a new symmetry breaking is required and this is provided by the $\alpha-$effect. The buoyancy of the convective cells in the stellar convective zone causes a helical twist on the toroidal magnetic field inducing its conversion into a poloidal configuration [80]. The buoyant motions are the consequence of density fluctuations and/or temperature variations and they generate an electromotive force that acts into the local magnetic field. To summarize, the convective turbulences are responsible for small-scale variations of the magnetic field, while the rotation with the consequent shear rules large-scale magnetic field formation and leads to the symmetry breaking needed to generate the dipole [56, 29, 80].

This continuous enhancement of the magnetic field forms magnetic structures and sudden increases of the luminosity emitted by the stellar atmosphere visible along the whole electromagnetic spectrum. Some of these magnetic structures are displayed in the right panel of Fig. 1.1 and explained in detail in Sect. 1.2 which deals with the diagnostic of these magnetic phenomena. The dynamo mechanism that rules the activity in later main-sequence stars (such as late$-$M) is still under discussion. From astroseismology measurements these stellar objects appear to be fully convective, so they lack the tachocline zone where large scale magnetic fields are formed in the $\alpha - \Omega$ dynamo model [11]. One way to assess the activity of such stars is to study how stellar activity varies with rotation in order to indirectly observe the effect of the dynamo's $\Omega-$contribution to the magnetic field.

1.2 Diagnostics of magnetic activity

Under the assumption of the solar-stellar analogy it is possible to use the detailed observations of the Sun to obtain information on stars that have the same or a similar interior structure as the Sun. As introduced in Sect. 1.1, the atmosphere of active stars consists of three layers that from the inside out are the *photosphere,*

---

[2]The activity cycle refers to periods of maximum and minimum sunspot counts, and its duration for the Sun is $\sim 11\,\text{yr}$ [79].

the *chromosphere* and the *corona*. The stellar magnetic field influences the whole atmosphere such that each layer displays activity features (and indicators).

As shown in the right panel of Fig. 1.1, dark spots are found in the photosphere. These regions are called *starspots* and they are cooler than the surrounding photosphere. Their lower temperature is due to the high local magnetic pressure that inhibits convective heat transfer from the interior [87]. The presence of these dark spots influences the photospheric optical emission, causing a decrease of the surface-averaged emitted intensity. Time-series photometry reveals the contribution of dark spots in the stellar light curve (LC). In the left panel of Fig. 1.3 the LC
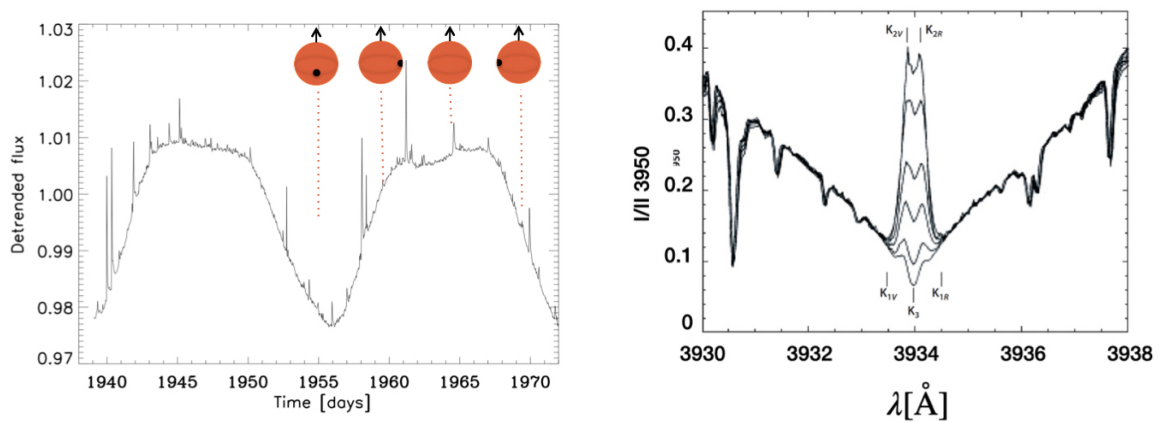
Fig. 1.3: The magnetic activity indicators of the photosphere and the chromosphere. **Left**: the optical light curve of an M dwarf observed with the K2 mission. The brightness modulation is due to the presence of starspots in the photosphere, while the flux spikes manifest flaring events during the whole observational time (Credit: Prof. Dr. Beate Stelzer). **Right**: a model reproduction of the spectroscopic CaII K line [36]. The wings in absorption come from the continuum emission of the photosphere, while the emission of the line core is due to a second ionization of the CaII K because of the magnetic heating occurring in the chromosphere.

of an M dwarf taken with the K2 mission[3], is shown. Since starspots are carried along the surface while the star rotates, their periodic brightness modulation provides the rotation period. Together with this modulation, sudden and energetic increases of the flux, called flares, appear in the LC in Fig. 1.3. These represent the photospheric contributions to powerful and sudden releases of magnetic energy. Thus, photometric monitoring data provide comprehensive diagnostics for both rotation and activity [65].

---

[3]The details of the K2 mission and other photometric monitoring instruments are discussed in Sect. 2.2.1.

Related to photospheric starspots are the hotter and brighter "active regions" in the chromosphere, see right panel in Fig. 1.1. From these regions the magnetic field lines rise in the corona where they form magnetic loops. When the magnetic pressure is high enough to not be sustained by the stellar plasma anymore, the structure tends to go back to an equilibrium state by releasing the energy in form of flare events. This release of magnetic energy can be observed in the whole electromagnetic spectrum, and the photospheric flares in the LC shown in the left panel of Fig. 1.3 are one of its manifestations. The standard model of solar flares that explains how energetic events occur in the atmosphere of active stars is explained in Sect. 1.3 where the coronal X-ray emission is discussed.

The chromospheric activity indicators are observable in the UV and Optical regions of the electromagnetic spectrum. The heated chromosphere produces emission in spectral lines such as Ca II H&K ($3933.66 - 3968.47$ Å) and Ca II infrared triplet (IRT, $8498.02 - 8542.09 - 8662.14$Å), Mg I triplet ($5167.32 - 5172.68 - 5183.60$ Å) and Mg II h&k ($2795.53 - 2802.71$ Å), all Balmer lines, and the Na I doublet ($5889.95 - 5895.92$ Å). The effect of the chromospheric activity is visible in the spectral line profiles as a decrease of the absorbed flux or as an emission in the central part, the line core, due to a second ionization that the specific element experiences as it moves towards the outer layers of the stellar atmosphere (see the right panel in Fig. 1.3). This spectral profile is typical of the Mg II h&k lines in the UV and the Ca II H&K and IRT in the optical. Moreover, the investigation of chromospheric activity is also traceable with the so-called *S-index* [35, 78]

$$S = \frac{H + K}{B + V} \tag{1.1}$$

were H and K are the full width half maximum of the CaII H and K lines in a ~ 1 Å wide window, and B and V represent the continuum emission taken on both sides of the line and measured in ~ 20 Å wide windows centered on 3900 Å and 4000 Å, respectively.

X-ray flares and coronal mass ejections (CME) are the activity indicators of the outermost atmospheric layer, the corona. Since the investigation of coronal

activity is the main topic of this work, Sect. 1.3 is fully dedicated to the description of coronal activity and its indicators.

1.3 Coronal X-ray emission

Fig. 1.4 shows an artist's view of Barnard's star which was discovered by the American astronomer E. E. Barnard. It is an M4 dwarf with one of the highest proper motions known for any star, i.e. it moves away from the Sun by $10.393''$ every year due to its very low distance to the Sun [1.828 pc, 23]. The figure visualizes flares and a prominent CME emitted from the star, that are observable in the X-ray region of the electromagnetic spectrum. Since the only spatially resolved active star on the main-sequence available to us is the Sun, the study of the physical phenomena providing such events is based on the comparison between the observations of the solar atmosphere with magneto-hydrodynamic (MHD) models computed accordingly to the parameters of the stellar sample under investigation.

Flares, including nanoflares explained in Sect. 1.1, are the result of magnetic reconnection. The standard 2D-model of a solar flare is an approximation that gives an idea about how the magnetic energy is released in the corona. This phenomenon takes place in the coronal loops (or eruptive prominences, see right panel in Fig. 1.1) that are formed by the rise of magnetic flux tubes from the inner atmosphere due to the buoyancy of the convective cells into which the magnetic field is frozen. A coronal loop appears with an $\Omega-$shape and it begins and ends in the photosphere with starspots as its footpoints. As explained in Sect. 1.1, when the flux tubes pass through the outer layers of the atmosphere, they are increasingly affected by the differential rotation of the star, as seen in the middle panels in Fig. 1.4 where the field lines are wrapping up because of the rotation, until they break. While the magnetic field re-configures its lines, energy is released into accelerating electrons that travel down along the field lines in the coronal loop [e.g. 49, and see bottom panel in Fig. 1.4]. During their descent along the field lines into the lower chromosphere the accelerated charged particles emit
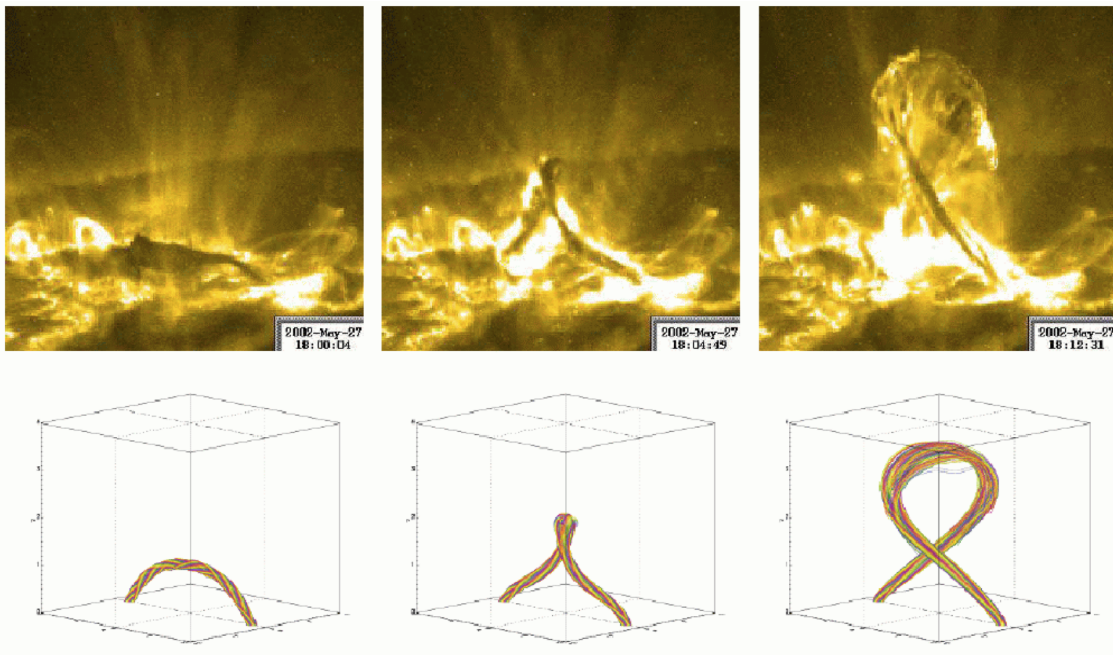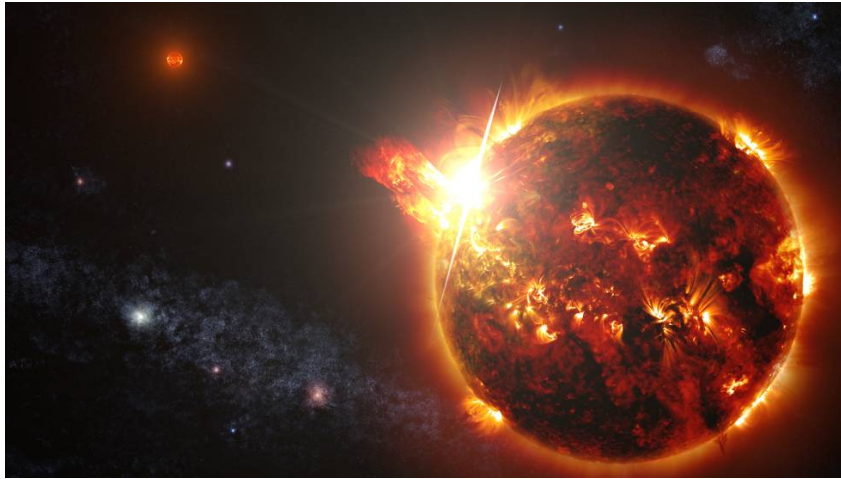
Fig. 1.4: **Top panel**: artist's view of Barnard's star (SpT = M4) where flares and a violent coronal mass ejection are shown. Credit: NASA's Goddard Space Flight Center. **Middle panels**: images of the solar eruption of 27th May 2002 observed at 195 Å with a model reconstruction from Aschwanden, AIA/HMI workshop, Monterey 2006. **Bottom right panel**: shows a schematic view of the standard solar flare model from Nakariakov et al. [49].
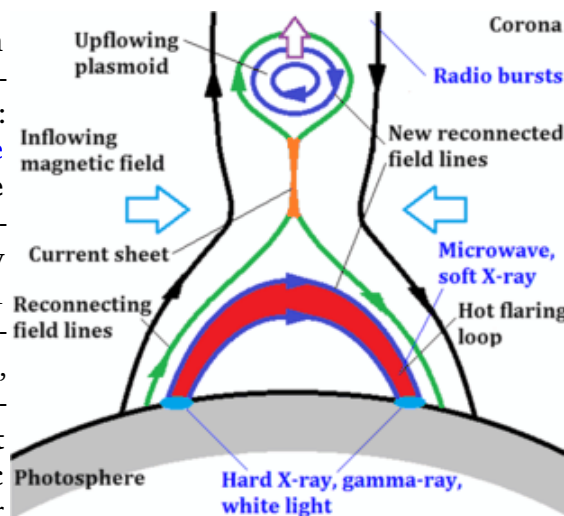
gyrosynchrotron[4] radiation in the microwave band, non-thermal hard X-rays and Gamma-ray bremsstrahlung. Bremsstrahlung radiation is emitted by a free–free interaction process between a free electron and the electric field of an atomic nucleus, during which it releases a photon. This interaction is called "free-free" radiation because the initially free electron remains free after the emission of the photon [81]. When the accelerated particles reach the photosphere the magnetic loop footpoints get heated and plasma evaporates upward into the corona. This evaporated thermal plasma fills up coronal magnetic flux tubes, emitting soft X-rays.

A CME is a more extreme phenomenon that seems to be linked to the stellar flare process, when a magnetic field line remains unconnected during the magnetic reconnection and this may violently expand outwards leading to the ejection of coronal plasma [19]. From the observations of the Sun scientists found that CMEs are much more common during the solar maximum phase of the sunspot cycle, when the solar magnetic activity is at its highest intensity and the solar atmosphere comprises more magnetic structures (sunspots, active regions, etc.). This suggests that CMEs are more likely to be related to the amount of energy that is stored by the magnetic field over a long period of time (e.g. half of the magnetic cycle) rather than to flare formation [26].

1.4 M dwarfs

My PhD work is focused on the study of activity of field M dwarfs, i.e. stars that are not members of any star cluster. M dwarfs are the smallest and coolest stars located on the main-sequence (MS) and they are by far the most common in our Galaxy. These stars are invisible to the naked eye since they have absolute visual magnitudes fainter than 10, as the Hertzsprung-Russell (HR) diagram in Fig. 1.5 shows. In fact, they are located in the faintest red area of the MS. Their temperatures and masses vary from $2300 - 3900$ K and $0.1 - 0.7 \, M_\odot$, respectively, as it is reported in the table *A Modern Mean Dwarf Stellar Color and Effective Temperature Sequence* maintained by E. Mamajek at `http://www.pas.rochester.`

---

[4]Synchrotron radiation is emitted when relativistic charged particles are subject to an acceleration perpendicular to their velocity. When particles move with a mid relativistic velocity the emission is called gyrosynchrotron radiation [13].
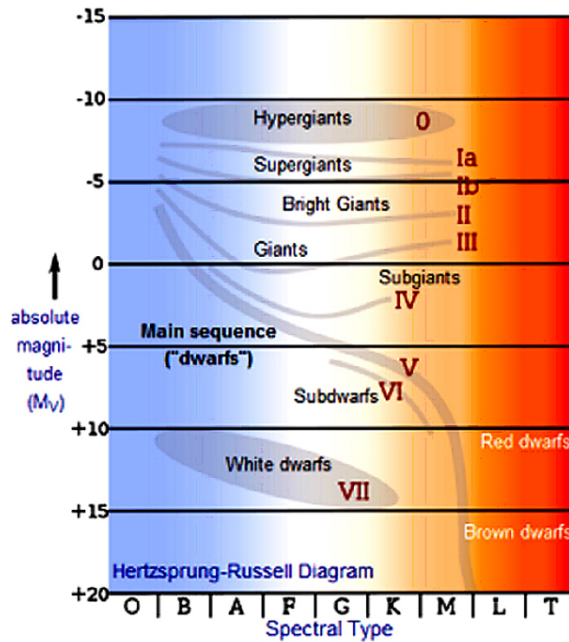
Fig. 1.5: Hertzsprung-Russell diagram shows the evolutionary stage of the stars. M dwarfs are located in the faintest red area of the main-sequence. Credit: Chandra observatory webpage.

`edu/~emamajek/EEM_dwarf_UBVIJHK_colors_Teff.txt`. It is known from stellar models that this sample of stars switches its internal structure from solar-like (inner radiative core + convective envelope) into fully convective. This transition occurs around $M_\star \approx 0.35\,M_\odot$, corresponds to SpT$\sim$ M 3.5 [11, 67]. In fully convective stars, when helium is produced by nuclear hydrogen burning, the internal chemical composition is constantly remixed throughout the whole star. This does not allow helium to build up at the core, therefore the period of fusion becomes longer. Thus, the evolution of low-mass M dwarfs is very slow, and they maintain a constant luminosity for trillions of years, besides very short term variability due to magnetic activity. Because of their slow evolution, no M dwarfs have yet been observed at stages more advanced than the main sequence.

In the last ~ 25 yrs new observations of M dwarfs indicate that many of these stars are surrounded by planets. In particular, Delfosse et al. [17] and Marcy et al. [44] were the first to discover giant planets around M dwarfs with Doppler measurements and precise radial velocity observations. In 2013 Bonfils et al. [8] with spectroscopy data from ESO/HARPS found "super-Earth" planets orbiting in what is called the *habitable zone* of a host M star, the distance within which liquid water can exist on the surface. Numerous scientists developed computational

models in order to study the planetary formation around low-mass stars. For example, Alibert and Benz [3] predicted that Earth-size planets are the most abundant, with a significant fraction of them having $10\,\%$ of the mass made of water, suggesting that many Earth-size planets orbiting M dwarf stars are covered with deep oceans.

Interesting is the case of the M8 dwarf TRAPPIST-1 in the constellation Aquarius that was discovered in 2000. In 2015 the host star-planet system of TRAPPIST-1 was studied by the group of Michaël Gillon with observations from the Transiting Planets and Planetesimals Small Telescope[5] (TRAPPIST) situated in the Chilean mountains at ESO's La Silla Observatory. With the photometric transit method, i.e. investigating the decrease of the emitted flux due to a planetary transit in front of the host star, they found 3 exoplanets orbiting around this star. Later, in 2017, NASA announced the discovery of 4 more planets observed with the *K*epler telescope[6]. Today the complete system counts 7 planets with the masses from between Mars-sized to slightly larger than Earth, and at least 3 of these planets are located within the habitable zone and may have liquid water on the surface [90].

Besides the discoveries regarding these planetary systems around M dwarfs, several factors may make the evolution of life unlikely. First, the habitable zone locates planets very close to the host-star such that the system planet$-$host star is tidally locked and consequently only one side of the planet would be in perpetual daylight. This could create enormous temperature variations from one side of the planet to the other, inconvenient for life to evolve [69, 32, 24]. Moreover, the variability due to the magnetic activity from M dwarf planet hosts may influence the formation and evolution of the planetary atmosphere as discussed above, preventing life to be formed. In fact, the atmosphere of our planet works as a shield against the UV radiation produced by the solar magnetic activity and the distance at which the Earth is located relative to the Sun contributes in preventing any destructive events for its atmosphere. As explained so far, stellar magnetic activity is linked to the parameters of the stars, in particular rotation and age play an important role in the determination of the emission from stellar coronae. For

---

[5]http://www.trappist.one/
[6]See Sect. 2.2.1 for the description of the Kepler mission.

this reason, the activity-rotation-age relation has been studied for decades and is still one of the most discussed topics related to the evolution of magnetic activity and exoplanet atmospheres.

1.5 Activity-rotation-age relation

The study of the rotation-age relation is based on "gyro-chronology", i.e. a method to estimate the age of low-mass stars from their rotation period. This approach was first proposed by Skumanich [83], when studying CaII emitted by the Sun and stars part of the Pleiades, Ursa Major, and Hyades, he found that the decay of the emission varies as the inverse square root of the age. Moreover, he found that the rotation period follows the same law, therefore it is a deterministic function of the age and mass of the stars ($P_{\mathrm{rot}} = P_{\mathrm{rot}}[t, M_\star]$). In this way, measuring two of these variables, e.g. rotation and mass, yields the third. From an observational point of view measurements of the stellar age are not easy to be taken, especially for M dwarfs. Age can be measured for stars in open clusters [e.g. Praesepe & Hyades, 18, 53], but there are no nearby open clusters older than $600\,\mathrm{Myr}$.

As explained in Sect. 1.1, the magnetic activity is powered by rotation when a convective envelope is present in the stellar structure. Moreover, according to Parker [57] stellar particles are able to escape the corona with supersonic speed as the gravity weakens with increasing distance from the star. These particles define what is called the "stellar wind", and when they leave the stellar corona they travel along the magnetic field lines causing the loss of stellar angular momentum, i.e. "magnetic breaking". The rotation is braked by this magnetized stellar wind, i.e. the rotational velocity decreases with age, as well as activity. This represents the physical scenario of the so called activity–rotation-age relation. As mentioned above, it is not always easy to observationally know the stellar age, especially for M dwarfs, therefore an alternative approach to study this relation is separately calibrating the activity-age and the activity-rotation relation. These two separate studies lead information on the magnetic braking and observational evidence of the stellar dynamo, respectively.

1.5.1 Activity-rotation relation
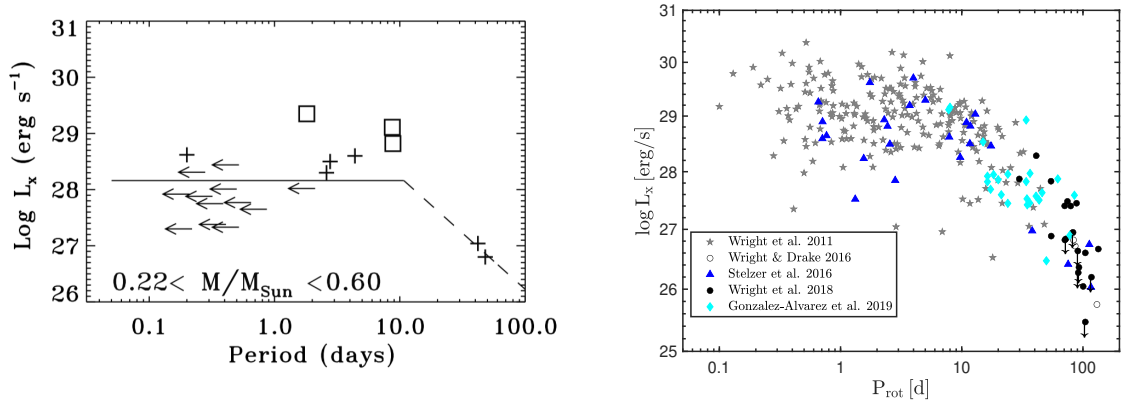
Fig. 1.6: The activity-rotation relation for M dwarfs in terms of $L_x - P_{rot}$, showing the two regimes: saturated for $P_{rot} \lesssim 10$ d and unsaturated for $P_{rot} \gtrsim 10$ d. **Left**: the historical results from Pizzolato et al. [62], with $v \sin i$ measurements of rotation periods translated into upper limits because of the unknown inclination of the stellar systems. **Right**: the results from the collection of literature data [92, 91, 84, 93, 25] that have been updated and homogenized in my work presented in Magaudda et al. [39] and explained here in Sect. 3.1.

Previous studies of the activity-rotation relation for M dwarf stars have shown two different regimes: the X-ray activity of fast-rotating stars does not depend on the rotation (saturated regime), and the X-ray activity of slowly rotating stars declines with increasing rotational period (unsaturated regime). This relation is typically expressed in terms of the X-ray luminosity (L_x) as a function of the rotational period (P_{rot}), or alternatively, in terms of the fractional X-ray luminosity (L_x/L_{bol}) as a function of the Rossby number (R_O). This latter one is a dimensionless number defined as the ratio between P_{rot} and convective turnover time (τ_{conv}), that is the time needed for a convective cell to rise to the surface. The use of R_O introduces a model dependence because τ_{conv} is not an observable parameter [92, 93, 39].

Noyes et al. [52] were the first to study the chromospheric activity of a sample of 13 slowly rotating MS stars, where also the Sun was included. Later, Pallavicini et al. [55] were the first to study the coronal X-ray emission as a function of spectroscopic velocity measurements ($v \sin i$) for a wide sample of stellar spectral type (O3-M). Then, Pizzolato et al. [62] studied this relation for late-type MS stars with X-ray data from the *ROSAT* satellite and P_{rot} values

calculated from $v \sin i$ measurements and translated into upper limits because of the unknown inclination of the stellar systems (see left panel in Fig. 1.6). About a decade later, many scientists investigated the activity-rotation relations for M dwarfs with rotational data extracted from photometric LCs that yield the spot rotation signal and, therefore, directly detect the rotation period without the ambiguity of inclination that is inherent in spectroscopic rotation measurements (see Sect. 1.3&1.2). In the right panel of Fig. 1.6 I show the results from Wright et al. [92], Wright and Drake [91], Stelzer et al. [84], Wright et al. [93], and González-Álvarez et al. [25] after I applied a meticulous updating and homogenizing process explained in detail in Sect. 3.1. The combination of this recent data allows a detailed analysis of the relation in the two regimes. In particular, compared to the historical relation from Pizzolato et al. [62], the unsaturated regime is now populated by a larger sample of stars leading to a thorough investigation of the rotation dependence for late-type stars.

1.5.2 Activity-age relation

Stars slow down their rotation throughout the main-sequence phase, during which they burn hydrogen into helium in the hot inner core. While they slow down, the dynamo efficiency also decreases over time. Studies of solar analogs with age in the range of $0.1 - 6.7$ Gyr show that the high-energy stellar emission varies with age with a power law [e.g. 69, 75]. In particular, the slope of the power law is monotonically steeper with the energy of the radiation, i.e. the stellar X-ray emission declines faster than the UV. From investigations of optical and UV activity [e.g. 16] it is known that the decrease of activity with age is linked to the flaring rate that also decreases with age. This suggests that the heating efficiency in corona decrease, therefore older MS stars have cooler coronae. Stelzer et al. [85] investigated the activity in the outer atmospheric layers (chromosphere, transition region and corona), analyzing the Hα, UV and X-ray emissions of ~ 160 M dwarfs within 10 pc. They found that the coronal X-ray emission of early M dwarfs (M0$-$M3) decreases faster than the UV radiation emitted from the chromosphere, analogous to the case of higher mass solar-type stars discussed above. Direct observations of the age-decay of activity are hampered for field M dwarfs, in fact

there are few stars with known age of $1\,\mathrm{Gyr}$ or older, as explained is Sect. 1.5. One way to predict the long-term evolution of stellar X-ray emission is combining observations with spin-down models [45, 1]. For example, to develop my work presented in Magaudda et al. [39], I made use of the angular momentum evolution models computed by Matt et al. [45]. The authors provide a stellar wind torque model based on the mass- and radius-dependencies of the stellar wind combined with the convective motions of the internal envelope of the star (see Sect. 1.1 for details on the stellar internal structure). In particular, they solved the angular momentum equation to obtain the spin rate of any star as a function of time for both the saturated and the unsaturated regime:

$$\Omega_\star = \Omega_i e^{-t/\tau_{\mathrm{sat}}} \qquad \text{(saturated)}$$
$$lim_{\Omega_\star << \Omega_{\mathrm{sat}}} \left(\frac{\Omega_\star}{\Omega_\odot} \right) \to \left(\frac{\tau_{\mathrm{unsat}}}{t} \right)^{\frac{1}{p}} \qquad \text{(unsaturated)}$$

where $\Omega_\star$ represents the angular velocity of the star, Ω_i is the initial stellar spin rate, t is the stellar age and τ_{sat} and τ_{unsat} are the times needed for a convective cell to rise into the outer atmosphere, respectively defined for the saturated and the unsaturated regime. In my work, we used three different initial spin rates ($P_{\mathrm{rot}} = 1.54$, 5.51 and $8.83\,\mathrm{d}$) from which we obtained the tracks for the age evolution of the rotation period computed in three mass bins (see Fig. 1.7), that I converted to a prediction of the activity-age relation. More details are found in Sect. 3.1, where I discuss the results of my work.

The study of stellar activity in terms of coronal X-ray emission and how it varies with stellar age is also of great importance in the field of planetary astrophysics and it brings information on how the formation and evolution of planetary atmosphere are affected by stellar X-rays. For example, how the atmosphere of a close-in planet is influenced by the radiation emitted by an active star and how the stellar emission affects its chemical composition is under investigation already for decades [31, 20, 61, 76]. In particular, atmospheric escape from a planet occurs when the molecular kinetic energy overcomes the gravitational energy, i.e. a molecule is moving faster than its escape velocity from the planet. There are thermal and non-thermal escape
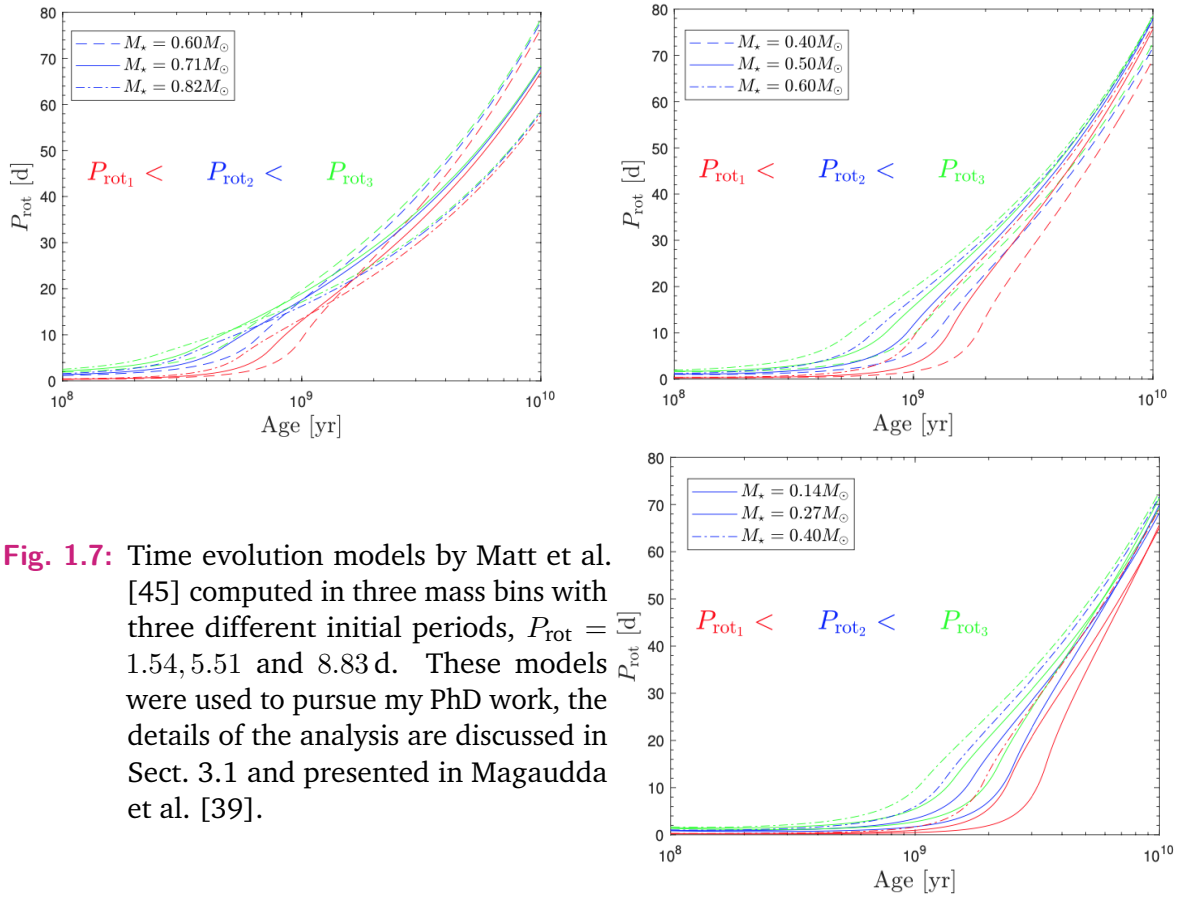
Fig. 1.7: Time evolution models by Matt et al. [45] computed in three mass bins with three different initial periods, $P_{\text{rot}} = 1.54, 5.51$ and 8.83 d. These models were used to pursue my PhD work, the details of the analysis are discussed in Sect. 3.1 and presented in Magaudda et al. [39].

mechanisms. For example, *Jeans escape* [81] is a thermal process that takes into account the variation of the particle kinetic energies. The average velocity of the particles in the planet atmosphere depends on the gas temperature, however when they collide with each other the velocity of the individual particles changes because of a gain or loss of kinetic energy. The kinetic energy is described by the Maxwell distribution, according to which particles in the high velocity tail escape more easily because their velocity is higher than the average one [81]. Another thermal mechanism is the *hydrodynamic escape* where the atmospheric particles absorb the thermal energy caused by the X-ray and extreme ultraviolet (XUV) radiation (e.g. from the host star) and they get accelerated until they reach the proper velocity in order to escape from the atmosphere of the planet [2]. To constrain these thermal mechanisms several aspects have to be taken into account. Heavier molecules are less likely to escape because at the same temperature they move slower than lighter molecules. Thus the gas atomic number already informs about the escape probability of an element, e.g. hydrogen is the element that most easily

escapes from an atmosphere. Also, at equal radius a planet with higher mass tends to have higher gravity, so the escape velocity tends to be greater and fewer particles will have the required amount of energy needed to escape [81]. In fact, gas giant planets still retain significant amounts of hydrogen, which on the other hand escape more readily from the Earth atmosphere. Last but not least, a close-in planet to the host star is more influenced by the emission of the host-star, therefore it has a hotter atmosphere with higher velocities and higher probability for the atmospheric particles to escape [20, 61].

A non-thermal escape mechanism is the *photo-evaporation*, according to which a molecule gets heated and accelerated by the interaction with a photon. If sufficient energy is provided, the molecule may reach the escape velocity of the planet and "evaporate" into space. Obviously, hydrogen is the most likely element to photoevaporate because the lower the mass number of the gas, the higher the velocity obtained by the interaction with a photon [46, 54, 94].

X-ray & Optical Satellites | 2

This project is based on the investigation of the X-ray activity-rotation relation with X-ray data from *XMM-Newton*, *Chandra* and *SRG-eROSITA* telescopes and photometric rotation periods from *K2* and *TESS* optical light curves. In addition, parallax and photometric measurements from the second data release of *Gaia* satellite (*Gaia*-DR2) have been adopted for the calculation of distances and stellar parameters. While the optical data are taken from catalogs or from the results of analyzes carried out by collaborators who actively contributed to the development of this work, the X-ray data were extracted and processed by me personally, which is why in the following sections I dedicate more space to the description of the X-ray satellites.

2.1 X-ray satellites

X-ray radiation is emitted from astronomical objects consisting of extremely hot gas at temperatures from about a million to hundreds of millions kelvin. Since the Earth's atmosphere absorbs the vast majority of X-rays, space-based telescopes are required to investigate the nature of X-ray sources. All X-ray satellites generally use Wolter telescopes consisting of nested cylindrical paraboloid and hyperboloid surfaces coated with iridium or gold and with incidence optics, i.e. mirrors that reflect X-rays at very shallow angles [88]. The data used for this project were obtained with *Chandra* and *XMM-Newton* satellites both launched in 1999, and with the extended ROentgen Survey with an Imaging Telescope Array (eROSITA) on board the Spectrum-Roentgen-Gamma (SRG) satellite launched in July 2019.

2.1.1 *Chandra*

The *Chandra* X-ray Observatory (CXO) is a space telescope launched by NASA on July 23, 1999 on board the Space Shuttle *Columbia*. Its orbit is highly elliptical and it allows to observe continuously for up to 55 hours during one total orbital period (65 hours) and with an angular resolution of $0.5''$. The Science Instrument Module (SIM) hosts two focal plane instruments (see Fig. 2.1), the Advanced CCD Imaging Spectrometer (ACIS) and the High Resolution Camera (HRC). When one
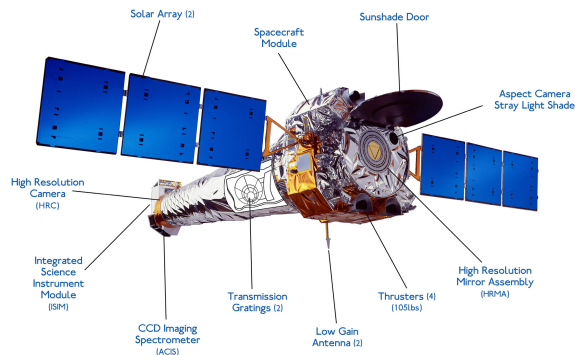
Fig. 2.1: *Chandra* X-ray Observatory carrying two focal plane spectrometers, ACIS and HRC, for high precision X-ray imaging and low resolution spectroscopy together with two high-resolution transmission gratings, the HETGS and LETGS. Credit: *Chandra* X-ray observatory webpage.

of these two instruments is called upon to take measurements the SIM rotates the requested spectrometer by putting it in front along the direction of the X-ray target. The incoming X-rays are focused by the mirrors into the focal plane, where the ACIS or HRC are aligned to capture the sharp images in photon counting mode.

The HRC has a unique imaging capability such that in combination with *Chandra* mirrors, it can detect image details as small as 0.5 arcseconds. The primary components of the HRC are two Micro-Channel Plates (MCP) that consist of a $10\,cm^2$ cluster of small lead-oxide glass tubes. The interaction between the tube coating and the detected X-rays releases electrons that are accelerated by high voltage throughout the tube. The continuous bouncing of the electrons off the tube walls generates more and more new particles until a cloud of about thirty million electrons is formed. A grid of wires detects this cloud of electrons allowing the determination of the incident X-ray position with great precision.

This instrument has no energy resolution so it does not provide the relevant measurements needed to carry out this PhD work, therefore data were requested with the Advanced charge-coupled devices (CCD) Imaging Spectrometer (ACIS).

The ACIS consists of 10 CCDs (Fig. 2.2) and provides low resolution images and spectra of the observed target. It operates in the photon energy range of $0.2-10$ keV and is capable of simultaneously capturing X-ray images and measuring the energy of the incoming signal. This instrument is very suitable for studying temperature variations in X-ray sources such as large clouds of hot gas in the intergalactic space, or investigating the chemical variations of supernova remnants. An example of a detected source with ACIS is presented in the right panel of

ACIS FLIGHT FOCAL PLANE
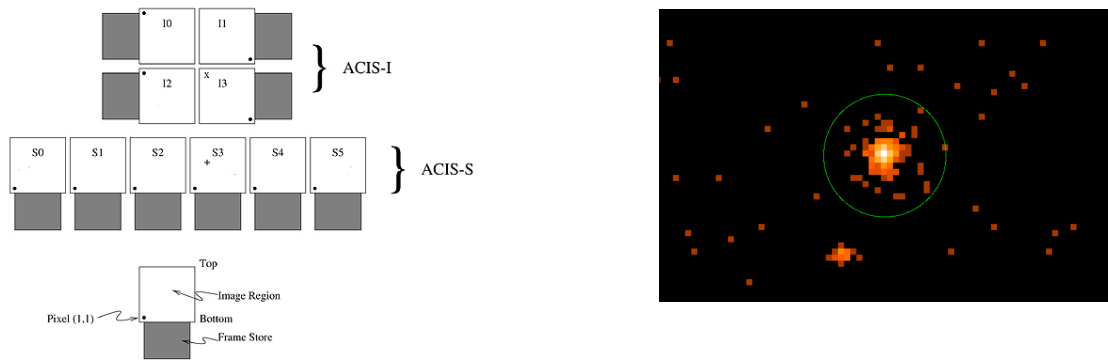
Fig. 2.2: **On the left**: a schematic representation of the 10 CCDs of ACIS [50]. **On the right**: an example of a *Chandra*/ACIS X-ray detection obtained with the CCD=S3 and with image size = $24''$ x $35''$.

Fig. 2.2 where the image shows one of the M dwarfs studied in this PhD project and detected in January 2016. The size of this image is $24''$ x $35''$ and the source is located at the center of CCD=S3.

In addition to ACIS and HRC two gratings are mounted on *Chandra* dedicated to high resolution spectroscopy: the High Energy Transmission Grating Spectrometer (HETGS) and the Low Energy Transmission Grating Spectrometer (LETGS). The incoming X-rays are diffracted by these gratings changing their direction depending on the emitted X-ray energy. By measuring the X-ray position with the HRC or ACIS, exact information on the energy responsible of the variation of the direction can be determined. The LETG grating is designed to cover an energy range of $0.08 - 2$ keV with a resolution of $40 - 2000$, while the HETG grating observes energies of $0.4 - 10$ keV and has a spectral resolution of $60 - 1000$. Since the M dwarfs investigated for my PhD project are too faint to be detected by these instruments, none of the gratings have been used for this work.

2.1.2 *XMM-Newton*

XMM-Newton is a mission of the European Space Agency (ESA) defined in the Horizon 2000 Programme and launched on December 10th, 1999. It consists of two X-ray spectrometers for low and high resolution measurements and a 30-cm optical/UV telescope. This allows *XMM-Newton* to offer simultaneous observations in two windows of the electromagnetic spectrum. The science instruments on board *XMM-Newton* are two types of European Photon Imaging Camera (EPIC/pn

and EPIC/MOS), two Reflection Grating Spectrometers (RGS) and an Optical Monitor (OM), see the spacecraft in Fig. 2.3. The three EPIC cameras (EPIC/pn,

Fig. 2.3: A schematic view of *XMM-Newton* satellite: three EPIC cameras and two RGS spectrometers are located in the focal plane, while the OM is located in the mirror support platform. Credit: *XMM-Newton* webpage.
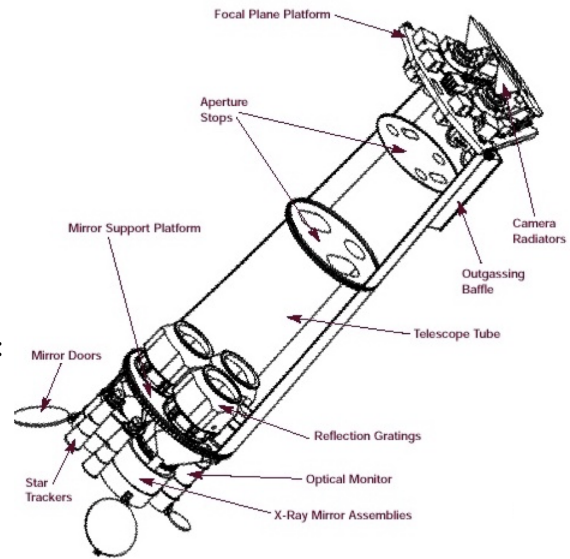
EPIC/MOS1 and EPIC/MOS2) and the two RGS spectrometers are located in the focal plane of the X-ray telescopes, while the OM is mounted on the mirror support platform alongside the X-ray mirror modules. All six *XMM-Newton* instruments can either work independently or simultaneously with the condition that the target brightness does not exceed the summed sensitivity. Two of the *XMM-Newton* X-ray telescopes are equipped with EPIC/MOS (Metal Oxide Semi- conductor) CCD arrays rotated by $90°$ with respect to each other, the third carries a PN-CCD camera called EPIC/PN. The EPIC cameras allow to perform extremely sensitive imaging observations over a field of view of $30'$ in the energy range of $0.2 - 12$ keV.

Analogous to the instruments on board *Chandra*, all EPIC CCDs operate in photon counting mode with a fixed and mode dependent frame readout frequency. The EPIC/pn has a larger quantum efficiency than the two EPIC/MOS cameras because its chips are back-illuminated, i.e. the wiring is located behind the photo-cathode layer so that the light directly strikes the photo-cathode layer without being influenced by passing through the wiring that causes reflection and reduces the input signal in front-illuminated chips. This increases the probability that an input photon is captured to $90\,\%$ [21]. Moreover, the EPIC/pn has a faster readout than the EPIC/MOS because each pixel column has its own readout node. The EPIC cameras can operate in different modes: (1) *full frame*, (2) *partial window*,

and (3) *timing mode*. In full frame mode all pixels are read out covering the whole field of view. Partial window mode is such that in the two EPIC/MOS part of the CCD chip is read out, 100×100 pixels in small window and 300×300 pixels in large window. In the EPIC/pn half of the area in all 12 CCDs is read out when it works in large window, while only one CCD is read out in small window. Finally, the timing operating mode for all EPIC cameras offers very high time resolution, keeping the spatial information only in one dimension.

The RGS design consists of two reflecting grating array units (RGA) and two focal plane camera units (RFC), located on the same X-ray telescope where the EPIC/MOS is mounted. Therefore, when an X-ray signal is captured by this instrument $40\,\%$ of the light is intercepted by the RGS and is deflected into a strip of CCD detectors offset from the telescope focal plane, while $44\,\%$ goes directly into the focal plane intercepted by the EPIC/MOS. The rest of the incoming signal is absorbed by the support of the instrumental structures. The RFC counts 9 large back-illuminated MOS CCDs, that register the position and the energy of each incoming photon. RGS can operate in *Spectroscopy* mode, where all CCDs are operating, or in *Small Window* mode, where only 1/4 CCDs is actively working. The energy range covered by the RGS is $0.35 - 2.5\,\mathrm{keV}$.
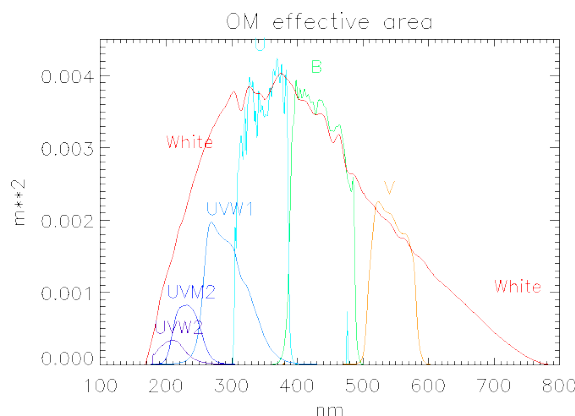
Fig. 2.4: The transmission curves of the six Optical Monitor filters [86].

In addition to the X-ray measurements, *XMM-Newton* provides also simultaneous optical/UV capability with the $30\,\mathrm{cm}$ OM co-aligned with the X-ray mirror modules. Due to the high sensitivity of the detector and the absence of atmospheric extinction, diffraction and background, the OM is well suited for observations of faint sources. However, it can easily be damaged by the emitted signal from optically very bright sources. The incoming light hits a pattern of mirrors, first

it is reflected by a primary onto a secondary that in turn reflects the light onto a rotatable $45°$ flat mirror located behind the primary where the light is focused onto one of two detector arrays. Along the light path, a filter wheel can be placed with several optical elements. These elements comprise two grisms and lenticular filters, i.e. three optical and three UV filters over the wavelength range $180 - 600$ nm (see the transmission curves in Fig. 2.4). The OM observes in *Fast mode*, where detailed information about the detected counts over time are provided so that the light curve of the target can be extracted and/or *Image* mode that provides more spatial coverage at the expense of timing information. When the OM observes in *I*mage mode it produces accumulated images, therefore there is no timing information of the incoming photons.

2.1.3 SRG-eROSITA

The *Spectrum-Roentgen-Gamma* (*SRG*) satellite is a space observatory developed by the Russian Academy of Science with the participation of Germany and launched the 13th July 2019. It carries two telescopes on board: the extended ROentgen Survey with an Imaging Telescope Array (eROSITA) built by Max Planck Institute for Extraterrestrial Physics (MPE) in Germany and the Astronomical Roentgen Telescope X-ray Concentrator (ART-XC) developed by Russia. To accomplish the scientific goals of this PhD among the telescopes on board SRG only eROSITA was used, therefore the following text is more focused on the description of this instrument.

During the first phase of commissioning and calibration (CalPV) eROSITA observed the sky while it was traveling to its final sky position, the stability point L2[1]. As part of the CalPV phase eROSITA provided its first X-ray catalog: the eROSITA Final Equatorial Depth Survey (eFEDS). Later, eROSITA started to scan the whole sky collecting data into the all-sky survey (eRASS) that will last for 4 years. The observation strategy consists on covering the whole sky every 6 months in the energy band of $0.2 - 10$ keV. The soft band $0.2 - 2$ keV is expected to be 25

---

[1]The L2-point lies on the opposite side of the Earth as it is seen from the Sun. The orbital motion of a spacecraft located here is balanced by the gravitational forces of these two astronomical objects, and the position behind the Earth prevents the distorted view of the sky that the spacecraft would have if located in the opposite side while passing in and out of the Earth's shadow.
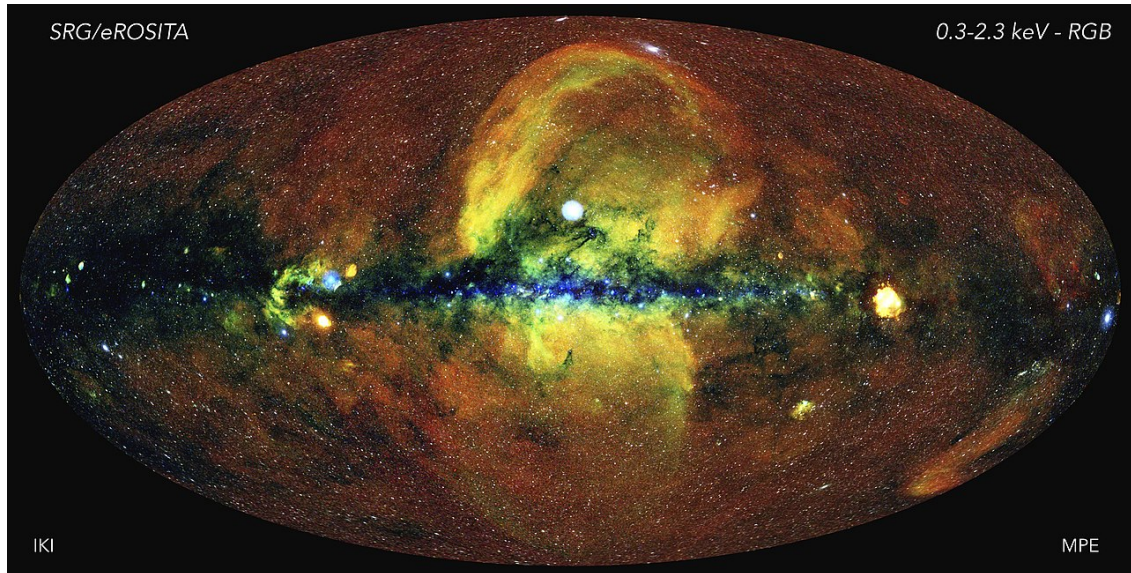
Fig. 2.5: **Top**: The first eROSITA all-sky map released in June 2020. During these 6 months of observation, eROSITA detected 77% Active Galactic Nuclei, 20% magnetically active stars and 2% galaxy clusters. The map shows also Milky Way structures such as the bubble in the bulge and the absorbing gas in the disk (in blue). Credit: J. Sanders, H. Brunner & eSASS team (MPE) / E. Churazov, M. Gilfanov (on behalf of IKI). **Right**: Schematic view of the eROSITA instrument: seven Wolter type telescopes observing in the broad energy band $0.2 - 10\,\mathrm{keV}$. Two star tracker and four radiators are needed to cool down the instrumental system [63].
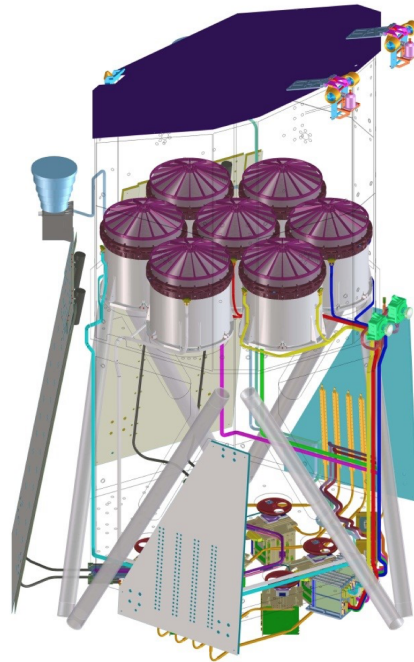
times more sensitive than the previous X-ray all-sky survey carried out with ROSAT [7] launched in 1990, and up to now eROSITA has already seen the entire sky 4 times. The primary aim of this new X-ray instrument is to study the large-scale structure of the Universe with the detection of large samples of galaxy clusters up to red-shifts $z > 1$. It will also lead to a revolutionary understanding of the evolution of supermassive black holes. Moreover, data from eROSITA will allow the investigation of a wide range of astrophysical phenomena such as X-ray binaries, active stars and diffuse emission within the Galaxy.

eROSITA is formed by a hexapod structure of seven identical Wolter-type telescope modules (TMs) with 54 nested gold-coated mirrors and a reading capacity of once per second with an accuracy of $3''$ [63]. The cameras were built at MPE and consist of X-ray CCDs manufactured from high-purity silicon. The instrumental system is constantly cooled to $-90°$ by 4 radiators located at the base of the telescope (see right panel in Fig. 2.5). The first all-sky survey (eRASS1) was completed on June 11, 2020 and announced officially by the MPE[2]. It contains data from 1.1 million sources among which $77\,\%$ are Active Galactic Nuclei, $20\,\%$ are stars with strong magnetically active coronae and $2\,\%$ are galaxy clusters. Few detections concern X-ray binaries, star forming regions, and supernova remnants. The map shown in Fig. 2.5 presents also some extended structures of the Milky Way such as the bubble in the bulge of the galaxy and the hot absorbing gas (in blue) in the disk.

2.2 Optical satellites

Optical observations are used in this PhD project as auxiliary data to pursue the scientific goals. In particular, light curves from the *K2* and *TESS* missions provided information about the stellar rotation, and *Gaia* parallaxes and photometry were needed to compute stellar distances and parameters.
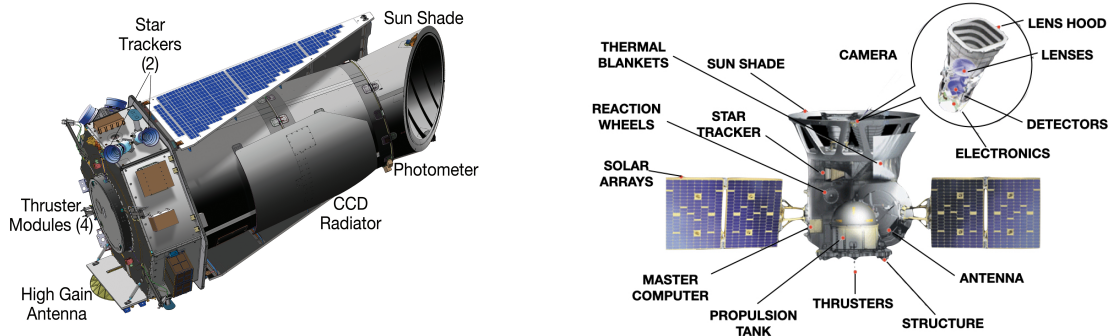
2.2.1 *K2* & *TESS*: rotation period measurements

The *Kepler* satellite was launched by NASA in 2009 with the scientific purpose of finding new transiting exoplanets by monitoring ~ 200.000 stars [9]. In addition,

---

[2]https://www.mpe.mpg.de/7461950/erass1-presskit

Fig. 2.6: **Left**: *Kepler* spacecraft launched by NASA in 2009. The only instrument on board *Kepler* is a 0.95 m Schmidt telescope with 105 x $105 \deg^2$ of field of view located right behind the Sun shade. **Right**: Scheme of *TESS* satellite launched by NASA in 2013. The cameras have a 24 x $24 \deg^2$ field of view with an aperture size of 10 cm in diameter each and are located at the front of the spacecraft. Credit: NASA and TESS webpage.

Kepler light curves can also be used to investigate stellar variability and eclipsing binaries.

The telescope contains a Schmidt camera with a front lens of 0.95 m and a 105 x $105 \deg^2$ of field of view. It collects optical photons every 29 minutes or 1 minute, called long and short cadence respectively, observing one region of the sky in the Cygnus and Lyra constellations. Its photometric precision is 20 part per million (ppm) in observing stars with $8 - 18$ *Kepler* magnitude between $430 - 890$ nm. In order to keep the solar panels always pointing to the Sun, the spacecraft rotated by $90°$ every 90 d, thus *Kepler* data are divided into $90-$day quarters.

The successor mission, Kepler Two-Wheel (K2), started right after the original *Kepler* mission ended (2013), due to the loss of two reaction wheels. In particular, the second mission was possible because engineers found a new way to stabilize the spacecraft, i.e. using the pressure of the solar light, allowing to do science for other three years where ~ 40.000 stars have been observed. During these last years, the telescope conducted 19 *Campaigns* of a duration of ~ 80 d where the satellite was kept fixed upon a single boresight position during each campaign.

The Transiting Exoplanet Survey Satellite (*TESS*) [70, 71] is an optical space telescope launched on April 18, 2018 by NASA and, similar to *Kepler*, designed
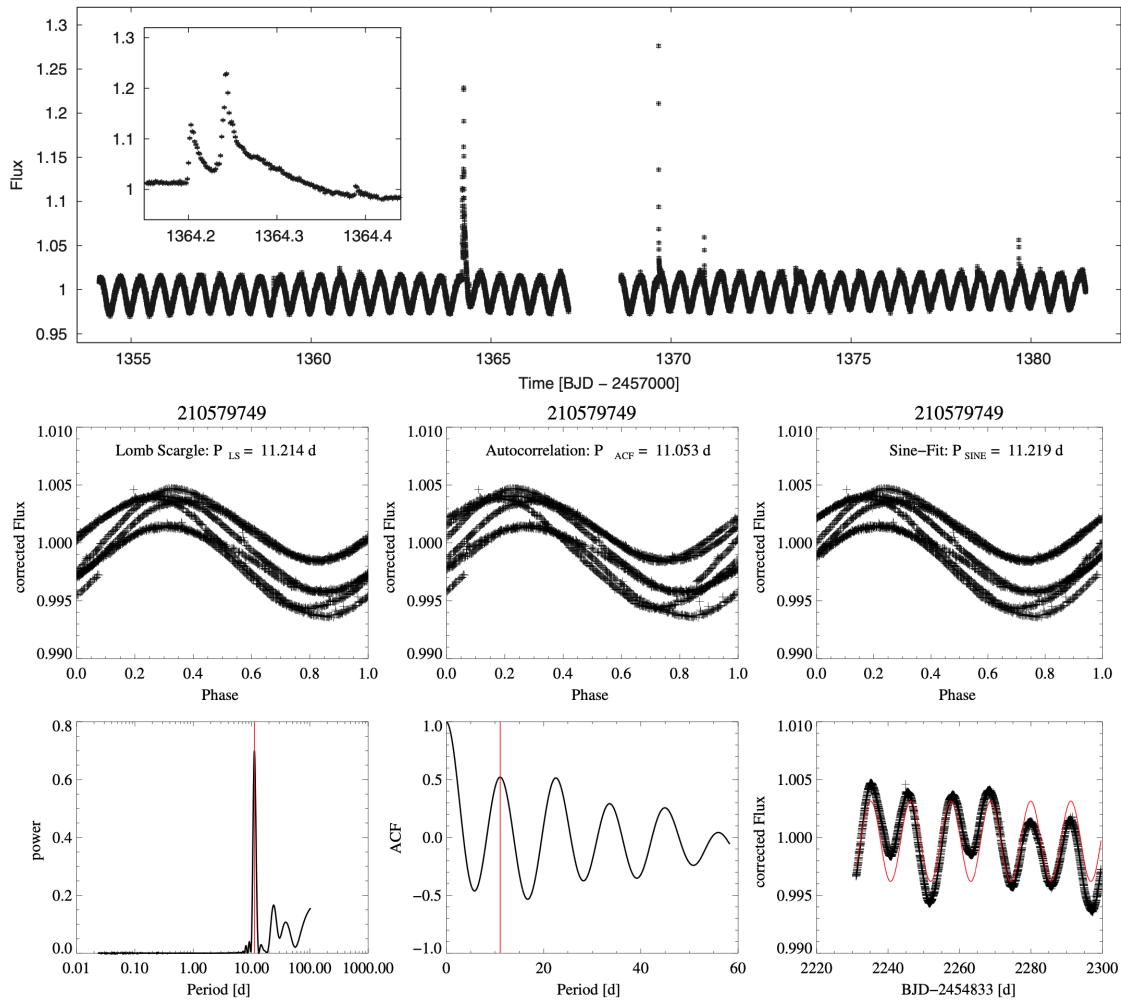
Fig. 2.7: **Top**: an example of a *TESS* light curve of an M dwarf, with a zoom into the flare detection around the timestamp 1364 min. **Middle**: the phase-folded light curves with the rotation periods determined from the three period search methods: Lomb-Scargle (LS), autocorrelation function (ACF), and sine-fitting. **Bottom**: The LS periodogram, the ACF and the original light curve with the superimposed sine fit [66].

to search for exoplanets using the transit method. It covers a sky area 400 times larger than that covered by the main *Kepler* mission. *TESS* is in a $2:1$ resonance with the Moon, meaning that it orbits around the Earth twice during the time in which the Moon orbits once. The instrument system on board *TESS* consists on four identical cameras with a field of view of 24x$96\,\mathrm{deg}^2$ each (see Fig 2.6). The detectors have a photometric precision amounting to 50 ppm in observing stars with $9-15$ *TESS* magnitude from the blue to the near-IR electromagnetic radiation, i.e. $600-1000\,\mathrm{nm}$.

TESS observes the sky in sectors of 24 x $96\,\mathrm{deg}^2$ each of which is monitored for two orbits around the Earth, i.e. $27\,\mathrm{d}$. During the prime mission, *TESS* observed the full sky divided into 26 different sectors of the sky and it delivered $\sim 11500\,\mathrm{LCs}$ [66]. An example of a *TESS* light curve of an M dwarf is shown in the top panel of Fig. 2.7, with a zoom on the flare detection around $\sim 1364\,\mathrm{min}$ [66]. *TESS*'s capability in observing the all-sky provides a huge amount of data, leading to a larger number of observed M dwarfs compared to *K2*. Therefore, this leads to a through investigation of the optical magnetic activity for variable M dwarfs through the analysis of the flare profiles in short- and long-cadence, 2 and 29 min between successive data points, respectively.

For the accomplishment of this PhD project, rotational periods from *K2* and *TESS* light curves were used. Although their extraction is not part of the tasks performed during this work, a general picture of what the procedure consists of is given here. As explained in Sect. 1.1, as a star rotates starspots are carried along the stellar photosphere and their contribution is visible in the emitted LC. In particular, their optical modulation is directly related to the rotational period of the star, so when the spot coverage on the photosphere is such as to periodically affect the emitted flux, it is possible to extract the rotational period. The determination of P_{rot} has been performed with three different methods, i.e. *Lomb-Scargle periodogram*[3] [LS, 37, 77], *autocorrelation function* (ACF), and *sine-fit*, and the adopted value is the average of the results coming from each procedure. The middle panels of Fig. 2.7 visualize the phase-folded light curves with the rotation periods resulting from the three methods, while the bottom panels show the LS periodogram, the ACF and the original light curve with the superimposed sine fit. The rotation periods extracted from *TESS* light curves are shorter than $\lesssim 15\,\mathrm{d}$ because it monitors a given sky field for about a month, and only periods shorter than about half the duration of a sector light curve are considered reliable [66].

---

[3]The LS is an algorithm for detecting and characterizing periodicity in sampled time-series. This method provides an estimate of the Fourier-like power relative to the period of oscillation [37, 77].

2.2.2 *Gaia* mission

Gaia is a space observatory developed by ESA, launched in 2013 and, similar to the *SRG*-eROSITA satellite, located in the Sun–Earth Lagrange point L2 [23]. The spacecraft is designed for astrometry with the aim to construct the largest and most precise 3D space catalog by collecting stellar parallaxes of astronomical objects, from which to calculate the distances.

The instrumentation on board *Gaia* consists of a Radial-Velocity Spectrometer (RVS), an astrometry instrument (Astro) and a photometry system (BP/RP) [72]. RVS is used to determine the velocity of astronomical objects along the line of sight through measurements of the Doppler shift affecting the spectral lines of high-resolution data between $847 - 874$ nm. Astro provides information on the angular position of stars with magnitude higher than 20 between $330 - 1050$ nm from which stellar parallaxes and proper motion are determined. Last but not least, BP/RP is composed of two low-resolution fused-silica prisms that disperse all the light incoming in the field of view, covering the blue ($330 - 680$ nm) and red ($640 - 1050$ nm) parts of the electromagnetic spectrum. The two instruments collect the spectral energy distribution providing information of the temperatures, gravities, metallicities, and reddenings for the detected targets. This project adopted distances and magnitudes from the second data release [*Gaia*-DR2, 22], however the early third data release (EDR3) was announced in December 2020 and lists almost twice as many astronomical sources as the DR2. The third data release is planned for the second half of 2022.

Results & Discussion 3

3.1 The rotation-activity-age relation of M dwarfs

In this chapter I summarize the results I obtained in the papers provided in Appendix [39, 41, 40, 48]. The primary investigation regards the study of the X-ray activity of M dwarfs and how it depends on the stellar rotation and mass. To achieve this goal, I constructed the largest and most homogeneous database of rotation and X-ray activity for field M dwarfs to date. Specifically, the sample presented in Magaudda et al. [39] consists of new X-ray data from the *XMM-Newton* and *Chandra* satellites requested for this study with P_{rot} extracted from *K2* mission LCs. These data have been combined with literature results that have been properly updated by me in order to homogenize all data sets (see left panel in Fig. 3.1).

The X-ray luminosities were calculated adopting *Gaia*-DR2 parallaxes [22] if reliable according to quality criteria defined by Lindegren et al. [34]. Photometric distances were adopted when *Gaia*-DR2 values were not validated, and they were calculated using photometric magnitudes from the USNO CCD AStrograph [UCAC4; 95] and the Two Micron All-Sky Survey [2MASS; 82] catalogs. The photometric magnitudes were applied to the empirical relation from Stelzer et al. [84] to compute the absolute magnitude in the Ks band (M_{Ks}) from $V - J$. Finally, M_{Ks} was used to calculate the stellar parameters using the empirical relations from Mann et al. [43, 42]. To adopt the same energy band as used in the works retrieved from the literature [e.g. 92, 91, 93], I extracted the X-ray luminosities (L_{x}) in the energy band of the *ROSAT* satellite ($0.1 - 2.4\,\mathrm{keV}$). As mentioned in Sect. 2.1.2, the recommended low-energy cutoff for *XMM-Newton* is $0.15\,\mathrm{keV}$, however I verified that including the counts between $0.10 - 0.15\,\mathrm{keV}$ would have changed the results only by $\approx 2\,\%$.

Besides the new rotation periods determined from *K2* light curves, the sample presented in Magaudda et al. [39] includes also rotation measurements from
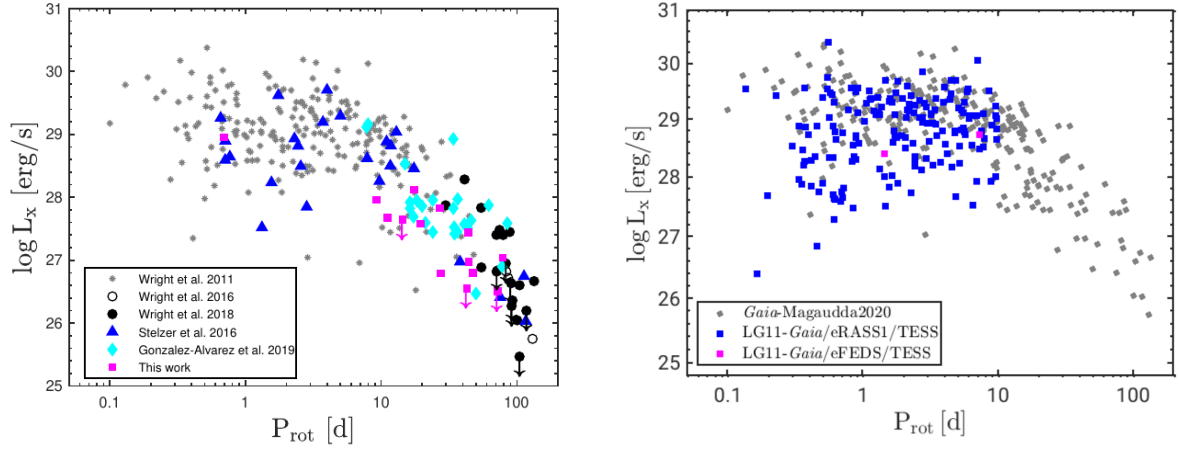
Fig. 3.1: The X-ray activity-rotation relation studied in my works presented in Magaudda et al. [39, 41]. **Left**: the sample includes homogenized and updated literature results combined with new X-ray data obtained with *XMM-Newton* and *Chandra* satellites and new rotation periods determined from *K2* light curves. **Right**: The activity rotation relation after including new results from eROSITA and *TESS* data analyzed in in my work presented in Magaudda et al. [41]. See Sect. 3.1 for more details.

the literature that were selected from the MEarth Project [91, 93], restricted to slower rotators in agreement with the choice of the authors to collect data for the uncorrelated regime, and measurements extracted from the spectroscopic lines of CaII H&K and Hα [25].

By performing a double power-law fit of the activity-rotation relation ($L_{\mathrm{x}} - P_{\mathrm{rot}}$), I found that the X-ray emission level in the saturated regime ($P_{\mathrm{rot}} \lesssim 10\,\mathrm{d}$) is not constant (also seen in the $L_{\mathrm{x}}/L_{\mathrm{bol}} - R_{\mathrm{O}}$ space). This result was previously observed by Reiners et al. [68], who investigated the $L_{\mathrm{x}}/L_{\mathrm{bol}} - R_{\mathrm{O}}$ dependence and suggested a possible residual mass-dependence of the dynamo in this regime. In particular, I observed a steeper slope in the saturated regime for low-mass M dwarfs ($M_\star \leq 0.4\,\mathrm{M_\odot}$) suggesting that the switch of the internal structure from solar-like to fully convective (see Sects. 1.1 & 1.4) may introduce a mass dependence of the dynamo.

I then combined the results from the fit of the $L_{\mathrm{x}} - P_{\mathrm{rot}}$ relation with spin-down models from Matt et al. [45] in order to quantify the age dependence of activity. The predicted L_{x}−age relation was then analyzed in three mass ranges adopted for the study of the activity-rotation relation (see Fig. 3.2), that separates very low mass M dwarfs (fully convective, $M_\star/M_\odot \leq 0.4$) from mid- ($0.4 \leq M_\star/M_\odot \leq 0.6$)
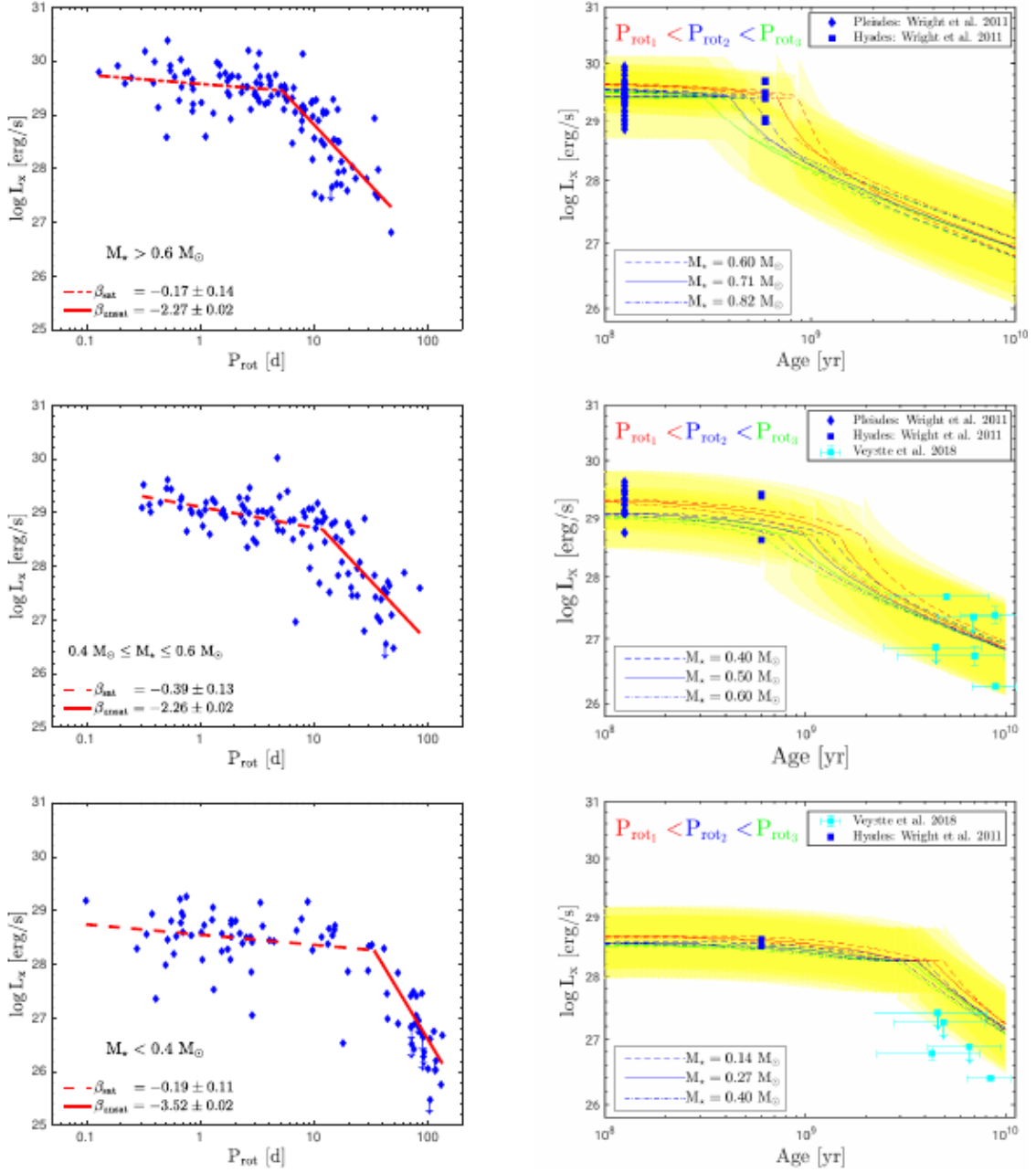
Fig. 3.2: Results presented in my work Magaudda et al. [39] where the empirical $L_x - P_{rot}$ relation with a double power law fit (left) is shown together with the predicted L_x−age relation (right). As explained in Sect. 3.1, the investigation is done in three mass bins and the calculated activity-age relation is compared to stars with known age and X-ray activity level. The yellow "tunnels" in the L_x−age relation show the vertical L_x−spread computed from the standard deviation of the observed activity-rotation relation.

and high-mass ($M_\star/M_\odot \geq 0.6$) M dwarfs, both of which are partially convective. Together with the predicted $L_\mathrm{x}-$age relation shown in Fig. 3.2 I included the standard deviation of the constructed X-ray luminosities in each mass range shown as a yellow "tunnel" in the same figure in order to consider the vertical $L_\mathrm{x}-$spread seen in the activity-rotation relation that comes from the mass-dependence of activity. The constructed relation places open cluster stars of known age [Pleiades and Hyades, 92] in the saturated regime and older field stars from Veyette and Muirhead [89] (age from ~ 4 to 9 Gyr) in the uncorrelated region of the relation. Interesting are the Hyades of the highest mass range that populate the area where the X-ray activity starts to drop. The presence of the $L_\mathrm{x}-$vertical spread in comparison to stars with different known age provides an estimate of the onset of the mass dependent activity decay. Considering the initial rotation periods used for the computation of the spin-down models from Matt et al. [45] and shown in Fig. 3.2 with the red, blue and green lines, we concluded that faster initial rotation periods provide the star to last longer in the saturated regime but once in the uncorrelated region the X-ray flux drops at higher rate than star with slower initial P_rot.

I contributed to the work presented in Modirrousta-Galian et al. [48] about the study of the exoplanet GJ 357b orbiting around the extremely inactive M dwarf GJ 357 M dwarf. Here, we compared my predicted $L_\mathrm{x}-$age relation, including the vertical $L_\mathrm{x}-$spread represented in light blue in Fig. 1 in Modirrousta-Galian et al. [48], with the empirical scaling relation $L_\mathrm{x}(t)$ by Penz and Micela [61]. This latter one was then used to find a lower limit for the age of GJ 357. The scaling law by Penz and Micela [61] is based on the observed X-ray luminosity functions of the Pleiades, Hyades and a nearby field star, Proxima Centauri. GJ 357 is a $\sim$M2 dwarf with $M_\star = 0.34\,\mathrm{M}_\odot$ [38], with a very low X-ray luminosity detected with *XMM-Newton*. According to my analysis (see Fig. 1 in Modirrousta-Galian et al. [48]), the L_x observed with *XMM-Newton* is comparable with that of the least active and slowest rotating M dwarfs in the same mass range, however it lies way below the predicted $L_\mathrm{x}-$age relation from my previous work [39]. This is a consequence of the overprediction of the X-ray emission for M dwarfs with very long rotation periods and masses between $0.14-0.4\,M_\odot$, caused by the spin-down

model of Matt et al. [45]. This model returns faster rotation periods than observed, causing these low-mass stars to stay longer in the saturated regime, contrary to what is seen from the comparison with stars of known age and X-ray luminosity (see, for example, the sample of Veyette and Muirhead [89] shown in the last panel to the right of Fig. 3.2). According to the comparison of the two $L_{\mathrm{x}}(t)$ relations [61, 39] with the observed X-ray luminosity of GJ 357 we found the lower limit of the age for this M dwarf planet host amounting to $\sim 5\,\mathrm{Gyr}$.

As explained in Sect. 1.4, the study of the X-ray emission from an active star defines habitability conditions for host planets. Numerous works have studied the evolution of planetary atmospheres to study how the X-ray emission from the host star affected the planets when they were still young. See Sect. 1.5.2 for more details of the possible phenomena caused by the interaction between the emission of the host star with the atmosphere of its planet. These studies are based on the determination of their atmospheric history by means of a backwards reconstruction of the XUV luminosities of the host star. In Modirrousta-Galian et al. [48] we conducted such a study based on the one-dimensional upper-atmosphere hydrodynamic model developed by Kubyshkina et al. [30]. These model grids are based on the photo-evaporation escape mechanism and computed for planets with masses from 1 to $39\,\mathrm{M}_\oplus$ and with a distance from the host star of $0.002 - 1.3\,\mathrm{au}$ that has a mass of $M_\star = 0.4 - 1.3\,\mathrm{M}_\odot$ and $L_{\mathrm{X}} = 10^{26} - 10^{30}\,\mathrm{erg/s}$. The goal was to reconstruct the atmospheric evolution of the planet-host GJ 357b, providing an upper bound of its initial atmospheric mass. Considering the derived age of the system ($\sim 5\,\mathrm{Gyr}$) and the lower bound of the X-ray luminosity derived from the scaling law of Penz and Micela [61] a linear extrapolation of the X-ray emission from the host GJ 357 M dwarf backwards in time. This resulted in an upper limit for the initial atmosphere mass of the planet-host GJ 357b amounting to $\sim 38\,\mathrm{M}_\oplus$ [48].

With the advent of the eROSITA and *TESS* missions, new X-ray data and photometric rotation periods have been added to the previous M dwarf sample for the study of the activity-rotation relation. In the right panel of Fig. 3.1 I present the new version of the relation where the contribution of eROSITA-*TESS* data almost doubled the statistics of the stellar sample in the saturation regime. In my paper
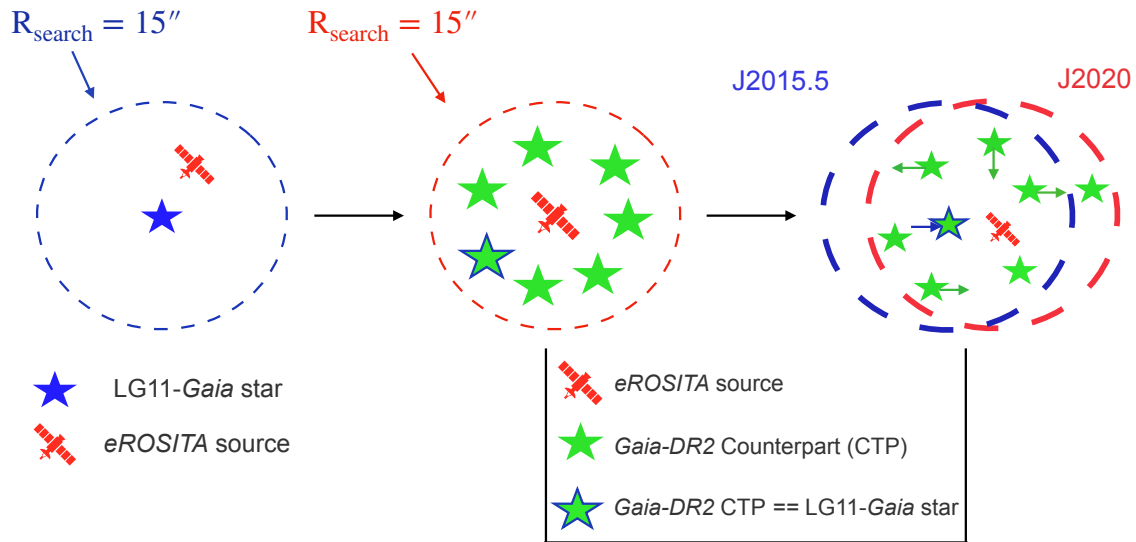
Fig. 3.3: A schematic view of the cross-match procedure adopted to ensure a solid identification of the correct eROSITA counterparts for the LG11-*Gaia* sample. First, I performed a direct match to search for the eROSITA detections around the optical coordinates (*Gaia*-DR2) within $15''$. Then, I ensured the association by performing a reverse match, i.e. looking for *Gaia*-DR2 sources around eROSITA coordinates with the same search radius. eROSITA and *Gaia* catalogs refer to two different observational epochs (2020 vs mid-2015), therefore I applied a P.M. correction once more in order to find the best counterpart. This latter was defined as the closest to an eROSITA source with the condition that the separation between the optical and the X-ray coordinates be smaller than 3 times the X-ray positional error.

Magaudda et al. [41] only stars with complete *Gaia*-DR2 data, i.e. distances and photometry, are considered and the calculation of stellar parameters is based on *Gaia*-DR2 distances and photometry. Therefore, I accordingly updated the data from my previous work discussed in Magaudda et al. [39] discarding all stars that do not satisfy this condition. In particular, all stars in this later work presented in Magaudda et al. [41] have stellar parameters based on M_{Ks} computed with *Gaia*-DR2 distances and the $V-$ band magnitude used in the empirical relations from Mann et al. [43, 42] is calculated with the conversion provided by Jao et al. [27], that makes use of *Gaia* magnitudes in the blue and red parts of the electromagnetic spectrum (see Sect. 2.2.2).

The search for eROSITA detections is performed through cross-matches between the SUPERBLINK proper motion catalog of nearby M dwarfs by Lépine and Gaidos [LG11, 33] with the eROSITA *Final Equatorial Depth Survey* (eFEDS) and the first eROSITA all-sky survey (eRASS1). The LG11 catalog was first associated

with the *Gaia*-DR2 catalog [22] and, after excluding all stars that do not have complete *Gaia*-DR2 data, the resulting LG11-*Gaia* catalog counts ~ 8500 stars.

To ensure the association of eROSITA counterparts to stars in the LG11-*Gaia* sample I carried out a meticulous cross-match. Its scheme is shown in Fig. 3.3. The first step was to perform a proper motion (hereafter P.M.) correction to the coordinates of the stars in the LG11-*Gaia* sample to the average observational epochs of eROSITA, i.e. the 5th November 2019 for eFEDS and the 10th March 2020 for eRASS1. The stars in this catalog are within 100 pc, thus, as for the case of Barnard's star discussed in Sect. 1.3, their proper motion[1] can reach more than $1''$ per year. After applying the P.M. correction, I conducted a "direct match" within $15''$ between the coordinates of the stars in the LG11-*Gaia* sample with those of eROSITA sources (see first panel from the left in Fig. 3.3). Then, I verified these eROSITA counterparts with a "reverse match", i.e. starting from eROSITA positions I looked for all possible *Gaia*-DR2 associations, with the same search radius adopted for the direct match. While there is one or few eROSITA counterparts around a LG11-*Gaia* star within $15''$ (in the "direct" match), several *Gaia* sources are located around a eROSITA source within the same region size (in the "reverse" match), among which the LG11-*Gaia* star is included (see middle panel of Fig. 3.3). An important aspect has to be taken into account: when matching with *Gaia* catalogs the output coordinates are refereed to its observational epoch, i.e. mid-2015 for DR2. Therefore, without further P.M. correction in this second step the comparison is done between two different observational epochs (*Gaia*-DR2 vs eROSITA, see rightmost panel in Fig. 3.3). Another P.M. correction has to be performed in order to identify the best counterpart, that we defined as the one that is closest to an eROSITA source and having the separation between *Gaia* and eROSITA coordinates less than 3 times the X-ray positional error. With this procedure, I confirmed the association of 14 LG11 stars with an eROSITA source detected during eFEDS and 673 during eRASS1. Finally, I confirmed my source identification by comparing my results with those from the NWAY algorithm, based on Bayesian statistics that assigns the probability of being the correct counterpart to every source within a

---

[1]The apparent motion of the star as it is seen from the center of mass of the solar system.
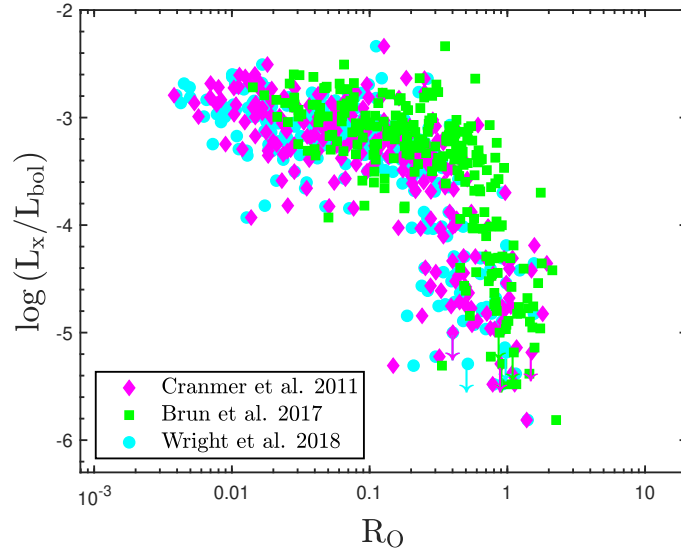
Fig. 3.4: Comparison of the activity-rotation relation obtained with different parametrizations of the convective turnover time (τ_{conv}) for the calculation of the Rossby number [14, 10, 93]. The model from Brun et al. [10] predicts a transition into the unsaturated regime at higher value of the Rossby number.

certain distance from the X-ray position. This algorithm is developed by other members of the eROSITA-DE consortium and discussed by Salvato et al. [73, 74].

The advent of eROSITA and *TESS* data allows to achieve unprecedented number statistics of fast rotating M dwarfs in the activity-rotation relation and to carry out an even more detailed analysis of the dependence of the X-ray activity on stellar mass mainly focused on M stars with rotation periods shorter than the transition to the uncorrelated regime.

3.2 Evidence of a spin-down evolution for M dwarfs

The study of the activity-rotation relation in terms of the fractional X-ray luminosity and Rossby number introduces a model dependence through the computation of τ_{conv}. In the work presented in Magaudda et al. [39] we studied how the $L_{\mathrm{x}}/L_{\mathrm{b}ol} - R_{\mathrm{O}}$ relation changes by adopting different $\tau_{\mathrm{c}onv}-$parametrizations (see Fig. 3.4). The main result is the shift towards higher R_{O} values of the transition into the unsaturated regime when adopting a $\tau_{\mathrm{conv}}-$parametrization compared to the others. Remarkable is the gap found for intermediate $L_{\mathrm{x}}/L_{\mathrm{bol}}-$level ($\sim -4$) also seen later when eROSITA and *TESS* have been included in the M dwarf sample
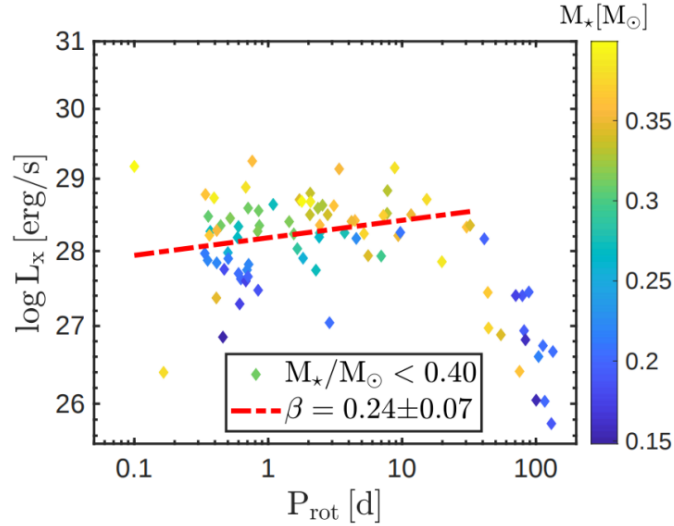
Fig. 3.5: Activity-rotation relation for low mass M dwarfs shown with a mass-color code together with the result of the power law fit performed for the saturated regime and presented in my paper Magaudda et al. [40]. The positive slope is a result of the paucity of low mass M dwarfs with intermediate rotation periods.

in Magaudda et al. [41] (right panel of Fig. 8 in Magaudda et al. [41]). This behavior requires further investigation, but it seems to suggest a phase of stalled rotational evolution followed by an episode of rapid spin-down [15, 47]. This might explain why there are more objects before the transition to the unsaturated regime, and a gap around the breaking point due to a subsequent rapid spin-down.

With the addition of new data from eROSITA and *TESS* I studied the saturated regime in the three mass bins, performing a power law fit in each mass range and neglecting the uncorrelated regime, where *TESS*-eROSITA combination does not enhance the number of stars. Surprisingly, the lowest mass bin of M dwarfs shows a positive slope (see Fig. 3.5), while a decrease of the X-ray level towards longer P_{rot} is seen in the saturated regime of high- and mid-mass M dwarfs. As shown in Fig. 3.5, in the saturated regime of the lowest mass bin the number of stars decreases while approaching the transition point into the uncorrelated regime. In particular, stars with $M_\star \leq 0.2\,M_\odot$ have either very short or very long rotation periods (beyond the saturated regime), leading to a paucity of interme-diate $P_{rot}-$values. This mass distribution distorts the fit, leading to an increase of the X-ray activity level in the saturated regime from short to mid-P_{rot}. *TESS* observations are able to cover these intermediate P_{rot} measurements, therefore an observational bias is not responsible of this finding. One explanation is a

mass-dependent P_{rot} effect, according to which very low mass M dwarfs experience a rapid loss of angular momentum that makes them skip the intermediate range of rotation periods and populate directly the unsaturated regime [51, 15, 47].

3.3 eROSITA sensitivity: improvements on the study of the X-ray emission

The analysis of the new X-ray data taken with eROSITA revealed its capability in detecting very faint M dwarfs. In fact, the advent of this new X-ray mission opened a new window for the investigation of the variability of coronal X-ray emission. Already the first eROSITA all-sky survey has a flux limit that is a factor $2 - 10$ fainter [see 6, 63] than the *ROSAT* 2 RXS catalog from which X-ray flux measurements were used in the work presented in Magaudda et al. [41]. This provided detections of faint M dwarfs that have been previously detected by *ROSAT* only because they were in a higher activity state.

Moreover, the distribution of eRASS1 detections shows a combined effect of the mass-dependence of the X-ray luminosity already discussed in Sect. 3.2 with the flux limit mentioned above: at a given distance the fraction of eRASS1 detections decreases for decreasing stellar masses. The majority of M dwarf X-ray detections are found in the unsaturated regime, where eROSITA is sensitive to detect stars with larger rotation periods that are not accessible to *TESS*. Last but not least, I found that early M stars are poorly sampled in the saturated regime, suggesting that they are already in an evolved phase of their spin-down history and probably located in the uncorrelated regime of the activity-rotation relation.

An interesting aspect of eROSITA is the all-sky survey measurements every 6 months that allow to investigate long-term variability. Already during the analysis of this PhD work I compared the two surveys available at that time (eFEDS and eRASS1) and I conducted a first variability study of the X-ray luminosity emitted by M dwarfs. Specifically, $2/6$ stars that have been detected during both eFEDS and eRASS1 observational epochs show a variation in the X-ray luminosity between the two surveys (see Fig. 12 in Magaudda et al. [41]).

3.4 Outlook

Considering the huge number of light curves available from the eROSITA all-sky surveys a thorough variability investigation is considered as future work. To put more constraints on X-ray flares and coronal variability experienced by M dwarfs a monitoring of their X-ray emission detected during the eROSITA surveys (every 6 months) will provide knowledge of the long-term variability of these stars. Moreover, a comparison with the numerous optical light curves provided by the *TESS* mission and combined with those from the future photometric space missions, such as PLATO, will enable multi-wavelength investigations that will be useful to characterize the flare formation at different stellar atmosphere depths. PLATO, the PLAnetary Transits and Oscillations of stars satellite, is planned to be launched in 2026 by ESA. It will observe two sky fields of $900\,\mathrm{deg}^2$ and it will provide new observations of more than ~ 3500 LG11-*Gaia* M dwarfs with a very short cadence amounting to $25\,\mathrm{s}$ [66].

Bibliography

[1] M. A. Agüeros, E. C. Bowsher, J. J. Bochanski, et al. "A New Look at an Old Cluster: The Membership, Rotation, and Magnetic Activity of Low-mass Stars in the 1.3 Gyr Old Open Cluster NGC 752". In: *ApJ* 862.1, 33 (July 2018), p. 33.

[2] Francis Albarède. "Hydrodynamic Escape". In: *Encyclopedia of Astrobiology*. Ed. by Muriel Gargaud, William M. Irvine, Ricardo Amils, et al. 2015, pp. 1145–1145.

[3] Y. Alibert and W. Benz. "Formation and composition of planets around very low mass stars". In: *A&A* 598, L5 (Feb. 2017), p. L5.

[4] Markus J. Aschwanden. *New Millennium Solar Physics*. Vol. 458. 2019.

[5] Sarbani Basu, H. M. Antia, and D. Narasimha. "Helioseismic measurement of the extent of overshoot below the solar convection zone". In: *MNRAS* 267 (Mar. 1994), p. 209.

[6] Th. Boller, M. J. Freyberg, J. Trümper, et al. "Second ROSAT all-sky survey (2RXS) source catalogue". In: *A&A* 588, A103 (Apr. 2016), A103.

[7] Boller, Th., Freyberg, M. J., Trümper, J., et al. "Second ROSAT all-sky survey (2RXS) source catalogue". In: *A&A* 588 (2016).

[8] X. Bonfils, X. Delfosse, S. Udry, et al. "The HARPS search for southern extra-solar planets. XXXI. The M-dwarf sample". In: *A&A* 549, A109 (Jan. 2013), A109.

[9] William J. Borucki, David Koch, Gibor Basri, et al. "Kepler Planet-Detection Mission: Introduction and First Results". In: *Science* 327.5968 (Feb. 2010).

[10] Allan Sacha Brun, Antoine Strugarek, Jacobo Varela, et al. "On Differential Rotation and Overshooting in Solar-like Stars". In: *ApJ* 836.2, 192 (Feb. 2017), p. 192.

[11] Gilles Chabrier and Isabelle Baraffe. "Structure and evolution of low-mass stars". In: *A&A* 327 (Nov. 1997), pp. 1039–1053.

[12] P. Charbonneau, J. Christensen-Dalsgaard, R. Henning, et al. "Helioseismic Constraints on the Structure of the Solar Tachocline". In: *ApJ* 527.1 (Dec. 1999), pp. 445–460.

[13] James J. Condon and Scott M. Ransom. *Essential Radio Astronomy*. 2016.

[14] Steven R. Cranmer and Steven H. Saar. "Testing a Predictive Theoretical Model for the Mass Loss Rates of Cool Stars". In: *ApJ* 741.1 (Nov. 2011).

[15] Jason Lee Curtis, Marcel A. Agüeros, Stephanie T. Douglas, and Søren Meibom. "A Temporary Epoch of Stalled Spin-down for Low-mass Stars: Insights from NGC 6811 with Gaia and Kepler". In: *ApJ* 879.1, 49 (July 2019), p. 49.

[16] James R. A. Davenport, Kevin R. Covey, Riley W. Clarke, et al. "The Evolution of Flare Activity with Stellar Age". In: *ApJ* 871.2, 241 (Feb. 2019), p. 241.

[17] X. Delfosse, T. Forveille, M. Mayor, et al. "The closest extrasolar planet. A giant planet around the M4 dwarf GL 876". In: *A&A* 338 (Oct. 1998), pp. L67–L70.

[18] S. T. Douglas, M. A. Agüeros, K. R. Covey, et al. "The Factory and the Beehive. II. Activity and Rotation in Praesepe and the Hyades". In: *ApJ* 795.2, 161 (Nov. 2014).

[19] Oddbjørn Engvold, Jean-Claude Vial, and Andrew Skumanich. *The Sun as a Guide to Stellar Physics*. 2019.

[20] N. V. Erkaev, Yu. N. Kulikov, H. Lammer, et al. "Roche lobe effects on the atmospheric loss from "Hot Jupiters"". In: *A&A* 472.1 (Sept. 2007), pp. 329–334.

[21] ESA: XMM-Newton SOC. *Users Guide to the XMM-Newton Science Analysis System*. Vol. 17. 2022.

[22] Gaia Collaboration, C. Babusiaux, F. van Leeuwen, et al. "Gaia Data Release 2. Observational Hertzsprung-Russell diagrams". In: *A&A* 616 (Aug. 2018).

[23] Gaia Collaboration, T. Prusti, J. H. J. de Bruijne, et al. "The Gaia mission". In: *A&A* 595, A1 (Nov. 2016).

[24] F. Gallet, C. Charbonnel, L. Amard, et al. "Impacts of stellar evolution and dynamics on the habitable zone: The role of rotation and magnetic activity". In: *A&A* 597 (2017).

[25] E. González-Álvarez, G. Micela, J. Maldonado, et al. "HADES RV Programme with HARPS-N at TNG. X. The non-saturated regime of the stellar activity-rotation relationship for M dwarfs". In: *A&A* 624, A27 (Apr. 2019), A27.

[26] Timothy Howard. *Coronal Mass Ejections: An Introduction*. Vol. 376. 2011.

[27] Wei-Chun Jao, Todd J Henry, Douglas R Gies, and Nigel C Hambly. "A Gap in the Lower Main Sequence Revealed by Gaia Data Release 2". In: *ApJ* 861.1 (2018), p. L11.

[28] James A. Klimchuk. "On Solving the Coronal Heating Problem". In: *Sol. Phys.* 234.1 (Mar. 2006), pp. 41–77.

[29] F. Krause and K. -H. Raedler. *Mean-field magnetohydrodynamics and dynamo theory*. 1980.

[30] D. Kubyshkina, L. Fossati, N. V. Erkaev, et al. "Overcoming the Limitations of the Energy-limited Approximation for Planet Atmospheric Escape". In: *ApJ* 866.2, L18 (Oct. 2018), p. L18.

[31] H. Lammer, F. Selsis, I. Ribas, et al. "Atmospheric Loss of Exoplanets Resulting from Stellar X-Ray and Extreme-Ultraviolet Heating". In: *ApJ* 598.2 (Dec. 2003), pp. L121–L124.

[32] Helmut Lammer, Manuel Güdel, Yuri Kulikov, et al. "Variability of solar/stellar activity and magnetic field and its influence on planetary atmosphere evolution". In: *Earth, Planets and Space* 64.2 (2012).

[33] Sébastien Lépine and Eric Gaidos. "An All-sky Catalog of Bright M Dwarfs". In: *AJ* 142.4, 138 (Oct. 2011), p. 138.

[34] L. Lindegren, J. Hernández, A. Bombrun, et al. "<i>Gaia</i> Data Release 2". In: *A&A* 616 (2018), A2.

[35] J. L. Linsky, S. P. Worden, W. McClintock, and R. M. Robertson. "Stellar model chromospheres. X. High-resolution, absolute flux profiles of the Ca II H and K lines in stars of spectral types F0 - M2." In: *ApJS* 41 (1979).

[36] Jeffrey L. Linsky. "Stellar Model Chromospheres and Spectroscopic Diagnostics". In: *ARA&A* 55.1 (Aug. 2017), pp. 159–211.

[37] N. R. Lomb. "Least-Squares Frequency Analysis of Unequally Spaced Data". In: *Ap Space Sci.* 39 (Feb. 1976).

[38] R. Luque, E. Pallé, D. Kossakowski, et al. "Planetary system around the nearby M dwarf GJ 357 including a transiting, hot, Earth-sized planet optimal for atmospheric characterization". In: *A&A* 628, A39 (Aug. 2019), A39.

[39] E. Magaudda, B. Stelzer, K. R. Covey, et al. "Relation of X-ray activity and rotation in M dwarfs and predicted time-evolution of the X-ray luminosity". In: *A&A* 638, A20 (June 2020), A20.

[40] E. Magaudda, B. Stelzer, and St. Raetz. "First eROSITA-TESS results for M dwarfs: Mass dependence of the X-ray activity rotation relation and an assessment of sensitivity limits". In: *Astronomische Nachrichten* 343.8 (Oct. 2022).

[41] E. Magaudda, B. Stelzer, St. Raetz, et al. "First eROSITA study of nearby M dwarfs and the rotation-activity relation in combination with TESS". In: *A&A* 661, A29 (2022).

[42] Andrew W. Mann, Gregory A. Feiden, Eric Gaidos, Tabetha Boyajian, and Kaspar von Braun. "ERRATUM: "HOW TO CONSTRAIN YOUR M DWARF: MEASURING EFFECTIVE TEMPERATURE, BOLOMETRIC LUMINOSITY, MASS, AND RADIUS" (ApJ, 804, 64)". In: *ApJ* 819.1 (Mar. 2016).

[43] Andrew W. Mann, Gregory A. Feiden, Eric Gaidos, Tabetha Boyajian, and Kaspar von Braun. "How to Constrain Your M Dwarf: Measuring Effective Temperature, Bolometric Luminosity, Mass, and Radius". In: *ApJ* 804.1, 64 (May 2015), p. 64.

[44] Geoffrey W. Marcy, R. Paul Butler, Steven S. Vogt, Debra Fischer, and Jack J. Lissauer. "A Planetary Companion to a Nearby M4 Dwarf, Gliese 876". In: *ApJ* 505.2 (Oct. 1998), pp. L147–L149.

[45] Sean P. Matt, A. Sacha Brun, Isabelle Baraffe, Jérôme Bouvier, and Gilles Chabrier. "The Mass-dependence of Angular Momentum Evolution in Sun-like Stars". In: *ApJ* 799.2, L23 (Jan. 2015), p. L23.

[46] G. Mellema, A. C. Raga, J. Canto, et al. "Photo-evaporation of clumps in planetary nebulae". In: *A&A* 331 (Mar. 1998), pp. 335–346.

[47] Travis S. Metcalfe and Ricky Egeland. "Understanding the Limitations of Gyrochronology for Old Field Stars". In: *ApJ* 871.1, 39 (Jan. 2019), p. 39.

[48] D. Modirrousta-Galian, B. Stelzer, E. Magaudda, et al. "GJ 357 b. A super-Earth orbiting an extremely inactive host star". In: *A&A* 641 (Sept. 2020).

[49] V. M. Nakariakov, V. Pilipenko, B. Heilig, et al. "Magnetohydrodynamic Oscillations in the Solar Corona and Earth's Magnetosphere: Towards Consolidated Understanding". In: *SSRv* 200.1-4 (Apr. 2016), pp. 75–203.

[51] Elisabeth R. Newton, Jonathan Irwin, David Charbonneau, et al. "The Hα Emission of Nearby M Dwarfs and its Relation to Stellar Rotation". In: *ApJ* 834.1, 85 (Jan. 2017), p. 85.

[52] R. W. Noyes, N. O. Weiss, and A. H. Vaughan. "The relation between stellar rotation rate and activity cycle periods." In: *ApJ* 287 (Dec. 1984), pp. 769–773.

[53] Alejandro Núñez, Marcel A. Agüeros, Kevin R. Covey, et al. "Linking Stellar Coronal Activity and Rotation at 500 Myr: A Deep Chandra Observation of M37". In: *ApJ* 809.2, 161 (Aug. 2015), p. 161.

[54] James E. Owen, Barbara Ercolano, and Cathie J. Clarke. "Protoplanetary disc evolution and dispersal: the implications of X-ray photoevaporation". In: *MNRAS* 412.1 (Mar. 2011), pp. 13–25.

[55] R. Pallavicini, L. Golub, R. Rosner, et al. "Relations among stellar X-ray emission observed from Einstein, stellar rotation and bolometric luminosity." In: *ApJ* 248 (1981), pp. 279–290.

[56] E. N. Parker. *Cosmical magnetic fields*. London: Oxford University Press, 1979.

[57] E. N. Parker. "Dynamics of the Interplanetary Gas and Magnetic Fields." In: *ApJ* 128 (Nov. 1958), p. 664.

[58] E. N. Parker. "Nanoflares and the Solar X-Ray Corona". In: *ApJ* 330 (July 1988).

[59] E. N. Parker. "Stimulated dissipation of magnetic discontinuities and the origin of solar flares." In: *Sol. Phys.* 111.2 (Sept. 1987), pp. 297–308.

[60] E. N. Parker. "Topological Dissipation and the Small-Scale Fields in Turbulent Gases". In: *ApJ* 174 (June 1972).

[61] T. Penz and G. Micela. "X-ray induced mass loss effects on exoplanets orbiting dM stars". In: *A&A* 479.2 (Feb. 2008), pp. 579–584.

[62] N. Pizzolato, A. Maggio, G. Micela, S. Sciortino, and P. Ventura. "The stellar activity-rotation relationship revisited: Dependence of saturated and non-saturated X-ray emission regimes on stellar mass for late-type dwarfs". In: *A&A* 397 (2003), pp. 147–157.

[63] P. Predehl, R. Andritschke, V. Arefiev, et al. "The eROSITA X-ray telescope on SRG". In: *A&A* 647, A1 (2021).

[64] Eric Priest. *Magnetohydrodynamics of the Sun*. 2014.

[65] St. Raetz, B. Stelzer, M. Damasso, and A. Scholz. "Rotation-activity relations and flares of M dwarfs with K2 long- and short-cadence data". In: *A&A* 637, A22 (2020), A22.

[66] Stefanie Raetz, Beate Stelzer, and Alexander Scholz. "The rotation-activity relation of M dwarfs: From K2 to TESS and PLATO". In: *AN* 341.5 (2020), pp. 519–556.

[67] A. Reiners and G. Basri. "On the magnetic topology of partially and fully convective stars". In: *A&A* 496.3 (Mar. 2009), pp. 787–790.

[68] A. Reiners, M. Schüssler, and V. M. Passegger. "Generalized Investigation of the Rotation-Activity Relation: Favoring Rotation Period instead of Rossby Number". In: *ApJ* 794.2, 144 (Oct. 2014), p. 144.

[69] Ignasi Ribas, Edward F. Guinan, Manuel Güdel, and Marc Audard. "Evolution of the Solar Activity over Time and Effects on Planetary Atmospheres. I. High-Energy Irradiances (1-1700 Å)". In: *ApJ* 622.1 (Mar. 2005), pp. 680–694.

[70] George R. Ricker, Joshua N. Winn, Roland Vanderspek, et al. "Transiting Exoplanet Survey Satellite (TESS)". In: *Space Telescopes and Instrumentation 2014: Optical, Infrared, and Millimeter Wave*. Ed. by Jr. Oschmann Jacobus M., Mark Clampin, Giovanni G. Fazio, and Howard A. MacEwen. Vol. 9143. Society of Photo-Optical Instrumentation Engineers (SPIE) Conference Series. Aug. 2014, 914320.

[71] George R. Ricker, Joshua N. Winn, Roland Vanderspek, et al. "Transiting Exoplanet Survey Satellite (TESS)". In: *Journal of Astronomical Telescopes, Instruments, and Systems* 1 (2015).

[72] D. Risquez, F. van Leeuwen, and A. G. A. Brown. "Dynamical attitude model for Gaia". In: *Experimental Astronomy* 34.3 (2012), pp. 669–703.

[73] M. Salvato, J. Buchner, T. Budavári, et al. "Finding counterparts for all-sky X-ray surveys with NWAY: a Bayesian algorithm for cross-matching multiple catalogues". In: *MNRAS* 473.4 (Feb. 2018), pp. 4937–4955.

[74] M. Salvato, J. Wolf, T. Dwelly, et al. "The eROSITA Final Equatorial-Depth Survey (eFEDS): Identification and characterization of the counterparts to the point-like sources". In: *A&A submitted* (2021).

[75] J. Sanz-Forcada, G. Micela, I. Ribas, et al. "Estimation of the XUV radiation onto close planets and their evaporation". In: *A&A* 532, A6 (Aug. 2011), A6.

[76] J. Sanz-Forcada, I. Ribas, G. Micela, et al. "A scenario of planet erosion by coronal radiation". In: *A&A* 511, L8 (Feb. 2010), p. L8.

[77] J. D. Scargle. "Studies in astronomical time series analysis. II. Statistical aspects of spectral analysis of unevenly spaced data." In: *ApJ* 263 (Dec. 1982).

[78]C. J. Schrijver, J. Cote, C. Zwaan, and S. H. Saar. "Relations between the Photospheric Magnetic Field and the Emission from the Outer Atmospheres of Cool Stars. I. The Solar CA II K Line Core Emission". In: *ApJ* 337 (Feb. 1989), p. 964.

[79]M. Schwabe. "Die Sonne. Von Herrn Hofrath Schwabe". In: *Astronomische Nachrichten* 20.17 (Mar. 1843), p. 283.

[80]Steven N. Shore. *An introduction to astrophysical hydrodynamics*. 1992.

[81]Steven N. Shore. *The Tapestry of Modern Astrophysics*. 2002.

[82]M. F. Skrutskie, R. M. Cutri, R. Stiening, et al. "The Two Micron All Sky Survey (2MASS)". In: *AJ* 131.2 (Feb. 2006).

[83]A. Skumanich. "Time Scales for Ca II Emission Decay, Rotational Braking, and Lithium Depletion". In: *ApJ* 171 (Feb. 1972), p. 565.

[84]B. Stelzer, M. Damasso, A. Scholz, and S. P. Matt. "A path towards understanding the rotation-activity relation of M dwarfs with K2 mission, X-ray and UV data". In: *MNRAS* 463.2 (Dec. 2016), pp. 1844–1864.

[85]B. Stelzer, A. Marino, G. Micela, J. López-Santiago, and C. Liefke. "The UV and X-ray activity of the M dwarfs within 10 pc of the Sun". In: *MNRAS* 431.3 (May 2013), pp. 2063–2079.

[87]John H. Thomas and Nigel O. Weiss. *Sunspots and Starspots*. 2008.

[88]Joachim E. Trümper and Günther Hasinger. *The Universe in X-Rays*. 2008.

[89]Mark J. Veyette and Philip S. Muirhead. "Chemo-kinematic Ages of Eccentric-planet-hosting M Dwarf Stars". In: *ApJ* 863.2, 166 (Aug. 2018), p. 166.

[90]David J. Wilson, Cynthia S. Froning, Girish M. Duvvuri, et al. "The Mega-MUSCLES Spectral Energy Distribution of TRAPPIST-1". In: *ApJ* 911.1, 18 (Apr. 2021), p. 18.

[91]Nicholas J. Wright and Jeremy J. Drake. "Solar-type dynamo behaviour in fully convective stars without a tachocline". In: *Nature* 535.7613 (2016).

[92]Nicholas J. Wright, Jeremy J. Drake, Eric E. Mamajek, and Gregory W. Henry. "The Stellar-activity-Rotation Relationship and the Evolution of Stellar Dynamos". In: *ApJ* 743.1 (2011).

[93]Nicholas J. Wright, Elisabeth R. Newton, Peter K. G. Williams, Jeremy J. Drake, and Rakesh K. Yadav. "The stellar rotation-activity relationship in fully convective M dwarfs". In: *MNRAS* 479.2 (2018).

[94]Yanqin Wu and Yoram Lithwick. "Density and Eccentricity of Kepler Planets". In: *ApJ* 772.1, 74 (July 2013), p. 74.

[95]N. Zacharias, C. T. Finch, T. M. Girard, et al. "VizieR Online Data Catalog: UCAC4 Catalogue (Zacharias+, 2012)". In: *VizieR Online Data Catalog*, I/322A (July 2012).

Webseiten

[50] NASA's flagship mission for X-ray astronomy. *Chandra X-ray Observatory*. URL: `http://www.gnu.org/licenses/gpl.html`.

[86] Team XMM-Newton Community Support. *XMM-Newton Users Handbook*. 2021. URL: `https://chandra.si.edu/about/science_instruments.html`.

Appendix: published papers

Astronomy
&
Astrophysics

Relation of X-ray activity and rotation in M dwarfs and predicted time-evolution of the X-ray luminosity[★]

E. Magaudda[1], B. Stelzer[1,2], K. R. Covey[3], St. Raetz[1], S. P. Matt[4], and A. Scholz[5]

[1] Institut für Astronomie und Astrophysik, Eberhard-Karls Universität Tübingen, Sand 1, 72076 Tübingen, Germany
e-mail: magaudda@astro.uni-tuebingen.de
[2] INAF – Osservatorio Astronomico di Palermo, Piazza Parlamento 1, 90134 Palermo, Italy
[3] Department of Physics & Astronomy, Western Washington University, Bellingham, WA 98225-9164, USA
[4] University of Exeter, Department of Physics & Astronomy, Physics Bldg., Stocker Road, Exeter EX4 4QL, UK
[5] SUPA, School of Physics & Astronomy, University of St Andrews, North Haugh, St. Andrews KY169SS, UK

ABSTRACT

The relation of activity to rotation in M dwarfs is of high astrophysical interest because it provides observational evidence of the stellar dynamo, which is poorly understood for low-mass stars, especially in the fully convective regime. Previous studies have shown that the relation of X-ray activity to rotation consists of two different regimes: the saturated regime for fast-rotating stars and the unsaturated regime for slowly rotating stars. The transition between the two regimes lies at a rotation period of ~10 d. We present here a sample of 14 M dwarf stars observed with *XMM-Newton* and *Chandra*, for which we also computed rotational periods from *Kepler* Two-Wheel (K2) Mission light curves. We compiled X-ray and rotation data from the literature and homogenized all data sets to provide the largest uniform sample of M dwarfs (302 stars) for X-ray activity and rotation studies to date. We then fit the relation between $L_x - P_{rot}$ using three different mass bins to separate partially and fully convective stars. We found a steeper slope in the unsaturated regime for fully convective stars and a nonconstant L_x level in the saturated regime for all masses. In the $L_x/L_{bol} - R_O$ space we discovered a remarkable double gap that might be related to a discontinuous period evolution. Then we combined the evolution of P_{rot} predicted by angular momentum evolution models with our new results on the empirical $L_x - P_{rot}$ relation to provide an estimate for the age decay of X-ray luminosity. We compare predictions of this relationship with the actual X-ray luminosities of M stars with known ages from 100 Myr to a few billion years. We find remarkably good agreement between the predicted L_x and the observed values for partially convective stars. However, for fully convective stars at ages of a few billion years, the constructed L_x-age relation overpredicts the X-ray luminosity because the angular momentum evolution model underpredicts the rotation period of these stars. Finally, we examine the effect of different parameterizations for the Rossby number (R_O) on the shape of the activity-rotation relation in $L_x/L_{bol} - R_O$ space, and we find that the slope in the unsaturated regime and the location of the break point of the dual power-law depend sensitively on the choice of R_O.

Key words. stars: low-mass – stars: activity – stars: rotation – stars: magnetic field – X-rays: stars

1. Introduction

Late-type stars emit X-rays from their outermost atmospheric layer. This is called the corona. The layer consists of a magnetically confined plasma with temperatures of up to several million Kelvin. The stellar corona was first observed in the Sun and is thought to be heated by the release of magnetic energy through a dynamo mechanism. For G-type stars, convection in the outer envelope together with differential rotation generates magnetic activity through an $\alpha\Omega$-dynamo mechanism (Parker 1955). The amount of magnetic energy that is released in the corona decreases over the stellar lifetime. This is a result of rotational spin-down that leads to decreased dynamo efficiency. The spin-down is driven by mass loss that interacts with the magnetic field. Stellar rotation and magnetism thus form a complex feedback system.

From the observations of the Sun, it is known that activity has distinct observable manifestations in each atmospheric layer.

The photosphere on a magnetically active star contains regions that are cooler and darker than their surroundings, called star spots. In these regions the magnetic pressure is so high that it overcomes the gas pressure and consequently inhibits the heat transport by convection. As an observable consequence, the light curve displays a periodic brightness modulation caused by the rotation of the dark spots (Eaton & Hall 1979; Bopp & Evans 1973). With space-based missions such as *Kepler* and its successor K2, we can therefore measure the stellar rotation period (P_{rot}) and detect the photometric variations because the magnetically active regions continuously cross the visible hemisphere as the star rotates. The outer two atmospheric layers, the chromosphere and the corona, can be analyzed with optical, UV, and X-ray observations (Güdel 2004; Durney et al. 1993).

Main-sequence stars with $M_\star \lesssim 0.35\,M_\odot$ (Chabrier & Küker 2006), corresponding roughly to spectral types equal to or later than M3.5, have fully convective interiors. They therefore lack the tachocline observed in solar-type stars, which invalidates the $\alpha\Omega$-dynamo mechanism. Possible alternative magnetic processes are an α^2-dynamo or a turbulent dynamo mechanism, for which the dependence on rotation has not yet been settled.

An observational way to indirectly examine the underlying stellar dynamo that causes the magnetic activity in solar- and

---

later-type stars is to study the relation of coronal activity to rotation. This relation is typically expressed in terms of the X-ray luminosity (L_x) as a function of the rotational period (P_{rot}), or alternatively, in terms of the ratio between the stellar X-ray and bolometric luminosities ($\frac{L_x}{L_{bol}}$) as a function of the Rossby number (R_O). This variable is a dimensionless number defined as the ratio between P_{rot} and the convective turnover time (τ_{conv}), the time needed for a convective cell to rise to the surface. Because τ_{conv} is not an observable parameter, the use of R_O introduces a model dependence or requires an ad hoc description.

Previous studies of the activity-rotation relation have shown two different regimes. In particular, for fast-rotating stars, the X-ray activity does not depend on the rotation (saturated regime), while on the other hand, the X-ray activity of slowly rotating stars declines with increasing rotational period (unsaturated regime). Pallavicini et al. (1981) were the first to study the coronal X-ray emission as a function of $v \sin i$ for a sample of stellar spectral type (O3–M). Later, Pizzolato et al. (2003) studied the coronal X-ray emission and stellar rotation in late-type main-sequence stars with X-ray data from the ROSAT satellite and calculated P_{rot} from $v \sin i$ measurements. All $v \sin i$ values have been translated into P_{rot} upper limits because of the unknown inclination of the stellar systems, and only two M dwarf stars were located in the unsaturated regime. Therefore the relation remained poorly constrained. Since then, Wright et al. (2011, 2018), Wright & Drake (2016), Stelzer et al. (2016) and González-Álvarez et al. (2019) have studied the X-ray activity-rotation relation of M dwarfs based on photometric P_{rot}, collecting much more information about the empirical connection between rotation and X-ray emission.

Because stellar rotation slows down throughout the main-sequence life of a star, the dynamo efficiency also decreases over time. This entails a decrease in X-ray luminosity. The joint evolution of rotation and activity is encoded in the empirical rotation-activity relation. Direct observations of the age decay of rotation and X-ray emission are hampered for M dwarfs by the lack of stars with known age. Direct observations of the age decay of rotation and X-ray emission are difficult to obtain for M dwarfs with known ages of 1 Gyr or older. The availability of precise light curves from the *Kepler*/K2 mission, coupled with targeted or serendipitous X-ray observations, has enabled detailed studies of the relation of age, rotation, and activity in several ~600 Myr benchmark open clusters (i.e., Praesepe & Hyades, Douglas et al. 2014, Núñez et al. 2015; M37, Núñez et al. 2017), but the rotation periods and activity measures required to calibrate models of angular momentum evolution are only now becoming available for M dwarfs in clusters older than 1 Gyr (i.e., NGC 752; Agüeros et al. 2018). For this reason, angular momentum evolution models for M dwarfs (Matt et al. 2015) have not been calibrated for stars beyond the ages of the Hyades (~600 Myr). Spin-down models can be used combined with the empirical rotation-activity relation to predict the long-term evolution of stellar X-ray emission, however.

In this work, we present an updated relation of X-ray activity to rotation in M dwarf stars and predict their L_x-age relation. In Sect. 2 we introduce the sample of M dwarfs that we studied, which includes new X-ray observations from *Chandra* and *XMM-Newton,* and new rotation periods from the K2 mission as well as a collection of the samples studied in the previous literature. In Sect. 3 we describe how we derived the stellar parameters and how we updated the literature sample to provide the largest and most homogeneous database to date for studies of M-dwarf rotation and coronal activity. In Sect. 4 we describe our analysis of the new *XMM-Newton* and *Chandra* observations,

and in Sect. 5 we present our selection and study of the rotation periods derived for the stars with new X-ray data. Section 6 contains the results of the observed relation of rotation to activity in terms of $L_x - P_{rot}$ and $L_x/L_{bol} - R_O$, and our construction of the L_x-age relation with help of the spin-down models. A summary and discussion of our results is presented in Sect. 7, followed by our conclusions and the outlook for further development in Sect. 8.

2. Sample selection

We observed 14 M-dwarf stars with *XMM-Newton* or *Chandra*. The sample was extracted from the stars of the Superblink proper motion catalog by Lépine & Gaidos (2011, henceforth LG11) that have K2 rotation period measurements. The LG11 catalog is an all-sky list of 8889 M dwarfs (SpT = K7 to M6) brighter than $J = 10$ mag and within 100 pc. Rotation periods have been determined for the LG11 stars in the K2 fields of campaigns C0–C4 by Stelzer et al. (2016), and the periods of the LG11 stars located in successive K2 campaigns were measured by us using the same methods (Raetz et al. 2019). For the X-ray observations obtained for the present study, we predominantly selected stars with long rotation periods ($P_{rot} > 10$ d). Our new *XMM-Newton* and *Chandra* sample covers periods of 0.6–79 d.

Together with the 14 new stars, we here present the whole sample from the previous literature on the X-ray activity-rotation relation of M dwarfs based on photometric periods, that is, Wright et al. (2011, 2018), Wright & Drake (2016), Stelzer et al. (2016), and González-Álvarez et al. (2019). The total sample we consider consists of 302 M dwarfs. To obtain a homogeneous sample, we applied some updates to the parameters of the stars from the literature. In the next section we describe our updating procedure together with the determination of the stellar parameters for our new sample of 14 stars with K2 rotation periods and deep X-ray observations.

3. Sample properties

In this section we explain the method we used to compute distances and stellar parameters for the 14 new X-ray observations (henceforth "our sample") and for all literature samples we list in Sect. 2. Throughout the paper we refer to the "full sample" when we consider the 14 new observations together with the 288 stars from the literature. First, we evaluated *Gaia*-DR2 parallaxes to obtain updated distances (henceforth d_{Gaia}). *Gaia*-DR2 contains spurious astrometric solutions (Arenou et al. 2018), therefore it is important to consider quality flags. To do so, we examined the available *Gaia* parallaxes for all samples using the filters provided by Lindegren et al. (2018) in their Appendix C. For the stars without *Gaia* parallax or stars that are not validated by the quality flags, we calculated photometric distances (henceforth d_{phot}). To this end, we made use of photometric magnitudes from the USNO CCD Astrograph (UCAC4)[1] and the Two Micron All-Sky Survey (2MASS) catalogs and applied the empirical relation from Stelzer et al. (2016) to calculate the absolute magnitude in the K band (M_{K_s}) from V to J. We then used M_{K_s} together with the observed apparent magnitude in K band (K_s) to derive the photometric distances. When we compared the two distance estimates, we identified 37 stars (~12%) for which $d_{Gaia} \geq 2 \cdot d_{phot}$, and for these cases, we

---

[1] We verified that the UCAC4 V_{mag} are reliable by comparing them with the *Gaia*-to-V_{mag} conversion from Jao et al. (2018).

Table 1. Stellar parameters of the 14 M dwarfs with new X-ray and rotation data.

K2 EPIC ID	M_{K_s} [mag]	$M_\star$ [$M_\odot$]	$R_\star$ [$R_\odot$]	M_{bol} [mag]	$\log_{10}\left(\frac{L_{\mathrm{bol}}}{L_\odot}\right)$	T_{eff} [K]	$V-J$ [mag]	P_{rot} [d]	D [pc]	FLAG$_D$ [1]
201718613	7.01 ± 0.06	0.31 ± 0.01	0.31 ± 0.01	9.75 ± 0.07	-2.00 ± 0.03	3260 ± 89	4.23	78.70	12.72 ± 0.42	0 0
212560714	5.54 ± 0.03	0.54 ± 0.01	0.52 ± 0.02	8.04 ± 0.05	-1.31 ± 0.02	3906 ± 93	2.76	27.57	36.00 ± 0.05	1 1
214787262	6.63 ± 0.04	0.37 ± 0.01	0.36 ± 0.01	9.33 ± 0.05	-1.83 ± 0.02	3382 ± 80	3.93	43.70	27.82 ± 0.07	1 1
201659529	6.58 ± 0.03	0.37 ± 0.01	0.36 ± 0.01	9.28 ± 0.05	-1.81 ± 0.02	3355 ± 80	3.95	44.24	23.39 ± 0.05	1 1
202059222	6.76 ± 0.05	0.35 ± 0.01	0.34 ± 0.01	9.48 ± 0.06	-1.89 ± 0.02	3308 ± 80	4.08	71.95	26.27 ± 0.61	0 0
202059188	6.75 ± 0.04	0.35 ± 0.01	0.34 ± 0.01	9.52 ± 0.05	-1.91 ± 0.02	3179 ± 81	4.44	0.69	28.74 ± 0.07	1 1
202059195	6.37 ± 0.04	0.40 ± 0.01	0.39 ± 0.01	9.12 ± 0.05	-1.74 ± 0.02	3311 ± 82	4.23	42.79	34.61 ± 0.10	1 1
202059210	4.47 ± 0.06	0.72 ± 0.02	0.71 ± 0.02	6.97 ± 0.07	-0.89 ± 0.03	3926 ± 84	2.81	17.40	54.37 ± 0.24	1 1
201364753	5.30 ± 0.03	0.58 ± 0.01	0.56 ± 0.02	7.82 ± 0.05	-1.23 ± 0.02	3854 ± 87	2.86	9.19	40.96 ± 0.09	1 1
202059198	5.81 ± 0.02	0.50 ± 0.01	0.47 ± 0.01	8.39 ± 0.04	-1.45 ± 0.02	3727 ± 99	3.14	26.93	23.30 ± 0.03	1 1
210579749	5.51 ± 0.02	0.55 ± 0.01	0.52 ± 0.02	8.10 ± 0.04	-1.34 ± 0.02	3643 ± 83	3.27	11.16	17.24 ± 0.01	1 1
214269391	4.95 ± 0.02	0.64 ± 0.01	0.62 ± 0.02	7.44 ± 0.05	-1.08 ± 0.02	3900 ± 101	2.76	19.56	17.66 ± 0.01	1 1
203869467	4.68 ± 0.04	0.69 ± 0.01	0.67 ± 0.02	7.17 ± 0.06	-0.97 ± 0.02	3951 ± 84	2.73	47.58	39.07 ± 0.94	0 0
201717791	4.59 ± 0.04	0.7 ± 0.01	0.69 ± 0.02	7.10 ± 0.05	-0.94 ± 0.02	3873 ± 90	2.84	14.40	46.45 ± 0.13	1 1

Notes. [1] FLAG$_D$ is the quality criteria we used to select the distance. The first column represents the quality flag of *Gaia* parallaxes from Lindegren et al. (2018) (1 means that it is validated, and 0 that it is not validated), the second column shows our criteria for the comparison between *Gaia* and photometric distances, explained in Sect. 3 (1 means that the *Gaia* distance is adopted, and 0 that the photometric distance is adopted). We used *Gaia* parallaxes if FLAG$_D$ = 11.
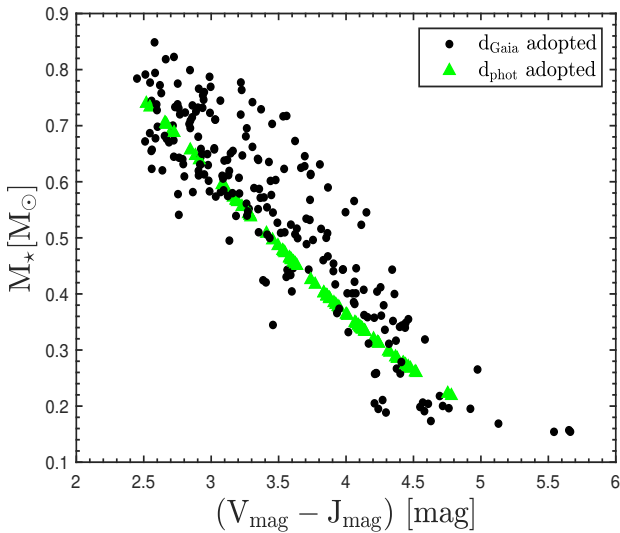
Fig. 1. Stellar masses as a function of $V_{\mathrm{mag}} - J_{\mathrm{mag}}$ for all 302 stars analyzed in this work. We distinguish stars for which we adopted *Gaia* distances (black filled circles) and those for which we adopted photometric distances (green filled triangles) following the criteria described in Sect. 3.

adopt the photometric distance throughout. There are no stars for which the *Gaia* distance is significantly smaller than the photometric distance. The FLAG$_D$ column in Tables 1 and B.1 shows the results of the applied distance quality criteria.

The first number indicates the Lindegren et al. (2018) filter (1 means that it is validated, and 0 that it is not validated), and the second number indicates our own condition (1 means that the *Gaia* distance is adopted, and 0 that the photometric distance is adopted). FLAG$_D$ = 11 means that both quality criteria are satisfied and we adopted *Gaia* parallaxes.

We used the empirical relations from Mann et al. (2015) and Mann et al. (2016) to calculate stellar parameters. In particular, we obtained stellar masses ($M_\star$) and radii ($R_\star$) from M_{K_s}, the effective temperature (T_{eff}) from $V-J$ and $J-H$, the bolometric correction (BC$_{K_s}$) from $V-J$, and the bolometric lumonosity L_{bol}

from BC$_{K_s}$. We list the stellar parameters for the 14 new observations in Table 1 and those for the literature sample in Table B.1. In Fig. 1 we show the relation between $M_\star$ and $V-J$ we found for the full sample. We note that according to our $V-J$ versus SpT calibration (Stelzer et al. 2016), stars with $V-J < 3$ mag are K-type stars. For the sake of simplicity, we do not distinguish these objects, but we recall that the full sample comprises $\approx 15\%$ of K-type stars.

Because we updated the distances for the literature samples, we had to recalculate the X-ray luminosity (L_x). In order to have a uniform data sample, we computed the L_x adopting the ROSAT energy band (0.1−2.4 keV) used in Wright et al. (2011, 2018), Wright & Drake (2016), for the full sample. Of the objects in Wright et al. (2011) we took only the field stars, and we scaled the published L_x values with $\left(\frac{d_{\mathrm{new}}}{d_{\mathrm{Wr+11}}}\right)^2$, where d_{new} is our new distance from Table B.1 and $d_{\mathrm{Wr+11}}$ is the distance used by Wright et al. (2011). For the stars from Wright & Drake (2016) and Wright et al. (2018), we calculated L_x from the fluxes listed in Wright et al. (2018) with our new distances. Because González-Álvarez et al. (2019) listed L_x for 0.1−2.0 keV, in order to obtain the X-ray luminosity in the 0.1−2.4 keV band, we returned to the ROSAT catalogs. In particular, we extracted the count rates from the bright (BSC: Voges et al. 1999) and faint (FSC: Voges et al. 2000) source catalogs and the second ROSAT All-Sky Survey Point Source Catalog (2RXS: Boller et al. 2016). These were converted into X-ray flux using the conversion factor (CF = 5.771×10^{-12} erg cm^{-2}/cts) obtained with the count-rate simulator WebPIMMS [2] for a 1T-APEC model with $kT = 0.5$ keV and $N_{\mathrm{H}} = 10^{19}$ cm^{-2}. The temperature value is derived from computing the mean coronal temperature for the stars from our new *XMM-Newton* and *Chandra* sample that have enough counts for the spectrum to be extracted (see Sect. 4.3), for which we find an average of 0.51 ± 0.03 keV.

The uncertainties of the X-ray luminosities were calculated with error propagation, using the variance formula for the uncertainties of the X-ray fluxes and distances. Wright et al. (2011)

---

[2] Count-rate simulator PIMMS: `http://heasarc.gsfc.nasa.gov/cgi-bin/Tools/w3pimms/w3pimms.pl`
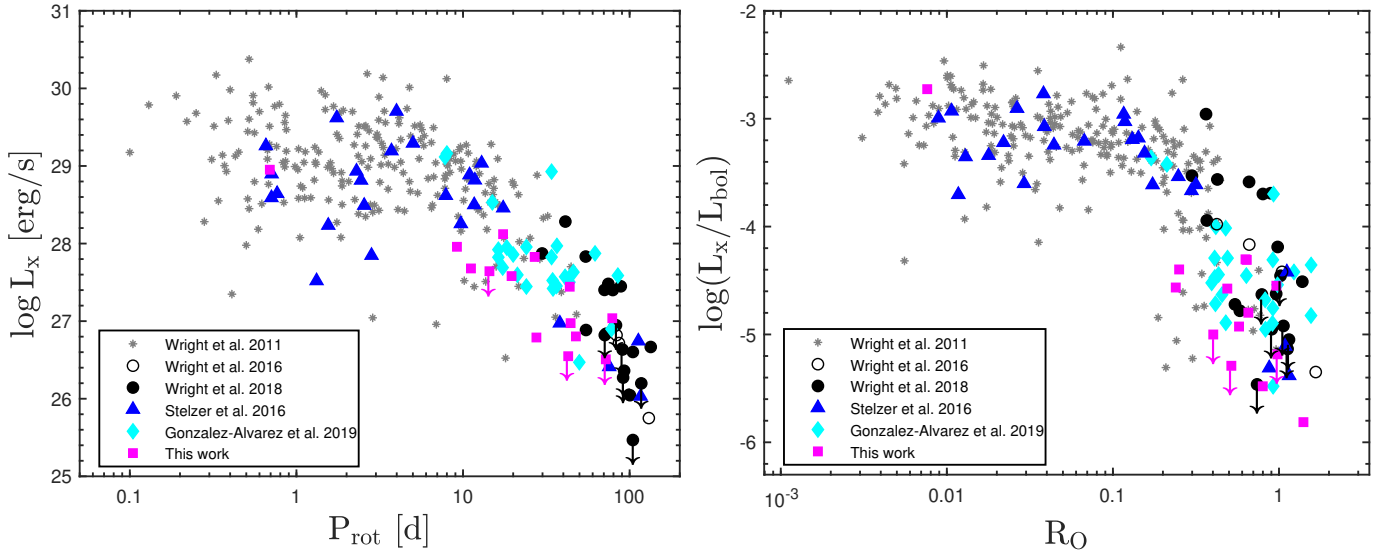
Fig. 2. *Left*: relation of activity to rotation in $L_x - P_{rot}$ space. The color scale is based on the origin of the sample, as explained in the inset. *Right*: same as the left panel, but for L_x/L_{bol} vs. Rossby number.

Table 2. X-ray journal of observations together with the results from the analysis explained in Sects. 4 and 6.3.

K2 EPIC ID	Mission	Obs. ID	Obs. date	Exp. time [ks]	Rate [$\times 10^{-3}$ counts s^{-1}]	$\log(L_x)$ [erg s^{-1}]	$\log\left(\frac{L_x}{L_{bol}}\right)$	$R_{O,C\&S}$	$R_{O,B}$	$R_{O,W}$
201718613	*XMM-Newton*	0820460101	2018-06-11	18.0	47.20 ± 2.20	27.03 ± 0.03	-4.54 ± 0.96	–	–	0.96
212560714	*XMM-Newton*	0820460201	2018-07-02	33.6	3.33 ± 0.57	26.78 ± 0.07	-5.48 ± 0.09	0.29	0.37	0.80
214787262	*XMM-Newton*	0820460301	2019-03-31	45.5	25.15 ± 1.27	27.44 ± 0.02	-4.30 ± 0.10	0.35	0.30	0.64
201659529	*XMM-Newton*	0843430401	2019-07-14	23.1	12.07 ± 1.05	26.97 ± 0.04	-4.79 ± 0.09	0.35	0.31	0.65
202059222	*Chandra*	17724	2015-12-07	14.7	<0.24	<26.50	< -5.20	0.56	0.41	0.98
202059188	*Chandra*	17725	2016-01-12	14.9	56.20 ± 3.20	28.95 ± 0.02	-2.70 ± 0.10	–	–	0.01
202059195	*Chandra*	17726	2015-12-02	15.0	<0.15	<26.54	< -5.30	0.33	0.34	0.52
202059210	*Chandra*	17727	2015-11-27	13.9	2.32 ± 0.81	28.12 ± 0.15	-4.60 ± 0.10	0.19	0.40	0.49
201364753	*Chandra*	17728	2016-03-26	8.8	0.52 ± 0.43	27.95 ± 0.11	-4.40 ± 0.10	0.09	0.17	0.25
" "	*Chandra*	18805	2016-03-31	5.8	2.36 ± 1.10	" "	" "	" "	" "	" "
202059198	*Chandra*	17729	2016-02-05	14.8	6.42 ± 0.36	27.82 ± 0.02	-4.30 ± 0.10	0.26	0.32	0.63
210579749	*Chandra*	21157	2018-10-22	9.4	3.24 ± 0.97	27.67 ± 0.13	-4.60 ± 0.10	0.10	0.18	0.24
214269391	*Chandra*	21158	2018-11-05	9.9	2.46 ± 0.84	27.58 ± 0.14	-4.90 ± 0.10	0.21	0.37	0.57
203869467	*Chandra*	21159	2019-01-20	27.7	0.08 ± 0.25	26.80 ± 0.02	-5.80 ± 0.01	0.51	0.84	1.40
201717791	*Chandra*	21160	2018-11-06	15.7	<0.41	<27.64	< -5.00	0.15	0.33	0.40

Notes. The $R_{O,C\&S}$ and $R_{O,B}$ columns are the R_O numbers from the normalized τ_{conv} relations by Cranmer & Saar (2011) and Brun et al. (2017) for stars with $T_{eff} > 3300$ K (see Sect. 6.3 for more details). The last column ($R_{O,W}$) shows the R_O number by Wright et al. (2018).

provided no uncertainties on the X-ray measurements, therefore we applied the mean percentage value of the X-ray flux error measured for the other samples, which is $\approx 15\%$.

We list in Table B.1 our updated results for the X-ray luminosities of the 288 stars from the literature. We also provide (in Col.7) the rotation period adopted from these previous studies. In particular, Wright et al. (2011) selected only photometric P_{rot} from the literature, Wright & Drake (2016) and Wright et al. (2018) used rotation measurements from the MEarth Project, which means that they were mostly in the slow-rotator regime. Stelzer et al. (2016) have determined the P_{rot} for the LG11 stars in the K2 field of campaigns C0 to C4, and González-Álvarez et al. (2019) analyzed time-series of high-resolution spectroscopy taking P_{rot} from activity indicators, that is, the CaII H&K and Hα spectral lines.

To illustrate the different samples, we show in Fig. 2 the updated relation of X-ray activity to rotation by combining all previous literature samples with our own data, listed in Tables 1

and B.1. For this plot the convective turnover times, τ_{conv}, were calculated using the empirical calibration by Wright et al. (2018).

4. X-ray data analysis

As explained above, we worked in the ROSAT energy band (0.1–2.4 keV) for consistency with most previous works. The results from the analysis of X-ray data for the new sample of 14 stars obtained with *Chandra* and *XMM-Newton* are listed in Table 2. In the following we describe the analysis of these observations.

4.1. XMM-Newton: EPIC

Four of the 14 new observations were obtained with *XMM-Newton*. We analyzed these 4 observations with the *XMM-Newton* Science Analysis System (SAS)[3] 17.0 pipeline. After

---

[3] SAS Data Analysis Threads: https://www.cosmos.esa.int/web/xmm-newton/sas-threads

Table 3. X-ray spectral parameters with 1σ uncertainties computed with the error pipeline provided in the XSPEC software package.

K2 EPIC ID	kT_1 [keV]	$\log(EM_1)$ [cm^{-3}]	kT_2 [keV]	$\log(EM_2)$ [cm^{-3}]	χ^2	d.o.f.	T_{mean} [keV]
201718613	0.17 ± 0.03	48.54 ± 0.07	0.73 ± 0.05	48.49 ± 0.07	0.8	69	0.44 ± 0.03
214787262	0.31 ± 0.02	50.17 ± 0.05	1.29 ± 0.21	49.77 ± 0.12	1.1	37	0.59 ± 0.06

data extraction, we filtered the event lists of EPIC/pn and EPIC/MOS. We extracted the light curve for the whole detector, and then we determined the good time intervals using the count rate ≤ 0.4 counts s^{-1} and count rate ≤ 0.35 counts s^{-1} as threshold for EPIC/pn and EPIC/MOS, respectively. We further filtered our data for pixel pattern (PATTERN = 0), event energies greater than 0.15 keV, and quality flag (FLAG = 0). We performed source detection using the SAS pipeline *edetect_chain* in the ROSAT energy band (0.15–2.4 keV) simultaneously for EPIC/pn and EPIC/MOS. Our lower energy threshold is slightly different from that of the ROSAT band. This is based on the fact that the recommended low-energy cutoff for *XMM-Newton* is at 0.15 keV. However, we quantified how much the count rate would differ if we included the counts between 0.10 and 0.15 keV, and it would be only $\approx 2\%$ greater. The extraction of spectra and light curves was performed considering a source region of 40″ centered on the source position with an adjacent source-free circular background region three times greater. We created the response matrix and ancillary response for the spectral analysis with the SAS tools RMFGEN and ARFGEN, and we rebinned the spectrum in order to have at least five counts for each background-subtracted spectral channel.

4.2. Chandra

The *Chandra* data analysis was carried out with the CIAO package[4]. We started our analysis with the new pipeline *chandra_repro*, which automatically reprocesses the event list by reading data from the standard data distribution and creating a new bad pixel file and a new level 2 event file. After this, we created an exposure-corrected image for CCD_ID = 7 of our ACIS-S observations in the ROSAT energy band (0.1–2.4 keV), and we determined the point spread function (PSF) map of the image with *mkpsfmap*, choosing 100% of the enclosed counts fraction (ecf = 1.0). At this point, we proceeded with the source detection with the *wavdetect* algorithm, which takes into account the PSF map, the exposure time, and a significance detection threshold, which we set to $\sigma = 10^{-5}$. This value is needed to identify a pixel as belonging to a source. Three of the ten stars observed with *Chandra* are undetected, and we calculated the flux upper limits. We calculated the count rates using *srcflux* for detected and undetected stars, giving the positions, the source, and background regions and the ROSAT energy band as inputs. In particular, we took the circular source region centered on our sources and a circular region for the background 10–15 times greater than the source regions. For undetected sources, *srcflux* computes the upper limit count rate using the Bayesian posterior probability distribution function, without assuming prior information for the intensities in the source and background apertures.

4.3. X-ray spectra

Spectral analysis was performed with XSPEC[5] version 12.10, fitting the two extracted spectra with more than 350 counts, using two isothermal APEC models. Each APEC model has three parameters: the plasma temperature (kT), the global abundance (Z), and the emission measure (EM). We fixed Z at $0.3\,Z_\odot$, the typical global abundance for late-type stars, and we left kT and EM free to vary. In particular, we performed a multi-fitting procedure for EPIC 201718613 by simultaneously fitting the spectra from the three instruments on board *XMM-Newton*. On the other hand, for EPIC 214787262, we fit only the EPIC/pn spectrum because EPIC and MOS have not enough counts to extract the spectra. The parameters of the best-fitting model are listed in Table 3 and the spectra are shown in Fig. 3. The emission measure is computed in logarithmic scale, and it is the square of the number density of free electrons integrated over the volume of the plasma. With the EM, we computed the mean coronal temperature (T_{mean}). In particular, T_{mean} is defined as

$$T_{mean} = \frac{\sum(EM_n \cdot T_n)}{\sum(EM_n)}, \tag{1}$$

where T_n and EM_n are the n-temperatures and n-EM of the fitted model. From the two T_{mean} (see Table 3), we found the average $kT = 0.51 \pm 0.03$ keV that we used together with $N_H = 10^{19}$ cm^{-2} to compute the conversion factors (CF) with WebPIMMS needed to determine the X-ray fluxes. In particular, we calculated the flux in the ROSAT energy band (0.1–2.4 keV) for the full sample, but for stars observed with *XMM-Newton*, the fluxes were extracted in the readapted energy band (0.15–2.4 keV), as explained in Sect. 4.1. In particular, for *Chandra* cycle 17, we found CF = 1.61×10^{-11} erg cm^{-2}/cts, for *Chandra* cycle 20, we found CF = 4.14×10^{-11} erg cm^{-2}/cts, and for *XMM-Newton*, we found CF = 1.19×10^{-12} erg cm^{-2}/cts.
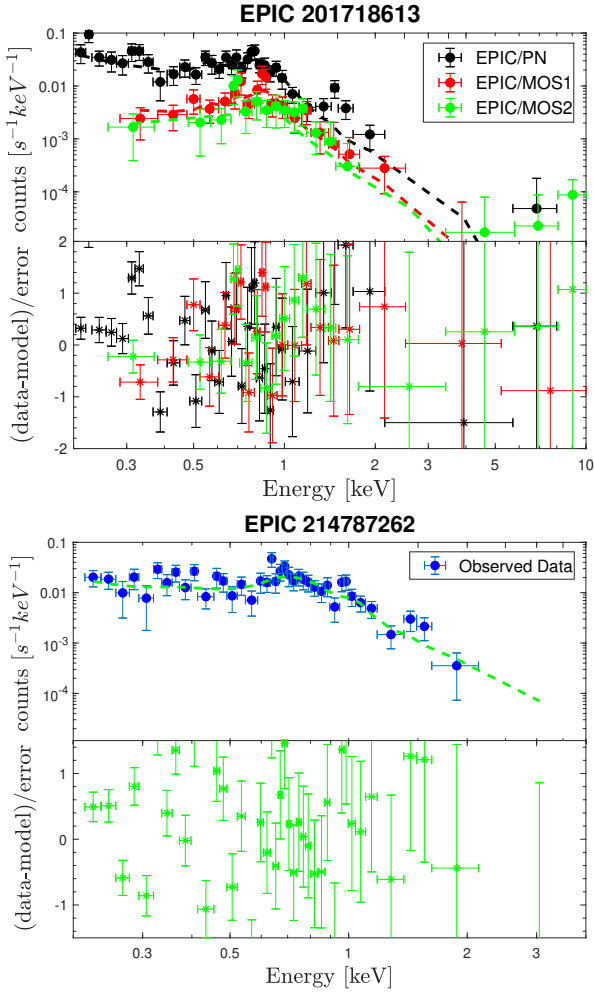
5. K2 analysis

Our 14 targets were selected because they have photometric monitoring observations by the K2 mission. K2 observed in two cadence modes, long cadence ($\sim$30 min data point cadence) and short cadence ($\sim$1 min data point cadence). While all 14 targets have light curves obtained in long-cadence mode, 3 targets were also observed with the $\sim$1 min data point cadence. We downloaded the fully reduced and corrected long-cadence light curves provided by Vanderburg & Johnson (2014) from the website of A. Vanderburg[6]. The rotation periods were measured using standard time-series analysis techniques, that is, the generalized Lomb-Scargle periodogram (GLS; Zechmeister & Kürster 2009), the autocorrelation function (ACF), and the fitting of the light curves with a sine function. While GLS and ACF are limited to periods shorter than the campaign duration of 70-80 d,

---

[4] The CIAO package is developed by the *Chandra* X-Ray Center for analyzing data from the *Chandra* X-Ray Telescope, it can be downloaded from http://cxc.harvard.edu/ciao/

[5] XSPEC NASA's HEASARC Software: https://heasarc.gsfc.nasa.gov/xanadu/xspec/

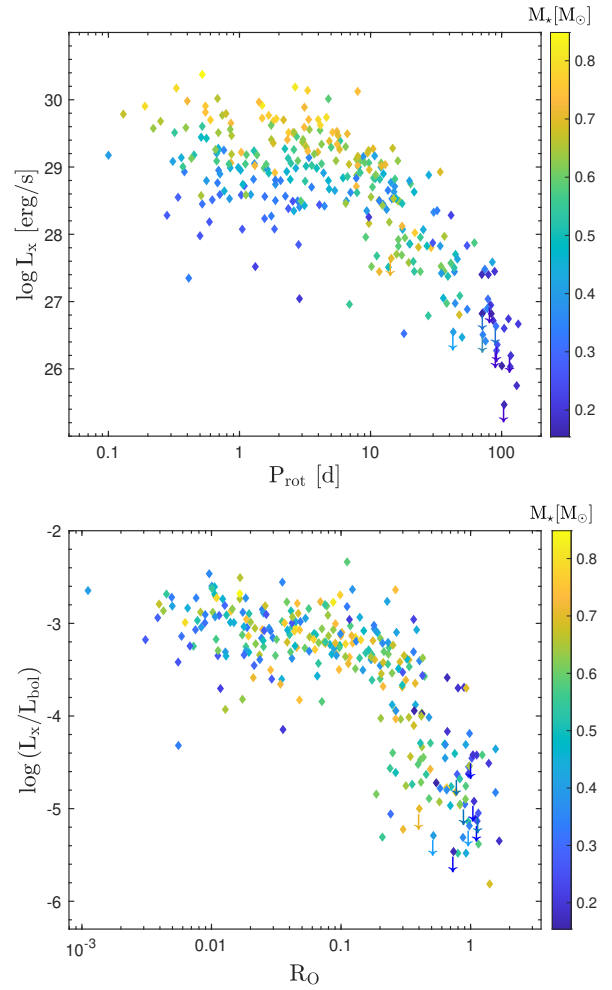[6] https://www.cfa.harvard.edu/~avanderb/k2.html

Fig. 3. EPIC X-ray spectra together with the best-fitting thermal APEC model (dashed line) for the two *XMM-Newton* observations with sufficient counts for spectral analysis. In particular, a simultaneously multifit for EPIC/pn and EPIC and MOS spectra of EPIC 201718613 and a single fit, again with two temperatures, for EPIC/pn data for EPIC 214787262 are shown.

Fig. 4. Relation of activity to rotation for all 302 stars we analyzed, displayed with a color code for the stellar mass. *Top*: relation in X-ray luminosity vs. rotation period space. *Bottom*: relation in terms of the ratio between X-ray and bolometric luminosities as a function of Rossby number.

the sine fitting allows us to constrain rotation periods even if they exceed the K2 monitoring time baseline, as is the case for EPIC 202059222, for example. For each target we obtained three estimates for the rotation period. Through by-eye inspection of the phase-folded light curves from each method, we selected the best-fitting period. When several methods yielded equally good periods, we adopted the average rotation period as the final value. A detailed description of our procedure for measuring rotation periods can be found in Raetz et al. (2020). Our final adopted values of the rotation periods are summarized in Table 1. The periods were found to agree within <5% with the values published by Stelzer et al. (2016), Raetz et al. (2019, 2020).

6. Relation of activity, rotation, and age

In this section we discuss the relation of X-ray activity, rotation, and age based on the full sample as is defined in Sect. 3. We use the result combined with angular momentum evolution models by Matt et al. (2015) to construct the time-evolution of the X-ray luminosity of M dwarfs. As we explained in Sect. 1, previous studies showed two different regimes of the rotation-activity relation, the saturated regime for fast-rotating stars with

$P_{rot} \leq P_{rot_{sat}}$ and the unsaturated regime for slowly rotating stars with $P_{rot} > P_{rot_{sat}}$. The convective turnover time rescales the sample by decreasing the horizontal spread in the unsaturated regime and shifting the break point between the saturated and unsaturated regime; normalizing the X-ray luminosity by the stellar bolometric luminosity decreases the vertical spread in both regimes, making the distinction of the two regimes more pronounced in the $L_x/L_{bol} - R_O$ space.

In Fig. 4 we show the full sample, plotted with a color-scale representing the stellar mass. Arrows denote upper limits. Three of these undetected sources come from our new X-ray data and seven are from Wright et al. (2018) (see Tables 2 and B.1 for more details). The best parameters for characterizing the relation between activity and rotation have long been debated. Here we study both the L_x-P_{rot} and $L_x/L_{bol}-R_O$ relation in Sects. 6.1 and 6.3, respectively.

6.1. X-ray luminosity versus rotation period

The observed activity-rotation relation in L_x-P_{rot} space (Fig. 4 top panel) shows a large vertical spread, amounting to ≈2 dex, in the saturated and unsaturated regime. Moreover, the X-ray activity in the saturated regime does not seem to show a constant

maximum value, but the L_x level instead appears to decrease from a maximum at the shortest rotation periods, declining toward the breaking point into the unsaturated regime.

For this reason, our approach is based on a broken power-law fit for the two regimes.

In particular, our fitting method requires three steps. We first use a Bayesian approach to infer the maximum likelihood parameters for a dual power law in the L_x versus P_{rot} space. Our implementation of this dual power-law model is based on routines originally developed by Douglas et al. (2014) for use with the emcee Markov chain Monte Carlo (MCMC) package (Foreman-Mackey et al. 2013) to infer the maximum likelihood parameters of the model. In detail, the dual power-law fit is calculated as shown in Eq. (2),

$$
L_x = \begin{cases} C_{sat} P_{rot}^{\beta_{sat}} & \text{if } P_{rot} \leq P_{rot,sat} \\ C_{unsat} P_{rot}^{\beta_{unsat}} & \text{if } P_{rot} > P_{rot,sat} \end{cases}, \tag{2}
$$

where $C_n = (L_{x_n}/P_{rot}^{\beta_n})$, with $n = (sat, unsat)$.

In our first iteration, likelihoods of each potential model are calculated using flat priors in each parameter ($2\,d < P_{rot,sat} < 50\,d$; $-4 < \beta_{sat} < 2$; $-5 < \beta_{unsat} < 1$), and allowing for a nuisance parameter to account for underestimated (multiplicative) errors. We infer maximum likelihood parameters by comparing each potential model output to the subset of the full sample with reliable detections (i.e., excluding nondetections from this first iteration) using 256 walkers that each take 10 000 steps in their MCMC chain. We discard the first half of each chain to allow the solutions to burn in, and measure the maximum likelihood values of each parameter as the median value of the remaining samples; we calculate 1σ uncertainties as half the distance between the 16th and 84th percentiles of the resulting posterior distribution. In practice, the latter nuisance parameter converged quite closely to 1, suggesting that the adopted uncertainties are appropriately close to their true values, therefore we do not report these values further.

In order to take the upper limits properly into account, in the next step we fit only the unsaturated regime, where all upper limits are located, using the Cenken method provided by the R-statistics package to calculate the Akritas–Theil–Sen (Akritas et al. 1995) nonparametric slope to the full censored dataset. To define the onset of the unsaturated regime in terms of P_{rot}, we used the result from the MCMC analysis in the previous step. To ensure that our measurement of the slope in the saturated regime was not unduly influenced by the omission of nondetections from the first MCMC fit, we then repeated the MCMC-based inference of the dual power-law fit, but forcing the slope in the unsaturated regime to remain within 0.02 of the value identified by the Cenken routine.

The results inferred from this three-step fitting process are shown in Fig. 5, and tabulated for reference in Table 4. As a result of this procedure, we found maximum likelihood parameters for a dual power-law fit to the full mass range of $\beta_{sat} = -0.14 \pm 0.10$, $\beta_{unsat} = -2.25 \pm 0.02$, and $P_{rot,sat} = 8.5 \pm 1.0\,d$. We quantify for the first time that the X-ray luminosity in the saturated regime is not constant but shows a small negative slope, that is, a decrease in L_x for higher P_{rot}. However, the uncertainties of β_{sat} indicate that this finding is tentative, with a significance at the ~1σ level for the full global fit.

Figure 4 clearly shows systematic trends with stellar mass. In particular, the saturated L_x level decreases for lower $M_\star$ and the $P_{rot,sat}$ turnover point is higher for lower $M_\star$. In order to search for differences in the activity-rotation relation of partially and fully convective stars, we therefore split the sample into three
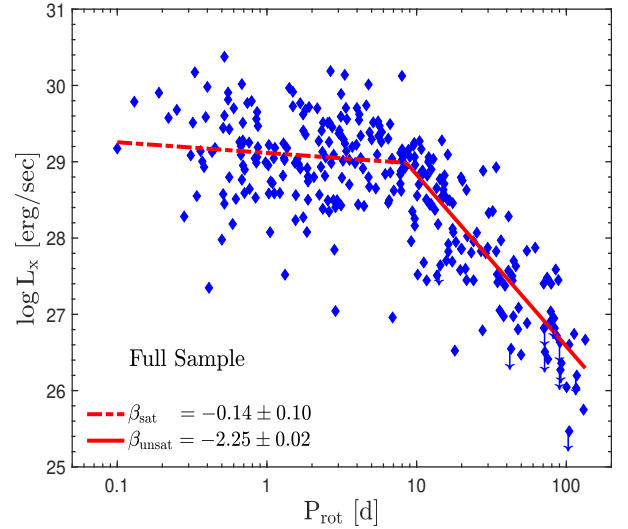

Fig. 5. Two-component fit (see Eq. (2)) to the activity-rotation relation for the full sample (see Sect. 6.1 for the fitting procedure).

stellar mass ranges: lower, medium, and higher stellar masses. We used the results from Jao et al. (2018), who assigned the transition to fully convective stars to $M_{K_s} = 6.7\,mag$ (dashed black line in Fig. 6); this corresponds to $V-J \approx 4\,mag$. This approach is justified a posteriori by the fact that at $M_{K_s} > 6.7\,mag$ there are mostly objects from Wright & Drake (2016) and Wright et al. (2018), where only M3 and later stars are included. Comparing Fig. 6 to the empirical relation between SpT and $V-J$ from Stelzer et al. (2016), we found that $V-J = 4\,mag$ corresponds to SpT $\sim$ M3.5. Based on the comparison of M_{K_s}, $V-J$, $M_\star$, and SpT, we therefore locate the fully convective transition at $M_\star = 0.4\,M_\odot$. In order to split the full sample into three $M_\star$ bins, we considered our fully convective mass transition and then subdivided the partially convective sample into two mass ranges. In particular, the three stellar mass ranges are (1) $0.14\,M_\odot \leq M_\star \leq 0.40\,M_\odot$, (2) $0.40\,M_\odot \leq M_\star \leq 0.60\,M_\odot$, and (3) $0.60\,M_\odot \leq M_\star \leq 0.82\,M_\odot$. The number of stars in each mass bin is given in Table 4. We recall that the highest mass bin also comprises late K-type stars.

We separately investigated the relation of activity to rotation in these three mass ranges by applying the same fitting procedure we used above. In Fig. 7 we show the results of our fitting analysis for the three mass ranges. For each mass range the saturated regime has a nonconstant X-ray activity level. The slope β_{sat} for the high-mass range is flatter than the slope for the low-mass range. The slope in the intermediate-mass range is the steepest. Nonetheless, the slope in the saturated regime is independently detected at the 1σ level in all three mass bins, which raises the statistical significance of this result above the 1σ confidence in the global fit. We confirmed the result found by Pizzolato et al. (2003) that the breaking point $P_{rot,sat}$ moves to longer periods with decreasing stellar mass. In the unsaturated regime the slopes are similar ($\beta_{unsat} \approx -2.2$) for the higher and the intermediate mass range, but the lowest mass range shows a much steeper decline of L_x with P_{rot} ($\beta_{unsat,<0.4\,M_\odot} = -3.5$). In Table 4 the fit parameters are listed for all mass ranges, together with the X-ray luminosity $\langle L_{x,sat} \rangle$ calculated at $P_{rot} = 1\,d$ with the fit procedure. From this we see that the X-ray activity level in the saturated regime displays a continuous decrease toward later SpT (also observed by Stelzer et al. 2016, on a much smaller sample).

Table 4. Results from fitting the relation of activity to rotation in $L_x - P_{rot}$ space for the full sample and three mass ranges (see Eq. (2) for more details).

Mass range	$N_\star$	β_{sat}	β_{unsat}	$P_{rot,sat}$ [d]	$\log(L_{x,sat})$ $(P_{rot} = 1\,d)$ [erg s^{-1}]
Full sample	302	-0.14 ± 0.10	-2.25 ± 0.02	8.5 ± 1.0	29.11 ± 0.11
$M_\star > 0.6\,M_\odot$	113	-0.17 ± 0.14	-2.27 ± 0.02	5.2 ± 0.7	29.56 ± 0.13
$0.4\,M_\odot \leq M_\star \leq 0.6\,M_\odot$	102	-0.39 ± 0.13	-2.26 ± 0.02	11.8 ± 2.0	29.10 ± 0.16
$M_\star < 0.4\,M_\odot$	87	-0.19 ± 0.11	-3.52 ± 0.02	33.7 ± 4.5	28.54 ± 0.20
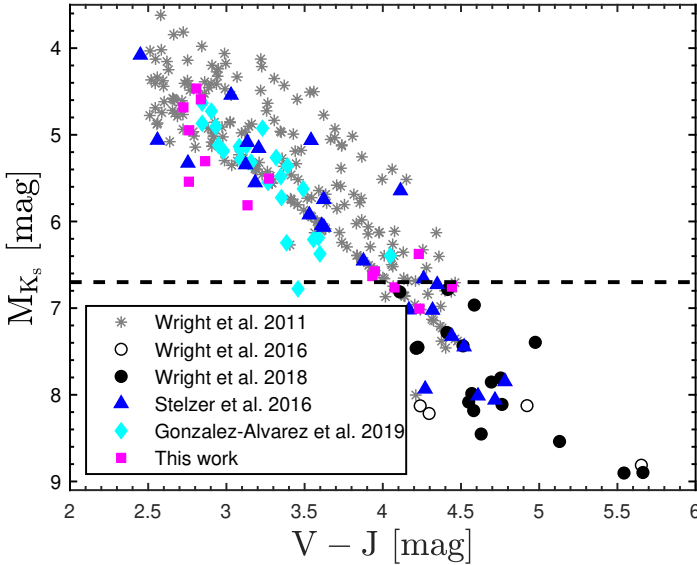
Fig. 6. Color-magnitude diagram for the full sample. The dashed black line shows the transition to fully convective stars at $M_{K_s} > 6.7$ mag, according to Jao et al. (2018).

6.2. X-ray luminosity vs. age

X-ray activity and rotation are both known to undergo significant change during the stellar lifetime. L_x decays by a factor 1000 from the pre-main sequence (PMS) to the main-sequence (MS; Preibisch & Feigelson 2005), for instance, presumably because the dynamo efficiency decreases. The rotation periods are observed to decrease during PMS contraction, starting from an initially broad distribution with $P_{rot} \sim 0.5$ to 10 d (depending on stellar mass; Irwin et al. 2011). The further evolution of the rotation rate during the MS life is thought to be ruled by angular momentum loss mediated by magnetic winds (Kawaler 1988). Different wind models have been developed to predict the rotational evolution, see Matt et al. (2015) and Garraffo et al. (2018) for M stars, for example. However, no theory exists that quantifies the decay in X-ray luminosity during the MS evolution, and the lack of field M dwarfs with known age has impeded an observational study of the L_x-age relation for ages beyond that of open clusters such as the Hyades.

6.2.1. Predicted relation of X-ray luminosity to age

Here we predict the time-evolution of the X-ray emission by combining the observed $L_x - P_{rot}$ relation from Sect. 6.1 with the spin-down models (P_{rot}-age) from Matt et al. (2015). We perform this analysis individually for the three mass bins considered in Sect. 6.1. We calculated the rotation periods for stars

with mass equal to the edges and the mean of the three mass bins, using the model of Matt et al. (2015), starting from an age of 5 Myr and evolving to an age of 10 Gyr. Because our observed $L_x - P_{rot}$ relations refer to a range of masses (see Table 4), we extracted the P_{rot} evolution from the angular momentum evolution model for the central mass of the bin, as well as for the mass of the lower and the upper boundaries. This allowed us to take the mass spread within each of our three mass bins into account. The rotational evolution depends on the initial rotation period ($P_{rot,in}$) of the star, which is not a unique value (see our discussion above), as is known from observations in regions of star formation. We therefore took this spread in the boundary conditions into account, and we investigated three different initial values for the rotation periods. These led to three tracks for given $M_\star$.

Our procedure for deriving an L_x-age relation, carried out for each of the three mass bins from Sect. 6.1 separately, is the following. We extracted for each mass value (the central mass of the bin, the lower and the upper mass boundaries) and ages from 5 Myr to 10 Gyr the rotation periods from the Matt et al. (2015) model using $P_{rot,in} = 1.54, 5.51$ and 8.83 d for the initial period. We thus obtained a total of nine tracks for the age evolution of the rotation period and three tracks for the three values of $P_{rot,in}$, and this for each of three masses. We show these tracks in Fig. A.1. Then we calculated the L_x value corresponding to each P_{rot} value from the appropriate best-fit relation given in Table 4. To consider the vertical spread observed in the saturated and unsaturated regimes of L_x versus P_{rot}, we assign the observed L_x standard deviation to the constructed X-ray luminosities in each mass range.

In the right panel of Fig. 7 we show our constructed L_x-age relation for each mass bin and for the three initial period values. The computed vertical spread is shown as the yellow region. The standard deviation in the predicted L_x is generally larger than the difference in tracks that is due to the different initial rates or different masses within the same mass bin.

6.2.2. Comparison to observations

The validity of the relation for the age-decay of X-ray luminosity that we constructed from the spin-down models and the empirical relation of X-ray activity to rotation can be tested with stars of known age and X-ray luminosity. Such samples are notoriously sparse in the M-dwarf regime. We took three such samples from the literature: M stars in the Pleiades (125 Myr), in the Hyades (~600 Myr), and field M dwarfs with individual ages determined from a chemo-kinematic study. The X-ray luminosities of these objects are plotted over the predicted L_x-age relation in the right panel in Fig. 7.

The X-ray luminosities of the Pleiades and Hyades were extracted from Wright et al. (2011), observed in the $0.1 - 2.4$ keV band. Wright et al. (2011) provide a list of stars with detected X-ray emission for both clusters, but no upper limits for stars
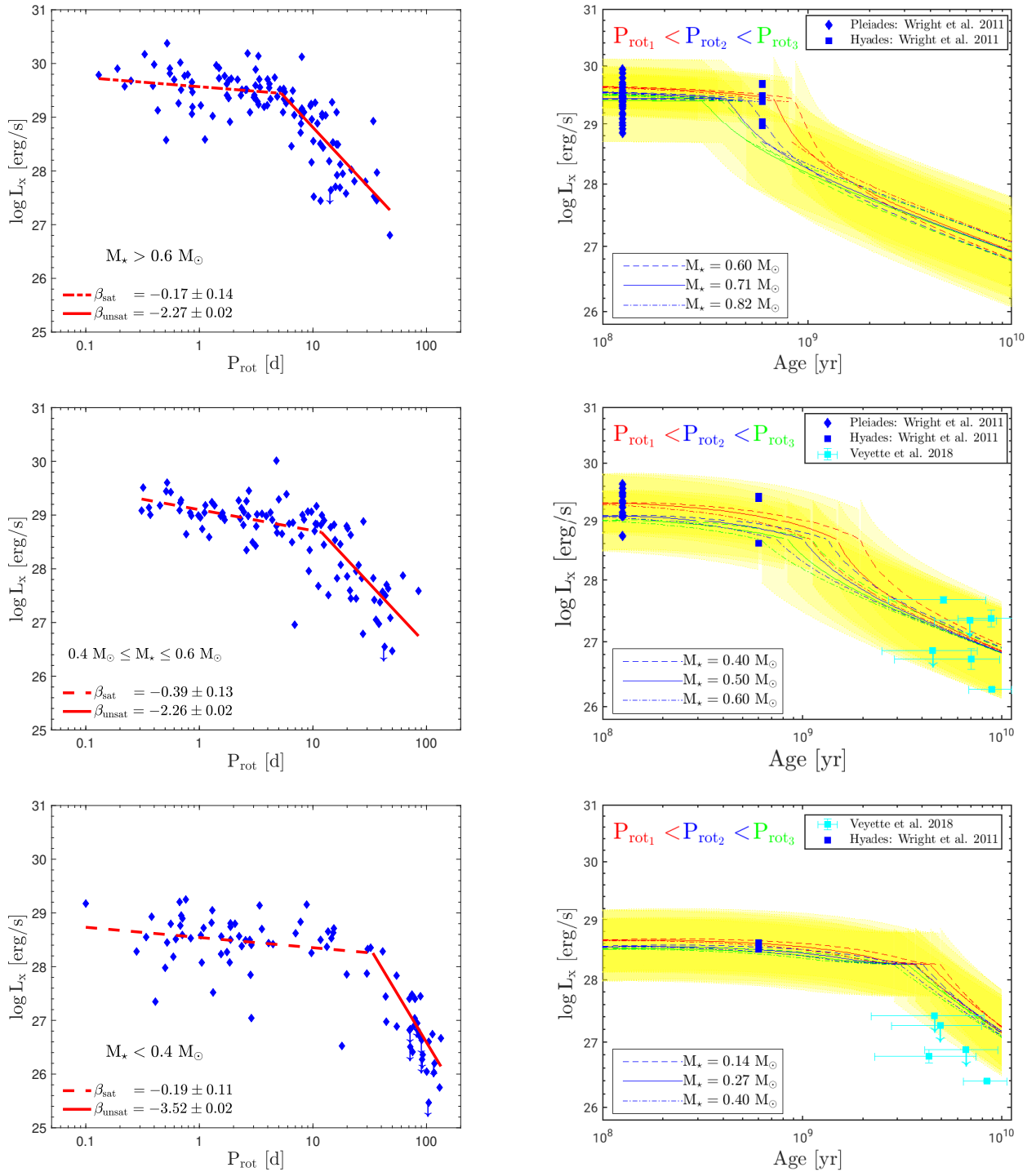
Fig. 7. *Left*: results of the activity-rotation relation fitting for the three mass ranges considered in this work. *Right*: retrieved L_x-age relation from angular evolution models for the same mass bins together with M dwarfs with known ages from the literature by Wright et al. (2011) (blue points) and Veyette & Muirhead (2018) (squared cyan). The yellow region shows the vertical L_x-spread from the standard deviation of the observed $L_x−P_{rot}$ relation. Three different initial rotation periods are shown: $P_{rot,1}$ = 1.54 d (red line), $P_{rot,2}$ = 5.51 d (blue line), and $P_{rot,3}$ = 8.83 d (green line). In the predicted L_x-age relation we show the model for the central mass bin (solid line), together with the lower and upper mass boundaries (dashed and dotted line, respectively).

with X-ray luminosities below the detection limit. They computed L_x with the adopted distance equal to 133 pc for stars in the Pleiades and 46 pc for stars in the Hyades.

Field stars were taken from Veyette & Muirhead (2018), who determined individual ages for 11 nearby planet-hosting M dwarfs using a combination of kinematics and chemical evo-

lution. First we calculated the distances and stellar parameters for these stars as described in Sect. 2 for the rotation-activity sample. Then we searched for X-ray detections of these stars in the ROSAT FSC (Voges et al. 2000), the ROSAT BSC (Voges et al. 1999), and the 3XMM-DR8 catalog (Rosen 2016). For the six stars that we were able to identify with a source in one

Table 5. Relevant parameters for the sample of M dwarfs from Veyette & Muirhead (2018).

Name	Age [Gyr]	D [pc]	$M_\star$ [$M_\odot$]	X-ray catalog	$\log(L_x)$ [erg s^{-1}]
GJ 176	$8.8^{+2.5}_{-2.8}$	9.473 ± 0.006	0.47 ± 0.02	RASS/FSC	27.38 ± 0.13
GJ 179	$4.6^{+3.5}_{-2.4}$	12.360 ± 0.009	0.33 ± 0.01	RASS	<27.42
GJ 436	$8.9^{+2.3}_{-2.1}$	9.755 ± 0.008	0.43 ± 0.01	3XMM-DR8	26.26 ± 0.02
GJ 536	$6.9^{+2.5}_{-2.3}$	14.412 ± 0.009	0.56 ± 0.01	RASS	<27.35
GJ 581	$6.6^{+2.9}_{-2.5}$	6.299 ± 0.002	0.40 ± 0.01	RASS	<26.88
GJ 617A	$5.1^{+3.2}_{-2.4}$	10.767 ± 0.003	0.58 ± 0.02	RASS/BSC	27.68 ± 0.05
GJ 625	$7.0^{+2.7}_{-4.1}$	6.473 ± 0.001	0.50 ± 0.02	RASS/FSC	26.74 ± 0.16
GJ 628	$4.3^{+3.1}_{-2.0}$	4.306 ± 0.001	0.33 ± 0.01	RASS/FSC	26.78 ± 0.10
GJ 649	$4.5^{+3.0}_{-2.0}$	10.382 ± 0.003	0.51 ± 0.21	RASS/FSC	<26.87
GJ 849	$4.9^{+3.0}_{-2.1}$	8.802 ± 0.003	0.40 ± 0.01	RASS/FSC	<27.27
GJ 876	$8.4^{+2.2}_{-2.0}$	4.675 ± 0.001	0.31 ± 0.01	3XMM-DR8	26.40 ± 0.01

Notes. FLAG$_D$ are not listed because all *Gaia* parallaxes are reliable for this sample (see text in Sect. 6.2.2).

of the above catalogs, we derived the X-ray luminosities from the cataloged count rates in the same manner in which we treated the stars from González-Álvarez et al. (2019) (see Sect. 3). For the remaining five stars, we estimated the upper limit on L_x based on the ROSAT All-Sky Survey (RASS). Specifically, we extracted the RASS exposure time at the location of each of the stars from the exposure maps available from the ROSAT webpage at the Max-Planck-Institut für extraterrestrische Physik[7]. Then we obtained the individual upper limit count rates from the estimated RASS sensitivity limit shown as lower envelope in the plot that shows the RASS count rate versus exposure time in Fig. 4 of Stelzer et al. (2013). In Table 5 we list all derived parameters for the stars from Veyette & Muirhead (2018) that are relevant for our purpose. These are the age with its uncertainty extracted from Veyette & Muirhead (2018) (Col. 2), the adopted distance derived from the quality criteria as defined in Sect. 3 (Col. 3, all *Gaia* distances are reliable for this sample, FLAG$_D$ = 11), the stellar mass (Col. 4), and the X-ray instrument and luminosity in the 0.1−2.4 keV band (Cols. 5 and 6).

Each star from Veyette & Muirhead (2018) is plotted on the right side of Fig. 7 in the respective panel corresponding to its individual stellar mass. Pleiades and Hyades stars from Wright et al. (2011) are plotted in Fig. 7, using the stellar masses they computed using $V-K_s$ magnitudes.

Our constructed L_x-age relation places the Pleiades M dwarfs in the saturated regime and the Hyades M dwarfs as well, except for the highest mass bin ($M_\star = 0.6-0.8\,M_\odot$), where the age of the Hyades corresponds to the turnover point between saturated and unsaturated regime. Interestingly, both open clusters span the full spread of X-ray luminosities inferred from the Matt et al. (2015) rotational evolution tracks and the observed L_x-P_{rot} relation of field M dwarfs (yellow region in Fig. 7).

The field M dwarfs from Veyette & Muirhead (2018) span ages from ∼4 to 9 Gyr and masses within the range of our two lower-mass bins. At a given age and mass, this sample presents a spread in X-ray luminosity of more than an order of magnitude. None of these stars has $M_\star > 0.6\,M_\odot$, corresponding to our high-mass bin. While the intermediate-mass stars ($M_\star = 0.4-0.6\,M_\odot$) fall within the predicted range of L_x (yellow zone in Fig. 7), the fully convective stars ($M_\star < 0.4\,M_\odot$) are clearly underluminous with respect to the prediction of our L_x-age relation. Our procedure overpredicts the X-rays of the fully convective

field M dwarfs because the spin-down model provides rotation periods that are faster than observed for these stars (as noted in Matt et al. 2015).
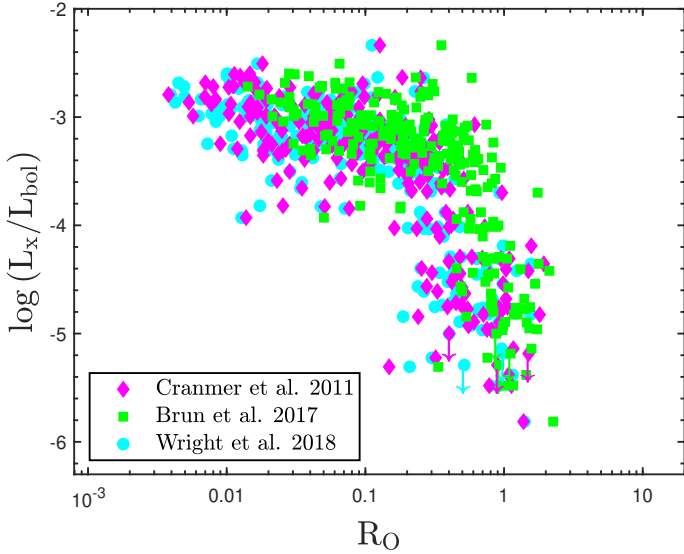
6.3. Fractional X-ray luminosity versus Rossby number

As described in Sect. 3, we computed the τ_{conv} for the full sample using the relation by Wright et al. (2018), which is valid over the range $1.1 < V-K_s < 7.0$. To investigate if this empirical τ_{conv} scale is consistent with theoretical values, we also constructed the $L_x/L_{bol}-R_O$ relation for the τ_{conv} parameterizations of Cranmer & Saar (2011) and Brun et al. (2017). The relation between τ_{conv} and T_{eff} of Cranmer & Saar (2011) is the result of a parameterized fit of 1D stellar structure models. Brun et al. (2017) presented the fluid Rossby number as a function of $M_\star$ and $\Omega_\star$ computed with 3D stellar models based on mixing length theory, and Wright et al. (2018) derived τ_{conv} empirically as a function of $V-K_s$ color from a study of the $L_x/L_{bol}-R_O$ relation for fully convective stars. Because the relations from Cranmer & Saar (2011) and Brun et al. (2017) are calibrated only for partially convective stars, we excluded from the analysis in $L_x/L_{bol}-R_O$ space all stars with $T_{eff} < 3300$ K, corresponding to $M_\star < 0.4\,M_\odot$.

It is important to note that the different scaling laws for τ_{conv} result in different values for the Sun. Therefore we normalized the three relations in order to obtain a fixed solar value. We scaled the Cranmer & Saar (2011) and Brun et al. (2017) parameterization to the one by Wright et al. (2018), taking the ratio between τ_{conv} for the Sun as normalization factor. In particular, we computed the solar τ_{conv} by Cranmer & Saar (2011) using $T_{eff,\odot} = 5778$ K (Brandenburg et al. 2017) and the solar τ_{conv} by Wright et al. (2018) with $(V-K)_\odot = 1.5$ mag[8]. Because Brun et al. (2017) provide R_O already normalized to the solar mass and rotation rate, we computed the solar τ_{conv} using $P_{rot,\odot} = 24.5$ d (Brandenburg et al. 2017). In Tables 2 and B.1 we list for each star the three R_O values from the different relations for τ_{conv}. In Fig. 8 we show how L_x/L_{bol} versus R_O changes according to the different adopted τ_{conv} parameterizations. The $L_x/L_{bol}-R_O$ relation with the Wright et al. (2018) and Cranmer & Saar (2011) τ_{conv} values are similar, but the Brun et al. (2017) parameterization is shifted toward higher R_O values and has a smaller spread in the unsaturated regime.

---

[7] http://www.xray.mpe.mpg.de/cgi-bin/rosat/rosat-survey

[8] http://mips.as.arizona.edu/~cnaw/sun.html

Fig. 8. Comparison of L_x/L_{bol} vs. R_O obtained for the three τ_{conv} parameterizations by Cranmer & Saar (2011) (purple filled rhombus), Brun et al. (2017) (green filled square), and Wright et al. (2018) (cyan filled circle).

We applied the fitting procedure used in Sect. 6.1 to the three L_x/L_{bol} versus R_O relations. The best-fit parameters are shown in Table 6. All three relations yield a nonconstant saturated level, that is, a decrease in L_x/L_{bol} for higher Rossby numbers, at the 3σ level. The $R_{O,sat}$ for the Brun et al. (2017) parameterization has a noticeably larger breaking point than those from Cranmer & Saar (2011) and Wright et al. (2018) calibrations. Moreover, the slope in the unsaturated regime from Brun et al. (2017) is steeper than the other two, showing a much more abrupt activity decrease toward higher R_O. Another interesting result is the visible and remarkable double gap around $0.2 \leq R_O \leq 1.2$, which corresponds to $-4.5 \leq L_x/L_{bol} \leq -3.5$ (see Fig. 8).

7. Discussion

We presented a thorough investigation of the shape of the relation of X-ray activity to rotation in L_x-P_{rot} space for a comprehensive sample of M dwarfs, and we studied for the first time, to our knowledge, the effect of the τ_{conv} calibration on this relation in $L_x/L_{bol}-R_O$ space. We created the largest and most homogeneous database of rotational periods and X-ray activity for field M dwarfs to date by taking new observations with *XMM-Newton* and *Chandra* satellites and updating data from the literature. We computed stellar parameters from calibrated photometry for a total of 302 stars with measured P_{rot} and L_x, including *Gaia* parallaxes when reliable according to Lindegren et al. (2018), and our own criteria. With our combination and homogenization analysis of the whole sample originating from previous studies, we reduced possible observational biases caused by the different limitations of the samples from the literature. In particular, because Wright et al. (2011), Stelzer et al. (2016) and González-Álvarez et al. (2019) used X-ray data from the archives without including upper limits in the analysis, this leads to a bias toward X-ray bright stars. On the other hand, Wright & Drake (2016) and Wright et al. (2018) selected stars from the MEarth project, where only fully convective stars with long P_{rot} are included. Our new sample with deep dedicated

Table 6. Results from the fitting procedure applied to the L_x/L_{bol} vs. R_O relation shown in Fig. 8, computed for the three τ_{conv} parameterizations described in Sect. 6.3.

Parameterization	β_{sat}	β_{unsat}	$R_{O,sat}$
Cranmer & Saar (2011)	-0.31 ± 0.08	-2.03 ± 0.01	0.19 ± 0.02
Brun et al. (2017)	-0.33 ± 0.08	-2.92 ± 0.02	0.41 ± 0.02
Wright et al. (2018)	-0.21 ± 0.08	-1.99 ± 0.01	0.14 ± 0.01

X-ray observations for 14 K2-selected M dwarfs avoids the X-ray brightness bias, but is limited to 14 stars.

We analyzed the L_x-P_{rot} relation by applying a two-slope power-law fit in three different mass ranges. Next to the known two-regime behavior with saturation for fast-rotating stars and decreasing L_x for higher P_{rot} above a certain threshold, we find that the L_x level in the saturated regime is not constant, but decreases slightly with increasing P_{rot}. In the saturated regime the lowest mass stars have the lowest X-ray luminosities, showing a large (≈ 2 dex) L_x spread (see the bottom panel of Fig. 4). Here we likely probe the rotation-independent decrease in X-ray emission in late-M dwarfs that has been ascribed to poor coupling between matter and magnetic field in the increasingly neutral atmospheres at the bottom of the MS and the ensuing shut-off of activity (Mohanty et al. 2002) probably caused by the increasing electrical resistivity in such cool atmospheres. We confirmed past results by Pizzolato et al. (2003) for which the breaking point between the two power laws occurs at higher P_{rot} as $M_\star$ decreases. However, in our several times larger sample, the values we find for the turnover points are much higher than those presented in their historical study.

The nonconstant X-ray emission level in the saturated regime was first noted by Reiners et al. (2014) in terms of L_x/L_{bol}. As possible explanation, they suggested a property of the dynamo or a residual mass-dependence in the saturated regime. We see the negative slope in each of the three mass bins we examined (see, e.g., the left panel in Fig. 7). The likely cause therefore is some rotation dependence of the dynamo even for these fast rotators. We measured a steeper slope in the unsaturated regime for stars with $M_\star < 0.4\,M_\odot$ (fully convective stars).

We used our best-fit parameters of the activity-rotation relation to construct the L_x-age relation using spin-down models by Matt et al. (2015). In the time-evolution tracks for a given narrow mass range at a certain mass-dependent point, the evolution of different initial periods starts to diverge. This is not visible in the L_x-age relation as long as the stars remain saturated, but when they drop out of saturation and L_x starts to decrease, the tracks with different initial periods also diverge in L_x-age space. However, the range of our predicted L_x for different initial P_{rot} at given age and mass (i.e., the tracks in the right panel in Fig. 7) is much smaller than the L_x-spread we inferred from the observed relation of X-ray activity to rotation (yellow region in Fig. 7). Therefore we cannot distinguish the X-ray evolution of stars with different initial rotation periods.

By comparing our constructed L_x-age relation to stars with known age, we found that the Hyades stars in our high-mass bin ($0.6-0.8\,M_\odot$; corresponding to late-K to early-M SpT) are located at the onset of the unsaturated regime in the L_x-age relation. The rotation periods of the Hyades in that mass range are ($\sim 10-20$ d; Douglas et al. 2019), which is roughly consistent with the P_{rot} at which the transition from the saturated to the unsaturated regime takes place. Moreover, our result shows that the Pleiades and Hyades stars span the full range of L_x in

the saturated regime, suggesting that the scatter of X-ray luminosity at a given rotation period has no evolutionary component from the zero-age MS onwards. Because the model by Matt et al. (2015) fails to produce the known long rotation periods (≥ 50 d) for M dwarfs, our model overpredicts the X-ray luminosity of fully convective field stars in our constructed relation of X-ray to age. This explains why in the fully convective bin the field M stars with gigayear-ages are located below the L_x expected from our relation.

We investigated for the first time, to our knowledge, how adopting different τ_{conv} parameterizations can affect the shape of the $L_x/L_{bol}-R_O$ relation. We performed this comparison for the Rossby numbers of Cranmer & Saar (2011), Brun et al. (2017), and Wright et al. (2018), which originate from different approaches and have different ranges of validity. In particular, the relation of Cranmer & Saar (2011) is valid only for stars with $T_{eff} \geq 3300$ K, Brun et al. (2017) can be applied to a wide range of stellar masses (from $0.4\,M_\odot$ to $1.2\,M_\odot$), and the relation of Wright et al. (2018) is valid over 1.1 mag $< V-K_s < 7.0$ mag. Therefore, the stars we considered in our investigation of $L_x/L_{bol}-R_O$ are the 242 out of the full sample that fulfill all these conditions.

We applied the same fitting procedure used for the L_x-P_{rot} relation to $L_x/L_{bol}-R_O$, and we identified the following interesting results: (1) all calibrations provide a decrease in L_x/L_{bol} in the saturated regime, (2) the parameterization by Brun et al. (2017) yields a much steeper β_{unsat} slope with a breaking point at higher R_O than those from Cranmer & Saar (2011) and Wright et al. (2018) parameterizations, and (3) there is a remarkable double gap in $L_x/L_{bol}-R_O$ space with a scarcity of objects slightly above and below $L_x/L_{bol} \sim 10^{-4}$ (e.g., the right panel in Fig. 2) that is difficult to explain as an observational bias.

As discussed above, Reiners et al. (2014) previously observed a slope in the saturated regime in $L_x/L_{bol}-R_O$. They examined a sample in a broad mass range ($M_\star \leq 1.4\,M_\odot$) and found a slope $\beta_{sat} = -0.16$. In our M dwarf sample we find a slightly steeper β_{sat} slope for all three τ_{conv} parameterizations (see Table 6). While above, based on L_x-P_{rot}, we argued that the existence of this slope is not a mass effect (because we see it in different mass bins), its actual steepness may depend on mass.

For the slope in the unsaturated regime, β_{unsat}, we find significantly different results from the three Rossby parameterizations. Wright et al. (2011) studied the $L_x/L_{bol}-R_O$ relation for partially convective stars, finding $R_{O,sat} = 0.16 \pm 0.03$, $\beta_{unsat} = -2.7$, and $(L_x/L_{bol})_{sat} = -3.13$. When the Cranmer & Saar (2011) and Wright et al. (2018) calibrations are used, our slope in the unsaturated regime is substantially smaller than that value ($\beta_{unsat} \simeq -2$), while Brun et al. (2017) yields a significantly larger slope ($\beta_{unsat} = -2.9$). This latter parameterization also yields a much higher value for the break-point $R_{O,sat}$ than Cranmer & Saar (2011) and Wright et al. (2018) and than the historical result by Wright et al. (2011). The L_x/L_{bol}-Rossby relation constructed with the Brun et al. (2017) Rossby numbers visibly produces the smallest scatter of the data points, suggesting that it best represents the presumed universal mass-dependent parameter that rules the activity-rotation relation, and which is usually identified with the convective turnover time.

We speculate that the remarkable gap we found in $L_x/L_{bol}-R_O$ space might be associated with a phase of stalled rotational evolution followed by an episode of rapid spin-down, which has recently been discussed in rotation studies of open clusters and solar-type field stars by Curtis et al. (2019) and Metcalfe & Egeland (2019). In these works the rotation-age relation is studied for G- and K-type stars. According to these

studies, stalling seems to last longer for lower stellar masses. This period stalling might lead to a pile-up of objects before the transition to the unsaturated regime, and combined with subsequent rapid spin-down, a gap around the breaking point in the relation of activity to rotation. We clearly see two such gaps in the $L_x/L_{bol}-R_O$ space. Moreover, the bottom panel of Fig. 4 demonstrates that this gap is present in different masses. If the evolution of the rotation period is responsible for these gaps, we would expect to see them in L_x-P_{rot} space. There is some evidence for two sparsely populated regions around $\log L_x \sim 28.2$ erg s^{-1} and $\log L_x \sim 27.2$ erg s^{-1}. The upper region occurs at periods of $P_{rot} \sim 10 \ldots 30$ d, corresponding to the period gap in the $M_\star - P_{rot}$ diagram of large samples from the *Kepler* mission (McQuillan et al. 2014). While this coincidence is intriguing, the "X-ray gap" and the search for its origin require further investigation.

The relation of activity to rotation can be also studied by analyzing the emission of typical chromospheric spectral lines. For instance, Newton et al. (2017) analyzed the activity from the H$_\alpha$ emission in $L_{H_\alpha}/L_{bol}-R_O$ space by applying a broken power-law fit. They calculated the Rossby numbers with the τ_{conv} parameterization from Wright et al. (2011), therefore their results are not directly comparable with ours.

8. Conclusions and outlook

The collected and updated database of this work reduced the observational biases in the relation of X-ray activity to rotation. This leads to a series of interesting results, including (1) a nonconstant saturated level of the X-ray emission, (2) a significant steepening of the slope in the unsaturated regime for fully convective stars, (3) possible "regions of avoidance" in the L_x and L_x/L_{bol} distribution that might be related to a discontinuous period evolution, and (4) the dependence of the shape of the $L_x/L_{bol}-R_O$ relation on the assumptions made for the convective turnover time. We moreover predicted for the first time the evolution of M-dwarf X-ray emission for ages beyond $\sim$600 Myr, that is, after the stars drop out of saturation. A focus of future studies should be the transition between saturated and unsaturated regimes of the rotation-activity relation, which is crucial for anchoring the dual power-law fit and to quantify the "X-ray gap". Unprecedentedly large samples can be expected from the All-Sky missions TESS and eROSITA, which yield P_{rot} up to 20 d and X-ray measurements 20 times deeper than ROSAT. These missions will be particularly useful to address these questions.
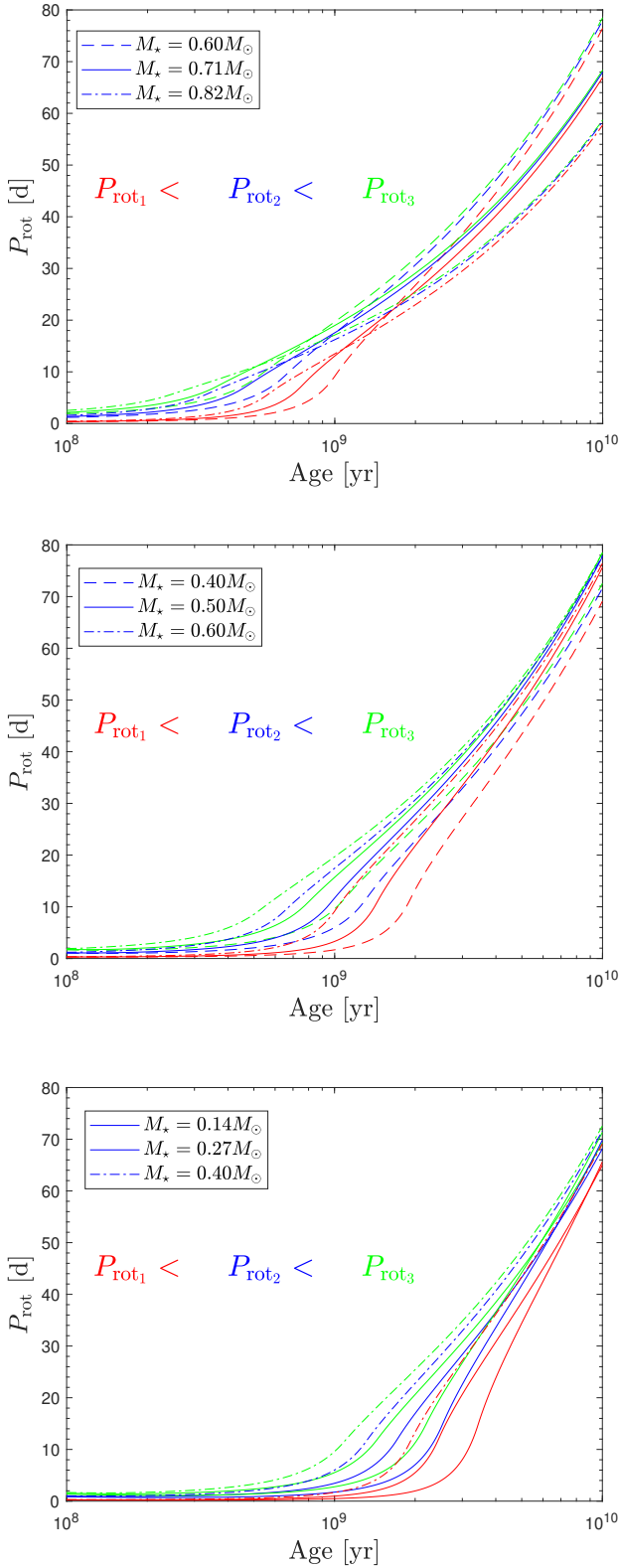
References

Agüeros, M. A., Bowsher, E. C., Bochanski, J. J., et al. 2018, ApJ, 862, 33
Akritas, M. G., Murphy, S. A., & Lavalley, M. P. 1995, JASA, 90, 170
Arenou, F., Luri, X., Babusiaux, C., et al. 2018, A&A, 616, A17

Boller, T., Freyberg, M. J., Trümper, J., et al. 2016, A&A, 588, A103
Bopp, B. W., & Evans, D. S. 1973, MNRAS, 164, 343
Brandenburg, A., Mathur, S., & Metcalfe, T. S. 2017, ApJ, 845, 79
Brun, A. S., Strugarek, A., Varela, J., et al. 2017, ApJ, 836, 192
Chabrier, G., & Küker, M. 2006, A&A, 446, 1027
Cranmer, S. R., & Saar, S. H. 2011, ApJ, 741, 54
Curtis, J. L., Agüeros, M. A., Douglas, S. T., & Meibom, S. 2019, ApJ, 879, 49
Douglas, S. T., Agüeros, M. A., Covey, K. R., et al. 2014, ApJ, 795, 161
Douglas, S. T., Curtis, J. L., Agüeros, M. A., et al. 2019, ApJ, 879, 100
Durney, B. R., De Young, D. S., & Roxburgh, I. W. 1993, Sol. Phys., 145, 207
Eaton, J. A., & Hall, D. 1979, ApJ, 227, 907
Foreman-Mackey, D., Hogg, D. W., Lang, D., & Goodman, J. 2013, PASP, 125, 306
Garraffo, C., Drake, J. J., Dotter, A., et al. 2018, ApJ, 862, 90
González-Álvarez, E., Micela, G., Maldonado, J., et al. 2019, A&A, 624, A27
Güdel, M. 2004, A&ARv, 12, 71
Irwin, J., Berta, Z. K., Burke, C. J., et al. 2011, ApJ, 727, 56
Jao, W.-C., Henry, T. J., Gies, D. R., & Hambly, N. C. 2018, ApJ, 861, L11
Kawaler, S. D. 1988, ApJ, 333, 236
Lépine, S., & Gaidos, E. 2011, AJ, 142, 138
Lindegren, L., Hernández, J., Bombrun, A., et al. 2018, A&A, 616, A2
Mann, A. W., Feiden, G. A., Gaidos, E., Boyajian, T., & Braun, K. V. 2015, ApJ, 804, 1
Mann, A. W., Feiden, G. A., Gaidos, E., Boyajian, T., & von Braun, K. 2016, ApJ, 819, 87
Matt, S. P., Brun, A. S., Baraffe, I., Bouvier, J., & Chabrier, G. 2015, ApJ, 799, L23
McQuillan, A., Mazeh, T., & Aigrain, S. 2014, ApJS, 211, 24

Metcalfe, T. S., & Egeland, R. 2019, ApJ, 871, 39
Mohanty, S., Basri, G., Shu, F., Allard, F., & Chabrier, G. 2002, ApJ, 571, 469
Newton, E. R., Irwin, J., Charbonneau, D., et al. 2017, ApJ, 834, 85
Núñez, A., Agüeros, M. A., Covey, K. R., et al. 2015, ApJ, 809, 161
Núñez, A., Agüeros, M. A., Covey, K. R., & López-Morales, M. 2017, ApJ, 834, 176
Pallavicini, R., Golub, L., Rosner, R., et al. 1981, ApJ, 248, 279
Parker, E. N. 1955, ApJ, 122, 293
Pizzolato, N., Maggio, A., Micela, G., Sciortino, S., & Ventura, P. 2003, A&A, 397, 147
Preibisch, T., & Feigelson, E. D. 2005, ApJS, 160, 390
Raetz, St., Stelzer, B., Scholz, A., 2019, Astron. Nachr., submitted
Raetz, S., Stelzer, B., Damasso, M., & Scholz, A. 2020, A&A, 637, A22
Reiners, A., Schüssler, M., & Passegger, V. M. 2014, ApJ, 794, 144
Rosen, S. 2016, VizieR Online Data Catalog, IX/47
Stelzer, B., & Neuhäuser, R. 2001, A&A, 377, 538
Stelzer, B., Marino, A., Micela, G., López-Santiago, J., & Liefke, C. 2013, MNRAS, 431, 2063
Stelzer, B., Damasso, M., Scholz, A., & Matt, S. P. 2016, MNRAS, 463, 1844
Vanderburg, A., & Johnson, J. A. 2014, PASP, 126, 948
Veyette, M. J., & Muirhead, P. S. 2018, ApJ, 863, 166
Voges, W., Aschenbach, B., Boller, T., et al. 1999, A&A, 349, 389
Voges, W., Aschenbach, B., Boller, T., et al. 2000, IAU Circ., 7432, 3
Wright, N. J., & Drake, J. J. 2016, Nature, 535, 526
Wright, N.J., Drake, J.J., Mamajek, E.E., & Henry, G.W. 2011, ApJ, 743
Wright, N. J., Newton, E. R., Williams, P. K., Drake, J. J., & Yadav, R. K. 2018, MNRAS, 479, 2351
Zechmeister, M., & Kürster, M. 2009, A&A, 496, 577

Appendix A: Age evolution of the rotation period

Fig. A.1. Time-evolution models by Matt et al. (2015) for three different initial rotation periods. In particular, $P_{rot_1} = 1.54$ d, $P_{rot_2} = 5.51$ d and $P_{rot_3} = 8.83$ d. The retrieved L_x–Age relation from time evolution models together with literature data by Stelzer & Neuhäuser (2001), Wright et al. (2011), and Veyette & Muirhead (2018). The three mass ranges are shown *from top to bottom*: $M_\star > 0.6\,M_\odot$, $0.4\,M_\odot \leq M_\star \leq 0.6\,M_\odot$, and $M_\star < 0.4\,M_\odot$.

Appendix B: Stellar parameters and X-ray results

Table B.1. Stellar parameters and updated X-ray results we computed for the 288 stars we took from the literature samples (Wright et al. 2011, 2018; Wright & Drake 2016; Stelzer et al. 2016; González-Álvarez et al. 2019).

Name	M_{K_s} [mag]	$M_\star$ [$M_\odot$]	$R_\star$ [$R_\odot$]	$\log_{10}\left(\frac{L_{bol}}{L_\odot}\right)$	$V-J$ [mag]	P_{rot} [d]	$\log(L_x)$ [erg/s]	$\log\left(\frac{L_x}{L_{bol}}\right)$	$R_{O,C\&S}$	$R_{O,B}$	$R_{O,W}$	D [pc]	$FLAG_{Gaia}$
HAT 122–01032	6.33±0.03	0.41±0.01	0.40±0.01	−1.73±0.04	4.26	4.38	28.91±0.01	−2.94±0.09	–	–	0.05	18.63±0.03	11
LP 149–56	5.85±0.03	0.49±0.01	0.47±0.01	−1.51±0.04	3.71	6.17	28.84±0.03	−3.24±0.10	0.14	0.25	0.10	29.56±0.05	11
G 172–1	7.14±0.10	0.30±0.01	0.29±0.01	−2.06±0.19	4.32	1.09	28.72±0.04	−2.81±0.23	–	–	0.01	14.77±0.71	01
UCAC4 729–006249	5.14±0.03	0.61±0.01	0.59±0.02	−1.16±0.03	2.80	8.35	29.09±0.03	−3.33±0.10	0.24	0.45	0.23	43.63±0.07	11
2MASS J00380001+4353454	4.24±0.16	0.76±0.03	0.76±0.04	−0.81±0.12	2.95	0.55	29.91±0.03	−2.87±0.34	0.01	0.07	0.01	97.19±1.32	11
1RXS J003926.5+381607	4.48±0.16	0.72±0.03	0.71±0.04	−0.89±0.13	2.77	3.08	29.36±0.12	−3.33±0.35	0.09	0.26	0.09	115.40±1.59	11
⋮	⋮	⋮	⋮	⋮	⋮	⋮	⋮	⋮	⋮	⋮	⋮	⋮	⋮

Notes. The last column shows the FLAG we used to verify if *Gaia* distances are reliable as explained in Sect. 3. The full table is available in electronic form at the CDS.

Astronomy & Astrophysics

GJ 357 b

A super-Earth orbiting an extremely inactive host star

D. Modirrousta-Galian[1,2], B. Stelzer[3,2], E. Magaudda[3], J. Maldonado[2], M. Güdel[4], J. Sanz-Forcada[5],
B. Edwards[6], and G. Micela[2]

[1] Università di Palermo, Department of Physics and Chemistry, Via Archirafi 36, 90126 Palermo, Italy
  e-mail: darius.modirrousta@inaf.it
[2] INAF – Osservatorio Astronomico di Palermo, Piazza del Parlamento 1, 90134 Palermo, Italy
[3] Institut für Astronomie & Astrophysik, Eberhard-Karls Universität Tübingen, Sand 1, 72076 Tübingen, Germany
[4] Institut für Astrophysik, Universität Wien, Türkenschanzstrasse 17, 1180 Wien, Austria
[5] Departamento de Astrofísica, Centro de Astrobiología (CSIC-INTA), ESAC Campus, Camino bajo del Castillo s/n,
  28692 Villanueva de la Cañada, Madrid, Spain
[6] Department of Physics and Astronomy, University College London, London, UK

ABSTRACT

Aims. In this paper we present a deep X-ray observation of the nearby M dwarf GJ 357 and use it to put constraints on the atmospheric evolution of its planet, GJ 357 b. We also analyse the systematic errors in the stellar parameters of GJ 357 in order to see how they affect the perceived planetary properties.

Methods. By comparing the observed X-ray luminosity of its host star, we estimate the age of GJ 357 b as derived from a recent *XMM-Newton* observation ($\log L_x$ [erg s^{-1}] = 25.73), with L_x− age relations for M dwarfs. We find that GJ 357 presents one of the lowest X-ray activity levels ever measured for an M dwarf, and we put a lower limit on its age of 5 Gyr. Using this age limit, we performed a backwards reconstruction of the original primordial atmospheric reservoir. Furthermore, by considering the systematic errors in the stellar parameters, we find a range of possible planetary masses, radii, and densities.

Results. From the backwards reconstruction of the irradiation history of GJ 357 b's we find that the upper limit of its initial primordial atmospheric mass is ∼38 $M_\oplus$. An initial atmospheric reservoir significantly larger than this may have survived through the X-ray and ultraviolet irradiation history, which would not be consistent with current observations that suggest a telluric composition. However, given the relatively small mass of GJ 357 b, even accreting a primordial envelope ≳10 $M_\oplus$ would have been improbable as an unusually low protoplanetary disc opacity, large-scale migration, and a weak interior luminosity would have been required. For this reason, we discard the possibility that GJ 357 b was born as a Neptunian- or Jovian-sized body. In spite of the unlikelihood of a currently existing primordial envelope, volcanism and outgassing may have contributed to a secondary atmosphere. Under this assumption, we present three different synthetic IR spectra for GJ 357 b that one might expect, consisting of 100% CO_2, 100% SO_2, and 75% N_2, 24% CO_2 and 1% H_2O, respectively. Future observations with space-based IR spectroscopy missions will be able to test these models. Finally, we show that the uncertainties in the stellar and planetary quantities do not have a significant effect on the estimated mass or radius of GJ 357 b.

Key words. planets and satellites: terrestrial planets – planets and satellites: atmospheres – planet–star interactions–
planets and satellites: physical evolution – X-rays: stars

1. Introduction

Nearby transiting planets, especially those also detected with the radial-velocity method, are very important targets for complete characterisation. A subset of these interesting bodies are terrestrial planets with masses comparable to that of the Earth. Even though theoretical models predict that they are very abundant (e.g. Schlichting et al. 2013; Simon et al. 2016), they are rare within our astronomical catalogues due to instrumental limitations. Therefore, detailed analyses of these planets are valuable in order for us to understand their physical properties. From this perspective, GJ 357 b is an intriguing exoplanet. It orbits a nearby star (π = 105.88 mas ± 0.06 from *Gaia* DR2) that displays very low magnetic activity. The optical emission line activity of GJ 357 is among the lowest for its spectral type (Schöfer et al. 2019), the Ca II $\log R'_{HK}$ value is −5.37 (Boro Saikia et al. 2018),

and a photometric rotation period of ∼78 d was inferred from combining data from different ground-based surveys (Luque et al. 2019). The planet, GJ 357 b, was detected by TESS (TOI 562.01) in Sector 8, with a transit depth of 1164 ± 66 ppm and a periodicity of 3.93 days, corresponding to an orbital distance of 0.035 ± 0.0002 AU. The system also includes two non-transiting super-Earths in wider orbits which appear to have larger masses ($M \sin i$ = 3.40 ± 0.46 $M_\oplus$ and $M \sin i$ = 6.1 ± 1 $M_\oplus$ for GJ 357 c and GJ 357 d respectively; Luque et al. 2019).

Regarding GJ 357 b, its mass and radius measurements are 1.84 ± 0.31 $M_\oplus$ and 1.22 ± 0.08 $R_\oplus$ (i.e. a density of 5.6 ± 1.2 g cm^{-3}), respectively (Luque et al. 2019), which is consistent with a telluric planet that most probably does not host a primordial atmosphere. Given that it may host a secondary atmosphere, and considering that secondary atmospheres can provide important clues as to the internal structure and evolution

of planets, we believe GJ 357 b is one of the best targets for spectroscopic observations with future instrumentation such as the *James Webb* Space Telescope (JWST, Greene et al. 2016), the Extremely Large Telescope (ELT, Brandl et al. 2018), Twinkle (Edwards et al. 2019), and Ariel (Tinetti et al. 2018). It is therefore important to predict what kind of atmosphere could exist on this planet and the type of evolution that it has undergone throughout its lifetime.

In this paper we evaluate the evolution and composition of the atmosphere of GJ 357 b based on the age estimate derived from our measurement of the X-ray luminosity of the host star, GJ 357. In Sect. 2 we present the new *XMM-Newton* data, their analysis, and interpretation including the age estimate we derive. In Sect. 3 we use that result to show that GJ 357 b may have formed with a primordial atmosphere as large as ∼38 $M_⊕$. However, we then argue that an atmosphere of this size would have been unlikely due to requiring an atypical formation history. After this, we produce synthetic spectra in Sect. 4 to show what one might expect from observational data of its atmosphere. In Sect. 5 we revisit and compare different ways to estimate the stellar parameters in order to assess the influence of these values on the planet radius and mass. We discuss and summarise our results in Sect. 6.

2. Constraints from X-ray data

GJ 357 was observed with *XMM-Newton* on 19 May 2019 (Obs-ID 0840841501) in the course of a systematic survey of X-ray activity in nearby M dwarfs (PI: Stelzer). These observations were designed to reach the deep sensitivity required to constrain the very faint X-ray luminosities of the least active M dwarf stars. Specifically, the X-ray properties derived from such data, in combination with the rotation period and in comparison to other samples of M dwarfs, enable us to estimate the age of the star, which is relevant for an assessment of the evolution of its planets.

2.1. X-ray data analysis

We analysed the X-ray observation with the *XMM-Newton* Science Analysis System (SAS)[1] 18.0 pipeline. Our analysis is focused on the data from the EPIC/pn instrument which provides the highest sensitivity.

The first analysis step was the extraction of the light curve for the whole detector which we inspected for time-intervals of high background. We identified such intervals using as a cutoff threshold a count rate value of $0.35\,\mathrm{cts\,s^{-1}}$. Those parts of the observations with a count rate above this value were excluded from the subsequent analysis, while the remaining ones define the good time intervals (GTIs). We found this method to give a relatively clean observation and a nominal exposure time of 29.76 ks which is reduced only by a few percent to 29.0 ks of GTIs. In addition, we filtered the data for pixel pattern (PATTERN ≤ 12) for an optimum trade-off between detection efficiency, spectral resolution, and quality flag (FLAG = 0); and we only retained events with energy greater than 0.2 keV where the spectral response function is well calibrated.

We performed the source detection using the SAS pipeline EDETECT_CHAIN in the full EPIC/pn energy range (0.15−12.0 keV) and in five narrower bands: (1) 0.15−0.3 keV, (2) 0.3−1.0 keV, (3) 1.0−2.4 keV, (4) 2.4−5.0 keV, (5) 5.0−

Table 1. X-ray spectral parameters of GJ 357 and flux in the 0.3−5.0 keV band.

kT [keV]	$\log EM$ [cm^{-3}]	χ^2_{red}	d.o.f. [*]	f_x (0.3−5.0 keV) [10^{-15}ergs cm^{-2} s^{-1}]
0.20 ± 0.10	47.69 ± 0.16	0.9	13	(2.90 ± 0.88)

Notes. The 2 σ uncertainties were computed with the error pipeline provided in the XSPEC software package. [*]Short for degrees of freedom.

12.0 keV. This analysis showed that above 5.0 keV the count rate of GJ 357 is approximately zero. The number of net source counts in the 0.15−5.0 keV band (i.e. the sum of bands 1–4) is 118 cts.

The extraction of spectrum and light curve was performed considering a source region of 15″ centred on the position obtained for GJ 357 from the source-detection process, with an annulus for the background region centred at the same position and with an inner radius three times larger than the source radius. We created the response matrix and ancillary response for the spectral analysis with the SAS tools, RMFGEN and ARFGEN, and we grouped the spectrum to a minimum of five counts for each background-subtracted spectral channel. We initially extracted the spectrum of GJ 357 in the 0.15−5.0 keV band, as suggested by the source detection. We then noticed that below 0.3 keV the source shows count fluctuations that do not follow the mean spectral trend. For this reason, the spectral fitting within the XSPEC environment[2] was performed for the 0.3−5.0 keV band. First, we used a one-temperature APEC model with frozen abundances ($Z = 0.3\,Z_⊙$). We then included a new model component (cflux) to calculate the flux in the chosen energy band, keeping the APEC model components fixed to the values obtained in the first step. The best-fitting model yields the coronal temperature (kT), the emission measure (EM), and the flux (f_x); all listed in Table 1. Due to the low number of counts in the spectrum this simple spectral shape provides an appropriate description of the data. We also tried to vary the abundances, and to fix them on the solar value, but this led to significantly poorer fits ($\chi^2_{\mathrm{red}} \sim 2$).

We extracted the light curve in the same energy band as the spectrum (0.3−5.0 keV) using the SAS pipeline EPICLCCORR which applies the background subtraction, and the corrections for dead time, exposure, and GTI. The light curve does not present obvious evidence for variability such as flares.

The majority of historical X-ray measurements for M dwarfs refer to the 0.1−2.4 keV band. Therefore, in order to be consistent with data from the literature to which we make reference in Sect. 2.2 we estimated the flux in the 0.1−2.4 keV energy band with XSPEC for our best-fitting model from Table 1, obtaining a scaling factor between the two energy bands (from 0.3−5.0 to 0.1−2.4 keV) amounting to 1.73 ± 0.73. We then calculated the X-ray luminosity in the 0.1−2.4 keV band from the scaled flux and the *Gaia* distance (9.44 ± 0.01 pc) that we calculated from the parallax given in the *Gaia*-DR2 archive. Because it is known that *Gaia*-DR2 contains spurious astrometric solutions (Arenou et al. 2018), we verified that the parallax of GJ 357 is reliable by evaluating the quality flags provided by Lindegren et al. (2018). The resulting value for the 0.1−2.4 keV X-ray luminosity is $\log L_x\,[\mathrm{erg\,s^{-1}}] = 25.73 \pm 0.23$. The relative error includes the uncertainty of the flux in the 0.3−5.0 keV energy band weighted with that of the scaling factor. We also used the
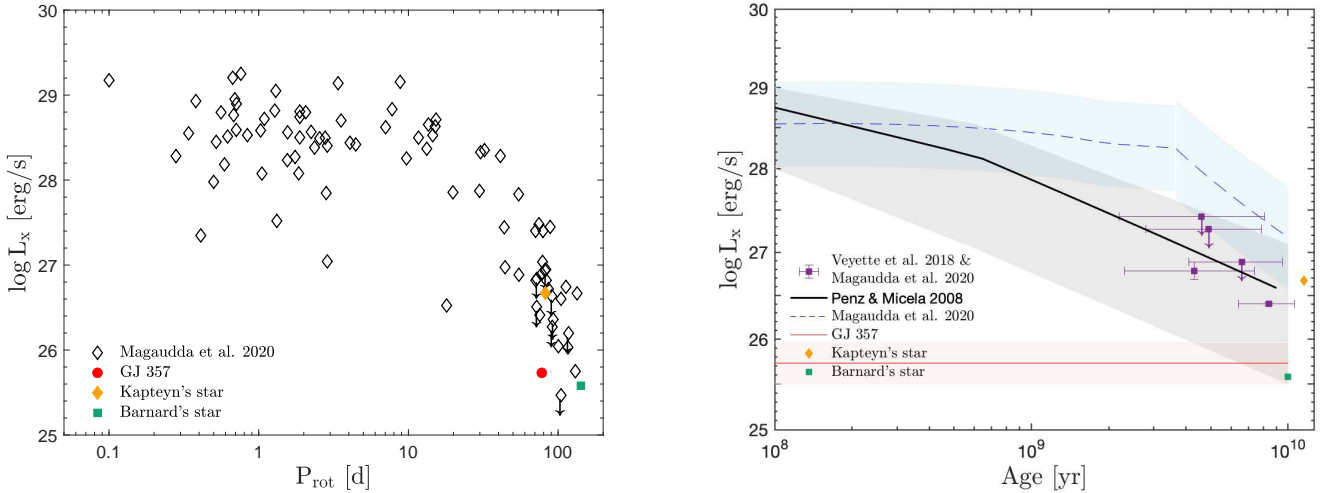
Fig. 1. GJ 357 compared to the activity−rotation−age relation of M dwarfs from Magaudda et al. (2020). *Left*: X-ray luminosity vs. rotation period; for GJ 357 the L_x measurement is derived from recent *XMM-Newton* data analysed in this paper and the P_{rot} value is from Luque et al. (2019). *Right*: X-ray luminosity vs. age reconstructed based on the observed $L_x - P_{rot}$ relation (*left panel*) and the angular momentum evolution models of Matt et al. (2015). In addition, the empirical scaling law from Penz & Micela (2008) is shown. Two M stars with known ages, Barnard's star (GJ 699) and Kapteyn's star (GJ 191), are added to the plots for reference.

Gaia distance together with the 2MASS apparent K_s−magnitude ($K_s = 6.47 \pm 0.02$ mag) to compute the absolute magnitude in the K_s-band (M_{K_s}). We combined M_{K_s} with the solar bolometric magnitude ($M_{bol,\odot} = 4.75$) to calculate the bolometric luminosity of GJ 357 ($L_{bol} = 0.015 \pm 0.001\,L_\odot$). Using this value we found a fractional X-ray luminosity of $\log(L_x/L_{bol}) = -6.05 \pm 0.09$.

2.2. The X-ray activity of GJ 357 in context and an age estimate

It is instructive to compare the X-ray properties of GJ 357 to those of other M dwarfs. Particularly relevant in the context of our article are the clues that X-ray activity can give on stellar age. We therefore compare GJ 357 to the recent results of Magaudda et al. (2020). The sample of this latter study includes both new data and a comprehensive compilation of the previous literature on the X-ray activity−rotation−age relation of M dwarfs. Magaudda et al. (2020) analysed all data in a homogeneous way, which required some updates to the literature results including the use of *Gaia* parallaxes.

In Fig. 1 we present the relation between X-ray luminosity and rotation period (L_x vs. P_{rot}) and the L_x-age relation from Magaudda et al. (2020) together with the respective parameter values of GJ 357. The sample shown here is restricted to stars in the mass range $0.14-0.4\,M_\odot$, to which GJ 357 belongs according to the stellar mass presented by Luque et al. (2019; $0.34\,M_\odot$) and our own analysis of the stellar parameters presented in Sect. 5 of this paper. Remarkably, the X-ray luminosity of GJ 357 is at the same level as that of the least active and slowest rotating M dwarfs in the same mass range (Fig. 1 − left panel). Only the exceptional sensitivity of *XMM-Newton* allows us to probe such low activity levels of even the most nearby M dwarfs.

The right hand side of Fig. 1 shows a derived L_x-age relation based on the observed $L_x − P_{rot}$ relation (left panel) and the angular momentum evolution models ($P_{rot} −$ age) from Matt et al. (2015), where the light blue shade represents the uncertainty of the X-ray luminosity at a given age, mainly originating from the spread of L_x at a given rotation period. Ages for field M dwarfs are extremely hard to determine and are available only

for a handful of stars. In Fig. 1 we overplot stars in the examined mass range $0.14-0.4\,M_\odot$ that have known individual ages. This sample includes some field M dwarfs, with ages derived by Veyette & Muirhead (2018) from kinematics and chemical evolution and X-ray luminosities presented by Magaudda et al. (2020). Moreover, we have included the notorious benchmark M dwarfs Kapteyn's star and Barnard's star with X-ray luminosities from Schmitt et al. (1995), rotation periods from Guinan et al. (2016) and Toledo-Padrón et al. (2019), and ages from Guinan et al. (2016) and Riedel et al. (2005).

As can be seen from Fig. 1 (right panel) the field stars with known age have systematically fainter X-ray activity than predicted by the L_x-age relation from Magaudda et al. (2020). This disagreement between observed and predicted L_x-age relations is not seen in the higher mass M and K dwarfs ($0.4-0.6\,M_\odot$ and $0.6-0.8\,M_\odot$ bins) that were studied in an analogous way by Magaudda et al. (2020). The likely cause of this discrepancy in the lowest-mass M dwarfs are shortcomings in the angular evolution models, which fail to predict the very long rotation periods of these objects, resulting in an over-prediction of their X-ray luminosities (see Magaudda et al. 2020, for further details). We have overplotted in Fig. 1 (right) the empirical scaling relation $L_x(t)$ from Penz & Micela (2008) which is based on observed X-ray luminosity functions (XLFs) of the Pleiades, the Hyades, and of nearby field stars. The X-ray luminosity function of the field M stars was derived from Schmitt & Liefke (2004) where stars were selected mainly from a modified version of the CNS 3 (short for the Catalog of Nearby Stars; Gliese & Jahreiß 1991), with the addition of nearby, very late-type stars discovered by near-infrared surveys. In order to estimate the decay of L_X with age, and because the determination of individual age for dM stars is very difficult, Penz & Micela (2008) assigned an average age of 6 Gyr to sample. Furthermore, these latter authors assumed that the luminosity of Prox Cen is a good estimate of the mean value of the X-ray luminosity function at 6 Gyr and that the observed spread is representative of the spread at each age (shown as the grey area around the relation in the figure). The final scaling law was obtained by interpolating between the data of the Pleiades, the Hyades, and the field stars.

While Fig. 1 shows that the shape of the L_x-age relation of M dwarfs remains uncertain, it nevertheless allow us to put a constraint on the age of GJ 357 directly from its observed X-ray luminosity (shown by the horizontal line in the right panel of Fig. 1 with its uncertainty in light-red shading). Similar to the other field M dwarfs, GJ 357 lies well below the X-ray luminosity for stars of its mass predicted by Magaudda et al. (2020). Moreover, the L_x of GJ 357 is lower than that of all M dwarfs with known age except for Barnard's star and is marginally consistent with the faint end of the dispersion around the distribution of Penz & Micela (2008).

We conclude that the age of GJ 357 is most likely higher than ~5 Gyr.

3. Backwards reconstruction

It is common within the literature to perform backwards reconstructions of exoplanet atmospheres in order to determine their histories (e.g. Locci et al. 2019; Modirrousta-Galian et al. 2020b). This is important as it can provide us with useful information concerning the formation and evolution of exoplanets. For instance, the bimodal distribution of exoplanet radii is believed by many to be caused by photoevaporation, which has been scrutinised by performing backwards reconstructions of exoplanet populations (e.g. Owen & Wu 2013, 2017; Modirrousta-Galian et al. 2020a). Furthermore, the remnant cores of planets, which once hosted large primordial atmospheres, are of great interest to the exoplanetary community as they provide us with an inference for the interior structure of bodies like Jupiter and Saturn (e.g. Mocquet et al. 2014; Armstrong et al. 2020). Accordingly, it is useful to know the size of the primordial atmosphere of GJ 357 b in order to better understand its formation, evolution, and current properties, and to decipher whether or not a star with an unusually low XUV flux can still greatly influence its host planets.

Before one can progress with the backwards reconstruction, there are a few aspects that need to be considered. The first is that given the mass and radius of this body, a hydrogen-rich atmosphere is unlikely. However, the observed density could be the result of a very iron-rich embryo that is engulfed within a thin primordial envelope. There are three main formation scenarios that could lead to a super-ferruginous composition. The first concerns surface vaporisation due to high temperatures. Whilst this may have taken place on Mercury (Cameron 1985), for more massive planets the efficiency of this mechanism drops precipitously due to the increasing gravitational force (Ito et al., in prep.). In addition, for the extreme thermodynamic conditions required for this process to take place, the retention of a hydrogen atmosphere is incompatible. Another possibility is that GJ 357 b formed exotically due to chemical/thermal gradients within the protoplanetary disc (Lewis 1972, 1974). The third potential argument is that collisional stripping resulted in the silicate mantle layers becoming ejected which results in a relatively high iron abundance. This mechanism has also been proposed for Mercury (Benz et al. 1988) and has been adopted to explain the density trends of some exoplanets (Marcus et al. 2010; Swain et al. 2019).

However, these "exotic" scenarios are unlikely as they require atypical formational paths and a relatively tenuous hydrogen atmosphere which is sensitive to atmospheric escape and would therefore have a short lifespan at the current orbital distance of GJ 357 b (e.g. Sanz-Forcada et al. 2011; Ehrenreich & Désert 2011; Lammer et al. 2013; Owen & Wu 2013, 2017; Jin et al. 2014; Jin & Mordasini 2018; Kubyshkina et al. 2018a; Locci et al. 2019; Modirrousta-Galian et al. 2020a). The atmospheric
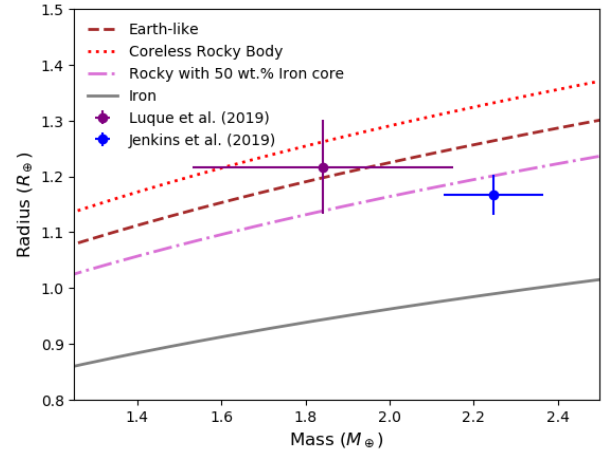
Fig. 2. Mass vs. radius for GJ 357 b using the coreless rocky (red dotted line), Earth-like (dark red dashed line), rocky with a 50 wt.% iron core (purple dash-dot line), and pure iron (grey line) models from Zeng & Sasselov (2013) and Zeng et al. (2016). The values for the mass and radius and their uncertainties are those from Luque et al. (2019, purple) and Jenkins et al. (2019, blue).

lifespan would be short because an M star is particularly active in its first year of life and so heavy mass losses would be expected. Therefore, while this peculiar composition is possible, GJ 357 b is most probably of Earth-like composition (see Fig. 2).

Given that the age of GJ 357 b (assumed to be coeval with its host star) is >5 Gyr, and that it most probably does not presently host a hydrogen envelope (see Sect. 3), one cannot accurately determine when its primordial atmosphere was lost, if it had one at all. This is problematic, because if one assumes that the atmosphere was lost earlier than it actually was, the primordial atmospheric mass would be underestimated. On the other hand, if the assumption for the time of the complete atmospheric loss is later than the true value then the reservoir would be overestimated. Furthermore, having a mass of $1.84 \pm 0.31 M_\oplus$ (and a radius of $1.217 \pm 0.084 R_\oplus$; Luque et al. 2019) the planets' gravity may have been too weak to accrete a large atmosphere. However, one could argue that if the surrounding nebular gas has a sufficiently small grain opacity and the planet has a low internal luminosity, enough nebular gas could be accreted to form a Neptunian- or even Jovian-sized body (Ikoma et al. 2000) even for a relatively small body like GJ 357 b.

To test this assumption, we performed a backwards reconstruction in which we determined the upper bound of GJ 357 b's initial atmospheric mass. This is the maximum primordial atmospheric mass that would have been fully eroded by XUV evaporation. This implies that an initial atmospheric reservoir smaller than or equal to this critical mass would be consistent with the current telluric composition. To do this we adopted the hydro-based approximation for XUV-induced evaporation of Kubyshkina et al. (2018b). We started from the derived age of the planet system ($\simeq 5$ Gyr) and we linearly extrapolated the XUV luminosity of the host star backwards in time. This was done by using the lower bound of the X-ray luminosity predicted by the scaling law from Penz & Micela (2008), which overlaps with the uncertainty range of the observed X-ray luminosity of GJ 357. Considering the lower bound rather than the average X-ray−age relation, we account for the unusually low X-ray luminosity of GJ 357 (which can be seen in Fig. 1). Our simulation ended when the star's age was 10^7 yr and its X-ray luminosity was $\approx 10^{29}$ erg s^{-1}. The starting value of L_x obtained

this way is in sufficient agreement with the observed range of X-ray luminosities for low-mass stars in the 10 Myr-old TW Hya association (10^{29}–10^{30} erg s^{-1}) derived by Kastner et al. (2016, see our comment at the end of the following paragraph).

From the backwards-calculated X-ray luminosity history of GJ 357 we estimated its EUV luminosities across time (L_{EUV}) by adopting the scaling law between L_{EUV} and L_x given by Sanz-Forcada et al. (2011). We input these values into the analytical "hydro-based" evaporation model by Kubyshkina et al. (2018b). In addition, for the radius evolution of the planet we adopted the mass−radius relation of a silicate embryo engulfed by a hydrogen envelope from Lopez & Fortney (2014). In a similar manner to these latter authors, we used the photosphere as the cut-off point for the planetary radius. Furthermore, their model only works for planets older than 100 Myr whereas we begin photo-evaporation at 10 Myr. In order to account for this, we assumed a constant interior luminosity from 10 to 100 Myr. However, we did not incorporate planetary migration into our mass-loss model (see Modirrousta-Galian et al. 2020b, for an example of evaporation-induced planetary migration). Therefore, by estimating how much hydrogen was lost from the moment the planet was born, we constrained the maximum allowed initial atmospheric reservoir. We note that the unknown details of the shape of the age decay of the stellar X-ray emission (see Sect. 2.2) do not affect the result considerably because most of the atmospheric erosion occurs in a very short time compared with the stellar age of this system. Furthermore, our result is robust against different detailed backwards paths in the L_X-age plane, since dM stars of the mass of GJ 357 evolve close to the saturation regime at least for 1 Gyr. Therefore, even if we were incorrect by an order of magnitude in estimating the precise value of the X-ray luminosity at a given time, the planet would still have lost its primordial atmosphere.

Our approach provides a theoretical upper bound on the initial atmospheric mass of $\sim$38 $M_\oplus$ with a radius of $\sim$14 $R_\oplus$. This is an upper bound because an atmospheric mass smaller than $\sim$38 $M_\oplus$ would have also resulted in the currently observed density, which is consistent with a telluric composition. The uncertainties in these predicted values are quite large, especially as the mass−radius relations for silicate bodies with hydrogen-rich envelopes are not yet fully understood. For example, if one assumes a high abundance of radioactive species then the internal luminosity would have resulted in a significantly larger radius than if one adopts a less luminous embryo (Lopez & Fortney 2014). In addition, the available literature shows a large variation in the radius of hydrogen-rich planets for low masses (e.g. Lissauer et al. 2011; Rogers et al. 2011; Lopez et al. 2012; Lopez & Fortney 2014), which will strongly influence the mass-loss history.

In any case, the large initial atmospheric mass predicted by our backwards reconstruction shows that even for stars that currently have remarkably low XUV luminosities, the mass-loss effects on their host planets can be substantial. Nevertheless, considering the small mass of GJ 357 b, accreting a hydrogen envelope of $\sim$38 $M_\oplus$ may have been difficult as an unusually low protoplanetary disc grain opacity, a very low embryo luminosity, and large-scale migration would have been required. This is improbable as firstly the metallicity of the star is only slightly below that of the Sun (see Sect. 5), from which we can infer that the protoplanetary disc had a relatively normal grain opacity. Secondly, in order to achieve low internal luminosities, GJ 357 b must have either lost the majority of its formational energy prior to accreting its hydrogen envelope (e.g. Ikoma et al. 2000), or stored it efficiently (e.g. Jespersen & Stevenson 2020) and

released it slowly over time. Whilst both of these modes are possible, generally it is believed that the embryo's luminosity plays a strong role in inhibiting gas accretion and even triggering its evaporation (Ginzburg et al. 2016, 2018). Thirdly, had GJ 357 b formed far out and then migrated inwards, one would expect a lower bulk density consistent with icy species, which is not compatible with the observed mass and radius measurements (Zeng & Sasselov 2013; Zeng et al. 2016, 2018). If one instead adopts a more typical accretionary model (i.e. with standard grain opacities, core luminosities, and a smaller migration) this would lead to a primordial atmosphere $\lesssim$0.02 $M_\oplus$ (calculated using the models from Ikoma & Hori 2012; Chachan & Stevenson 2018) which would have been fully eroded away by XUV-irradiation in less than 10 Myr (Kubyshkina et al. 2018b). Considering all of the above, our calculation shows that GJ 357 b was probably not born as a Neptunian body or a gas giant which contrasts strongly with planets such as 55 Cancri e or CoRoT-7b that had the potential to have been significantly more massive in the past due to their large masses and tight orbits (e.g. Ehrenreich & Désert 2011; Kubyshkina et al. 2018a).

Conversely, Jenkins et al. (2019) find that GJ 357 b has a substantially higher density, consistent with a metal-rich composition (i.e. a core that is $\simeq$60 wt.% of the total mass). However, an alternative explanation for this high density is that GJ 357 b is a compressed, icy remnant core of a planet that originally had a large hydrogen envelope (Mocquet et al. 2014; Modirrousta-Galian et al. 2020a). New observational data further support this possibility as shown by the "T2" trend in Swain et al. (2019). The label "T2" is given to a population of planets which increase in density for progressively smaller radii. Swain et al. (2019) propose that this trend could be caused by highly compressed remnant cores. The mass and radius values of GJ 357 b from Jenkins et al. (2019) lie within the density trend found by Swain et al. (2019), which could be suggestive of a highly compressed planet that once hosted a large hydrogen envelope[3]. Comparing the results from Luque et al. (2019) and Jenkins et al. (2019) shows that there is a clear ambiguity in the composition and history of GJ 357 b. However, it must be noted that there is a small overlap in the uncertainties of Luque et al. (2019) and Jenkins et al. (2019) that allows for both mass and radius values to be equal and compatible with a more typical rocky composition with a $\simeq$50 wt.% iron core. Nevertheless, a spectroscopic analysis of the atmospheric composition could be performed to reduce this ambiguity, and we discuss this possibility further in Sect. 4.

4. Synthetic atmospheric spectra

Whilst GJ 357 b probably lost its primordial atmosphere, geological processes may have subsequently formed a secondary, volcanic one. Therefore, performing a spectroscopic analysis may reveal insights into its internal structure, the redox state of the mantle, and its history.

Several studies investigate the outgassing of super-Earths (e.g. Kite et al. 2009; Noack et al. 2017; Dorn et al. 2018). The interior modelling of super-Earths and sub-Neptunes is a deeply

---

[3] Swain et al. (2019) used the energy-limited mass-loss equation (e.g. Erkaev et al. 2007) which usually predicts mass losses 100−1000 (and sometimes as much as $\sim$10^9) times smaller than the hydro-based model, which includes thermal effects (Kubyshkina et al. 2018b). Therefore, even though the authors focus on highly irradiated planets, the greater influence that stars have on super-Earths and sub-Neptunes predicted by the hydro-based approximation shows that the "T2" trend is also relevant to our situation.

complex issue, and a thorough review cannot be made within this manuscript. Nevertheless, within the literature it is generally believed that when silicate bodies become more massive than ~5 $M_\oplus$, convection becomes inhibited (e.g. Tackley et al. 2013; Miyagoshi et al. 2015, 2017, 2018; Dorn et al. 2018). However, GJ 357 b is small enough that most models are consistent with convection and hence volcanism being plentiful. For instance, if one assumes a stagnant lid model then Dorn et al. (2018) predict an outgassed mass of ~10^{20} kg (~5×10^{-5} $M_\oplus$) for CO_2. Notwithstanding, other typical volcanic gases such as SO_2 and H_2O would also be expected, although the redox state of the mantle will ultimately dictate the chemical composition of the atmosphere. For example, if GJ 357 b formed under oxygen-poor conditions, one might expect more reduced atmospheric species such as H_2S. These distinct models could be verified with a spectroscopic analysis of the atmosphere which will be possible with future space missions (explained later in this section).

In this section we use the TauREx code (Al-Refaie et al. 2019) to generate synthetic spectral models for GJ 357 b based on our assumption that a volcanic atmosphere is present and that GJ 357 b did not form under reduced conditions. TauREx is a Bayesian program that is optimised to process the molecular line lists from the ExoMol project (see Tennyson et al. 2016, for details) to either generate forward spectral models of exoplanetary atmospheres or, in its retrieval mode (inverse model), interpret exoplanet atmospheric data by fitting them with a transmission or emission model. To create a forward spectrum, the following parameters are required:

– temperature and spectral type of the host star;
– mass (M_p) and radius (R_p) of the exoplanet;
– atmospheric thermodynamic properties;
– gas mixing ratios;
– wavelength range modelled;
– presence of clouds or hazes and their properties (i.e. distribution, location, particle size and shape).

For the stellar temperature, spectral type, planetary radius, and planetary mass we used the values given in Luque et al. (2019) which are ≈3505 K, M2.5 V, 1.84 $R_\oplus$, and 1.217 $M_\oplus$ respectively[4]. For the stellar spectra we use the data files from the PHOENIX library (for more information see Hauschildt & Baron 1999, 2010).

To maintain consistency with the simplicity of our models, we adopt an isothermal atmospheric profile within the photospheric region. This is a reasonable assumption as the effective temperature of GJ 357 b is large (>500 K). We simulate the atmosphere using the plane-parallel approximation, with pressures ranging from 10^{-9} to 10^2 bar, uniformly sampled in log-space with 100 atmospheric layers. We note that the actual surface pressure is unknown as it is very sensitive to the specific atmospheric properties such as the opacities, composition, and temperature profile. However, at pressures above 10 bar, the atmosphere is likely opaque and therefore does not contribute to any of the observed features. Here, we present three potential compositions: 100% CO_2, 100% SO_2, and 75% N_2, 24% CO_2 and 1% H_2O.

The line lists were taken from Polyansky et al. (2018), Rothman et al. (2010, 2013) for H_2O, CO_2 and SO_2 respectively. For each of these we showcase both a cloud-free atmosphere and one with an opaque grey cloud layer at 0.01 bar which mutes the features seen. These are simplified circumstances but highlight the type and strength of features that could be seen through

_____
[4] In Sect. 5 we present alternative methods to obtain the stellar mass and radius and the values derived with them.
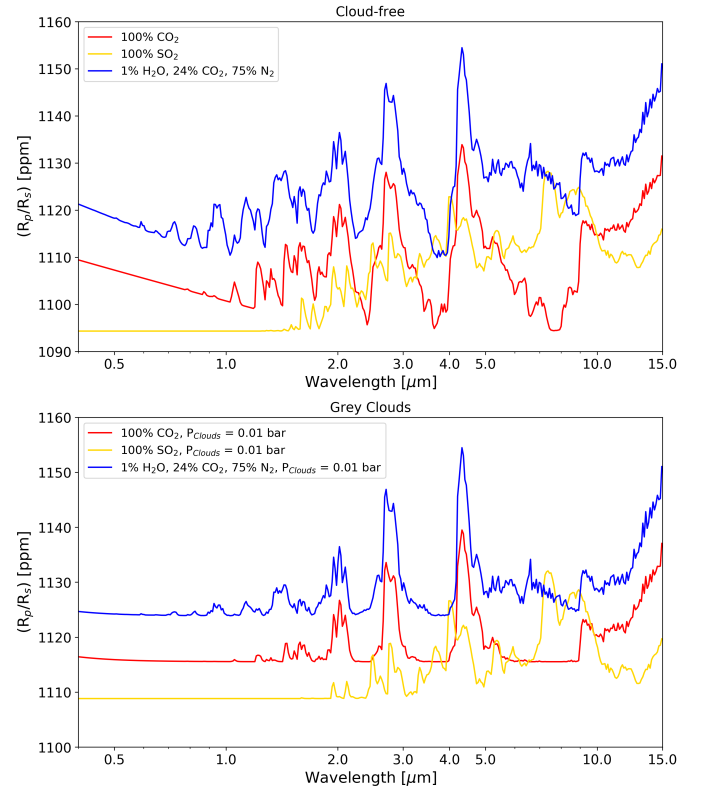
Fig. 3. Synthetic spectra of GJ 357 b generated using the TauREx code. Our diagram includes the synthetic spectra of 100% CO_2 (red), 100% SO_2 (yellow), and a mixed atmosphere with 75% N_2 along with 1% H_2O and 24% CO_2 (blue). We show these forward models for the cloud-free case (*top*) and in the presence of opaque grey clouds at 0.01 bar (*bottom*).

transmission spectroscopy of this planet. We model these spectra over the range 0.4–15 μm and our synthetic spectra are shown in Fig. 3.

We are aware that the presence of nitrogen-rich atmospheres on warm or hot super-Earths is a subject of much dispute. For example, nitrogen atmospheres have been proposed on some molten super-Earths such as 55 Cancri e (e.g. Angelo & Hu 2017; Hammond & Pierrehumbert 2017; Miguel 2019; Zilinskas et al. 2020). However, there are problems with this model, such as for example the inability of nitrogen to trigger efficient cooling, resulting in eventual hydrodynamical losses (e.g. Tian et al. 2008; Lichtenegger et al. 2010; Airapetian et al. 2017; Johnstone et al. 2019). Furthermore, some argue that exogenous and endogenous processes could trigger the deposition of atmospheric N_2 (e.g. Navarro-González et al. 2001; Parkos et al. 2018; Lammer et al. 2019). Nevertheless, it is not the objective of the present study to challenge or support the possibility of N_2 atmospheres on warm or hot super-Earths and so we include nitrogen within our synthetic spectrum as a proof of concept.

In any case, given the brightness of the host star and the significant features over the wavelength ranges covered by Twinkle (0.5–4.5 μm, Edwards et al. 2019), Ariel (0.5–7.8 μm, Tinetti et al. 2018), and the *James Webb* Space Telescope (JWST, 0.6–12 μm), the atmospheric composition of GJ 357 b could be constrained using these instruments which would provide important information for the interior structure and geochemistry of the planet. Additionally, the G141 grism of the *Hubble* Space Telescope's Wide Field Camera 3, which covers 1.1–1.7 μm, may be sensitive enough to infer the presence of water. A sufficiently

high abundance of water could indicate a large-scale planetary migration from beyond the ice-line to its current location or a late planetesimal bombardment. Conversely, chemical species such as CO_2 and SO_2 would indicate an Earth-like composition with a volcanically active past.

We acknowledge that we have simulated a relatively ideal case for the transmission profile which neglects the possible presence of complex hazes that might be expected to be present in the atmosphere of a volcanic planet. We also do not account for chemical reactions between the different species. There are many processes that could alter the chemical composition of the atmosphere. One such process is XUV-irradiation which could substantially affect the stability of molecules. The XUV irradiation that GJ 357 b receives is approximately equal to eight times that of Venus but it also has a stronger gravitational force. In addition, the presence of a geomagnetic field could further mitigate the XUV-induced photoevaporation (Owen & Adams 2019). Furthermore, even in the absence of a geomagnetic field, the effects of ionising photons could be suppressed if an ionosphere forms that interacts with the escaping ions. This mechanism is thought to take place on Venus (Zhang et al. 2012) and it may explain how some volatiles such as water vapour are still retained (albeit, in small abundances). We understand that some species can dissociate into their elemental constituents when exposed to XUV irradiation, which would ultimately affect the bulk atmospheric composition. Water for example would form oxygen and hydrogen and whilst oxygen may be retained due to its heavier mass, the hydrogen could be lost. However, due to this being a multivariate problem we still consider water but in a low abundance (1%) in our synthetic spectra as it could be present. To summarise, while the actual spectrum of the planet may display a higher complexity because of the simplifying assumptions in our synthetic spectra, our model highlights atmospheric spectral features that might plausibly be detected in an eventual observational study of GJ 357 b. A thorough investigation of the ability of current and upcoming facilities to disentangle potential atmospheric scenarios is left for future work.

5. The robustness of the planetary density

Our model for the secondary atmosphere of GJ 357 b is based on the bulk density of the planet that is derived from its mass and radius. In addition to the typical uncertainties associated with radial-velocity and photometric measurements used to derive the ratios between planetary and stellar masses and radii, one of the main sources of systematic error are the estimates of the stellar mass and radius. This is because the planetary properties are all measured as a function of the stellar quantities. In order to verify the robustness of our results against errors due to the methods used to derive the stellar properties, we recorded the changes in the planetary density for various estimates of the stellar parameters. In particular, we consider the stellar mass (M_*) and radius (R_*) derived in the following distinct ways.

First, we followed the methodology from Maldonado et al. (2015, hereafter MA15)[5] which is based on the use of optical high-resolution spectra from HARPS. A total of 53 spectra were downloaded from the ESO archive[6], which were collected from radial-velocity measurements and co-added into one single spectrum. Initially, the effective temperature and metallicity of the star are computed from ratios of pseudo equivalent widths of

[5] https://github.com/jesusmaldonadoprado/mdslines
[6] http://archive.eso.org/wdb/wdb/adp/phase3_spectral/form?phase3_collection=HARPS

spectral features. The effective temperature is calibrated using stars with interferometric estimates of their radii and is in the revised scale by Mann et al. (2013). The stellar metallicities provided by MA15 are based on the photometric M_K-[Fe/H] relationship by Neves et al. (2012). Derived values of $T_{\rm eff}$ and [Fe/H] are 3461 ± 68 K and -0.14 ± 0.09 dex, respectively. MA15 also provides empirical calibrations to derive the stellar evolutionary parameters as a function of the stellar effective temperature and the metallicity. The mass scale in MA15 is based on the NIR photometric calibration of Henry & McCarthy (1993) and has typical uncertainties of the order of 13%. MA15 derive their own stellar mass−radius relationship using stars with known interferometric radius and low-mass eclipsing binaries. Typical uncertainties in the radius are of the order of 12%.

Secondly, we obtain R_* and M_* from the empirical radius−magnitude and mass−magnitude relationships of Mann et al. (2015, their Eqs. (4) and (10)). Here we used the *Gaia* parallax to obtain the absolute $K_{\rm s}$ band magnitude from the 2 MASS measurement (see Sect. 2.1). This method was applied in the activity−rotation−age study of M dwarfs of Magaudda et al. (2020). Therefore, we refer to these results as MSC 20.

We also consider the published values from Schweitzer et al. (2019, hereafter SC19). Their analysis comprises the following steps: First, bolometric luminosities ($L_{\rm bol}$) are determined by integration of the available photometry. Then, effective temperature ($T_{\rm eff}$) and stellar metallicity ([Fe/H]) are obtained by fitting the optical CARMENES spectra to a set of PHOENIX-ACES synthetic spectra. Surface gravity, $\log g$, is fixed by a $T_{\rm eff}$−$\log g$ relation from theoretical 5 Gyr isochrones (Passegger et al. 2018). The stellar radius is computed from $T_{\rm eff}$ and $L_{\rm bol}$ using the Stefan-Boltzmann law. Finally, the authors derive the stellar mass using their own mass−radius relationship calibrated with a sample of 55 eclipsing M dwarf binaries (their Eq. (6)). In the following, we denote these values as ($M_{\rm M-R}$, $R_{\rm SB}$).

In addition to these estimates, SC19 compared their values of stellar mass and radius with those obtained from another three methods: (i) spectroscopic mass ($M_{\log g}$) derived from the values of $\log g$, and radius computed before. (ii) Photometric mass ($M_{\rm M-Ks}$) computed using the mass−2MASS $K_{\rm s}$ magnitude relation by Mann et al. (2019). (iii) Mass and radius based on the PARSEC evolutionary models ($M_{\rm PAR}$, $R_{\rm PAR}$) computed using a Bayesian approach applied to the PARSEC stellar library as in del Burgo & Allende Prieto (2018).

Table 2 provides the stellar mass and radius for each analysis method. The most important difference between the methods arises from the use of different mass−luminosity and mass−radius relationships. In order to test the effect of the stellar mass on the determination of the planetary mass we made use of the published values of the radial-velocity semi-amplitude, $K_* = (1.52 \pm 0.25)$ ms^{-1} and orbital period, $P = 3.93072^{+0.00008}_{-0.00006}$ days (Luque et al. 2019). We then derived for each estimate of the stellar radius a value for the radius of GJ 357 b using the relation $R_{\rm P}/R_{\star} = 0.0331 \pm 0.0009$ (Luque et al. 2019). Using the $R_{\rm P}$ and $M_{\rm P}$ values derived that way, an estimation of the planetary density was performed. The results are provided in Table 2, while Fig. 4 shows the position of GJ 357 b in the radius-versus-mass diagram according to our different estimates.

We find that the mass and radius values for GJ 357 b based on a given method to derive the stellar parameters of the host star exhibit considerable uncertainties. However, our comprehensive comparison of different ways to calculate the stellar parameters of GJ 357 shows that all of these methods yield consistent results in terms of the planet mass and radius. Therefore, the
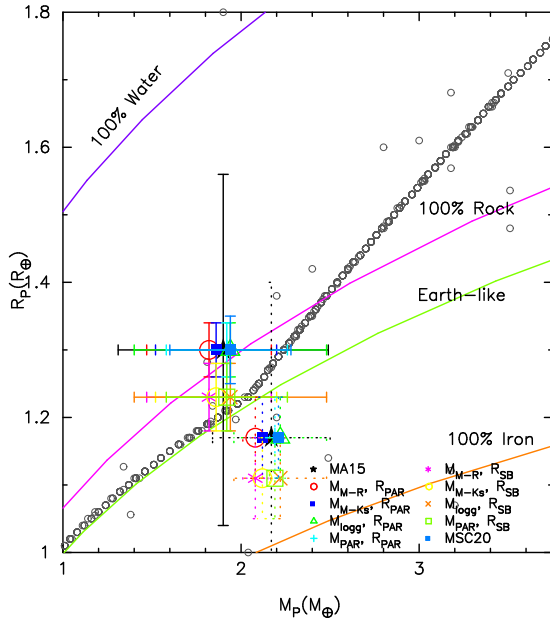
Table 2. Planetary parameters of GJ 357 b derived from the different datasets of stellar parameters of GJ 357.

Dataset[†]	$M_\star$ ($M_\odot$)	$R_\star$ ($R_\odot$)	m_P[LU] ($M_\oplus$)	R_P[LU] ($R_\oplus$)	ρ_P[LU] (g cm^{-3})	m_P[JE] ($M_\oplus$)	R_P[JE] ($R_\oplus$)	ρ_P[JE] (g cm^{-3})
MA15	0.36 ± 0.08	0.36 ± 0.07	1.90 ± 0.59	1.30 ± 0.26	4.76 ± 3.18	2.17 ± 0.33	1.17 ± 0.23	7.45 ± 4.59
SC19: M_{M-R}, R_{PAR}	0.3368 ± 0.0150	0.3601 ± 0.007	1.82 ± 0.35	1.30 ± 0.04	4.55 ± 0.99	2.08 ± 0.07	1.17 ± 0.06	7.12 ± 1.05
SC19: M_{M-Ks}, R_{PAR}	0.3477 ± 0.0084	0.3601 ± 0.007	1.86 ± 0.34	1.30 ± 0.04	4.65 ± 0.96	2.12 ± 0.04	1.17 ± 0.06	7.27 ± 1.05
SC19: $M_{\log g}, R_{PAR}$	0.3716 ± 0.064	0.3601 ± 0.007	1.94 ± 0.54	1.30 ± 0.04	4.86 ± 1.44	2.22 ± 0.26	1.17 ± 0.06	7.60 ± 1.41
SC19: M_{PAR}, R_{PAR}	0.3653 ± 0.0071	0.3601 ± 0.007	1.92 ± 0.34	1.30 ± 0.04	4.80 ± 0.98	2.19 ± 0.03	1.17 ± 0.06	7.52 ± 1.09
SC19: M_{M-R}, R_{SB}	0.3368 ± 0.015	0.3419 ± 0.011	1.82 ± 0.35	1.23 ± 0.05	5.32 ± 1.23	2.08 ± 0.07	1.11 ± 0.06	8.32 ± 1.38
SC19: M_{M-Ks}, R_{SB}	0.3477 ± 0.0084	0.3419 ± 0.011	1.86 ± 0.34	1.23 ± 0.05	5.43 ± 1.20	2.12 ± 0.04	1.11 ± 0.06	8.50 ± 1.39
SC19: $M_{\log g}, R_{SB}$	0.3716 ± 0.064	0.3419 ± 0.011	1.94 ± 0.54	1.23 ± 0.05	5.68 ± 1.74	2.22 ± 0.26	1.11 ± 0.06	8.88 ± 1.78
SC19: M_{PAR}, R_{SB}	0.3653 ± 0.0071	0.3419 ± 0.011	1.92 ± 0.34	1.23 ± 0.05	5.61 ± 1.22	2.19 ± 0.03	1.11 ± 0.06	8.78 ± 1.44
MSC20 method	0.37 ± 0.007	0.36 ± 0.01	1.94 ± 0.34	1.30 ± 0.05	4.85 ± 1.03	2.21 ± 0.03	1.17 ± 0.06	7.59 ± 1.19

Notes. [†]MA15 (Maldonado et al. 2015); SC19 (Schweitzer et al. 2019): M_{M-R} mass from mass-radius relationship; M_{M-Ks} photometric mass; $M_{\log g}$ spectroscopic mass; M_{PAR} PARSEC-based mass; R_{PAR} PARSEC-based radius; R_{SB} radius from the Stefan-Boltzmann's law; IRPH: Mass and radius from the relationships by Mann et al. (2015). m_P[LU], R_P[LU], ρ_P[LU] refer to the planetary parameters obtained using the planetary Keplerian amplitude and the planet-to-star radius ratio by Luque et al. (2019), while m_P[JE], R_P[JE], ρ_P[JE] estimates are based on the analysis by Jenkins et al. (2019).

Fig. 4. Position of GJ 357 b in the radius-versus-mass diagram. Different colours indicate the planetary parameters derived using the different datasets of stellar masses and radii. Continuous lines indicate the estimates based on the Keplerian amplitude and planet-to-star radius ratio by Luque et al. (2019) while dotted lines show the results based on the analysis by Jenkins et al. (2019). A few exoplanets from NASA's exoplanets archive are overplotted as grey circles. Different planetary models (from Zeng & Sasselov 2013; Zeng et al. 2016) are also shown for comparison.

stellar parameters introduce negligible effects on our model for the atmospheric mass and composition of GJ 357 b.

As mentioned previously, another factor that might influence the estimation of the planetary density is the analysis used on the computation of the Keplerian amplitude and the ratio $R_P/R_\star$ due to the GJ 357 b planet. Indeed, recently Jenkins et al. (2019, Table 4) provided a slightly larger Keplerian amplitude $K_\star = (1.7372^{+0.0054}_{-0.0007} \mathrm{ms}^{-1})$ and a smaller star-to-planet radius ratio, $R_P/R_\star = 0.02981 \pm 0.0013$. This translates into higher

masses and densities for GJ 357 b, which are also listed in Table 2 and shown in Figs. 2 and 4. The slightly different planetary parameters between Jenkins et al. (2019) and Luque et al. (2019) might be related to the use of different datasets. While Jenkins et al. (2019) use HARPS, UVES, and HIRES data, the analysis done in Luque et al. (2019) also includes CARMENES and PSF data. If the planetary densities based on the Jenkins et al. (2019) results are considered, the composition of the planet would be consistent with a telluric planet that has a core $\simeq 60\%$ (Zeng et al. 2016) of the total mass or with the icy remnant core of a planet which once hosted a large primordial atmosphere (Mocquet et al. 2014; Modirrousta-Galian et al. 2020a). However, as explained previously, the uncertainties in the measured values allow for a more typical rocky composition.

6. Summary and conclusions

Our analysis of GJ 357 b and its host star has led to the following results and conclusions:

From a recent *XMM-Newton* observation we derived an extremely low X-ray luminosity for GJ 357 ($\log L_x$ [erg s^{-1}] = 25.7 in the $0.1-2.4$ keV ROSAT band). When compared to the L_x of most similar-mass M dwarfs with known ages and to different L_x age laws for M dwarfs (Magaudda et al. 2020; Penz & Micela 2008) this low X-ray activity indicates that GJ 357 is at least 5 Gyr old and possibly significantly older. Under the assumption that the star and planet formed at a similar time, we can assume 5 Gyr to be a conservative estimate for the age of the planet system.

Using the X-ray luminosity of GJ 357 with our above estimate for the age of the system and the empirical L_x-age relation from Penz & Micela (2008) we performed a backwards reconstruction of GJ 357 b's primordial atmospheric mass. We find a theoretically maximum envelope mass of $\sim 38 \, M_\oplus$. However, it is unlikely that GJ 357 b accreted an envelope this massive, as its small central mass would have hindered its ability to collect gas. Conversely, if one adopts the mass and radius measurements from Jenkins et al. (2019) instead of those from Luque et al. (2019), then GJ 357 b has a density consistent with a compressed remnant core (Mocquet et al. 2014). Its high density could be suggestive of an initially large atmospheric mass.

Taking account of the known parameters of the host star and the estimated planet mass and radius, we have produced three different synthetic IR spectra representing the potential secondary atmosphere of GJ 357 b. Our test cases comprise (a) 100% CO_2, (b) 100% SO_2, (c) 75% N_2 with 24% CO_2 and 1% H_2O. The actual atmospheric content of this planet should be accessible to upcoming space missions, such as Ariel, JWST, and Twinkle, which will allow us to test our predictions. Finally, a detailed analysis of the uncertainties in the stellar and planetary parameters shows that despite the uncertainties being considerable, they do not have significant effects on our results.

References

Airapetian, V. S., Glocer, A., Khazanov, G. V., et al. 2017, ApJ, 836, L3
Al-Refaie, A. F., Changeat, Q., Waldmann, I. P., & Tinetti, G. 2019, arXiv e-prints [arXiv:1912.00759]
Angelo, I., & Hu, R. 2017, AJ, 154, 232
Arenou, F., Luri, X., Babusiaux, C., et al. 2018, A&A, 616, A17
Armstrong, D. J., Lopez, T. A., Adibekyan, V., et al. 2020, Nature, 583, 39
Benz, W., Slattery, W. L., & Cameron, A. G. W. 1988, Icarus, 74, 516
Boro Saikia, S., Marvin, C. J., Jeffers, S. V., et al. 2018, A&A, 616, A108
Brandl, B. R., Absil, O., Agócs, T., et al. 2018, SPIE Conf. Ser., 10702, 107021U
Cameron, A. G. W. 1985, Icarus, 64, 285
Chachan, Y., & Stevenson, D. J. 2018, ApJ, 854, 21
del Burgo, C., & Allende Prieto, C. 2018, MNRAS, 479, 1953
Dorn, C., Noack, L., & Rozel, A. B. 2018, A&A, 614, A18
Edwards, B., Rice, M., Zingales, T., et al. 2019, Exp. Astron., 47, 29
Ehrenreich, D., & Désert, J.-M. 2011, A&A, 529, A136
Erkaev, N. V., Kulikov, Y. N., Lammer, H., et al. 2007, A&A, 472, 329
Ginzburg, S., Schlichting, H. E., & Sari, R. 2016, ApJ, 825, 29
Ginzburg, S., Schlichting, H. E., & Sari, R. 2018, MNRAS, 476, 759
Gliese, W., & Jahreiß, H. 1991, Preliminary Version of the Third Catalogue of Nearby Stars, The Astronomical Data Center CD-ROM: Selected Astronomical Catalogs
Greene, T. P., Line, M. R., Montero, C., et al. 2016, ApJ, 817, 17
Guinan, E. F., Engle, S. G., & Durbin, A. 2016, ApJ, 821, 81
Hammond, M., & Pierrehumbert, R. T. 2017, ApJ, 849, 152
Hauschildt, P. H., & Baron, E. 1999, J. Comput. Appl. Math., 109, 41
Hauschildt, P. H., & Baron, E. 2010, A&A, 509, A36
Henry, T. J., & McCarthy, Donald W., J. 1993, AJ, 106, 773
Ikoma, M., & Hori, Y. 2012, ApJ, 753, 66
Ikoma, M., Nakazawa, K., & Emori, H. 2000, ApJ, 537, 1013
Jenkins, J. S., Pozuelos, F. J., Tuomi, M., et al. 2019, MNRAS, 490, 5585
Jespersen, C. K., & Stevenson, D. J. 2020, AAS Meeting Abstracts, 174.07
Jin, S., & Mordasini, C. 2018, ApJ, 853, 163
Jin, S., Mordasini, C., Parmentier, V., et al. 2014, ApJ, 795, 65
Johnstone, C. P., Khodachenko, M. L., Lüftinger, T., et al. 2019, A&A, 624, L10
Kastner, J. H., Principe, D. A., Punzi, K., et al. 2016, AJ, 152, 3
Kite, E. S., Manga, M., & Gaidos, E. 2009, ApJ, 700, 1732
Kubyshkina, D., Fossati, L., Erkaev, N. V., et al. 2018a, A&A, 619, A151
Kubyshkina, D., Fossati, L., Erkaev, N. V., et al. 2018b, ApJ, 866, L18
Lammer, H., Erkaev, N. V., Odert, P., et al. 2013, MNRAS, 430, 1247
Lammer, H., Sproß, L., Grenfell, J. L., et al. 2019, Astrobiology, 19, 927
Lewis, J. S. 1972, Earth Planet. Sci. Lett., 15, 286
Lewis, J. S. 1974, Science, 186, 440
Lichtenegger, H. I. M., Lammer, H., Grießmeier, J. M., et al. 2010, Icarus, 210, 1
Lindegren, L., Hernández, J., Bombrun, A., et al. 2018, A&A, 616, A2
Lissauer, J. J., Fabrycky, D. C., Ford, E. B., et al. 2011, Nature, 470, 53
Locci, D., Cecchi-Pestellini, C., & Micela, G. 2019, A&A, 624, A101
Lopez, E. D., & Fortney, J. J. 2014, ApJ, 792, 1
Lopez, E. D., Fortney, J. J., & Miller, N. 2012, ApJ, 761, 59
Luque, R., Pallé, E., Kossakowski, D., et al. 2019, A&A, 628, A39
Magaudda, E., Stelzer, B., Covey, K. R., et al. 2020, A&A, 638, A20
Maldonado, J., Affer, L., Micela, G., et al. 2015, A&A, 577, A132
Mann, A. W., Gaidos, E., & Ansdell, M. 2013, ApJ, 779, 188
Mann, A. W., Feiden, G. A., Gaidos, E., Boyajian, T., & von Braun, K. 2015, ApJ, 804, 64
Mann, A. W., Dupuy, T., Kraus, A. L., et al. 2019, ApJ, 871, 63
Marcus, R. A., Sasselov, D., Hernquist, L., & Stewart, S. T. 2010, ApJ, 712, L73
Matt, S. P., Brun, A. S., Baraffe, I., Bouvier, J., & Chabrier, G. 2015, ApJ, 799, L23
Miguel, Y. 2019, MNRAS, 482, 2893
Miyagoshi, T., Kameyama, M., & Ogawa, M. 2015, J. Geophys. Res. Planets, 120, 1267
Miyagoshi, T., Kameyama, M., & Ogawa, M. 2017, Earth, Planets, and Space, 69, 46
Miyagoshi, T., Kameyama, M., & Ogawa, M. 2018, Earth, Planets, and Space, 70, 200
Mocquet, A., Grasset, O., & Sotin, C. 2014, Phil. Trans. R. Soc. Lond. Ser. A, 372, 20130164
Modirrousta-Galian, D., Locci, D., & Micela, G. 2020a, ApJ, 891, 158
Modirrousta-Galian, D., Locci, D., Tinetti, G., & Micela, G. 2020b, ApJ, 888, 87
Navarro-González, R., McKay, C. P., & Mvondo, D. N. 2001, Nature, 412, 61
Neves, V., Bonfils, X., Santos, N. C., et al. 2012, A&A, 538, A25
Noack, L., Rivoldini, A., & Van Hoolst, T. 2017, Phys. Earth Planet. Inter., 269, 40
Owen, J. E., & Adams, F. C. 2019, MNRAS, 490, 15
Owen, J. E., & Wu, Y. 2013, ApJ, 775, 105
Owen, J. E., & Wu, Y. 2017, ApJ, 847, 29
Parkos, D., Pikus, A., Alexeenko, A., & Melosh, H. J. 2018, J. Geophys. Res. Planets, 123, 892
Passegger, V. M., Reiners, A., Jeffers, S. V., et al. 2018, A&A, 615, A6
Penz, T., & Micela, G. 2008, A&A, 479, 579
Polyansky, O. L., Kyuberis, A. A., Zobov, N. F., et al. 2018, MNRAS, 480, 2597
Riedel, A. R., Guinan, E. F., DeWarf, L. E., Engle, S. G., & McCook, G. P. 2005, AAS Meeting Abstracts, 206, 09.04
Rogers, L. A., Bodenheimer, P., Lissauer, J. J., & Seager, S. 2011, ApJ, 738, 59
Rothman, L., Gordon, I., Barber, R., et al. 2010, J. Quant. Spectr. Rad. Transf., 111, 2139
Rothman, L. S., Gordon, I. E., Babikov, Y., et al. 2013, J. Quant. Spectr. Rad. Transf., 130, 4
Sanz-Forcada, J., Micela, G., Ribas, I., et al. 2011, A&A, 532, A6
Schlichting, H. E., Fuentes, C. I., & Trilling, D. E. 2013, AJ, 146, 36
Schmitt, J. H. M. M., & Liefke, C. 2004, A&A, 417, 651
Schmitt, J. H. M. M., Fleming, T. A., & Giampapa, M. S. 1995, ApJ, 450, 392
Schöfer, P., Jeffers, S. V., Reiners, A., et al. 2019, A&A, 623, A44
Schweitzer, A., Passegger, V. M., Cifuentes, C., et al. 2019, A&A, 625, A68
Simon, J. B., Armitage, P. J., Li, R., & Youdin, A. N. 2016, ApJ, 822, 55
Swain, M. R., Estrela, R., Sotin, C., Roudier, G. M., & Zellem, R. T. 2019, ApJ, 881, 117
Tackley, P. J., Ammann, M., Brodholt, J. P., Dobson, D. P., & Valencia, D. 2013, Icarus, 225, 50
Tennyson, J., Yurchenko, S. N., Al-Refaie, A. F., et al. 2016, J. Mol. Spectr., 327, 73
Tian, F., Kasting, J. F., Liu, H.-L., & Roble, R. G. 2008, J. Geophys. Res. Planets, 113, E05008
Tinetti, G., Drossart, P., Eccleston, P., et al. 2018, Exp. Astron., 46, 135
Toledo-Padrón, B., González Hernández, J. I., Rodríguez-López, C., et al. 2019, MNRAS, 488, 5145
Veyette, M. J., & Muirhead, P. S. 2018, ApJ, 863, 166
Zeng, L., & Sasselov, D. 2013, PASP, 125, 227
Zeng, L., Sasselov, D. D., & Jacobsen, S. B. 2016, ApJ, 819, 127
Zeng, L., Jacobsen, S. B., Sasselov, D. D., et al. 2018, AGU Fall Meeting Abstracts, 2018, P53C–2985
Zhang, T. L., Lu, Q. M., Baumjohann, W., et al. 2012, Science, 336, 567
Zilinskas, M., Miguel, Y., Mollière, P., & Tsai, S.-M. 2020, MNRAS, 494, 1490

The Early Data Release of eROSITA and Mikhail Pavlinsky ART-XC on the SRG mission

First eROSITA study of nearby M dwarfs and the rotation-activity relation in combination with TESS[*]

E. Magaudda[1], B. Stelzer[1,2], St. Raetz[1], A. Klutsch[1], M. Salvato[3,4], and J. Wolf[3,4]

[1] Institut für Astronomie und Astrophysik, Eberhard-Karls Universität Tübingen, Sand 1, 72076 Tübingen, Germany
   e-mail: `magaudda@astro.uni-tuebingen.de`
[2] INAF – Osservatorio Astronomico di Palermo, Piazza Parlamento 1, 90134 Palermo, Italy
[3] Max-Planck-Institut für extraterrestrische Physik, Giessenbachstr. 1, 85748 Garching, Germany
[4] Exzellenzcluster ORIGINS, Boltzmannstr. 2, 85748 Garching, Germany

ABSTRACT

We present the first results with the ROentgen Survey with an Imaging Telescope Array (eROSITA) on board the Russian Spektrum-Roentgen-Gamma mission, and we combine the new X-ray data with observations with the Transiting Exoplanet Survey Satellite (TESS). We used the SUPERBLINK proper motion catalog of nearby M dwarfs as input sample to search for eROSITA and TESS data. We extracted *Gaia* DR2 data for the full M dwarf catalog, which comprises ~9000 stars, and we calculated the stellar parameters from empirical relations with optical/IR colors. Then we cross-matched this catalog with the eROSITA Final Equatorial Depth Survey (eFEDS) and the first eROSITA all-sky survey (eRASS1). After a meticulous source identification in which we associated the closest *Gaia* source with the eROSITA X-ray detections, our sample of M dwarfs is defined by 687 stars with SpT = K5..M7 (673 from eRASS1 and 14 from eFEDS). While for eRASS1 we used the data from the source catalog provided by the eROSITA_DE consortium, for the much smaller eFEDS sample, we performed the data extraction, and we analyzed the X-ray spectra and light curves. This unprecedented data base for X-ray emitting M dwarfs allowed us to place a quantitative constraint on the mass dependence of the X-ray luminosity, and to determine the change in the activity level with respect to pre-main-sequence stars. TESS observations are available for 489 of 687 X-ray detected M dwarfs. By applying standard period search methods, we were able to determine the rotation period for 180 X-ray detected M dwarfs. This is about one-forth of the X-ray sample. With the joint eROSITA and TESS sample, and combining it with our compilation of historical X-ray and rotation data for M dwarfs, we examined the mass dependence of the saturated regime of the rotation-activity relation. A first comparison of eROSITA hardness ratios and spectra shows that 65% of the X-ray detected M dwarfs have coronal temperatures of ~0.5 keV. We performed a statistical investigation of the long-term X-ray variability of M dwarfs by comparing the eROSITA measurements to those obtained ~30 yr earlier during the ROSAT all-sky survey (RASS). Evidence for X-ray flares is found in various parts of our analysis: directly from an inspection of the eFEDS light curves, in the relation between RASS and eRASS1 X-ray luminosities, and in a subset of stars that displays hotter X-ray emission than the bulk of the sample according to the hardness ratios. Finally, we point out the need to obtain X-ray spectroscopy for more M dwarfs to study the coronal temperature-luminosity relation, which is not well constrained by our eFEDS results.

Key words. stars: low-mass – stars: activity – stars: rotation – stars: magnetic field – X-rays: stars

1. Introduction

M dwarfs are the most numerous stars in the Galaxy. Long overlooked because of their relative faintness, they have lately become of central interest for astronomy because they are important as hosts of habitable planets (Tarter et al. 2007). Understanding the evolution of planets around M dwarfs and their potential for hosting life requires good knowledge of stellar magnetic activity because planetary atmospheres react sensitively to both short-wavelength (UV, extreme ultraviolet, and X-ray) radiation and stellar winds.

Investigating the activity tracers in different wavelength bands provides information about the magnetic phenomena occurring in the stellar atmosphere layers. For instance, the activity of the deeper atmospheric regions, that is, photosphere and chromosphere, is traced by the emission of specific optical lines, such as Ca II and Hα. Reiners et al. (2012), West et al. (2015),

and Newton et al. (2016, 2017) studied the Hα emission ($L_{H\alpha}$) of M dwarfs and its variation with the rotation periods. They found that M dwarfs with high Hα emission ($L_{H\alpha}$) have short rotation periods, and a marginal emission is seen from slowly rotating M stars.

Magnetic activity in the outermost atmospheric layer, the corona, is visible in X-rays. In particular, the X-ray emission of M dwarfs is of paramount importance for several unresolved problems in stellar astrophysics. Being a manifestation of magnetic heating, the UV and X-ray emissions of late-type stars are proxies for the efficiency of stellar dynamos. In analogy to the Sun, standard ($\alpha\Omega$) stellar dynamos are thought to be driven by convection and rotation, and they are located in the tachocline, which connects the radiative interior and the convective envelope (Parker 1993). As a consequence, the X-ray emission of M dwarfs can be expected to undergo drastic changes at the transition where stellar interiors become fully convective (SpT ~ M3). Early studies have given controversial results; the occurrence of a qualitative change in X-ray emission across this boundary is debated (e.g. Rosner et al. 1985; Fleming & Stone 2003). More

---

recently, based on an improved mass function, an exceptionally large spread of the X-ray emission level and rotation rates was observed for spectral types M3 to M4 (Reiners et al. 2012; Stelzer et al. 2013). This spread is likely a signature of ongoing spin-down and an associated decay in dynamo efficiency, but it may also indicate a transition related to the fact that stellar interiors become fully convective.

Through their link with the dynamo, the secular evolution of the high-energy radiative output of a star and its angular momentum should occur in parallel. This evolution likely depends on the initial conditions, which differ from star to star. Depending on the initial rotation after the disk phase, it takes a G-type star from a few tens to a few hundred million years to spin down to $\approx 1-10$ times the solar rotation rate (Johnstone & Güdel 2015; Tu et al. 2015). In contrast, M dwarfs stay in the saturation regime for much longer. Even for a $0.5\,M_\odot$ star (SpT $\sim$ M1/M2), saturation may last as long as 1 Gyr for half of the objects (Johnstone & Güdel 2015; Magaudda et al. 2020), resulting in the prolonged irradiation mentioned above. The wide spread of rotation rates in mid M-type stars is likely the major cause for their wide spread in X-ray luminosities mentioned above.

The *Einstein* and ROSAT satellites have provided the first significant numbers of X-ray detections from M dwarfs (Fleming et al. 1988; Fleming 1998; Schmitt & Liefke 2004). However, Stelzer et al. (2013) showed that about 40% of the closest M dwarfs, those in a volume of 10 pc around the Sun, have remained below the detection threshold of the ROSAT all-sky survey (RASS). RASS observations have also been the main resource for seminal studies of the rotation-activity relation, for instance, Pizzolato et al. (2003) and Wright et al. (2011). In contrast to the first studies of the link between stellar rotation and magnetic activity (Pallavicini et al. 1981), these works made use of photometric rotation measurements that avoid the ambiguity caused by the generally unknown inclination angle that affects studies based on spectroscopic $v \sin i$ measurements.

Magaudda et al. (2020) have presented a comprehensive study of the relation between rotation, X-ray activity, and age for M dwarfs. Therein we updated and homogenized data from the literature and added new very sensitive observations from dedicated observations with the X-ray satellites *XMM-Newton* and *Chandra* and the photometry mission K2, from which we derived rotation periods. The new results included a significantly steeper slope in the unsaturated regime for stars beyond the fully convective transition as compared to early-M dwarfs. We confirmed that the X-ray emission level of fast-rotating stars (i.e., those in the saturated regime) is not constant, as was previously mentioned by Reiners et al. (2014). Moreover, we calculated the evolution of the X-ray emission for M dwarfs older than $\sim$600 Myr by combining the results from the empirical $L_x - P_{rot}$ relation with the evolution of P_{rot} predicted by the angular momentum evolution model of Matt et al. (2015).

All previous observational work on X-ray activity-rotation relations is based on data that have been collected over decades with different telescopes and instruments, and with a focus on different regions of the parameter space. This introduces various biases. New space missions with an all-sky observing strategy are now available. They allow acquiring X-ray and rotation data for statistical samples with well-characterized stellar parameters that are biased only by a relatively uniform sensitivity limit. This offers new prospects for systematic studies of the X-ray emission of M dwarfs, and, in particular, their rotation-activity relation. We present here the first results from a combined study using the extended ROentgen survey with an Imaging Telescope Array (eROSITA; Predehl et al. 2021) on the Russian

Spektrum-Roentgen-Gamma (SRG) mission to measure X-ray luminosities and the Transiting Exoplanet Survey Satellite (TESS; Ricker et al. 2014) to obtain rotation periods. We search the sample of M dwarfs compiled from the SUPERBLINK proper motion survey by Lépine & Gaidos (2011) for eROSITA and TESS data, and we homogeneously characterize the stars using *Gaia* data. More details about our samples are given in Sect. 2, and we describe the construction of our input catalog of M dwarfs with additional information from *Gaia* in Sect. 3. The eROSITA and TESS data analysis is described in separate sections (Sects. 4 and 5) for the two subsamples we examined that are described in Sect. 2 because we pursue different, complementary scientific goals with the two samples. The presentation and interpretation of our results are found in Sect. 6, where we also present our findings in context with previous work about the rotation-activity relation. In Sect. 7 we summarize our conclusions and give an outlook to future studies in this field.

2. Database

This work is based on the SUPERBLINK proper motion catalog of nearby M dwarfs from Lépine & Gaidos (2011; hereafter LG11). The LG11 catalog is an all-sky list of 8889 M dwarfs (photometric spectral types K7 to M6) brighter than $J = 10$ mag and within 100 pc.

In this work we study the X-ray emission of M dwarfs from LG11 in two data sets: the eROSITA Final Equatorial-Depth Survey (eFEDS), and the first eROSITA All-Sky survey (eRASS1). eFEDS corresponds to a $\sim$140 sq.deg large area in the southern sky that was observed in four individual field scans during the calibration and performance verification (CalPV) phase (Predehl et al. 2021) of eROSITA (see Brunner et al. 2022). For the sake of simplicity, we refer to each field scan observation as "field". While an official eFEDS X-ray source list will be made public in the data release related to this A&A special issue, we used the preliminary catalog produced at the MPE as eRASS1 database.

The X-ray samples from eFEDS and eRASS1 and the way we treat them in this work are complementary. The eFEDS fields comprise a relatively small number of stars, for which we present a detailed X-ray study including eROSITA light curves and spectra. The part of our study that makes use of eRASS1 data is focused on global properties, taking advantage of the large number of targets provided by the all-sky survey. In particular, we study hardness ratios as a proxy for the coronal temperature and the long-term variability in the X-ray luminosity of M dwarfs in comparison to eFEDS and ROSAT data, and the relation between X-ray emission and rotation periods derived from TESS light curves. A complete discussion of the X-ray properties of the M dwarf sample based on a spectral and temporal analysis of eRASS1 data for individual stars is beyond the scope of this work. Similarly, for the M dwarfs in eFEDS, we provide an exhaustive analysis of TESS data using both 2 min and 29 min cadences, while our analysis is restricted to the 2 min light curves for the much larger eRASS1 sample.

In Table 1 we anticipate the number of targets in the various catalogs studied throughout this paper. The definitions of the samples are provided in the subsequent sections.

3. Preparation of the M dwarf catalog

To thoroughly characterize the M dwarf sample, we exploited *Gaia* data and published empirical calibrations for stellar parameters based on photometry. Our match of the LG11 catalog with the second data release of the *Gaia* mission (*Gaia*-DR2,

Table 1. Number of stars in the different samples of main-sequence M dwarfs.

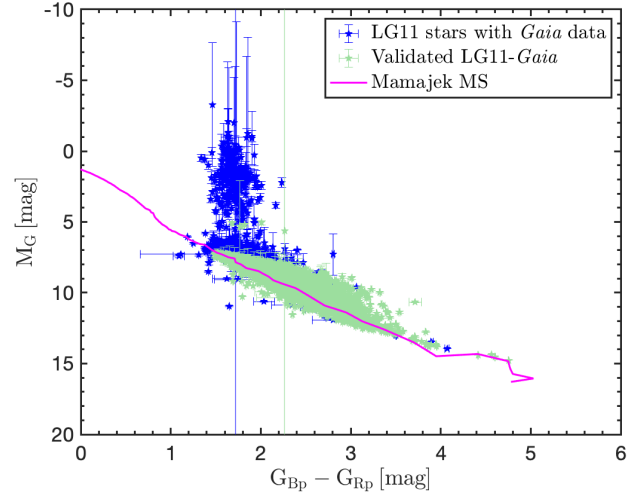| Sample name	'full'	'validated'
LG11-*Gaia*	8229	7319
LG11-*Gaia*/eFEDS	14	13
LG11-*Gaia*/eRASS1	673	580
LG11-*Gaia*/eFEDS/TESS [(1)]	3	3
LG11-*Gaia*/eRASS1/TESS [(1)]	172	135

Notes. See Sects. 3, 4.2, and 5.2 for the definitions. [(1)]Only stars with reliable TESS rotation period are included in these samples.

Gaia Collaboration 2018b) is explained in detail in Appendix A. We found that the majority of the M dwarfs from the LG11 catalog have counterparts (CTPs) in *Gaia* DR2, and about 2% have multiple *Gaia* DR2 matches that are common proper motion (P.M.) pairs. Our procedure includes a comparison of the P.M. values from LG11 and from *Gaia* DR2, and a comparison of 2 MASS magnitudes for the objects from LG11 with the J -band magnitudes inferred from *Gaia* DR2 photometry. This removes *Gaia* sources within our search radius of 3″ that are not related to the LG11 M dwarfs.

Our final target list holds 9070 objects (8917 stars with *Gaia* counterparts, including the 181 common proper motion (CPM) companions and 153 stars without a *Gaia* counterpart). We matched this catalog with Bailer-Jones et al. (2018, hereafter BJ 18) to obtain *Gaia* DR2 distances, d_{BJ18}. We found that 531 entries from our catalog do not have data in BJ 18, including the 153 stars without any *Gaia* counterpart. The stars for which we have a distance from BJ18 include 20 without *Gaia* photometry. We removed these stars because we aim at a well-characterized sample, and we calculated the spectral types (SpTs) from the $G_{BP} - G_{RP}$ color with the values provided for the main sequence by E. Mamajek[1].

In Fig. 1 we show the *Gaia* color-magnitude diagram (CMD) for the 8519 stars with *Gaia* distance and photometry. This sample includes the companions in CPM binaries. The *Gaia* CMD shows two distinct populations: the main sequence, and a cluster of stars above it centered at $G_{BP} - G_{RP} \sim 1.7$ (corresponding to late-K SpT according to the Mamajek scale). We took $M_G = 5$ mag as a rough dividing line between the two populations, and show the distance distributions of these two groups in the left panel of Fig. 2.

Here it is evident that all main-sequence stars are within 300 pc, with a strong peak around ~50 pc, while the remaining stars, which make up ~3.4% of the whole sample, cover a wide range of distances from ~100 pc to ~1.5 kpc and include a few outliers with distance up to 5 kpc that are not shown in the figure. Based on their position in Fig. 1 and their large distances, these stars are probably giants that contaminate the LG11 dwarf star catalog. LG11 discussed the compromise in their catalog between the aim of catching as many M dwarfs as possible, including those with small sky motion, and reducing the contamination with M giants. They argued that the majority of red giants have proper motions lower than their cutoff, $\mu = 40$ mas yr^{-1}, and they applied additional cuts in absolute magnitude, reduced

[1] The table A Modern Mean Dwarf Stellar Color and Effective Temperature Sequence is maintained by E. Mamajek at http://www.pas.rochester.edu/~emamajek/EEM_dwarf_UBVIJHK_colors_Teff.txt


Fig. 1. *Gaia* CMD based on DR2 data for the LG11 sample with *Gaia* distance and photometry. The pink line represents the main sequence by E. Mamajek (see footnote 1). A residual contamination by giant stars is present. Stars with $M_G > 5$ mag and $M_{K_s} > 4.6$ (the magnitude above which the polynomial relations between photometry and stellar parameters of Mann et al. (2015) are valid) are highlighted in green.

proper motion, and colors. Nevertheless, the over-density of optically bright stars at low Galactic latitude discussed by LG11 suggests the presence of unrecognized giants, consistent with our finding.

Our study is focused on dwarf stars, and therefore we concentrate below on the main-sequence stars ($M_G > 5$ mag). Henceforth, this sample of 8229 stars is called the LG11-*Gaia* sample (see Table 1). To calculate their stellar parameters, we applied the empirical relations from Mann et al. (2015, 2016), which these authors calibrated on spectroscopically confirmed M dwarfs. Specifically, Mann et al. (2015) obtained stellar masses ($M_\star$) from the absolute magnitude in the 2MASS K_s band (M_{K_s}), the bolometric correction (BC_{K_s}) from $V - J$, and the bolometric luminosity (L_{bol}) from BC_{K_s}. For the application of these relations to our LG11-*Gaia* sample, we calculated the M_{K_s} values from d_{BJ18} and the apparent K_s magnitude. For the stars for which BJ18 reported no *Gaia* distance, we considered adopting the photometric distances calculated as described by Magaudda et al. (2020) from M_{K_s} obtained from an empirical relation with $V - J$. However, when we revisited the Magaudda et al. sample, we realized that it includes a small number of stars with FGK spectral types for which the M_{K_s} values derived from the photometric distances have yielded a mass in the M-type regime. To avoid this contamination, we therefore decided to limit the sample studied in this work to stars with *Gaia* distance and photometry, for which we can determine reliable SpT and stellar parameters. The Mann et al. (2015, 2016) relations have been calibrated for the range $4.6 < M_{K_s} < 9.8$. When we consider this criterion, our sample is reduced to a total of 7319 stars. This subsample, which fulfills the validity range of Mann et al. (2015), is highlighted in Fig. 1 in green and is henceforth referred to as the validated LG11-*Gaia* sample (see Table 1).

In the right panel of Fig. 2 we compare the full LG11-*Gaia* sample of main-sequence stars (red) and the subset of the validated main-sequence (green) stars in terms of their distance distribution. As expectedly, the validated sample, which is defined by a magnitude cut, comprises (with a few exceptions) the more nearby stars. Our work is based on these two samples of main-sequence M dwarfs.
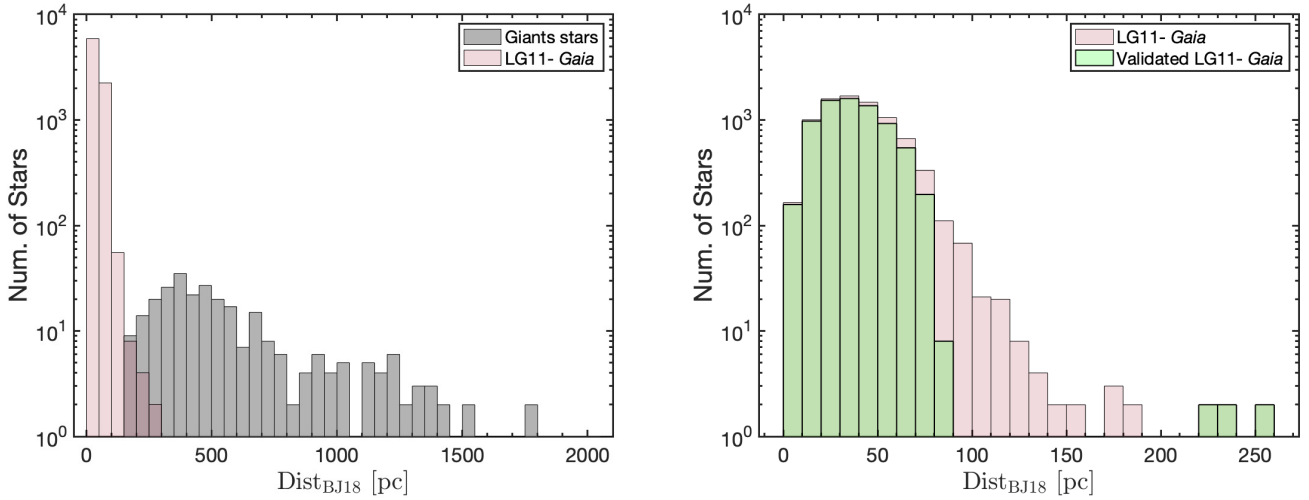
Fig. 2. Distance distributions (d_{BJ18}) for various subsamples of the LG11 catalog according to our match with *Gaia* DR2. *Left*: giant stars (in gray) and main-sequence stars (in red). *Right*: zoom into the main-sequence sample (red) and subsample of validated main-sequence stars (green). See text in Sect. 3.

Specifically, this article is focused on two subsamples of the LG11-*Gaia* stars: those that are located within the eFEDS fields (Sect. 3.1), and those that are detected in eRASS1 (Sect. 3.2). In the parts of our analysis that rely on the stellar mass, we restrict the sample to the validated stars.

3.1. M dwarfs in the eFEDS fields

An official X-ray source catalog for the eFEDS fields was produced in parallel with our work and is presented by Brunner et al. (2022). Our own eROSITA data analysis, which is limited to M dwarfs from the LG11 catalog, is described in Sect. 4.1.1. This analysis involved source detection in the whole eFEDS field. We found 24376 X-ray sources. As a cross-check of our results, we compared our X-ray source catalog with the official catalog (eFEDS_c001_V7_main) produced by Brunner et al. (2022). First, we found a discrepancy between the X-ray coordinates of our catalog and those in eFEDS_c001_V4_main. We suspect that this is due to an astrometric correction that was used in eFEDS_c001_V4_main to correct for the mean linear offset between the X-ray sources and the *Gaia* positions of objects in the *Gaia*-unWISE catalog of candidate active galactic nuclei (AGN) by Shu et al. (2019). This offset is different for each of the four eFEDS fields and is given in Table 1 of Brunner et al. (2022). We applied these corrections to the X-ray coordinates of our catalog and verified that this removed the offset between the X-ray positions in our catalog and eFEDS_c001_V4_main. Finally, we calculated the final absolute coordinates (RA_CORR, DEC_CORR) by applying Eq. (1) from Brunner et al. (2022) to our X-ray catalog.

We then used our catalog with the corrected X-ray coordinates to search for X-ray detections in the LG11-*Gaia* sample. Thirty-one M dwarfs from our sample lie within the eFEDS field boundaries. We based our match between optical and X-ray position on *Gaia* coordinates and proper motions from our LG11-*Gaia* catalog. We first corrected the coordinates of our stars by their P.M. to the eFEDS mean epoch (November 5, 2019), and then we matched them with our final X-ray coordinates (RA_CORR, DEC_CORR). In this way, we found 15 matches within 15″. We cross-checked our detections by matching the P.M.-corrected LG11-*Gaia* sample with the official eFEDS catalog as well. We found all the 15 stars that we detected

in our catalog. The positional uncertainties of all X-ray sources in the eFEDS field were investigated by Brunner et al. (2022). We verified that for our matches with the LG11-*Gaia* M dwarfs, the corresponding parameter (RADEC_ERR) is smaller than our match radius.

While it is quite plausible that the M dwarfs from the LG11 catalog emit in X-rays, the limited sensitivity of eROSITA combined with its modest spatial resolution requires a cross-check for other possible optical CTPs to the eROSITA sources. This means that we have to verify the associations between our target stars and the detected X-ray sources. We pursue here a conservative approach, that is, we aim at keeping only those M dwarfs in our sample that we consider secure CTPs to the X-ray sources. We base this assessment on the separation between the optical and X-ray position with respect to that of other *Gaia* objects in the vicinity.

To determine alternative possible *Gaia* CTPs for each of the 15 X-ray sources, we performed a reverse match (RM), in which we searched for all *Gaia* sources within 15″ of the X-ray coordinates from our catalog (RA_CORR, DEC_CORR). In this way, we found a total of 21 potential *Gaia* CTPs, including 14 stars from the LG11-*Gaia* sample. Then we inspected the separations between the X-ray positions and the *Gaia* coordinates for the 21 *Gaia* sources ($Sep_{X,opt}$). Hereby, we considered the P.M. correction to the mean eFEDS observing date for the *Gaia* sources that are identified with a star in our input catalog. As a result, the star from LG11-*Gaia* is the closest *Gaia* object to an X-ray source for all 14 cases, and these M dwarfs define our list of bona fide eFEDS X-ray emitters. The missing object is a high proper motion star that is not recovered in the reverse match because the P.M. correction can be applied only a posteriori, and a search radius of 15″ is too small for this star. Therefore we increased the search radius up to 20″, finding the *Gaia* source associated with this M dwarf, which is not the closest *Gaia* counterpart, however. Adhering to our conservative approach, we excluded this star from our LG11-*Gaia*/eFEDS sample. This sample therefore consists of 14 M dwarfs. All but one of them are also part of our validated LG11-*Gaia*/eFEDS sample (see Table 1). Finally, we compared the X-ray optical separation ($Sep_{X,opt}$) with the uncertainties on the X-ray positions from our X-ray source catalog (RADEC_ERR). We found that all 14 LG11-*Gaia* stars in our eFEDS X-ray emitter sample have $Sep_{X,opt} < 3 \times$ RADEC_ERR,
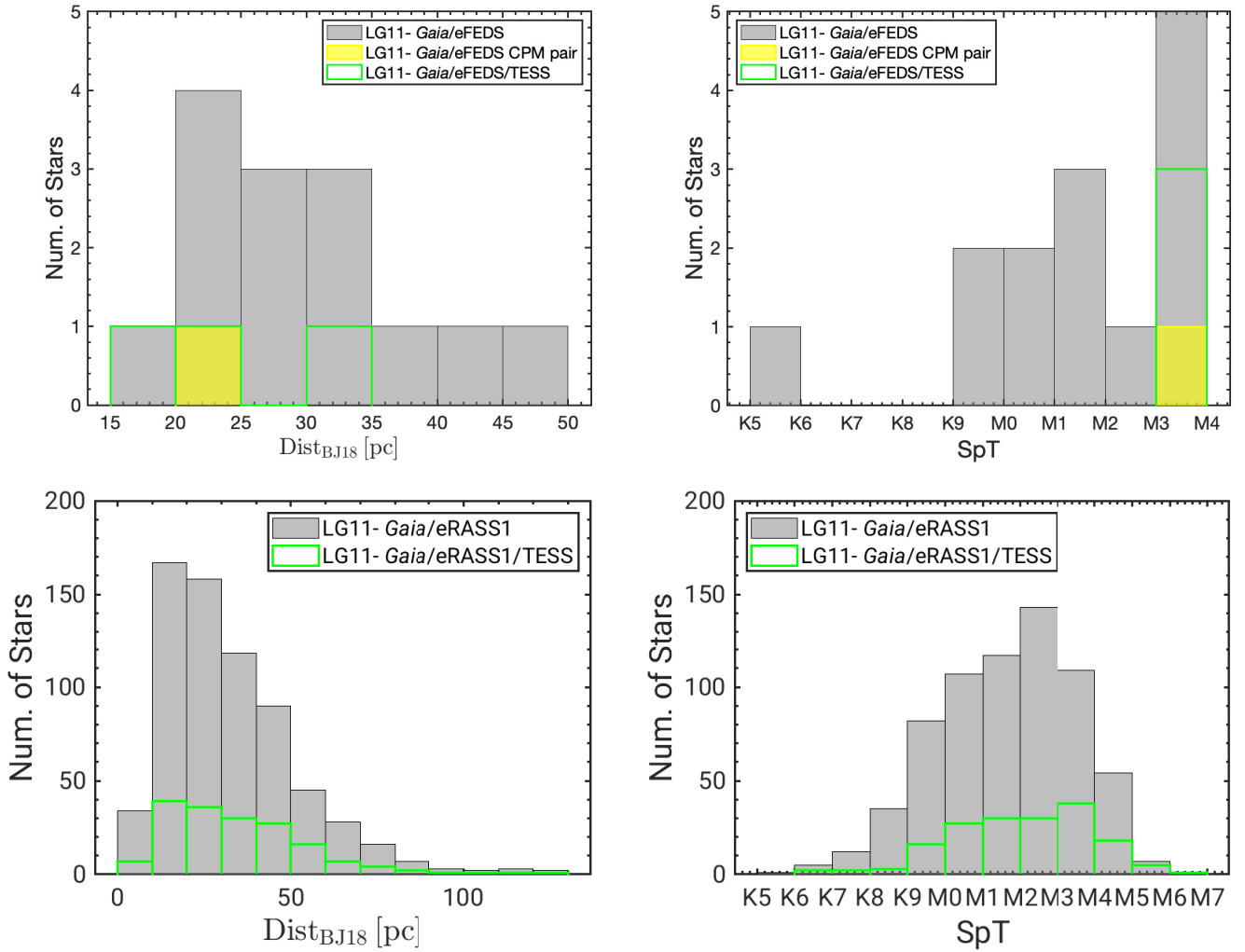
Fig. 3. Distribution of *Gaia* distances from Bailer-Jones et al. (2018) and spectral types calculated from $G_{bp} - G_{rp}$. *Top panel*: gray histogram is the distribution for the stars from LG11-*Gaia* in the eFEDS fields. The green contours represent the distance and SpT distribution for those stars observed by TESS. We show the CPM pairs in yellow. *Bottom panel*: stars from the LG11-*Gaia* sample identified in the preliminary eRASS1 catalog. For simplicity, we do not show the four CPM pairs here because they represent only 4% of the sample.

which confirms that the association of the M dwarfs with the eFEDS X-ray sources is consistent with the positional accuracy of eROSITA. These there include one CPM pair that has the same X-ray source associated with each component of the system, but that is resolved by *Gaia* and 2MASS. We chose to ascribe the X-ray emission to the component that is closest to the X-ray source, and we treated it in the same manner as the single stars. Because the two stars in the CPM pair have similar stellar parameters ($M_\star$ and SpT), this approach does not influence our results.

In the upper row of Fig. 3 we show the distribution of the distances and spectral types for our LG11-*Gaia*/eFEDS sample. Fig. 3 (top panels) also highlights the one CPM pair of the sample, as well as the subsample of stars with TESS rotation period, that is, 3 out of 14 stars (see Sect. 4.2). The *Gaia* source IDs, stellar parameters, and distances for the 14 LG11/*Gaia* stars in our eFEDS sample are listed in Table 2.

3.2. M dwarfs detected in eRASS1

For the cross-match of our LG11-*Gaia* catalog with the eRASS1 catalog (v201008), we used the *Gaia* coordinates, corrected

for their proper motions to the rough mean observing date of eRASS1 (March 10, 2020). We cross-matched these extrapolated positions of the M dwarfs with the boresight-corrected coordinates (Col. RA_CORR, DEC_CORR) of the eRASS1 catalog within a radius of 25″. At about 10″, the cumulative histogram of identifications flattens out. The cross-matching radius is a compromise between defining a complete sample and avoiding selecting wrong counterparts. Based on the shape of the cumulative separation distribution, we therefore only considered the matches within 15″. After removing ten stars that are located in the half of the sky that is propriety of the Russian eROSITA consortium the catalog results in 842 X-ray sources. The choice of 15″ as identification radius amounts to only ~2% fewer sources than the 25″ match radius and ~5% more sources than would be in a 10″ radius.

Analogous to the procedure in Sect. 3.1, we performed a reverse match to uncover the *Gaia* sources that are alternative potential CTPs to the X-ray sources. In this match, we searched for all *Gaia* sources within 15″ of the boresight corrected positions of the 842 eRASS1 sources. This resulted in a total of 2148 potential *Gaia* counterparts. These multiple optical CTPs should include all 842 LG11-*Gaia* M dwarfs that were identified in the

Table 2. Stellar parameters and distances of the eROSITA samples of M dwarfs.

LG11 name [1]	*Gaia*-DR2 designation [2]	SpT	Dist$_{BJ18}$ [3] [pc]	M_{K_s} [4] [mag]	$M_\star$ [4] [$M_\odot$]	Binary
			LG11-*Gaia*/eFEDS sample			
PM I08551+0132	577602496345490176	K9.4	20.53 ± 0.02	0.03 ± 0.03	0.67 ± 0.01	0
PM I08570+0103	576773808175184768	M0.1	48.98 ± 0.12	0.04 ± 0.04	0.60 ± 0.01	0
PM I08590+0151	576970105360152192	K5.3	40.89 ± 0.47	0.14 ± 0.14	0.78 ± 0.02	0
..	..	..	..	..	..	..
..	..	..	..	..	..	..
			LG11-*Gaia*/eRASS1 sample			
PM I00016−7613	4684946035804965632	M2.3	34.50 ± 0.03	5.91 ± 0.03	0.48 ± 0.01	0
PM I00054−3721	2306965202564506752	M1.4	4.34 ± 0.00	6.33 ± 0.02	0.41 ± 0.01	0
PM I00082−5705	4919497979411495296	M2.9	12.80 ± 0.01	6.86 ± 0.02	0.33 ± 0.01	0
..	..	..	..	..	..	..
..	..	..	..	..	..	..

References. [1]Lépine & Gaidos (2011). [2]Gaia Collaboration (2018b). [3]Bailer-Jones et al. (2018). [4]Calculated with the relations from Mann et al. (2015, 2016). The full table is available at the CDS.
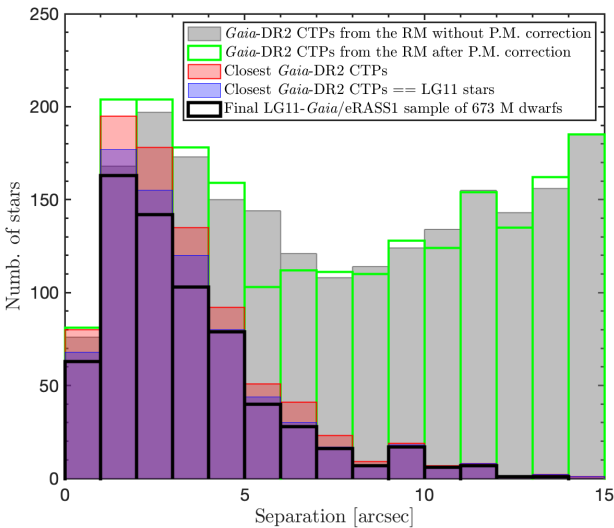
Fig. 4. Separation between the X-ray to optical positions for the 842 direct matches of LG11-*Gaia* stars with the eRASS1 catalog. All 2148 possible *Gaia*-DR2 CTPs found with the reverse match within 15″ are shown in gray. The same objects after the application of their P.M. correction are plotted in green. The red histogram represents the *Gaia*-DR2 CTP that is closest to each eRASS1 source of our sample, the 734 closest *Gaia* CTPs that correspond to the LG11-*Gaia* stars studied in this work are shown in blue, and the final LG11-*Gaia*/eRASS1 sample of 673 M dwarfs is shown in black.

first match with an X-ray source. In practice, we recovered only 840 of them. This is explained by the fact that two stars are not recovered within 15″ because of their high proper motions. These cases are similar to the case discussed in Sect. 3.1, for which a search radius of 15″ was too small.

In Fig. 4 we show the distribution of the separations between the *Gaia*-DR2 and eRASS1 positions in gray. We inspected the separations between X-ray position and *Gaia* coordinates for all potential *Gaia* CTPs considering the P.M. correction to the mean eRASS1 observing date for the *Gaia* sources that are identified with a target star. In this way, we found that the star from the LG11-*Gaia* list is the closest *Gaia* object to an X-ray source in

732 cases. Specifically, to find the two stars from the LG11-*Gaia* sample with very high proper motion that are not recovered in the reverse match, we increased the search radius to 45″. This leads to 734 closest *Gaia* CTPs that are identified with a star from our LG11-*Gaia* catalog, that is 87% of the original eRASS1 sample. These objects are shown in blue in Fig. 4. The closest *Gaia* counterparts to the remaining 108 eRASS1 sources are represented in the red histogram.

Fifteen of the 734 objects for which the closest *Gaia* counterpart is identified with an LG11-*Gaia* star have a visual companion. The components of these binary systems are associated with the same X-ray source, thus special attention is needed. By definition of how we identified multiples in the LG11 catalog, these systems are resolved by *Gaia*. However, 11 of them are associated with a single 2MASS source. Because we cannot determine reliable stellar parameters for these systems, we disregarded them. For the remaining four CPM pairs that are resolved with *Gaia* and 2MASS but not with eROSITA, we adopted the same approach as for the only binary in the LG11-*Gaia*/eFEDS sample (see Sect. 3.1), that is, we ascribed the X-ray emission to the component of the binary that is closest to the X-ray position. In one of these four CPM pairs that are resolved with 2MASS, one component has no complete *Gaia* data, and thus it was removed in the first place from our LG11-*Gaia* sample (see Sect. 3). Moreover, this component is not the closest component to the X-ray source and would have been removed in any case.

Finally, we removed all stars from the 723 objects for which Sep$_{X,opt}$ was higher than three times the uncertainty on the X-ray position in the eRASS1 catalog (RADEC_ERR). This left 673 eRASS1 X-ray sources, and these define our eRASS1 M dwarf sample, LG11-*Gaia*/eRASS1. Of these, 580 stars are also included in our validated LG11-*Gaia*/eRASS1 sample (see Table 1).

The *Gaia* DR2 source IDs, stellar parameters, and distances for the LG11-*Gaia*/eRASS1 sample are presented in Table 2, and their histograms of distance and SpT are shown in the bottom panels of Fig. 3. The subsample with TESS rotation periods that is described in Sect. 5.2 is overlaid, together with the four stars that have a comoving companion. These distributions are similar to those of the M dwarfs in the eFEDS (displayed in the top
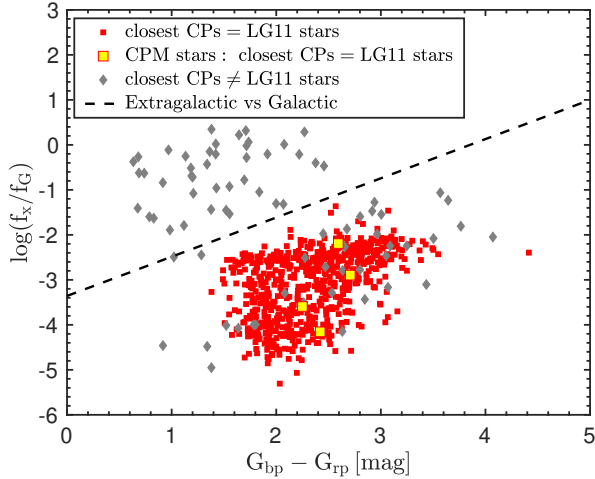
Fig. 5. X-ray-to-optical flux ratio vs. *Gaia* color for the closest optical counterparts to the X-ray sources selected from the match of LG11-*Gaia* with the eRASS1 catalog. Two distinct regions are visible: the extragalactic area with high $\log(f_x/f_G)$ values and relatively blue *Gaia* color, and the star region with lower values of $\log(f_x/f_G)$ and redder *Gaia* color, separated by the dashed black line we derived from Fig. B3 in Stelzer et al. (2022). The filled red squares are the 673 eRASS1 sources that we identified as M dwarfs (see text in Sect. 3.2), and the filled yellow squares represent the four stars that have a comoving companion. We show only the sources with $\mathrm{Sep_{X,opt}}$ < 3 x RADEC_ERR.

panels of the same figure), but their number statistics are higher by more than 20 times. Figure 3 also shows that the subsample observed by TESS is a representation of the X-ray detected stars that is unbiased in terms of distance and SpT.

The source identification is always a compromise between completeness and avoiding to include wrong counterparts. As explained in Sect. 3.1, we aimed to define secure X-ray associations with main-sequence stars from the LG11 catalog at the expense of possibly missing some of them as X-ray emitters. Therefore, we removed all but those M dwarfs that were determined through the above analysis to have the smallest separation to the X-ray source. The nature of the remaining closest *Gaia* CTPs, that is, those that are not part of the LG11-*Gaia* catalog, is not of interest to our work. However, a quick assessment can be done with help of a diagram that combines the X-ray-to-optical flux ratio, f_x/f_G, with *Gaia* color. On the basis of eROSITA observations from the eFEDS fields, Stelzer et al. (2022) showed the separation of stars and extragalactic objects in this diagram. In Fig. 5 the closest *Gaia* CTPs of our reverse match are split into two strongly populated areas. In this figure we only considered the objects with $\mathrm{Sep_{X,opt}}$ < 3 x RADEC_ERR. The 673 M dwarfs from LG11-*Gaia*/eRASS1 are located in the lower right corner, including the four stars that have a comoving companion (highlighted in yellow). Most of the remaining closest *Gaia* CTPs that are not objects from our input catalog are located in the upper left corner of the diagram, which defines the extragalactic region.

3.3. Comparison with the source identification with NWAY

As a cross-check on our source identification procedure, we compared our lists of eROSITA-detected M dwarfs from eFEDS and eRASS1 with the eROSITA sources identified with the NWAY algorithm (Salvato et al. 2018). NWAY is an open-source[2] code based on a Bayesian statistics that assigns the probability of being the correct counterpart to every source within a certain

---

[2] https://github.com/JohannesBuchner/nway

distance from the X-ray position. The probability is computed taking into account spatial information (separation between the sources, positional accuracy, and number densities) and priors constructed using a training sample of X-ray sources with a secure counterpart, regardless of their galactic or extragalactic nature. Specifically, for eFEDS (Salvato et al. 2022), the prior was built using optical and mid-infrared photometry from *Gaia*-DR2 and the Legacy Survey DR8 (LS8; Dey et al. 2019) using 20 705 sources listed in the *XMM-Newton* serendipitous source catalogue (3XMM; Rosen 2016). The trained prior was tested on a sample of about 3500 *Chandra* sources that were assigned artificial eROSITA positional errors. An NWAY match on this simulated dataset indicated a purity and completeness in correct association of about 96%, and only 2% have a possible alternative counterpart.

The comparison of our results with those of NWAY_LS8 showed that all 14 eFEDS X-ray sources that we identified with an LG11-*Gaia* star are associated with the same star by NWAY. For eRASS1, the NWAY catalog is incomplete because it is limited to the sky coverage of the LS8 survey. For this reason, we can compare the LG11-*Gaia* catalog and the result from NWAY for only 382 out of 842 (~45%) eRASS1 sources. The comparison is explained in detail in Appendix B. Here we present a short summary for eRASS1, for which the matching was more complicated.

We found an agreement for 93% of our sample. For the vast majority of them (326), the eRASS1 source is identified with our method and with NWAY to an LG11-*Gaia* M star. In 11 cases, however, we removed an LG11-*Gaia* star from our final M dwarf list because it is not the closest counterpart to the X-ray source. Here we are more conservative than NWAY because we are restricted to the closest matches, and we therefore lose 3% of the presumed M dwarf X-ray emitters from our final LG11-*Gaia*/eRASS1 catalog. On the other hand, NWAY-LS8 misses 11 LG11-*Gaia* stars that we confirmed by visual inspection of sky images as plausible counterparts to the corresponding eRASS1 source.

Although the NWAY-LS8 eRASS1 catalog is not yet complete, we conclude that there is excellent agreement with the results we found from our position-based approach. However, in this preliminary version of the NWAY_LS8 catalog for eRASS1, the coordinates are not corrected for possible proper motion of the sources, resulting in a misidentification of the counterpart for fast-moving objects, and for this reason, we consider our association more reliable in the few dubious cases.

4. Data analysis for the eFEDS fields

4.1. eROSITA

M dwarf stars are soft X-ray emitters. In early versions of our data reduction, we realized that no photons were collected at energies above 5.0 keV for the stars detected in our sample. The lowest energy recommended to be used with eROSITA data is 0.2 keV (Predehl et al. 2021). Therefore, we performed the analysis in the 0.2−5.0 keV energy band. In the following, we explain the details of the data extraction and analysis regarding the M dwarfs in the eFEDS fields.

4.1.1. Data extraction

We analyzed the eFEDS c946 processing data using the eSAS-Susers_200602 software release. We extracted eFEDS data in parallel with the construction of the official catalog, therefore both the processing and the software release we used are not the

Table 3. Basic X-ray parameters of the LG11-*Gaia*/eFEDS and LG11-*Gaia*/eRASS1 samples.

LG11 name	RA_CORR [deg]	DEC_CORR [deg]	RADEC_CORR [arcsec]	Sep$_{X,opt}$ [arcsec]	ML_RATE_0 $\times 10^{-3}$ [cnt s^{-1}]	DET_ML_0
LG11-Gaia/eFEDS sample						
PM I08551+0132	133.781820	1.540727	4.00	0.67	31.87 ± 6.97	30.38
PM I08570+0103	134.270789	1.057574	4.61	5.36	14.96 ± 5.06	10.24
PM I08590+0151	134.758412	1.864988	2.38	2.01	80.68 ± 10.13	113.11
..	..	..	..	..	..	..
..	..	..	..	..	..	..
LG11-Gaia/eRASS1 sample						
PM I00016−7613	0.416684	−76.230118	3.09	2.47	110.61 ± 31.42	31.66
PM I00054−3721	1.395104	−37.370675	5.11	10.36	81.23 ± 34.24	11.28
PM I00082−5705	2.070065	−57.096650	4.86	6.41	79.60 ± 30.13	11.15
..	..	..	..	..	..	..
..	..	..	..	..	..	..

Notes. The data are from our own eFEDS X-ray source catalog and from the preliminary eRASS1 catalog, and they refer to the 0.2−5.0 keV band. The full table is available at the CDS.

same as were published by the consortium. The data processing provides seven events files in the whole eROSITA energy band (0.2−10.0 keV), one for each telescope and camera system on board eROSITA. We merged the seven files to create one single event and image file filtered for corrupted events in the energy range 0.2−5.0 keV. We calculated the exposure map and the detection mask, which are needed for the source detection, in the same energy band. We computed the background map with the `erbackmap` routine, using a smooth fit with a smoothing value of 15. Source detection was performed using the `ermldet` pipeline, for which we adopted a minimum threshold for the detection maximum likelihood of 6.0.

We detected a total of 24 376 X-ray sources in the combined four eFEDS fields. The slight difference with respect to the number of sources in the eFEDS_c001_V4_main catalog (27 910 sources) is most likely to be attributed to the different parameters that were set in the extraction process. These differences have no effect on our study, as we showed in Sect. 3.1, where we anticipated our result for the identification of our M dwarf target list with the eFEDS X-ray sources.

The basic X-ray parameters of the 14 M dwarfs detected in eFEDS are given in Table 3. In particular, we provide the name of the star in LG11 (Col. 1), the X-ray coordinates with their uncertainty (Cols. 2−4), the offset between the proper-motion-corrected optical position and the X-ray coordinates (Col. 5), the 0.2−5.0 keV count rate obtained from the source detection procedure (Col. 6), and the detection maximum likelihood in the same energy band (Col. 7).

We also carried out a spectral and temporal analysis for these stars. To this end, we used the `srctool` routine and selected a circular region for the source (with radius of 30″−40″ depending on the source brightness). The analysis of the light curves and spectra is explained in Sects. 4.1.2 and 4.1.3.

4.1.2. Spectral analysis

Spectral analysis was performed with XSPEC[3] version 12.10. We carried out the spectral fitting only for the 10 out of the 14 detected sources that have more than 30 net source counts. We

used a two-temperature thermal model (APEC[4]) except for one star, which is the faintest of the stars for which we have a reasonable spectrum and which can be described by a one-temperature APEC model.

Each APEC component has three parameters: the plasma temperature (kT), the global abundance (Z), and the emission measure (EM). The emission measure is the square of the number density of free electrons integrated over the volume of the emitting plasma, and it is obtained from the normalization factor of the XSPEC fit combined with the source distance. We fixed Z at 0.3 $Z_\odot$, the typical coronal abundance for late-type stars (Favata et al. 2000; van den Besselaar et al. 2003; Robrade & Schmitt 2005; Maggio et al. 2007), and we left kT and EM free to vary. We computed the mean coronal temperature (T_{mean}) by weighting the temperatures of the individual APEC components by their EM,

$$T_{mean} = \frac{\sum (EM_n \cdot T_n)}{\sum (EM_n)}, \tag{1}$$

where $n = 1, 2$ for the two components of the best-fitting model. The parameters of the best-fitting model including the values of T_{mean} are listed in Table 4, and the spectra are shown in Fig. C.1. One of the ten stars is the binary discussed in Sect. 3.1 that is unresolved with eROSITA, that is, the spectra of two stars are summed. Because the masses of the two components are equal (see Table 2), we can assume the X-ray spectra to be similar, and therefore we treated this spectrum in the same way as the others.

We computed the fluxes in the 0.2−5.0 keV band, f_x, with the *flux* routine provided by XSPEC. For all stars that are too faint for spectral analysis, we calculated a conversion factor (CF$_{eFEDS}$) for transforming the count rate to flux. We defined CF$_{eFEDS}$ as the ratio of the flux and count rate of each source for which we analyzed the spectrum. In particular, we used the fluxes computed with XSPEC and the count rates we found in the source detection. Then we calculated the mean value,

$$\langle CF_{eFEDS} \rangle = mean\left(\frac{f_x}{Ct.Rate}\right). \tag{2}$$

---

[3] XSPEC NASA's HEASARC Software: https://heasarc.gsfc.nasa.gov/xanadu/xspec/

[4] More information about APEC model used by XSPEC software can be found at https://heasarc.gsfc.nasa.gov/xanadu/xspec/manual/node135.html

Table 4. X-ray spectral parameters for the ten M stars in eFEDS with more than 30 counts in the 0.2−5.0 keV band.

Name	kT_1 [keV]	$\log(EM_1)$ [cm^{-3}]	kT_2 [keV]	$\log(EM_2)$ [cm^{-3}]	χ^2_{red}	d.o.f.	T_{mean} [keV]
PM I08551+0132	0.11 ± 0.03	50.75 ± 0.37	..	..	0.4	3	0.11 ± 0.03
PM I08590+0151	0.20 ± 0.06	50.67 ± 0.12	0.80 ± 0.18	50.45 ± 0.15	0.4	9	0.42 ± 0.07
PM I09034−0023	0.30 ± 0.02	51.23 ± 0.06	1.25 ± 0.20	51.05 ± 0.08	1.0	19	0.67 ± 0.07
PM I09050+0226	0.23 ± 0.03	50.67 ± 0.07	0.99 ± 0.16	50.40 ± 0.07	0.8	8	0.50 ± 0.06
PM I09050+0250	0.50 ± 0.23	49.93 ± 0.27	5.49 ± -1.10	50.39 ± 0.22	1.2	5	4.22 ± 0.82
PM I09161+0153	0.25 ± 0.01	51.12 ± 0.04	0.99 ± 0.04	51.00 ± 0.03	1.2	25	0.57 ± 0.02
PM I09201+0347	1.00 ± 0.06	50.60 ± 0.05	..	..	1.2	12	1.00 ± 0.06
PM I09205+0135	0.25 ± 0.02	51.44 ± 0.05	0.98 ± 0.06	51.33 ± 0.05	1.0	16	0.57 ± 0.03
PM I09238+0008	0.11 ± 0.08	50.55 ± 1.40	0.77 ± 0.13	50.40 ± 0.08	0.1	6	0.38 ± 0.07
PM I09308+0227	0.31 ± 0.02	50.73 ± 0.06	1.22 ± 0.20	50.44 ± 0.11	0.5	10	0.62 ± 0.07

Notes. 1σ uncertainties were computed with the ERROR pipeline provided in the XSPEC software package.

Table 5. Measurements of X-ray activity and rotation derived by us from eROSITA, ROSAT, and TESS data.

LG11 name	HR_1 [cts s^{-1}]	HR_2 [cts s^{-1}]	$(\log L_x)_{eROSITA}$ [erg s^{-1}]	$(\log L_x)_{ROSAT}$ [erg s^{-1}]	$\log(L_x/L_{bol})$	TIC number	P_{rot} [d]	flag_p	R_0
			LG11-*Gaia*/eFEDS sample						
PM I08551+0132	−0.52	−1.00	27.10 ± 0.10	..	−5.47 ± 0.04	265373654	..	..	..
PM I08570+0103	0.10	−1.00	27.52 ± 0.15	..	-4.87 ± 0.04	265440550	..	..	..
PM I08590+0151	0.11	−1.00	28.29 ± 0.05	..	−4.11 ± 0.04	..	..	..	..
..	..	..	..	..	..	..	..	..	..
..	..	..	..	..	..	..	..	..	..
			LG11-*Gaia*/eRASS1 sample						
PM I00016−7613	0.35	−0.90	28.09 ± 0.12	..	−3.96 ± 0.04	266878145	..	..	..
PM I00054−3721	0.63	−1.00	26.15 ± 0.18	..	−5.75 ± 0.03	120461526	..	..	..
PM I00082−5705	0.04	−1.00	27.08 ± 0.16	..	−4.57 ± 0.04	201287746	..	..	..
..	..	..	..	..	..	..	..	..	..
..	..	..	..	..	..	..	..	..	..

Notes. The full table is available at the CDS.

We excluded the two stars with d.o.f. ≤ 5 (see Table 4) from the calculation of the mean because the coronal temperatures we derive for them are not typical of M dwarf stars, and this is likely the result of the poor statistics of the spectrum. From the eight stars with good-quality spectra, we obtained $\langle CF_{eFEDS} \rangle = 7.81 \times 10^{-13} \pm 7.48 \times 10^{-14}$ erg cnt^{-1} cm^{-2}.

We determined the X-ray fluxes of the four detected stars without a spectral fit (i.e., those with fewer than 30 net counts) and the two stars with a poor spectral fit by combining their count rates with $\langle CF_{eFEDS} \rangle$. The X-ray luminosities were determined by combining the fluxes with the distances from Table 2, and the X-ray to bolometric ratios, $\log(L_x/L_{bol})$ in Table 5 were obtained using the L_{bol} values derived with the relations of Mann et al. (2015, 2016). The eFEDS X-ray luminosities are presented in Table 5 together with the ROSAT and TESS parameters derived in the following sections.

We verified with the eFEDS X-ray spectra that the L_x values we calculated for the 0.2−5.0 keV band differ from those for a softer energy band (0.2−2.4 keV) at a level of 1% or lower. This can be easily understood from Fig. C.1, where the spectra drop steeply above ~1 keV. Therefore, we use the broader standard eROSITA band in the remainder of this paper for our eROSITA detections, also when we compare eROSITA and ROSAT measurements.

4.1.3. Light-curve analysis

Each of the four eFEDS fields was scanned by eROSITA in the direction of the longer side of the individual fields. Thus, eROSITA has visited a given object within the eFEDS fields several times with a time lapse between one and the next visit that depends on the position of the object. As a consequence of this observing mode, light curves of individual sources are defined by short (<100 s) intervals of data taking (called one 'visit'), separated by longer data gaps during which the satellite scans through the rest of the field, turns around, and approaches the source again. Generally, the length of the data gaps alternates between two values, except for sources that are located in the middle of the eFEDS fields along the scanning direction, where all data gaps have an approximately equal length.

We performed the light curve extraction with the dedicated source products pipeline, srctool, which is part of the eSASS software. We worked in the energy band between 0.2 and 5.0 keV, and we used the same source and background regions as we adopted for the spectral analysis.

As explained above, in survey mode, a regularly binned light curve is dominated by data gaps. We therefore used the REGULAR option to produce light curves with regularly spaced bins in which time intervals without data are automatically discarded. We performed tests with different bin sizes to identify the best

value for each source in order to avoid bins with a very low number of counts and a correspondingly large uncertainty because they start near the end of a visit. As explained above, because the visits are not regularly spaced, a large bin size was required to reach this goal. The binning we determined from our tests is between 1 and 3 ks; this was chosen individually for each source. For stars located in the scanning direction near the edge of the eFEDS fields, this means that we averaged over two successive visits.

The light curves of all 14 stars from our sample that are detected in the eFEDS fields are shown in Fig. D.1, where the individual bin size is indicated for each star in the legend. The uncertainties of the count rate are automatically calculated by the eSASS pipeline, and they depend on the uncertainties of the source and background counts, the fractional telescope collecting area, and the fraction of the time bin that overlaps with the input good time intervals (GTIs) that have been calculated by the eSASS pipeline during the extraction of the events file. During its first and last visit, the source is located at the edge of the field of view and the fractional telescope collecting area and the fractional temporal coverage become smaller. Consequently, the error bars increase.

A systematic analysis of the variability of all sources detected in the eFEDS field is presented by Boller et al. (2022). This variability study refers to all objects in the official eFEDS source catalog, which comprises our 14 detected M dwarfs. We extracted the variability metrics for these 14 stars from the catalog of Boller et al. (2022). Specifically, this catalog provides the normalized excess variance (NEV) as defined by Boller et al. (2016) and its uncertainty. The eFEDS variability tests carried out by Boller et al. (2022) on the full eFEDS sample were performed on light curves with bin sizes of 100 s. The ratio of these two quantities represents the probability that the source is variable in units of Gaussian σ. We find that five of the LG11-*Gaia*/eFEDS sample have a well-determined NEV and its uncertainty. In the eFEDS fields, the net count statistics is low for most sources, such that the NEV is unconstrained. Only for one of the M dwarfs that is identified as variable is the NEV $\sigma > 3$, and another one has $\sigma > 2.5$. These two stars are PM I09161+0153, the brightest star in our sample (in terms of X-ray count rate), for which the visual inspection of the light curve indicates a likely ongoing flare at the beginning of the observation, and PM I09201+0347, which shows a smoother and longer-lasting variability throughout the eFEDS light curve.

4.2. TESS

To retrieve TESS data, we uploaded our target list of the 14 M dwarfs from the LG11-*Gaia*/eFEDS catalog to the *Barbara A. Mikulski* Archive for Space Telescopes (MAST) interface and found TESS data for 13 stars. We used the J2000 coordinates from LG11 for the match, with a match radius of 1″. Because the pixel scale of TESS is so large (21″ per pixel), a P.M. correction or its omission does not influence the result. Many stars have two TIC numbers, and we determined the correct TIC counterpart by comparing the magnitudes of the multiband photometry provided in the TIC with the values listed for the LG11 star in Simbad and ESASky.

All but one of the 13 stars have short (two-minute) cadence light curves. The remaining star was observed in full-frame image (FFI) mode only. The observation of the eFEDS fields was performed by TESS in its Sectors 7 and 8 during January and February 2019, and we downloaded the data from the MAST portal.

4.2.1. Analysis of the two-minute cadence light curves

For our analysis, which consisted of three steps, we used the presearch data conditioning simple aperture photometry (PDCSAP) light curves. TESS assigns a quality flag to all measurements, including data that are of poor quality, but also data that might be of lower quality or could cause problems for transit detection after applying a detrending software (Thompson et al. 2016). Hence, removing all flagged data points by default could impede the detection of real astrophysical signals or the interpretation of systematics. Therefore, we removed all flagged data points except those of 'impulsive outliers' (which could be real stellar flares) and 'cosmic ray in collateral data' (bits 10 and 11) in step 1 of the analysis. In a second step, we normalized the light curves by dividing all data points by the median flux.

The third analysis step is the search for rotation periods. To this end we used three different methods, the generalized Lomb-Scargle periodogram (GLS; Zechmeister & Kürster 2009), the autocorrelation function (ACF), and fitting the light curves with a sine function. We first used this approach on data from the K2 mission, and all details on our period search can be found in Stelzer et al. (2016) and Raetz et al. (2020). For the analysis with GLS we had to bin the data by a factor of 3 because the implementation we use[5] can only deal with up to 10 000 data points.

4.2.2. Analysis of the full-frame images

Because one of our targets with available TESS data does not have a light curve with a 2-min cadence, we decided to extract the long (29-min) cadence light curves of all 13 targets from the FFIs. To create a light curve, we performed aperture photometry. Instead of using all FFIs, we made use of the so-called postcards, which are an intermediate data product from the FFI analysis tool ELEANOR (Feinstein et al. 2019). Postcards are 148 × 104 pixel background-subtracted cutout regions of the FFIs that are time-stacked, including all cadences for which observations are available. We converted the postcard cubes into individual fits images. Sectors 7 and 8 include 1093 and 968 cadences, respectively. Photometry was performed following the procedures described by us in Raetz et al. (2016), for instance. In short, for the aperture photometry with ten different aperture radii, we used a user script based on the standard IRAF routine *phot*. Our script allows us to obtain simultaneous photometry of all stars in an image. For this purpose, a list of the pixel coordinates of all detectable stars was created using SOURCE EXTRACTOR (SEXTRACTOR; Bertin & Arnouts 1996). As the positions of the stars on the CCDs do not change during a sector, a single file with pixel coordinates was used for all cadences. Finally, we derived differential magnitudes using an optimized artificial comparison star (Broeg et al. 2005). Because TESS has an image scale of ~21 arcsec per pixel, we found the optimal aperture radius for all targets to be 2 pixels. The resulting light curves of sector 8 show strong systematic effects at the beginning of the observations and after the observation gap caused by the data downlink at Earth perigee. We removed all affected data points, leading to final light curves with 1093 and ~650 data points for sectors 7 and 8, respectively.

The long-cadence light curves show smaller scatter than the short cadence light curves. Figure 6 shows as an example the comparison of the 2-min cadence PDCSAP light curve and the 30-min light curve extracted from the FFIs for PM I09034-0023 (TIC 893123) observed by TESS in Sector 8. Although the two

---

[5] Fortran Version v2.3.01 released: 2011-09-13 by Mathias Zechmeister.
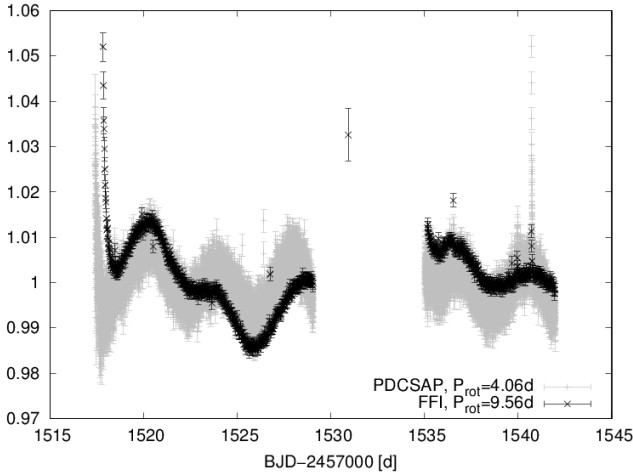
Fig. 6. Comparison of the pipeline-produced PDCSAP light curve of PM I09034-0023 (TIC 893123, gray) and our own photometry (black) extracted from the full frame images. Within the error bars, the two light curves agree with each other, while the scatter is much larger for the light curve with the two-minute cadence. The shape of the light curve is different, however, which results in different estimates of the rotation period.

light curves agree within their error bars, the scatter is much lower in the FFI light curve. For this particular star, the FFI light curve indicates a double-hump shape, in contrast to the single sinusoidal shape in the PDCSAP light curve. Furthermore, the detrending of the strong systematic effects of Sector 8 might introduce artifacts that could cause an incorrect determination of the rotation period. Therefore we applied the period search as explained in the previous section to the long-cadence light curves as well.

4.2.3. Note on the binary star

Our list of the 13 LG11-*Gaia*/eFEDS stars observed with TESS includes the one close visual binary pair from Sect. 3.1. With the large pixel scale of TESS, these stars cannot be resolved individually. Consequently, the automatic pixel masks of the short-cadence data that are centered on the stellar position are slightly offset from each other, resulting in slightly different light curves. For the FFI, we defined the pixel mask ourselves, and we only created one light curve per binary pair.

4.2.4. Outputs of the light-curve analysis

For each target, we obtained six values for the rotation period: three for the long-cadence light curves, and three for the short-cadence light curves. By-eye inspection of the phase-folded light curves determined the best-fitting period. If several methods resulted in a similar value, we computed the average. The standard deviation was used to determine the uncertainties. In addition, we used the formulas given in Gilliland & Fisher (1985) to calculate an error for the rotation period. As the final uncertainty, we adopted the maximum of the standard deviation and the calculated error. We detected rotation periods for five targets from the LG11-*Gaia*/eFEDS sample. By repeating the period search on the residuals of the light curve after subtracting the dominant period, we found that one star shows an additional shorter period. Another star exhibits a double-hump shaped light curve; we discussed this in Sect. 4.2.2. We excluded

these two stars with ambiguous period signal from our quantitative analysis, although we show them in the figures with separate symbols from the reliable sample. To summarize, only 3 of the 13 eFEDS M dwarfs have a reliable period detection, and they represent our LG11-*Gaia*/eFEDS/TESS sample (see Table 1). All of them are validated with the Mann et al. (2015) relations. The most significant period is listed for all five stars in Table 5, and a flag is provided for those that are not considered for the reasons described above.

5. Data analysis for eRASS1

5.1. eROSITA

In principle, the same analysis steps described and carried out for the eFEDS data in Sect. 4.1 can be applied to eRASS data. However, we defer this in-depth study to a future work.

The X-ray parameters used in this work were directly extracted from the eRASS1 catalog. We list in Table 3 the same parameters as for the X-ray detections found in the eFEDS fields for the 673 LG11-*Gaia*/eRASS1 stars. Next to the LG11 name (Col. 1), we provide the X-ray coordinates with their uncertainty (Cols. 2–4), the offset between proper-motion-corrected optical position and the X-ray coordinates (Col. 4), the 0.2–5.0 keV count rate (Col. 5), and the 0.2–5.0 keV detection maximum likelihood (Col. 6).

Because a systematic analysis of spectra and light curves such as that of Sects. 4.1.2 and 4.1.3 is beyond the scope of this work, we used the conversion factor $\langle CF_{eFEDS} \rangle$ derived from the eFEDS data to compute the X-ray fluxes for the eRASS1 detected M dwarfs. X-ray luminosities and L_x/L_{bol} ratios were then determined with the distances and L_{bol} values from Table 2. The L_x and L_x/L_{bol} values are listed in Table 5, together with the same parameters for the eFEDS detections.

5.2. TESS

Analogous to the case of eFEDS (Sect. 4.2), we loaded the list of 673 X-ray detected stars from our LG11-*Gaia*/eRASS1 catalog into MAST to define the sample of stars with TESS data, and we matched it with the target list of TESS using the J2000 coordinates in LG11 with a match radius of 1″. We found that 476 of the LG 11-*Gaia* M dwarfs detected in eRASS1 have been observed with TESS. We recall the all-sky nature of eRASS1, which implies that the M dwarfs from this sample are distributed over all TESS sectors. Of the 476 stars, 125 were observed in multiple sectors. The subset of the LG11-*Gaia*/eRASS1 sample observed with TESS includes three of four comoving binary systems from Sect. 3.2.

For the stars from the LG11-*Gaia*/eRASS1 sample, we examined only the two-minute-cadence TESS data in the way described in Sect. 4.2.1. The adopted values for the rotation periods were determined with the procedure described in Sect. 4.2.4.

We were able to determine rotation periods for 217 stars, but we consider 39 of these periods to be not reliable because the period is longer than half the duration of the observation. The periods of these stars are flagged in Table 5. Through inspection by eye, we found that three more stars show a second period that was not identified as the dominant period with our period-search methods, and an additional three stars have a light curve that looks double-humped like the light curve in the eFEDS sample discussed in Sect. 4.2.2. We removed these six stars from the sample, and we defined this sample as LG11-*Gaia*/eRASS1/TESS for our further analysis. This

sample comprises 172 stars. We note that for completeness, the removed six stars with ambiguous P_{rot} are shown in the figures distinguished with the plotting symbol from the stars from the LG11-*Gaia*/eRASS1/TESS sample. The period with the highest significance is given in Table 5, together with a flag that identifies the stars that were removed from the rotation sample as described above. Taking the calibration range of Mann et al. (2015) into account, we obtained a validated LG11-*Gaia*/eRASS1/TESS of 135 stars.

6. Results and discussion

6.1. eROSITA M dwarf population

We studied the X-ray emission of the M dwarfs from the LG11 catalog with matches in *Gaia* DR2 in two different eROSITA surveys: the eFEDS observation, which covers 142 sq. deg in the southern hemisphere, and the first full all-sky survey, eRASS1. These two eROSITA samples together provide the X-ray luminosities of 687 M dwarfs, which exceeds our previously compiled sample (Magaudda et al. 2020) in size by more than a factor of two, historical samples from RASS by a factor of 7 (NEXXUS; Schmitt & Liefke 2004), and the sample from *Einstein* by a factor of 24 (Fleming et al. 1988).

Thirty objects in the list of 8229 main-sequence M dwarfs provided by LG11 that have a *Gaia* DR2 counterpart are located in the eFEDS fields. This matches the all-sky space density average (30 out of 142 ≈ 8229 out of 41 253 stars per sq.deg) almost exactly. We detected 14 of these 30 M dwarfs, which is nearly 50% of the sample. The average space density of X-ray detected M dwarfs in the eFEDS sample therefore is 14 out of 142 ≈ 0.10 stars per sq. deg.

Our analysis of the eRASS1 catalog has provided the largest sample of X-ray emitting M dwarfs to ate, namely 673 stars, which is a detection rate of 8.3% of our input sample LG11-*Gaia*. The eRASS1 space density of X-ray detected M dwarfs is 673 out of 20 626 ≈ 0.033 stars per sq.deg (considering half of the sky comprised in our version of the eRASS1 catalog). This is lower by a factor three than for eFEDS, which can be explained by the shorter exposure time (on average) during the all-sky survey.

The typical eFEDS exposure time is ~1 ksec per sky position. The exposure time, and therefore the flux limit, during eRASS strongly depends on the sky position and is therefore not a universal value for a sample distributed over the sky. We can, however, give a rough value of $f_{lim,eRASS1} \sim 3 \times 10^{-14}\,erg\,cm^{-2}\,s^{-1}$. At this value, the distribution of fluxes detected for our M dwarfs drops steeply, and the flux of only ~2% of the detections is lower than this. Defining the flux limit in the same way as for eRASS1 (i.e., as that value f_x that is exceeded by 98% of the stars in the sample), we find $f_{lim,eFEDS} \sim 2 \times 10^{-14}\,erg\,cm^{-2}\,s^{-1}$, which is slightly deeper than that of eRASS1. We therefore conclude that the eFEDS and eRASS1 detection statistics are qualitatively consistent with each other. A more detailed comparison, however, is prohibited by the low number statistics in the eFEDS fields.

6.2. Mass-dependence of activity and rotation

Both activity and rotation are known to depend on stellar mass. While a detailed investigation of the rotation-mass relation has come within reach with the *Kepler* mission, statistical samples for X-ray to mass studies within a spectral subclass have not been available so far. In Fig. 7 we show X-ray activity diagnostics and

rotation periods versus stellar mass, that is, $L_x - M_\star$ (left panel), $L_x/L_{bol} - M_\star$ (right panel), and $P_{rot} - M_\star$ (bottom panel) for M dwarfs. For the X-ray to mass relations, we considered the LG11-*Gaia*/eFEDS and LG11-*Gaia*/eRASS1 samples, while for the $P_{rot} - M_\star$ relation, we show the X-ray detected M dwarfs with rotation period, that is, the LG11-*Gaia*/eFEDS/TESS and LG11-*Gaia*/eRASS1/TESS samples and the stars with two periods (green symbols) that are not considered in our quantitative analysis. We include in all panels data from Magaudda et al. (2020) (in gray), which comprise new *XMM-Newton*, *Chandra*, and K2 mission observations and a collection of results from the literature that we updated in Magaudda et al. (2020).

The X-ray luminosities from Magaudda et al. (2020) were extracted in the ROSAT energy band (0.1−2.4 keV). As explained in Sect. 4.1.2, our use of a different energy band for the eROSITA data (0.2−5.0 keV) does not bias the results. Magaudda et al. (2020) extracted distances from *Gaia*-DR2 parallaxes (Gaia Collaboration 2016, 2018a) and validated them using Lindegren et al. (2018) and our own quality criteria. To be consistent with the LG11-*Gaia*/eROSITA samples, we retrieved *Gaia* distances from BJ18, and for Fig. 7 and the subsequent analysis in Sect. 6.3, we cleaned the sample from Magaudda et al. (2020) by removing all stars that lack *Gaia* photometry and/or distance and the nine upper limits presented in the original sample. To calculate the stellar parameters, we followed the recipes described in Sect. 3. Moreover, we identified and removed 13 stars with $M_G < 5$ mag. These updates are motivated by a comparison of masses and spectral types analogous to the one carried out for the LG11 catalog in Sect. 3. With these restrictions, the sample from Magaudda et al. (2020, henceforth referred to as *Gaia*-Magaudda2020) includes 259 stars with $0.15 \leq M_\star/M_\odot \leq 0.85$.

In Fig. 7 we consider the full mass range obtained from the M_{Ks} values of the stars, but strictly speaking, masses above $0.7\,M_\odot$ are not validated because the M_{Ks} values of these stars are beyond the calibrated range of the relation from Mann et al. (2015). We decided to show the full mass range because there is no obvious qualitative change in the $L_x - M_\star$ relation at this boundary, and we take this as a justification to extrapolate the underlying $M_\star - M_{Ks}$ relation.

Figure 7 shows that for a given stellar mass, we observe a spread of 2−3 orders of magnitude in the X-ray activity level, except for the lowest ($M_\star \lesssim 0.3\,M_\odot$) and highest masses ($M_\star \gtrsim 0.7\,M_\odot$), where the spread is smaller. At the low-mass end, only the upper part of the L_x values is clearly detectable in our flux-limited eROSITA observations, while the high-mass end corresponds to the transition to spectral type K, which is not fully sampled in the LG11 catalog. We calculated the median and standard deviation in mass bins of $\Delta M_\star = 0.1\,M_\odot$ for the combined M dwarf sample from the literature and from this eROSITA study. The resulting values are overlaid on the data in red for the validated mass range. In the intermediate-mass range, which is best sampled by our catalog, the standard deviation is ~0.73 for L_x and ~0.75 for L_x/L_{bol}, in logarithmic scale. We fit the two X-ray to mass relations for the combined literature and eROSITA sample with a linear function in log-log space, finding a slope of $+2.84 \pm 0.25$ for $L_x - M_\star$ and -0.10 ± 0.10 for $L_x/L_{bol} - M_\star$. The best-fit relations are given in Table 6, and we display the fits in Fig. 7. Interestingly, the historical study of M dwarfs by Fleming et al. (1988) on a very limited sample (~30 field M stars with $0.15 \leq M_\star/M_\odot \leq 0.6$) reported a similar slope to ours for the $L_x - M_\star$ relation within the uncertainty. The numbers for the average X-ray activity level across all masses in the M dwarf regime must be considered an upper limit because even
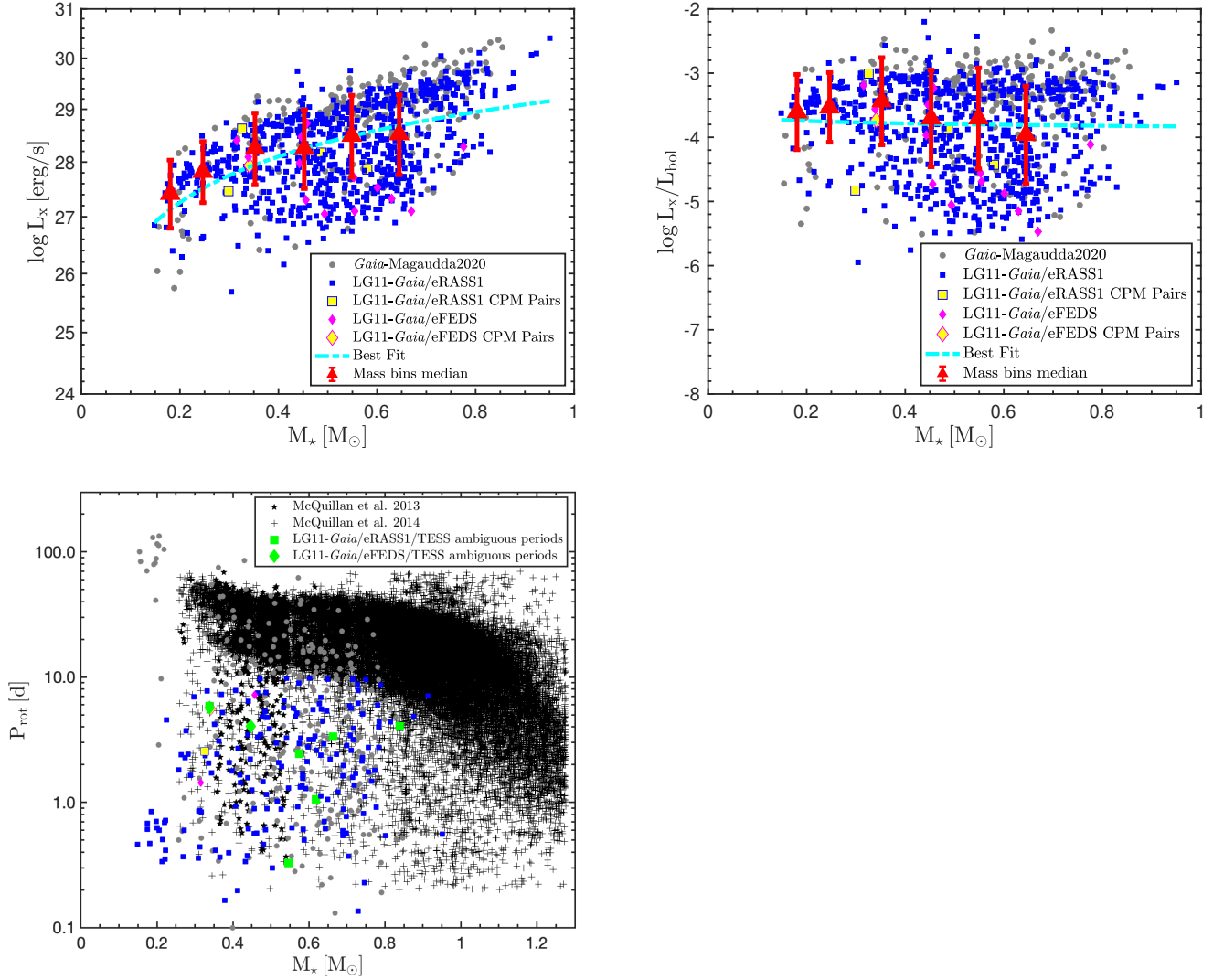
Fig. 7. X-ray activity and rotation vs. mass: blue and pink show the eRASS1 and eFEDS M dwarf samples, respectively, and gray shows the revised sample from Magaudda et al. (2020); see the legend inside the panels for other literature data and highlighted specific subsamples. In the *top panels*, the median and the standard deviation of the data are presented in red for bins with a width of 0.1 $M_\odot$. *Top left*: X-ray luminosity vs. mass and best fit (cyan). *Top right*: X-ray over bolometric luminosity vs. mass and best fit (cyan). *Bottom left*: rotation period vs mass; for the stars with double-humped TESS light curves, the shorter of the two periods is shown.

in a volume of 10 pc around the Sun, ~40% of the M dwarfs are still undetected in X-rays (Stelzer et al. 2013). We show the X-ray activity level for $M_\star = 0.5\,M_\odot$ in Cols. 3 and 5 in Table 6. We defer a more detailed discussion and comparison to literature studies to Sect. 6.3.

In the bottom panel of Fig. 7, we inspect the $P_{rot} - M_\star$ relation of our samples in comparison to data from McQuillan et al. (2013), which cover the mass range of $0.3-0.55\,M_\odot$ with selection criteria based on T_{eff} and $\log g$ values from the *Kepler* input catalog, and McQuillan et al. (2014), which is the extension of that study to all stars with $T_{eff} < 6500\,$K. The rotation periods of the sample from Magaudda et al. (2020) were extracted from light curves of the K2 mission, the MEarth project, and ground-based observations, and they cover a broad range of values from 0.1 d to ~100 d. As explained by McQuillan et al. (2014) and Stelzer et al. (2016), the $P_{rot} - M_\star$ relation shows a bimodal period distribution for lower masses and an upper envelope of the period distribution that increases for decreasing masses. Similar results were found, for instance, by West et al. (2015) and

Newton et al. (2017) by studying the chromospheric activity of M dwarfs through their Hα emission. They observed higher P_{rot} for lower-mass stars ($M_\star \leq 0.25\,M_\odot$), which also appear to be less active than the more rapidly rotating and more massive stars. In particular, Newton et al. (2017) proposed a mass-dependent rotational period threshold for the ignition of the Hα emission. Furthermore, they argued that the paucity of mid- to late-M dwarfs with intermediate rotation periods in their sample is probably caused by a period range over which stars quickly lose angular momentum. The boundary between active and inactive M stars coincides with the rotation period at which the rapid evolution phase ceases, suggesting that the Hα emission and M dwarfs with intermediate P_{rot} are connected. In the data compiled by Magaudda et al. (2020) (gray in Fig. 7), we encountered the same paucity of M stars in the intermediate P_{rot} regime at the lowest masses, and we confirm the upward trend for stars with the longest periods and lowest masses.

The periods in our eROSITA and TESS samples are biased because TESS stares at a given field for only about a month, and

Table 6. Results obtained from fitting $L_x - M_\star$ and $L/L_{bol} - M_\star$ for the full sample (LG11-*Gaia*-eFEDS, LG11-*Gaia*-eRASS1 and *Gaia*-Magaudda20) and for the saturated subsamples, i.e., stars with $P_{rot} \leq P_{sat}$; see Sects. 6.2 and 6.3 for details.

Sample	$\beta_{L_x - M_\star}$	$\log(L_x)$ $(M_\star = 0.5\,M_\odot)$ [erg s^{-1}]	$\beta_{L_x/L_{bol} - M_\star}$	$\log\left(\frac{L_x}{L_{bol}}\right)$ $(M_\star = 0.5\,M_\odot)$
Full	$+2.84 \pm 0.25$	28.37 ± 0.07	-0.10 ± 0.10	-3.79 ± 0.03
Saturated	$+3.10 \pm 0.27$	28.89 ± 0.08	$+0.36 \pm 0.25$	-3.24 ± 0.08

Notes. We show the slopes for the $L_x - M_\star$ and $L_x/L_{bol} - M_\star$ relations (Cols. 2 and 4), and in Cols. 3 and 5, the L_x-, L_x/L_{bol} level refers to the mass distribution center ($M_\star = 0.5\,M_\odot$).
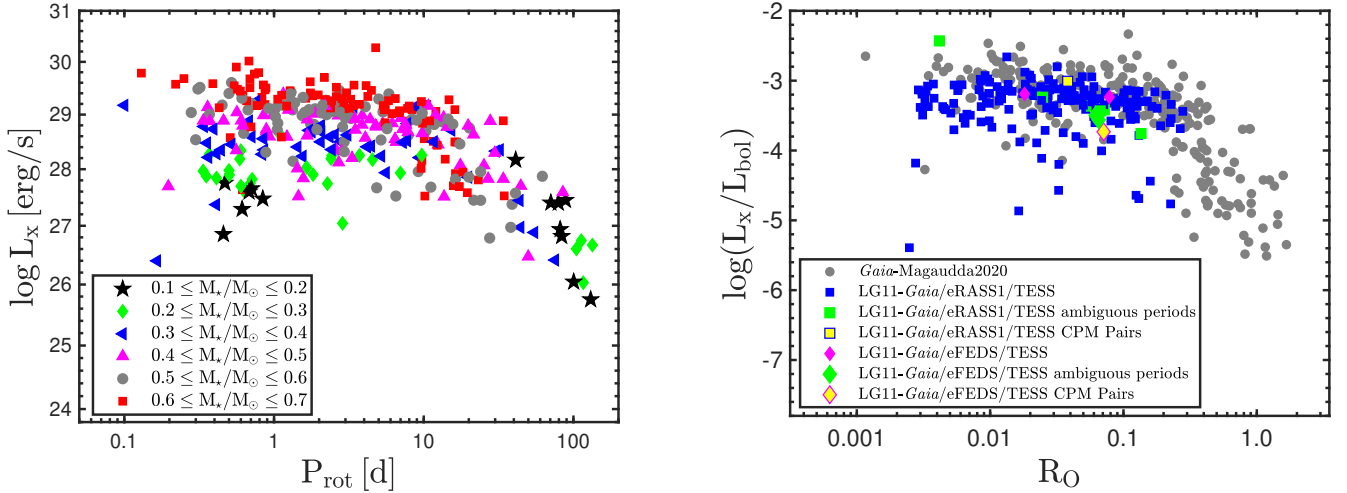
Fig. 8. X-ray activity-rotation relations. *Left*: X-ray luminosity vs rotation period with mass-color code in steps of $0.1\,M_\odot$. *Right*: X-ray luminosity as a fraction of bolometric luminosity vs. Rossby number. See the legend, the caption of Fig. 7, and the text in Sect. 6.3 for the subsamples we display.

we considered periods longer than about half the duration of a sector light curve to be unreliable. The eROSITA/TESS sample of LG11-*Gaia* stars is therefore located in the range of fast rotators, which is a sparsely populated region in unbiased surveys for stellar rotation periods. Interestingly, TESS covers this regime entirely, that is, up to the transition (at $P_{rot} \sim 10\,d$) at which the bulk of the M dwarfs are situated. With eRASS1, we added some very low-mass stars with fast rotation to the $P_{rot} - M_\star$ relation, showing that the lowest-mass stars span the widest range of periods, and that the vast majority of rotation rates in between the extremes have not yet been covered by X-ray observations for this mass range.

6.3. Rotation-activity relation

In the previous section, we showed that with the new eROSITA/TESS sample, we can study the regime up to $P_{rot} \sim 10\,d$, which corresponds to the saturated regime in the rotation-activity relation. Here, we present the X-ray activity-rotation relation we constructed with the results obtained from eROSITA and TESS observations of the validated LG11-*Gaia* sample, combined with the stars of the sample from Magaudda et al. (2020), revised as described in Sect. 6.2, which we also restricted to the stars with M_{Ks} in the calibration range of Mann et al. (2015). This validated *Gaia*-Magaudda20 sample contains 197 M dwarfs. The plots of X-ray activity versus rotation diagnostics are shown in Fig. 8.

Sections 4.2.4 and 5.2 showed that 489 out of 687 LG11-*Gaia*/eFEDS and LG11-*Gaia*/eRASS1 stars are detected

eROSITA X-ray detection and are also observed by TESS observations. The sub-sample with reliable TESS rotation period consist of 3 and 135 stars for eFEDS and eRASS1, respectively. The new eROSITA/TESS data therefore nearly double the sample that was previously available for studies of the X-ray activity-rotation relation.

Previous studies (Pizzolato et al. 2003; Wright et al. 2011, 2018; Wright & Drake 2016; Magaudda et al. 2020) revealed two different regimes of the rotation-activity relation: a saturated regime for fast-rotating stars with $P_{rot} \leq 10\,d$, and an unsaturated regime for slowly rotating stars with $P_{rot} > 10\,d$. These two regimes are clearly present in Fig. 8, but the new eROSITA/TESS samples cover only the saturated part. In the left panel, we present the activity-rotation relation with a color-mass code in bins of $0.1\,M_\odot$. In the saturated regime, a systematic decrease in average X-ray luminosity with decreasing stellar mass is evident, reflecting the trend that is seen in the direct $L_x - M_\star$ relation for the full sample, which is displayed in Fig. 7. A further investigation of the X-ray activity level in the saturated regime through fitting the data in X-ray to rotation space and a consideration of the sample biases will be presented by Magaudda et al. (in prep.).

In the right panel of Fig. 8, we use the same color-code as in Fig. 7 to distinguish the various samples used in this work for the rotation-activity relation in terms of the X-ray fractional luminosity (L_x/L_{bol}) versus Rossby number (R_O). The Rossby number is defined as the ratio of the rotation period and the convective turnover time (τ_{conv}), which is not a directly observable parameter. Here as well as in Magaudda et al. (2020), we adopted the
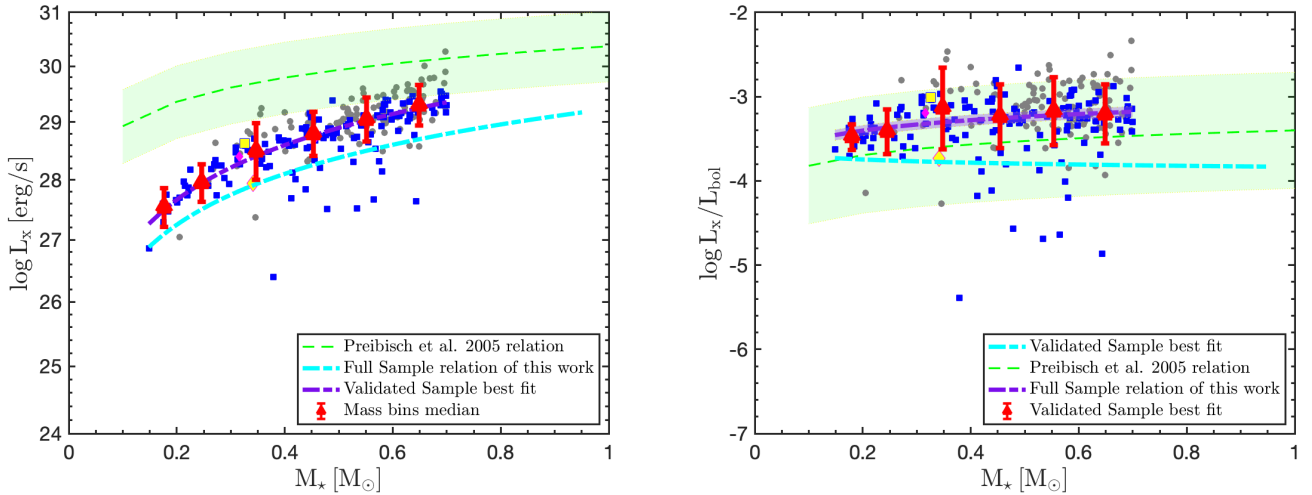
Fig. 9. X-ray activity vs mass for the validated samples (see legend in Figs. 7 and 8) restricted to the saturated stars, i.e., stars with $P_{\rm rot} \leq 8.5$ d, best fit (violet) and median plus standard deviation of the data (red) in bins of 0.1 $M_\odot$. The fit to the young stars in the Orion Nebular cluster provided by Preibisch et al. (2005) is also shown, together with the standard deviation of this fit (green) and the best fit we found for the full M dwarf sample presented in the top panels of Fig. 7 (cyan). *Left*: X-ray luminosity vs. mass. *Right*: X-ray over bolometric luminosity vs. mass.

empirical calibration of $\tau_{\rm conv}$ with $V - K_s$ magnitude provided by Wright et al. (2018). The Rossby numbers obtained from the TESS rotation period values are provided in Table 5. The right panel of Fig. 8 shows that switching from the $L_{\rm x} - P_{\rm rot}$ space to the $L_{\rm x}/L_{\rm bol} - R_{\rm O}$ space, the rotation-activity relation changes its structure. For the eROSITA/TESS samples, the most relevant difference between the two diagrams is the decrease in vertical spread in the saturated regime when the X-ray luminosity is normalized by the bolometric luminosity.

We can use the unprecedented statistics in the saturated regime to examine the mass dependence of the X-ray emission of fast rotators within the M spectral class. Fast rotators represent the younger population of M dwarfs (age < 1 Gyr, according to Magaudda et al.) for partially convective stars, and up to ~4 Gyr for stars with $M_\star < 0.4\,M_\odot$. To this end, we defined a subsample of M dwarfs by combining our new data and the revised validated *Gaia*-Magaudda20 sample that we limited to stars with detected rotation period that fulfill the criterion $P_{\rm rot} < P_{\rm sat} = 8.5$ d. Here $P_{\rm sat}$ is the period at the transition from the saturated to the unsaturated regime. Our adopted value for $P_{\rm sat}$ is the one from Magaudda et al. (2020) in their full M dwarf sample. Figure 8 shows that with this choice, we avoid including unsaturated stars.

The distributions of X-ray activity versus stellar mass for this fast-rotator sample are shown in Fig. 9. As in Fig. 7, we also display the median and standard deviation of the data in bins with a width of 0.1 $M_\odot$. The linear fit obtained for these stars (blue) yields a slope of 3.10 ± 0.27 for $L_{\rm x}$ and 0.36 ± 0.25 for $L_{\rm x}/L_{\rm bol}$ (see Table 6). For comparison, we insert in Fig. 9 the fits obtained in Sect. 6.1 for our full sample and the result of Preibisch & Feigelson (2005), who performed the same type of linear fit, but for the T Tauri stars in the Orion Nebular cluster (ONC) with $M_\star < 2\,M_\odot$.

First, we can observe that the exclusion of unsaturated stars barely changes the slope of the $L_{\rm x} - M_\star$ relation, but it converts the marginally negative slope in $L_{\rm x}/L_{\rm bol} - M_\star$ space into a marginally positive one. The dedicated studies of slowly rotating fully convective stars by Wright & Drake (2016); Wright et al. (2018) reported that the unsaturated regime is dominated by the more massive M dwarfs, which have shorter spin-down timescales, however. In the center of our mass distribution ($\approx 0.5\,M_\odot$), the X-ray / mass relation for the saturated subsample

is shifted by ~0.5 dex to higher activity levels than in the full sample. Because the full sample is likely still incomplete and includes the saturated subsample, this poses only a lower limit to the change in X-ray emission level between <1 Gyr and several Gyr old M dwarfs.

The slope of $L_{\rm x} - M_\star$ we derived for our field M dwarfs is significantly higher than the one for the ONC from Preibisch et al. (2005) ($\beta_{\rm ONC} = 1.44 \pm 0.10$). The X-ray luminosities of the Orion sample are shifted upward with respect to the field dwarfs because of the young age of the ONC. The decrease in $L_{\rm x} - M_\star$ relation between the ONC and our saturated subsample encodes the evolution between 1 Myr and $\lesssim 1$ Gyr, which is ~2.0 dex in logarithmic space for the low-mass end (~0.15 $M_\odot$) and ~0.8 dex at the high-mass end (0.7 $M_\odot$). In terms of normalized X-ray luminosity, our two M dwarf distributions are within the uncertainty of the $L_{\rm x}/L_{\rm bol} - M_\star$ relation of the ONC. Remarkably, our saturated sample, which spans the same range of periods as the ONC (e.g., Choi & Herbst 1996; Rodríguez-Ledesma et al. 2009), is located in the upper half of the ONC distribution, which means that the $L_{\rm x}/L_{\rm bol}$ levels of fast-rotating field M dwarfs are at least as high as thos of pre-main-sequence stars. As noted by Preibisch et al. (2005), this apparently reduced activity level for the pre-main-sequence stars arises because the ONC sample includes accreting stars, which have lower X-ray luminosities than nonaccretors.

6.4. Relation of coronal temperature to luminosity

In Fig. 10 we show the eFEDS M dwarfs whose X-ray temperature and luminosity were determined from the spectral analysis (see Table 4) in a scatter plot. As we explained in Sect. 4.1, we excluded the two stars with d.o.f. ≤ 5 because the statistics of their spectra is poor. For comparison, we also show the results from Johnstone & Güdel (2015) for a sample of GKM stars collected by these authors from the literature and the recent *XMM-Newton* measurement for the planet host star GJ 357 from Modirrousta-Galian et al. (2020). Star GJ 357 is a representative of the faintest and coolest M dwarf coronae studied so far.

The stars from the Johnstone & Güdel (2015) sample are among the most well-known dwarf stars in the solar neighborhood, and for some of them, the stellar parameters have been
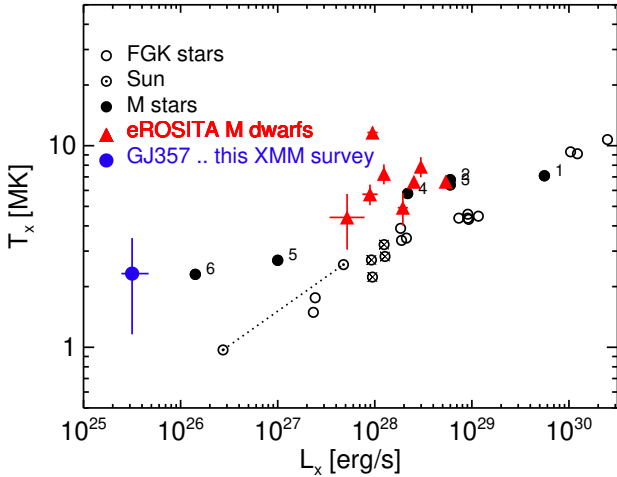
Fig. 10. Coronal temperature vs. X-ray luminosity for M dwarfs with eROSITA spectra (red circles), compared to FGKM stars from Johnstone & Güdel (2015) (black circles) for which according to our updated analysis there are six M dwarfs (filled circles and individually labeled: 1 – AU Mic, 2 – EV Lac, 3 – AD Leo, 4 – YZ CMi, 5 – Prox Cen, and 6 – SCR 1845). Stars labeled low-mass ($M_\star \leq 0.65\,M_\odot$) in Johnstone & Güdel (2015) but which have SpT K are marked with a cross. At the faint and cool end lies the planet-hosting M dwarf GJ 357 from Modirrousta-Galian et al. (2020) (blue circle).

determined very precisely in dedicated studies. However, for the sake of homogeneity, we selected the M dwarfs from their sample with the same procedure, explained in Sect. 3, as we applied to the full LG11 catalog. Specifically, we computed the SpTs from $G_{BP} - G_{RP}$ (see Sect. 3 and footnote 1). This provided six M dwarfs, the same as are given M spectral type in SIMBAD. We note in passing that all of them except SCR J1845-6357 (henceforth SCR1845) lie within the validation range of the Mann et al. (2015) relations. According to the literature, SCR J1845-6357 is a late-M dwarf (SpT M8.5; Robrade et al. 2010), and its M_{Ks} value is slightly higher than the upper boundary of the range calibrated by Mann et al. (2015). The six stars we selected have $M_\star \lesssim 0.7\,M_\odot$ according to the Mann et al. (2015) relation. These stars are highlighted as filled black circles in Fig. 10. Their X-ray properties are adopted from Johnstone & Güdel (2015), except for the X-ray luminosity of Prox Cen, for which we used the value from Ribas et al. (2016), $\log L_x\,[\mathrm{erg\,s^{-1}}] = 27$.

The six M dwarfs from Johnstone & Güdel (2015) alone delineate a rather well-defined correlation between T_x and L_x, and GJ 357 is roughly consistent with an extension of this relation at the faint and cool end. We note that Johnstone & Güdel (2015) have distinguished stars in two mass bins, above and below $M_\star = 0.65\,M_\odot$. They determined the stellar masses from $B - V$ colors using the evolutionary models of An et al. (2007). In this way, they included four more stars in their low-mass group with respect to the six we selected. In Fig. 10 these stars are found among the open circles, where they are marked with a cross. These stars have SpT early-K, and they are displaced downward with respect to the M dwarfs.

The eROSITA sample comprises a narrow range of X-ray luminosities that is limited by the sensitivity of the eFEDS observation. However, in contrast to the literature sample, the stars from eFEDS display a significant spread in terms of T_x. As explained in Sect. 4.1.2, the X-ray luminosities of the eFEDS stars are insensitive to variations in the energy band within the typical range of ROSAT and eROSITA data. The mean upward

shift of the eFEDS sample is therefore unlikely to be the result of an observational bias. Moreover, scatter is seen within the eFEDS sample itself, which has been analyzed in a homogeneous way. We caution, however, that the star with the highest T_x value is the only one from the eFEDS sample that was analyzed with a 1-T spectral model, and it presents evidence for variability in its light curve (see Appendix D).

A larger database of homogeneous coronal temperature measurements for M dwarfs is needed to explore the $T_x - L_x$ relation, and in particular, its spread and a possible influence of flares. The eRASS represents a such valuable database. While a detailed spectral analysis of hundreds of M dwarfs detected in eRASS will be presented in a later work, here we use hardness ratios (HR) as a proxy for the coronal temperature.

6.5. eROSITA hardness ratios

The analysis of hardness ratios does not involve the stellar parameters. Based on the argument put forth in Sect. 6.1, we therefore also consider the stars outside the validation range of the Mann et al. (2015) relations.

We used the three energy bands provided by the eRASS1 catalog, the soft ($0.2-0.6\,\mathrm{keV}$), medium ($0.6-2.3\,\mathrm{keV}$), and hard ($2.3-5.0\,\mathrm{keV}$) band, to define hardness ratios as follows:

$$\mathrm{HR_1} = \frac{\mathrm{Rate}_m - \mathrm{Rate}_s}{\mathrm{Rate}_m + \mathrm{Rate}_s} \tag{3}$$

$$\mathrm{HR_2} = \frac{\mathrm{Rate}_h - \mathrm{Rate}_m}{\mathrm{Rate}_h + \mathrm{Rate}_m}, \tag{4}$$

where $\mathrm{HR_1}$ is the count rate ratio of the medium and soft energy bands, while $\mathrm{HR_2}$ is calculated between the hard and the medium energy bands. The two hardness ratios are given for the eROSITA -detected stars in Table 5.

In Fig. 11 we show the scatter plot of $\mathrm{HR_2}$ versus $\mathrm{HR_1}$ for the LG11-*Gaia*/eRASS1 and the LG11-*Gaia*/eFEDS sample. A large fraction of the stars ($\sim 60\%$) have no counts in the hard energy band ($\mathrm{HR_2} = -1$), and most of them are clustered at $0.2 \leq \mathrm{HR_1} \leq 0.6$ ($\sim 65\%$ of the total sample). This range of $\mathrm{HR_1}$ includes all but two stars for which we analyzed the eFEDS spectra. We thus can conclude that moderately positive values of $\mathrm{HR_1}$ are associated with soft plasma of $\lesssim 0.5\,\mathrm{keV}$. According to Foster et al. (2022), this range of $\mathrm{HR_1}$ values corresponds to plasma of $0.2...0.35\,\mathrm{keV}$. We caution, however, that their analysis is based on a 1-T model, while our sample shows that two temperatures are required to adequately describe the eROSITA spectra of M dwarfs. Therefore, the calibration between $\mathrm{HR_1}$ and kT from Foster et al. (2022) may not be applicable to our sample.

Concerning $\mathrm{HR_2}$, the curious objects are those that are not at the soft limit, that is, those with $\mathrm{HR_2} > -1$. They can be broadly distinguished into two groups: one is clustered near the $\mathrm{HR_2}$ soft bound and intermediate $\mathrm{HR_1}$ values ($\sim 30\%$ of the whole sample), and the other scattered throughout the parameter space ($\sim 10\%$). The first are likely represented by M dwarfs with a slightly hotter corona than those at $\mathrm{HR_2} = -1$, while for the second group, a plausible hypothesis for their harder spectra is flaring activity. The analysis of all individual eRASS1 light curves in a future study will allow us to further examine this interpretation.

6.6. X-ray variability

We analyzed the eROSITA light curves of 14 M dwarfs detected during eFEDS. While 12 of them did not show any significant variation, 2 showed a likely flare: an event ongoing at
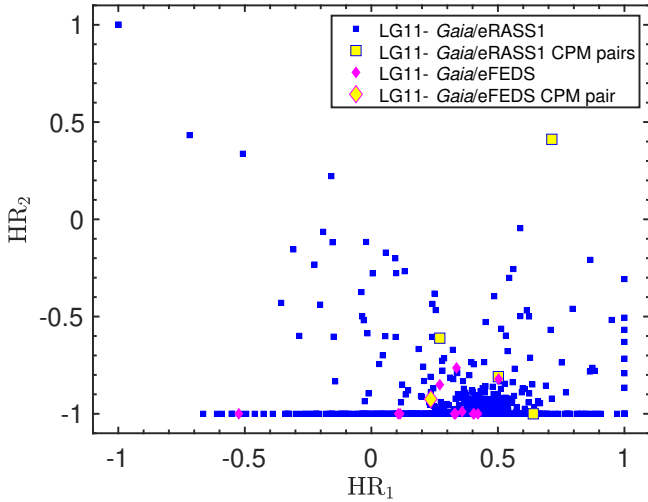
Fig. 11. eROSITA hardness ratios of LG11-*Gaia* M dwarfs detected in eFEDS (filled pink diamonds) and in eRASS1 (filled blue squares); see text in Sect. 6.5 for the definition of the hardness ratios. We show the CPM pairs in eFEDS and in eRASS1 samples in yellow.
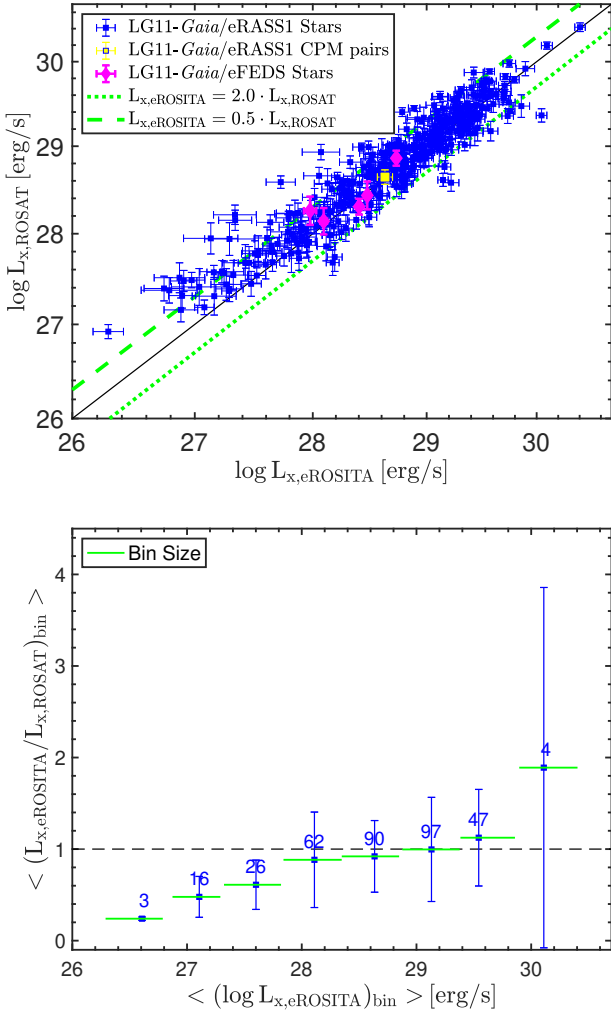

Fig. 12. Comparison between X-ray luminosities observed during eFEDS (log $L_{\rm x,eFEDS}$) and eRASS1 (log $L_{\rm x,eRASS1}$). $L_{\rm x,eRASS1}$ is more than twice higher than $L_{\rm x,eFEDS}$ for the two stars above the dashed red line.

the beginning of the observation for PM I09161+0153, and a smoother longer-lasting variability throughout the detection for PM I09201+0347. These results are also confirmed by the eFEDS variability study performed by Boller et al. (2022). We refer to Sect. 4.1.3 and Appendix D for more details.

An analysis of short-term variability in the much larger eRASS1 sample is beyond the scope of this work. However, we present here a comparison between ROSAT, eFEDS, and eRASS1 X-ray luminosities based on the LG11-*Gaia*/eFEDS and LG11-*Gaia*/eRASS1 samples. This study probes variability on timescales of years. While the ROSAT all-sky survey (RASS) predates the mean eRASS1 epoch by about 29 years (the middles of the surveys were on January 1, 1991, and March 10, 2020, respectively) eFEDS and eRASS1 differ by a few months. eFEDS was carried out between November 4 and November 6, 2019, and eRASS1 started on December 13, 2019, and lasted for six months.

6.6.1. Comparison between eFEDS and eRASS1

We found that six LG11-*Gaia* M dwarfs are detected with eROSITA during eFEDS and eRASS1. We used the $L_{\rm x}$ values calculated in Sects. 4.1 and 5.1 for eFEDS and eRASS1 stars, respectively.

In Fig. 12 we show the comparison between the observed X-ray luminosities during the two different eROSITA epochs. Two stars showed $L_{\rm x}$ higher by a factor of two during eRASS1 than during eFEDS. From the eFEDS light curves in Fig. D.1, we know that PM I09201+0347 was detected during a flare. Therefore, the fact that the star was on average brighter during eRASS1 indicates that likely another, brighter flare occurred during the all-sky survey. A flare during eRASS1 is also a probable explanation for the change in X-ray luminosity of the other star, PM I08551+0132. In a future work, we will examine the X-ray variability of M dwarfs during eRASS in detail.

6.6.2. Comparison between eROSITA and ROSAT

For the comparison on longer (decades) timescales, we cross-matched the LG11-*Gaia*/eFEDS and LG11-*Gaia*/eRASS1 samples with the ROSAT catalogs after correcting their *Gaia*-DR2
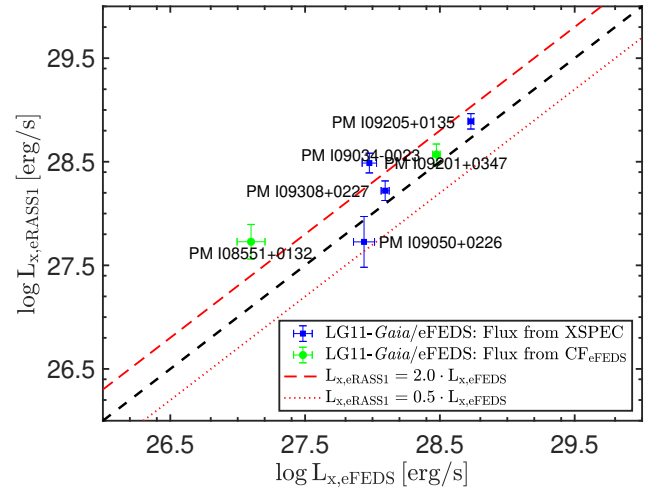
coordinates with the proper motions to the mean RASS epoch (January 1991). Following our conservative approach, we used a search radius of 30″, which is somewhat smaller than the values applied in other works on RASS data (e.g., Neuhaeuser et al. 1995). We found five stars from the LG11-*Gaia*/eFEDS sample and 340 from the LG11-*Gaia*/eRASS1 sample in the Second ROSAT All-Sky Survey Point Source Catalog (2RXS; Boller et al. 2016). We converted the count rates listed in the ROSAT catalogs into flux by adopting the ROSAT conversion factor from Magaudda et al. (2020) (CF = 5.77×10^{-12} erg cm^{-2} cnt^{-1}). From the fluxes and distances, we then computed the X-ray luminosities observed with ROSAT (log $L_{\rm x,ROSAT}$), which refer to the 0.1−2.4 keV energy band. These values are presented in Table 5.

In Fig. 13 we show the comparison between $L_{\rm x,eROSITA}$ and $L_{\rm x,ROSAT}$. We note again that this comparison is not affected by the different energy bands used for data from the two instruments. We find that 12 stars have $L_{\rm x,eROSITA} > 2 \cdot L_{\rm x,ROSAT}$ and 53 stars have $L_{\rm x,eROSITA} < 0.5 \cdot L_{\rm x,ROSAT}$. All these variations are significant, that is, the error bars do not reach to the 1:1 line. It is striking that the X-ray luminosities in Fig. 13 are distributed symmetrically around the 1:1 line for log $L_{\rm x}$ [erg s^{-1}] ≥ 28, but the distribution shows an upward curvature for lower luminosities. eROSITA has a higher sensitivity than the RASS. The flux limit of eRASS1 is a factor 2−10 fainter than that of the 2 RXS catalog; see values given by Boller et al. (2016) and Predehl et al. (2021). Therefore, the stars at the eROSITA detection limit are expected to be undetected during RASS, unless they were in a higher activity state (e.g., a flare) during the ROSAT survey. This is a likely explanation for the observation that at the faint end the ROSAT luminosities are higher than those measured by eROSITA.

In order to quantify the systematic deviation between the brightness seen in eROSITA and RASS for low-luminosity sources, we grouped $\log(L_{\rm x,eROSITA})$ with a bin size of 0.5 and calculated the mean of the ratio of the luminosities observed with eROSITA and with ROSAT for each bin, $\langle L_{\rm x,eROSITA}/L_{\rm x,ROSAT}\rangle_{\rm bin}$. In the bottom panel of Fig. 13 we show the result of this statistical test, indicating the bin width (horizontal green lines), the number of stars in each bin (label at the tops of each data point), and the standard deviation of the mean of $L_{\rm x,eROSITA}/L_{\rm x,ROSAT}$ in each bin as error bars. This ratio becomes

Fig. 13. Comparison between the X-ray luminosities from eROSITA (eRASS1 and eFEDS) and those from ROSAT (RASS) for the LG11-*Gaia* sample. *Top panel*: scatter plot. CPM pairs are highlighted in yellow. *Bottom panel*: ratio of the eROSITA and ROSAT luminosities in logarithmic bins of width 0.5 in X-ray luminosity, quantifying the systematic trend. Labels at the tops of the data points represent the number of stars in each bin. The vertical bars are the standard deviations, and the horizontal bars denote the bin width.

increasingly lower for lower L_x, and it is significantly lower than one at the faint end. This systematic trend supports our above interpretation as an effect of sensitivity limits combined with intrinsic source variability.

7. Conclusions and outlook

We presented a comprehensive study of the X-ray activity of M dwarfs and its relation with stellar rotation. The careful match of our input target list, the proper motion catalog by Lépine & Gaidos (2011), with *Gaia* DR2 data provides more reliable stellar parameters for these stars than the values used in previous studies on the same argument. Of the ~8300 nearby M dwarfs from this LG11-*Gaia* catalog, ~8% have an X-ray detection in the first eROSITA All-Sky survey, and this X-ray sample is skewed to nearby stars (with a peak in their distance distribution at ~20 pc). A subset of only about 1 out of 4 of the eROSITA-detected M dwarfs have detectable rotation periods in TESS light

curves. We can therefore state that eROSITA X-ray measurements are a much more sensitive diagnostic for magnetic activity than star spot amplitudes measured with TESS.

From an eROSITA survey of the CalPV phase (the so-called eFEDS fields), we derived the first coronal luminosities and temperatures for M dwarfs obtained from eROSITA X-ray spectra. The resulting rate-to-flux conversion factor was the basis for the X-ray luminosities we determined for the faint majority of our sample stars, and the same CF can be used in future eROSITA studies of faint M dwarfs.

We examined the mass dependence of M dwarf X-ray activity on an unprecedentedly large sample, and we quantified its slope ($L_x \sim M_\star^\beta$, $\beta = 2.84 \pm 0.25$), which is considerably steeper than the slope measured for the pre-main-sequence stars from the ONC study of Preibisch et al. (2005) ($\beta_{\rm ONC} = 1.4$), and it is offset toward lower luminosities by a factor that depends on the mass, that is, on the 2.0 logarithmic dex for $M_\star = 0.15\,M_\odot$ and 0.8 dex for $M_\star = 0.65\,M_\odot$. For a given mass, our validated M dwarfs display a spread in L_x of 0.6 decades. The true scatter is likely significantly larger because of the incompleteness of eRASS1 and eFEDS related to the flux limit discussed above.

The most obvious candidate for explaining the broad range of X-ray activity levels for a given M dwarf mass is a distribution of rotation periods (and ensuing dynamo efficiency). Our X-ray selected sample in the validated M dwarf mass range presents periods between 0.10 and 8.35 d, where the upper boundary is mostly produced by the duration of the TESS campaigns (~27 d). The possible influence of the flux limit of eROSITA on the $P_{\rm rot}$ distribution of the sample can be examined in a direct study of the activity-rotation relation. We found that in the saturated regime, which by coincidence reaches roughly up to our period boundary of ~10 d, the eROSITA data comprise some stars with very faint X-ray emission ($\log L_x/L_{\rm bol} \approx -4... - 5$). These are downward outliers in the saturated part of the rotation-activity relation, and their origin needs further investigation. On the basis of their $\log(L_x/L_{\rm bol})$ values, we might conjecture that eRASS can reach into the bulk of the stars in the unsaturated regime of slow rotators, but that facilities capable of providing longer periods must be used to detect their corresponding rotation signal.

With respect to ROSAT, even the first all-sky survey of eROSITA reaches lower X-ray activity levels, as we showed in our direct comparison of RASS and eRASS1 luminosities for the 345 M dwarfs that are detected in both surveys. These stars are about half of the eRASS1 sample. The majority of the other half that is not detected in RASS is near the eRASS1 detection limit (with ML_CTS_0 $\lesssim$ 20). Adding data from the other seven eROSITA surveys will provide access to X-ray detections of more and fainter M dwarfs in the near future.

Similarly, significant quantitative progress can be expected in our understanding of the coronal temperature distribution in M dwarfs, for which no statistical samples are available so far. Our results from the spectral analysis of about a dozen X-ray bright M dwarfs in eFEDS combined with the eROSITA hardness ratios for the full (but mostly faint) X-ray detected sample has shown that at least two-thirds of the eROSITA-detected M dwarfs have typical coronal temperatures of ~0.5 keV (corresponding to ~6 MK). Our analysis of eROSITA/eFEDS spectra also shows that the relation between L_x and T_x of M dwarfs is poorly known so far. The huge number of relatively bright X-ray emitters in eRASS may place new constraints on this, however.

Finally, eROSITA has opened a new window for variability studies of coronal X-ray emission. Our comparison with RASS data has confirmed the evidence from previous much smaller

samples of M dwarfs (e.g., Marino et al. 2000) that large changes of the X-ray luminosity are rare. Specifically, only 17% of our combined eROSITA/RASS sample displays variability by more than a factor of two between the two surveys. Because the most obvious candidates for X-ray variability in M dwarfs are flares, this low-variability amplitude clearly arises from the averaging over survey exposures (typically 6–8 intervals of ~40 s duration each and separated by ~4 h in case of eRASS). About one-third of the 14 M dwarfs detected in the eFEDS have significantly variable eROSITA light curves. Detailed studies of these short-term light curves are required to extract better estimates for the brightness scale of the variations. Moreover, the huge number of these light curves that is available with eROSITA should enable placing limits on the flare frequency of M dwarfs in the X-ray domain for the first time.

References

An, D., Terndrup, D. M., Pinsonneault, M. H., et al. 2007, ApJ, 655, 233
Bailer-Jones, C. A. L., Rybizki, J., Fouesneau, M., Mantelet, G., & Andrae, R. 2018, AJ, 156, 58
Bertin, E., & Arnouts, S. 1996, A&AS, 117, 393
Boller, T., Freyberg, M. J., Trümper, J., et al. 2016, A&A, 588, A103
Boller, T., Schmitt, J. H. M. M., Buchner, J., et al. 2022, A&A, 661, A8 (eROSITA EDR SI)
Broeg, C., Fernández, M., & Neuhäuser, R. 2005, Astron. Nachr., 326, 134
Brunner, H., Liu, T., Lamer, G., et al. 2022, A&A, 661, A1 (eROSITA EDR SI)
Choi, P. I., & Herbst, W. 1996, AJ, 111, 283
Dey, A., Schlegel, D. J., Lang, D., et al. 2019, AJ, 157, 168
Favata, F., Reale, F., Micela, G., et al. 2000, A&A, 353, 987
Feinstein, A. D., Montet, B. T., Foreman-Mackey, D., et al. 2019, PASP, 131, 094502
Fleming, T. A. 1998, ApJ, 504, 461
Fleming, T., & Stone, J. M. 2003, ApJ, 585, 908
Fleming, T. A., Liebert, J., Gioia, I. M., & Maccacaro, T. 1988, ApJ, 331, 958
Foster, G., Poppenhaeger, K., Ilic, N., & Schwope, A. 2022, A&A, 661, A23 (eROSITA EDR SI)
Gaia Collaboration (Prusti, T., et al.) 2016, A&A, 595, A1
Gaia Collaboration (Babusiaux, C., et al.) 2018a, A&A, 616, A10
Gaia Collaboration (Brown, A. G. A., et al.) 2018b, A&A, 616, A1
Gilliland, R. L., & Fisher, R. 1985, PASP, 97, 285
Johnstone, C. P., & Güdel, M. 2015, A&A, 578, A129
Lang, D. 2014, AJ, 147, 108
Lépine, S., & Gaidos, E. 2011, AJ, 142, 138
Lindegren, L., Hernández, J., Bombrun, A., et al. 2018, A&A, 616, A2
Magaudda, E., Stelzer, B., Covey, K. R., et al. 2020, A&A, 638, A20
Maggio, A., Flaccomio, E., Favata, F., et al. 2007, ApJ, 660, 1462
Mann, A. W., Feiden, G. A., Gaidos, E., Boyajian, T., & von Braun, K. 2015, ApJ, 804, 64
Mann, A. W., Feiden, G. A., Gaidos, E., Boyajian, T., & von Braun, K. 2016, ApJ, 819, 87
Marino, A., Micela, G., & Peres, G. 2000, A&A, 353, 177
Matt, S. P., Brun, A. S., Baraffe, I., Bouvier, J., & Chabrier, G. 2015, ApJ, 799, L23
McQuillan, A., Mazeh, T., & Aigrain, S. 2013, ApJ, 775, L11
McQuillan, A., Mazeh, T., & Aigrain, S. 2014, ApJS, 211, 24
Merín, B., Salgado, J., Giordano, F., et al. 2017, ASP Conf. Ser., 512, 495
Modirrousta-Galian, D., Stelzer, B., Magaudda, E., et al. 2020, A&A, 641, A113
Neuhaeuser, R., Sterzik, M. F., Schmitt, J. H. M. M., Wichmann, R., & Krautter, J. 1995, A&A, 297, 391
Newton, E. R., Irwin, J., Charbonneau, D., Berta-Thompson, Z. K., & Dittmann, J. A. 2016, ApJ, 821, L19
Newton, E. R., Irwin, J., Charbonneau, D., et al. 2017, ApJ, 834, 85
Pallavicini, R., Golub, L., Rosner, R., et al. 1981, ApJ, 248, 279
Parker, E. N. 1993, ApJ, 408, 707
Pizzolato, N., Maggio, A., Micela, G., Sciortino, S., & Ventura, P. 2003, A&A, 397, 147
Predehl, P., Andritschke, R., Arefiev, V., et al. 2021, A&A, 647, A1
Preibisch, T., & Feigelson, E. D. 2005, ApJS, 160, 390
Preibisch, T., Kim, Y.-C., Favata, F., et al. 2005, ApJS, 160, 401
Raetz, S., Schmidt, T. O. B., Czesla, S., et al. 2016, MNRAS, 460, 2834
Raetz, S., Stelzer, B., Damasso, M., & Scholz, A. 2020, A&A, 637, A22
Reiners, A., Joshi, N., & Goldman, B. 2012, AJ, 143, 93
Reiners, A., Schüssler, M., & Passegger, V. M. 2014, ApJ, 794, 144
Ribas, I., Bolmont, E., Selsis, F., et al. 2016, A&A, 596, A111
Ricker, G. R., Winn, J. N., Vanderspek, R., et al. 2014, SPIE Conf. Ser., 9143, 914320
Robrade, J., & Schmitt, J. H. M. M. 2005, A&A, 435, 1073
Robrade, J., Poppenhaeger, K., & Schmitt, J. H. M. M. 2010, A&A, 513, A12
Rodríguez-Ledesma, M. V., Mundt, R., & Eislöffel, J. 2009, A&A, 502, 883
Rosen, S. 2016, VizieR Online Data Catalog: IX/47
Rosner, R., Golub, L., & Vaiana, G. S. 1985, ARA&A, 23, 413
Ruiz, A., Corral, A., Mountrichas, G., & Georgantopoulos, I. 2018, A&A, 618, A52
Salvato, M., Buchner, J., Budavári, T., et al. 2018, MNRAS, 473, 4937
Salvato, M., Wolf, J., Dwelly, T., et al. 2022, A&A, 661, A3 (eROSITA EDR SI)
Schmitt, J. H. M. M., & Liefke, C. 2004, A&A, 417, 651
Shu, Y., Koposov, S. E., Evans, N. W., et al. 2019, MNRAS, 489, 4741
Skrutskie, M. F., Cutri, R. M., Stiening, R., et al. 2006, AJ, 131, 1163
Stelzer, B., Marino, A., Micela, G., López-Santiago, J., & Liefke, C. 2013, MNRAS, 431, 2063
Stelzer, B., Damasso, M., Scholz, A., & Matt, S. P. 2016, MNRAS, 463, 1844
Stelzer, B., Klutsch, A., Coffaro, M., Magaudda, E., & Salvato, M. 2022, A&A, 661, A44 (eROSITA EDR SI)
Tarter, J. C., Backus, P. R., Mancinelli, R. L., et al. 2007, Astrobiology, 7, 30
Taylor, M. B. 2005, ASP Conf. Ser., 347, 29
Thompson, S. E., Fraquelli, D., Van Cleve, J. E., & Caldwell, D. A. 2016, Kepler Archive Manual, Kepler Science Document KDMC-10008-006
Tu, L., Johnstone, C. P., Güdel, M., & Lammer, H. 2015, A&A, 577, L3
van den Besselaar, E. J. M., Raassen, A. J. J., Mewe, R., et al. 2003, A&A, 411, 587
Wenger, M., Ochsenbein, F., Egret, D., et al. 2000, A&AS, 143, 9
West, A. A., Weisenburger, K. L., Irwin, J., et al. 2015, ApJ, 812, 3
Wright, N. J., & Drake, J. J. 2016, Nature, 535, 526
Wright, N. J., Drake, J. J., Mamajek, E. E., & Henry, G. W. 2011, ApJ, 743, 48
Wright, N. J., Newton, E. R., Williams, P. K., Drake, J. J., & Yadav, R. K. 2018, MNRAS, 479, 2351
Zechmeister, M., & Kürster, M. 2009, A&A, 496, 577

Appendix A: Identification of *Gaia* DR2 counterparts to the M dwarfs from LG11

We matched the LG11 catalog with the second data release of the *Gaia* mission (*Gaia* DR2, Gaia Collaboration 2018b) using the proper motions (P.M.) given in LG11 to correct the epoch 2000 coordinates provided in the LG11 catalog to the *Gaia* epoch (J2015.5). Then we performed a multicone search with a search radius of 3″ around each target in LG11 with TOPCAT (Taylor 2005). In this step, we found 9638 *Gaia* entries for the 8889 LG11 stars, 736 of which have multiple matches (723 doubles and 13 triples). To identify reliable *Gaia* counterparts and to avoid sources in the search radius that do not belong to our targets (i.e., that are no companions to our targets), we used two additional criteria.

Firstly, we calculated for all *Gaia* entries in our matched catalog the total *Gaia* P.M. by taking the square root of the quadratic sum of the proper motions in right ascension and in declination. Then we computed the difference between the total LG11 proper motion and the total *Gaia* proper motion. The histogram of this proper motion difference shows a Gaussian shape with a sharp edge at ±0.2″/yr when only the stars with a single *Gaia* match are considered. Therefore, we removed all *Gaia* counterparts from the full list that show a proper motion difference outside this range. This criterion reduced our catalog to 8779 entries, 440 of which show multiple *Gaia* matches. During this step, all stars without proper motions given in *Gaia* DR2 were also removed. As a second step, we converted the *Gaia* magnitudes into J-band magnitudes (which we call J_{Gaia}) using the relation given on the ESA webpage[6]. Then we calculated the difference between the Two Micron All-Sky Survey (2MASS; Skrutskie et al. 2006) J-band magnitude listed in the LG11 catalog and J_{Gaia}. Significant differences between these magnitudes can arise when two adjacent *Gaia* sources are not resolved in 2MASS. The two *Gaia* sources often form a common proper motion (CPM) pair. Therefore, to keep in our catalog the CPM pairs with a moderate J-band magnitude difference that are potentially composed of two M stars, we removed all *Gaia* counterparts with $J_{\text{Gaia}} - J > ±2$ mag. After this removal of wrong identifications and faint companions that are not relevant as a potential X-ray source, the catalog contained 8489 entries, 169 of which still show multiple *Gaia* matches. We note that in this step, all *Gaia* counterparts without magnitudes in *Gaia* DR2 were removed as well. The 169 multiple matches were checked through inspection by eye using ESASky[7] (Merín et al. 2017), and 150 of them were found to be comoving pairs.

After the application of our selection criteria, 571 LG11 stars were found to have no *Gaia* counterpart, either because their *Gaia* data are missing or incomplete, that is, no proper motions and/or no magnitudes are available in DR2. These stars were removed during the cleaning process described above. To recover the *Gaia* IDs for the targets with incomplete data, our initial 3″ multicone match was repeated for these 571 stars. We found that 414 of them have *Gaia* matches (but with incomplete photometric and/or astrometric information), and 33 of them have multiple *Gaia* sources in the search radius. The multiple matches were again checked with an inspection by eye, and we found that 30 of them are CPM pairs. As a final check for our match, we used the cross-identification function of the SIMBAD astronomical database (Wenger et al. 2000). We uploaded the list of target names from LG11 and converted them into *Gaia* DR2 SOURCE_ID. The results of our match procedure explained in the previous paragraphs and the output from SIMBAD were compared, and if they were not consistent, an inspection by eye was applied. (SIMBAD does not always provide the correct *Gaia* ID for a given target, which is why we performed the match procedure described above).

As the final result, we found 8917 *Gaia* counterparts for 8736 targets from the LG11 catalog. *Gaia* data are not available for the remaining 153 LG11 targets. The excess of Gaia counterparts represents the 180 stars for which we found common proper motion companions of $|\Delta J| \leq 2$ mag, one of which is a triple system. These objects add to the binary stars that are listed as resolved pairs in the original LG11 catalog (104 binary pairs). Because the CPM companions discovered through our match of the LG11 catalog with *Gaia* DR2 were added to our table, the total number of objects in our target list is 9070 (8917 stars with *Gaia* counterparts, including the CPM companions and 153 stars without a *Gaia* counterpart).

Appendix B: Independent cross-check of the source identification with NWAY

To examine the reliability of our position-based source identification procedure, we took advantage of the catalogs of counterparts for eFEDS and eRASS1 identified within the eROSITA_DE collaboration. For eFEDS, we used the catalog presented by Salvato et al. (2022), where NWAY (Salvato et al. 2018) and ASTROMATCH (Ruiz et al. 2018) algorithms were applied and tested. They found an agreement for 88 % in the counterpart identification, with NWAY having higher completeness and purity (above 96 %). In this catalog, less than 1 % of the sources have a secure counterpart identified only by ASTROMATCH. For this reason, we speak here only of NWAY. For eRASS1, we used a preliminary catalog of counterparts that were obtained with NWAY, ran with the same photometric priors and astrometric setup as for eFEDS. The counterparts were identified using the photometry provided in LS8, where images were calibrated to *Gaia*-DR2 and photometry was obtained in g, r, and z bands from the three individual imaging surveys. In addition, the photometry was forced at the optical positions on unWISE maps for all sources detected in the combined grz image using the TRACTOR algorithm from Lang (2014). For the bright sources, the catalog lists the *Gaia*-DR2 properties.

Appendix B.1: eFEDS

For eFEDS, we checked the counterparts of the 14 X-ray sources that we associated with a LG11-*Gaia* M dwarf. The match with the eFEDS NWAY catalog through the *eROSITA* unique source identification shows that 12 of them have assigned the same *Gaia* counterpart. The other 2 do not have a *Gaia* source ID in the NWAY catalog for eFEDS source counterparts, but a simple cross-match in coordinates indicates a separation of less than ∼ 0.01″ between our counterparts and those listed in Salvato et al. (2022), clearly demonstrating that these are indeed the same sources. The failure to identify the *Gaia* CTP upon construction of the NWAY catalog is due to the high P.M. of these two stars.

---

[6] https://gea.esac.esa.int/archive/documentation/GDR2/Data_processing/chap_cu5pho/sec_cu5pho_calibr/ssec_cu5pho_PhotTransf.html
[7] sky.esa.int

Appendix B.2: eRASS1

For eRASS1, we examined the 842 X-ray sources identified by us with an LG11-*Gaia* star in the first step of our identification procedure (see Sect. 3.2). We recall that our final list LG11-*Gaia*/eRASS1 comprises only 673 stars, a subsample of these 842.

LS8 did not completely cover the eRASS1, and for this reason, the comparison can be made only for 382 sources. Among these 382 eRASS1 sources, 347 are associated in NWAY-LS8 with the same *Gaia*-ID that we found as closest CTP to the eRASS1 source, but 21 out of 347 are not our LG11-*Gaia* stars, and we have disregarded them in our final catalog after the reverse match. Of the remaining 35 eRASS1 sources that are present in NWAY-LS8, five have a nonzero probability according to NWAY-LS8 for more than one optical counterpart to be associated with this *eROSITA* source. For all of them, the LG11-*Gaia* star is one of the possible counterparts. Moreover, NWAY-LS8 assings a different *Gaia* source to 19 objects (i.e., not our closest CTP) as the most likely CTP, and the NWAY-LS8 counterpart for the remainder (11 objects) is not matched to a *Gaia*-DR2 source.

It is important to consider that in the current version of the NWAY-LS8 catalog of the eRASS1 counterparts, no attempt was made to correct the coordinates of the sources for proper motion. This biasing the results specifically against the type of sources that are presented in this paper. Therefore, we investigated the 11 objects without *Gaia*-ID in NWAY-LS8 through visual inspection on ESASky, finding that the LG11-*Gaia* star is indeed the best CTP for all. For example because its P.M. points towards the eRASS1 position or because there is no other optical/NIR bright object nearby. The lack of a CTP in NWAY probably arises because of the high P.M. of the stars.

For the remaining 19 objects to which NWAY associates a different CTP with the eRASS1 source than we did, NWAY-LS8 chose the LG11-*Gaia* star for 11, while we excluded these stars from our final sample based on our reverse match, which showed that they are not the closest CTP to the X-ray position. Another 3 are part of CPM systems for which NWAY-LS8 chose the *Gaia* ID of the companion, and for one, neither the object selected with NWAY nor the LG11-*Gaia* star is the closest CTP to the eRASS1 source. For the 4 remaining eRASS1 sources, we disagree with NWAY-LS8, which does not consider the LG11-*Gaia* M dwarf as the best association, although it is the closest CTP.

To summarize, of the 842 eRASS1 sources with a LG11-*Gaia* star in our 15″ search radius, we were able to compare 382 with NWAY-LS8. NWAY-LS8 disagrees with our results for the counterpart for 1 % of X-ray sources that we associate with a LG11-*Gaia* M dwarf (4 out of 382). On the other hand, according to NWAY-LS8, we incorrectly discarded 3 % of the LG11-*Gaia* stars (11 out of 382) in our reverse match because they are not the closest counterpart to the X-ray position. NWAY-LS8 missed 3 % (11 cases) of the LG11-*Gaia* stars because the input catalog adopted for the identification of the counterpart did not correct the coordinates of the moving sources for proper motion. To conclude, the two methods of source identification agree for 93 % of the objects.

Appendix C: Best-fit spectral model

Fig. C.1 displays the *eROSITA* spectra from the eFEDS observation for the ten brightest M dwarfs in the field, as discussed in Sect. 4.1.2. The best-fitting model from Table 4 is overlaid, and the bottom panels show the residuals between data and model.

Appendix D: eFEDS light curves

Fig. D.1 comprises the *eROSITA* light curves from the eFEDS observation for the 14 detected M dwarfs in these fields. The timing of the data intervals in these light curves is a consequence of the survey mode employed in the data acquisition for the eFEDS fields and is described in Sect. 4.1.3.

PM I08551+0132

PM I09050+0250

PM I090205+0135

PM I08590+0151

PM I090161+0153

PM I090238+0008

PM I09034-0023

PM I090201+0347

PM I090308+0027
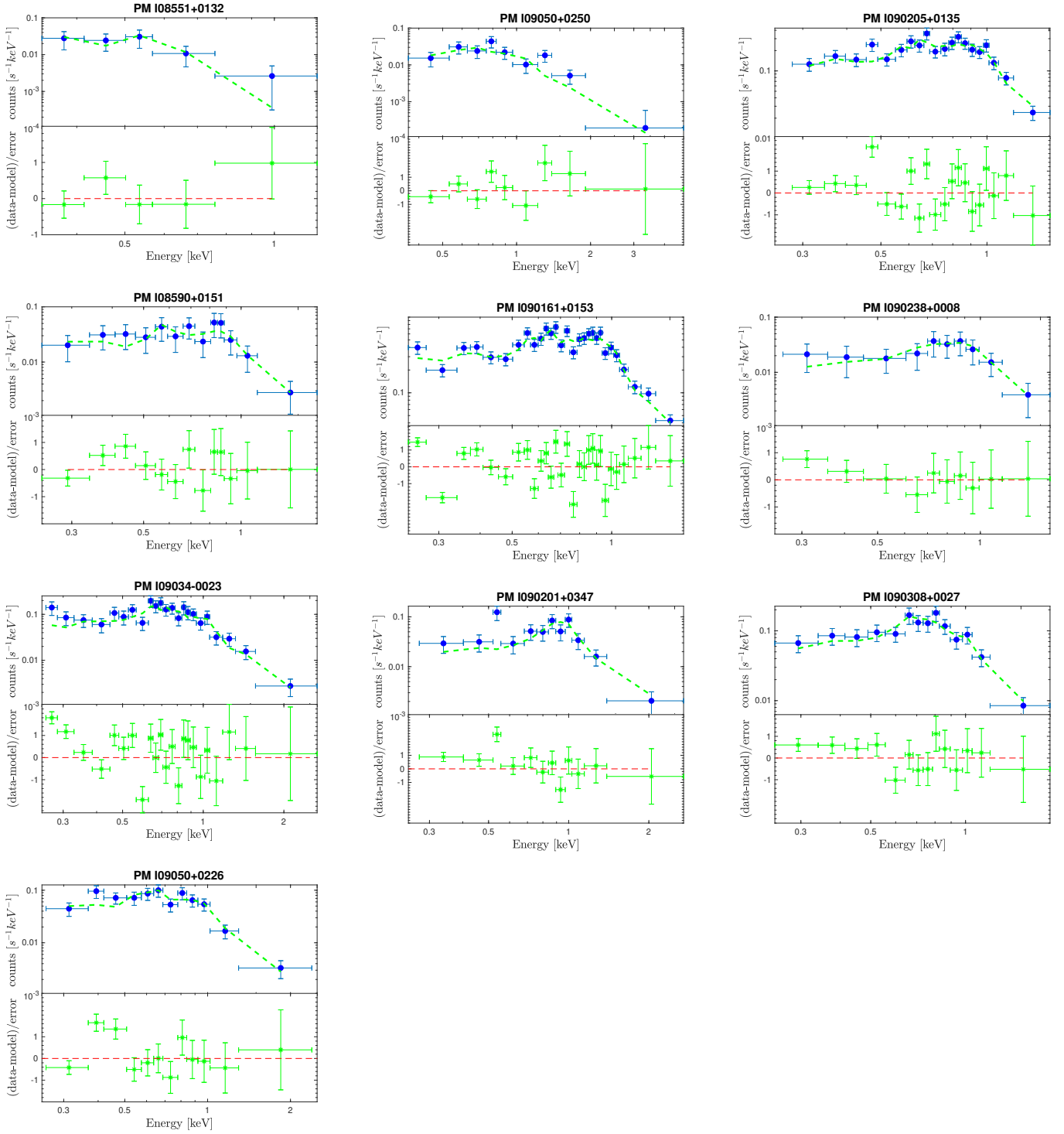
PM I09050+0226

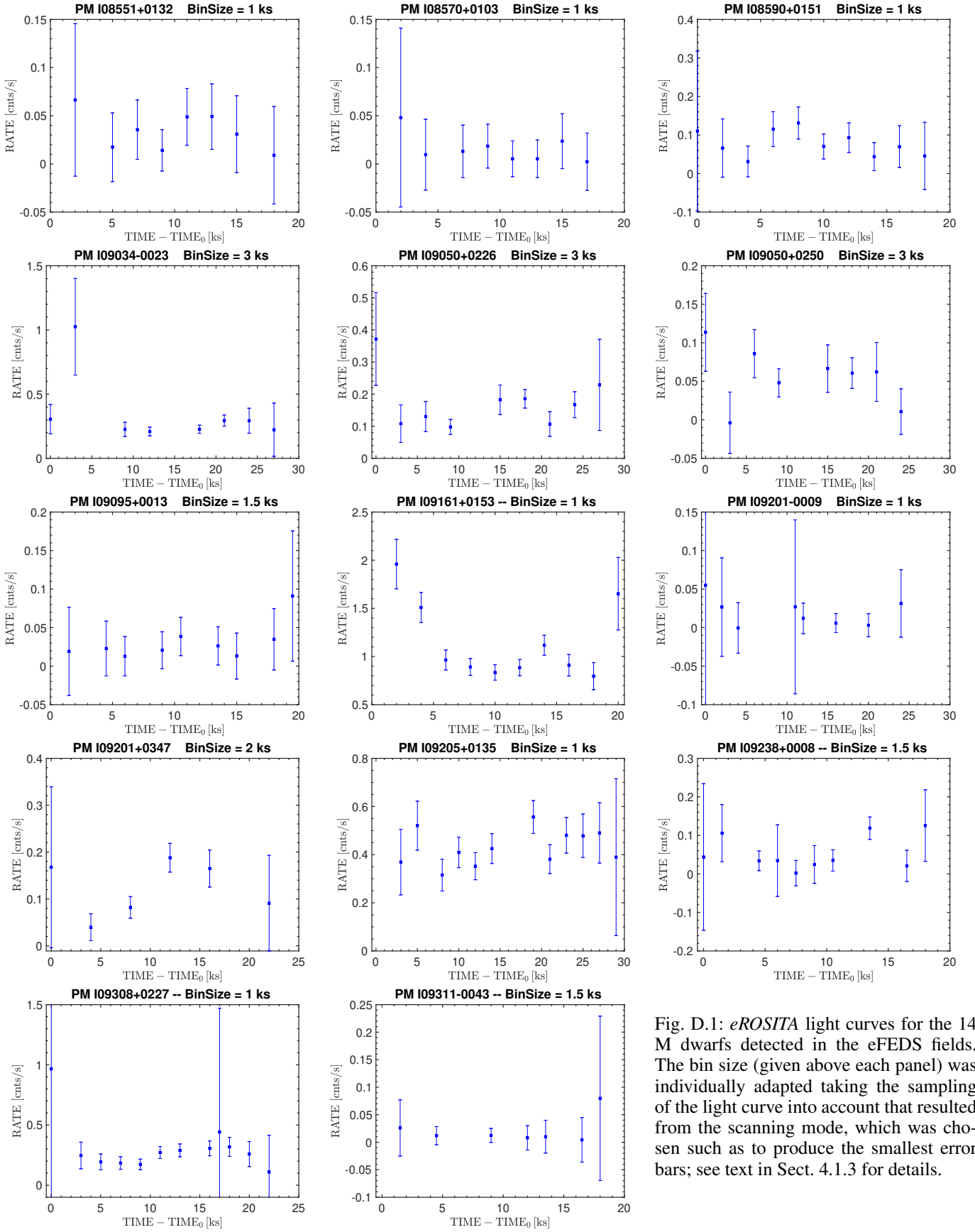Fig. C.1: *eROSITA* spectrum, best-fit thermal model, and residuals for the ten sources in the eFEDS fields with > 30 counts.

Fig. D.1: *eROSITA* light curves for the 14 M dwarfs detected in the eFEDS fields. The bin size (given above each panel) was individually adapted taking the sampling of the light curve into account that resulted from the scanning mode, which was chosen such as to produce the smallest error bars; see text in Sect. 4.1.3 for details.

Astronomische Nachrichten

PROCEEDING

First eROSITA-*TESS* results for M dwarfs: Mass dependence of the X-ray activity rotation relation and an assessment of sensitivity limits

E. Magaudda[1] | **B. Stelzer**[1,2] | **St. Raetz**[1]

[1]Institut für Astronomie und Astrophysik, Eberhard-Karls Universität Tübingen, Tübingen, Germany

[2]INAF—Osservatorio Astronomico di Palermo, Palermo, Italy

Correspondence
E. Magaudda, Institut für Astronomie und Astrophysik, Eberhard-Karls Universität Tübingen, Sand 1, D-72076, Tübingen, Germany.
Email: magaudda@astro.uni-tuebingen.de

Abstract

We present a study of the activity-rotation relation for M dwarf stars, using new X-ray data from the *ROentgen Survey with an Imaging Telescope Array (eROSITA)* on board the Russian Spektrum-Roentgen-Gamma mission (SRG), combined with photometric rotation periods from the *Transiting Exoplanet Survey Satellite (TESS)*. The stars used in this work are selected from the superblink proper motion catalog of nearby M dwarfs. We study the 135 stars with both a detection in the first eROSITA survey (eRASS1) and a rotation period measurement from *TESS* jointly with the sample of 197 superblink M dwarfs re-adapted from our previous work. We fit the activity-rotation relation for stars with rotation periods shorter than ~ 10 d (saturated regime) using three mass bins. The surprising positive slope for stars in our lowest mass bin ($M_\star \leq 0.4 M_\odot$) is due to a paucity of stars with intermediate rotation periods ($\sim 1 - 10$ d), probably caused by fast period evolution. The much higher fraction of eRASS1 detections compared to stars that have also rotation periods from *TESS* shows that eROSITA is also sensitive for slower rotating M dwarfs that are in the unsaturated regime with periods inaccessible to *TESS*.

KEYWORDS

stars: Activity, stars: Late-type, stars: Rotation, stars: X-rays

1 | INTRODUCTION

Solar- and later-type main sequence and giant stars experience magnetic activity in the inner and outer atmosphere. The mechanism that powers and enhances the magnetic field in solar-like stars is known to be an $\alpha\Omega$-dynamo, that is, it operates with combined contributions of the convective motions of the outer stellar envelope (α) and the stellar rotation (Ω). As a consequence, cooler regions than the surroundings, so-called dark spots, form in the photosphere, while brighter and hotter structures arise in chromosphere and corona. The latter ones produce copious UV, X-ray, and radio emission. In later-type stars, close and beyond the fully convective transition (SpT $\sim$ M3), the

mechanism driving the continuous formation and variation of magnetic fields is not well understood. An indirect measure of this phenomenon is investigating the coronal activity-rotation relation, typically expressed in terms of the X-ray luminosity (L_x) as a function of the rotational period (P_{rot}). Pallavicini et al. (1981) were the first to investigate the coronal X-ray emission as a function of rotational velocity for a wide range of stellar spectral types (O3 to M). Later, Pizzolato et al. (2003) focused their study on late-type main-sequence stars with X-ray data from the *ROSAT* satellite and P_{rot} calculated from *vsini* measurements. In this early work the activity-rotation relation presents two different regimes: (1) saturated, where the activity of fast rotators does not depend on rotation, and (2) unsaturated, where the X-ray activity of slowly rotating stars decreases with increasing rotation period.

In the most recent work from Magaudda et al. (2020) we presented a comprehensive study of the relation between rotation, X-ray activity, and age for ~ 300 M dwarfs. We homogenized data from the literature (González-Álvarez et al. 2019; Stelzer et al. 2016; Wright et al. 2011, 2018; Wright & Drake 2016) and added in new very sensitive observations from dedicated observations with the X-ray satellites *XMM-Newton* and *Chandra* and the photometry mission *K*2 from which we derived rotation periods. We found a significantly steeper slope in the unsaturated regime than previous works for fully convective stars and we confirmed a non-constant X-ray emission level in the saturated regime, as first proposed by Reiners et al. (2014).

In this article, we combine our previous results on the X-ray activity-rotation relation (Magaudda et al. 2020) with those obtained from new observations with the *extended ROentgen survey with an Imaging Telescope Array* (eROSITA; Predehl et al. 2021) on the Russian Spektrum Roentgen-Gamma (SRG)[1] mission and the *Transiting Exoplanet Survey Satellite* (TESS; Ricker et al. 2014).

We use the eROSITA and *TESS* sample compiled by Magaudda et al. (2022), on the basis of the superblink proper motion survey by Lépine & Gaidos (2011) (LG11, ~ 9000 M dwarfs), that we characterized with *Gaia*-DR2 data. We refer to Magaudda et al. (2022) for more information on the derivation of our final catalog of LG11-*Gaia* M dwarfs detected with eROSITA and with *TESS* observations. More details on the sample used for the analysis of the activity-rotation relation treated in this work are also given in Section 2, and we present the results in Section 3, with an investigation of the possible observational biases related to them. In Section 4, we summarize our conclusions and give an outlook to future studies in this field.

---

[1] http://srg.iki.rssi.ru/?page_id=676&lang=en.

2 | SAMPLE

We selected M dwarfs from the superblink proper motion catalog of nearby M dwarfs from Lépine & Gaidos (2011) choosing only stars with complete photometry from the second data release of the *Gaia* mission (*Gaia* DR2, Gaia Collaboration et al. 2018) and distance from Bailer-Jones et al. (2018) (hereafter LG11-*Gaia*). In particular, we study the X-ray emission of our LG11-*Gaia* sample during the first eROSITA All-Sky survey (eRASS1). We use the preliminary catalog produced by the eROSITA consortium that is based on data collected from December 2018 to June 2019. We retrieve P_{rot} from *TESS* light curves with 2-min cadence. A complete discussion of the eROSITA/*TESS* source identification and data analysis is found in Magaudda et al. (2022).

The sample used in this work includes the LG11-*Gaia* M dwarfs detected with eROSITA and with reliable P_{rot} from *TESS* light curves. We refer to it as the LG11-*Gaia*/eRASS1/*TESS* sample. The relations we used to calculate stellar parameters (Mann et al. 2015, 2016) are valid for stars with $4.6 < M_{Ks} < 9.8$ and $0.1 < R_\star/R_\odot < 0.7$, therefore we keep only the sub-sample for which these conditions apply and we call it the "validated" LG11-*Gaia*/eRASS1/*TESS* catalog.

Next to the 'validated' LG11-*Gaia*/eRASS1/*TESS* sample we use the *MagauddaGaia20* catalog, that was selected from the one used in Magaudda et al. (2020) where for consistency we consider only X-ray detected sources (i.e. we disregard all upper limits) with complete *Gaia*-DR2 and in the validity range of the relations from Mann et al. (2015, 2016), amounting to 197 stars.

3 | RESULTS & DISCUSSION

3.1 | The X-ray activity-rotation relation

New data from the eROSITA and *TESS* satellites provide unprecedented statistics of fast rotating M dwarfs located in the saturated regime of the X-ray activity-rotation relation. In Figure 8 from Magaudda et al. (2022) we can appreciate the capability of eROSITA in detecting stars. In fact, the amount of X-ray detected stars we present in Magaudda et al. (2022) is the largest to date for M dwarfs in the saturated regime ($P_{rot} \lesssim 10$ d), and extends to the lowest X-ray luminosities measured for fast rotators so far. The absence of stars with higher P_{rot} is explained by the duration of the *TESS* campaigns (~ 27 d) which impedes the detection of periods of slower rotators, and consequently a study of the non-saturated region of the relation. Thus, our new analysis is focused on the saturated regime, where

we added the new "validated" LG11-*Gaia*/eRASS1/*TESS* sample to *MagauddaGaia20*.

In Magaudda et al. (2020) we provided a statistical analysis of both the saturated and the unsaturated regimes. Therein we analyzed the activity-rotation relation first for the whole sample and then derived it within three mass bins, (1) $M_\star/M_\odot > 0.6$, (2) $0.4 \leq M_\star/M_\odot \leq 0.6$, and (3) $M_\star/M_\odot < 0.4$.

Following that work, we analyze here the $L_x - P_{rot}$ relation in the saturated regime of the full new sample, that is, 'validated' LG11-*Gaia*/eRASS1/*TESS* plus *Magaudda-Gaia20* stars, and then in individual mass bins.

In the analysis of our new sample across the whole 'validated' mass range we use the transition from the saturated to the non-saturated regime found in Magaudda et al. (2020) for the full mass sample ($P_{sat} = 8.5$ d) to define the saturated region for the sample. We performed a power law fit to the $L_x - P_{rot}$ data for the full new sample. The best fit parameters are listed in Table 1 and the value for the slope is also shown in Figure 1. Surprisingly, a positive slope is found, i.e. L_x increases with increasing P_{rot}, contrary to all previous studies of the saturated regime that found $L_x \approx$ const or a slightly decreasing slope (Magaudda et al. 2020; Reiners et al. 2014).

TABLE 1   Best fit parameter results

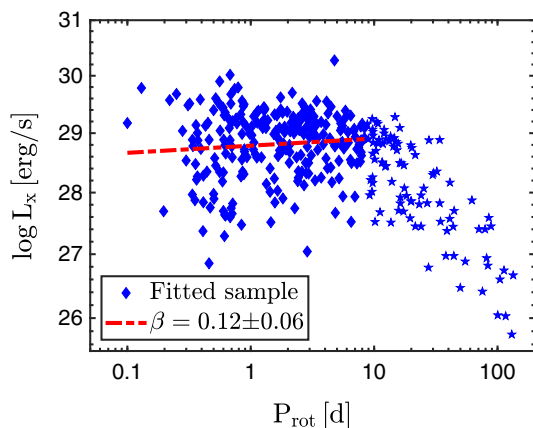| Mass bin	Nstars	β	Intercept [erg/s]
Full sample	242	$+0.12 \pm 0.06$	28.78 ± 0.03
$M_\star/M_\odot > 0.6$	56	-0.05 ± 0.09	29.36 ± 0.03
$0.4 \leq M_\star/M_\odot \leq 0.6$	120	-0.19 ± 0.06	28.90 ± 0.03
$M_\star/M_\odot < 0.4$	72	$+0.24 \pm 0.07$	28.18 ± 0.04

FIGURE 1   The X-ray activity-rotation relation for the sample of this work, where new X-ray data from eROSITA and photometric rotation periods from *TESS* were added to the sample presented by Magaudda et al. (2020). The power law fit in the saturated regime, $P_{rot} \leq 8.5$ d (red dashed line), and its slope β are shown

To examine potential observational biases, we analyzed the relation in three different mass bins, each with its own maximum period for the saturated regime ($P_{rot,sat}$) from the analysis performed by Magaudda et al. (2020). In particular, $P_{rot,sat}$ ($M_\star/M_\odot > 0.6$) = 5.2 ± 0.7 d, $P_{rot,sat}$ ($0.4 \leq M_\star/M_\odot \leq 0.6$) = 11.8 ± 2.0 d and $P_{rot,sat}$ ($M_\star/M_\odot < 0.4$) = 33.7 ± 4.5 d. In Figure 2 we show the results of the power law fits for the three mass bins, and the best fit parameters are, as before, listed in Table 1. It is evident that the slope is positive only in the lowest mass bin. In this bin L_x covers a wide range, going from the minimum L_x-level detected for M dwarfs with very short P_{rot} measurements ($P_{rot} \leq 0.5$ d) to almost its maximum value. In the bottom panel of Figure 2 we present the $L_x - P_{rot}$ relation for the lowest mass bin with a $M_\star$-color code. Here we can see that the period distribution of very low mass stars ($M_\star/M_\odot \leq 0.2$) is composed of stars with very short or very long P_{rot} (in the saturated and unsaturated regime, respectively). Observational biases are strong as already mentioned in Magaudda et al. (2020) and Magaudda et al. (2022): very long rotation periods are taken from Wright et al. (2018) who selected data from the MEarth project to study the slow rotator regime. *TESS* observations provide periods shorter than ~ 15 d because *TESS* monitors a given field for only about a month, and we considered reliable all P_{rot} shorter than about half the duration of a sector light curve. However, these biases cannot explain the absence of stars with $P_{rot} \approx 1 - 10$ d that is present in these very low mass stars ($M_\star/M_\odot < 0.2$). The paucity of very low mass M dwarfs with intermediate rotation periods is probably caused by fast angular momentum loss that carries the stars in little time from being fast to slow rotators (Newton et al. 2017). Hence, in this scenario it is intrinsically rare to observe late M dwarfs with rotation periods of $\approx 1 - 10$ d.

In the highest and the intermediate mass bins the $L_x - P_{rot}$ relation shows a marginally negative slope ($\beta_{high} = -0.05 \pm 0.09$ and $\beta_{int} = -0.19 \pm 0.06$) more in line with previous estimates, although slightly smaller than what we found in Magaudda et al. (2020), where $\beta_{high} = -0.17 \pm 0.14$ and $\beta_{int} = -0.39 \pm 0.13$.

3.2 | eROSITA detection sensitivity

Through the study of the activity-rotation relation in Section 3.1 we encountered observational biases that call for a thorough investigation of the eROSITA detection statistics for the different mass bins.

The LG11-*Gaia* sample, with stellar parameters that are within the validation range of the relations from Mann et al. (2015, 2016), counts 7319 stars with complete *Gaia*-DR2 data, that is, photometry and distance. Eight
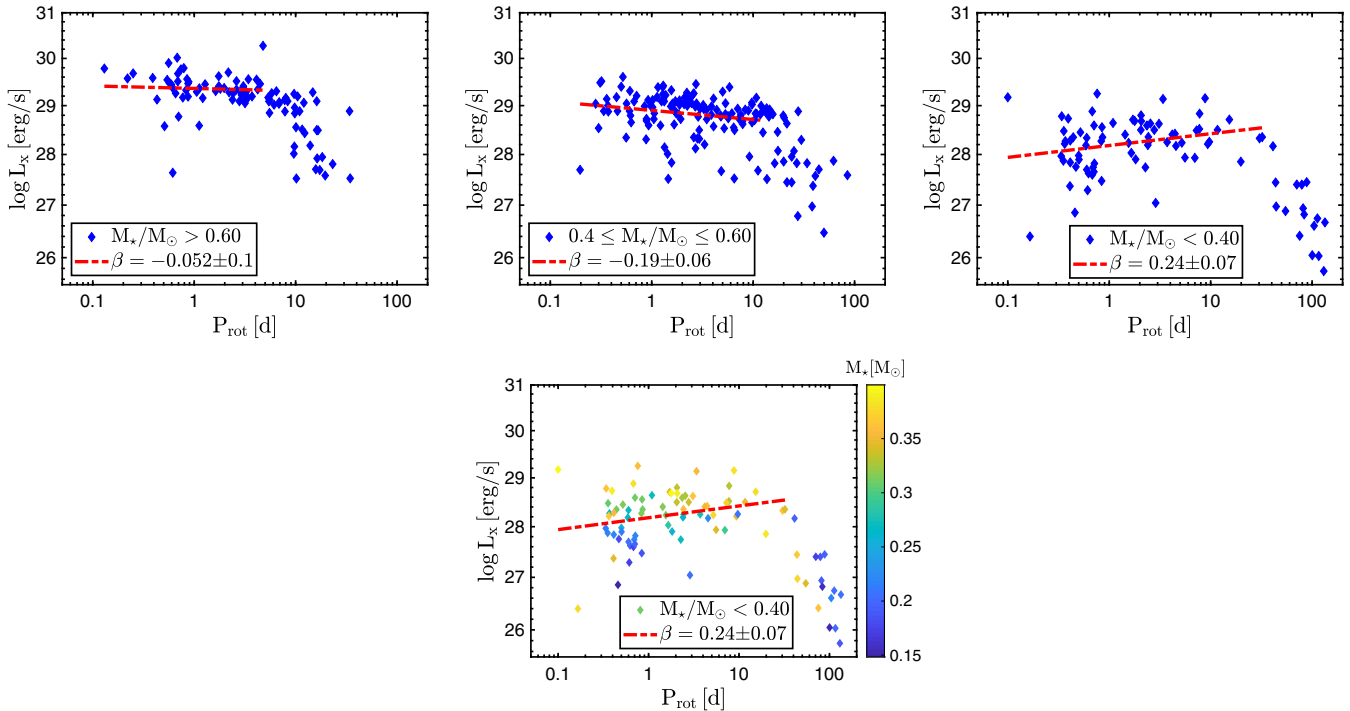
FIGURE 2 $L_x - P_{rot}$ relation and power law fits in the stellar mass bins defined in Section 3.1

percent of this sample is identified with eRASS1 sources, and ~6% is detected in eRASS1 and has a *TESS* 2-min light curve. We extracted reliable P_{rot} from *TESS* light curves for 135 stars. This corresponds to ~2% of the whole LG11-*Gaia* sample and 23% of the eRASS1 detections. Thus, as we mentioned in Magaudda et al. (2022), monitoring coronal X-ray emission with eROSITA is more efficient in identifying stellar magnetic activity than photometric starspots with *TESS*.

To investigate the eROSITA detection statistics we explored the distance ($Dist_{BJ18}$) and mass distributions of the different samples, and how they relate to the detection efficiency of the instrument.

We separated the LG11-*Gaia* sample into the three $M_\star$-bins used in Section 3.1. In Figure 3 we distinguish the complete LG11-*Gaia* sample (gray histogram) from those sources detected with eROSITA and those having both an eROSITA detection and reliable *TESS* P_{rot} (red and green histograms, respectively). The LG11-*Gaia* catalog consists of nearby ($Dist_{BJ18} < 100$ pc) and bright ($J < 10$ mag) M stars according to the selection criteria adopted by Lépine & Gaidos (2011). In Figure 3 the maximum distance is indeed ~ 100 pc with 0.05% outliers with distances up to ~ 250 pc for massive M dwarfs and it decreases for lower mass stars that are fainter.

From Figure 3 we see that the eRASS1 distance limit is only slightly lower than that of the LG11-*Gaia* catalog as a whole, but the fraction of eRASS1 detections decreases with distance. This is quantified in Figure 4

where we present the fraction of X-ray detected LG11-*Gaia* M dwarfs vs distance separately for the three $M_\star$-bins. In other words, we show the ratio between the red and the gray histograms of Figure 3. As a measure for the statistics, we indicate the number of X-ray detected stars in each distance bin attached to the plotting symbol. From this representation, it is evident that at a given distance the fraction of eRASS1 detected stars decreases with decreasing mass. Apart from one outlier in the intermediate mass bin, the detection fraction for lower distances reaches up to ≈30% while it is <10% for distances beyond ≈ 20 pc.

Comparing the eRASS1 sample to the subsample that also has reliable rotation periods from TESS (red and green histograms in Figure 3) we can see that there is no clear difference in their distance limit, but the amount of detected stars in the eRASS1 sample is larger than the one in the subsample with reliable P_{rot}, especially for the highest mass bin. In Figure 5 we show the L_x distribution for M dwarfs with $M_\star/M_\odot > 0.6$ for the eRASS1 sample with the one for eRASS1 stars with reliable P_{rot} (same color code as in Figure 3). We see that periods have been detected only in the stars with the highest $\log L_x$ ($\gtrsim 29.0$ erg/s). According to the activity-rotation relation for the highest mass bin (top left panel in Figure 2) stars with $L_x \lesssim 29$ erg/s are expected to have $P_{rot} \gtrsim 10$ d. We have verified that the situation is similar for the intermediate-mass bin. Therefore, except for the lowest-mass M dwarfs, eRASS1 can detect X-ray emission from unsaturated stars, for which we cannot detect rotation periods with *TESS*.
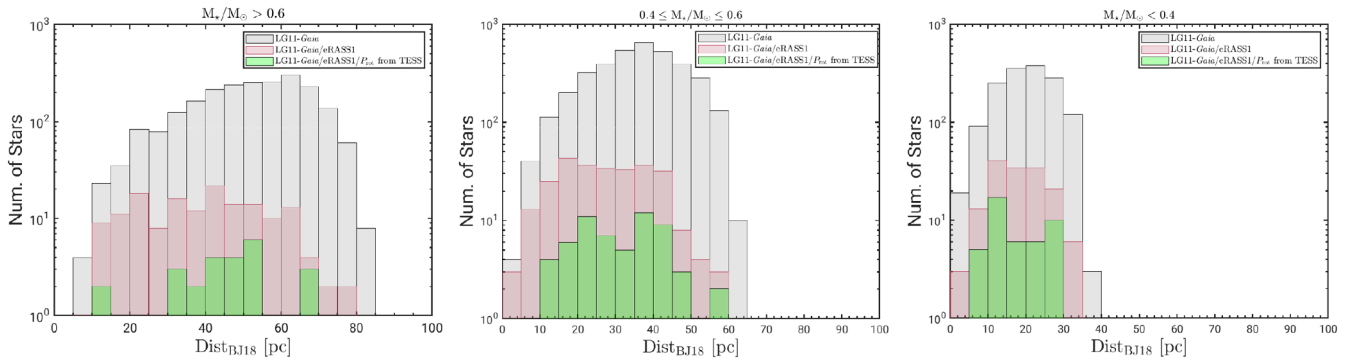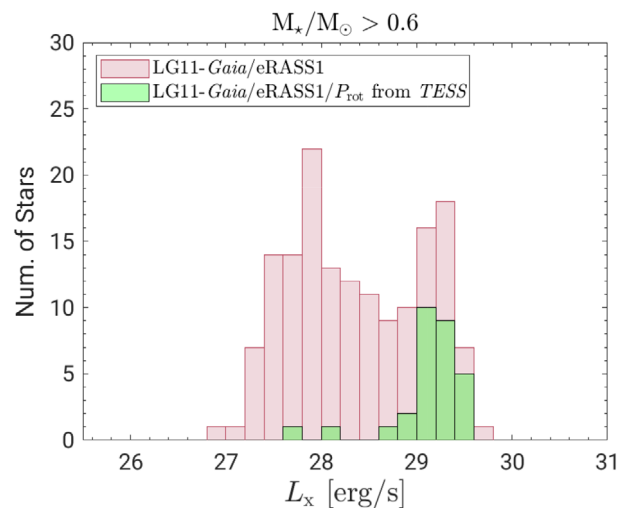
FIGURE 3 Distance distributions in the three stellar mass bins defined in Section 3.2 for the full LG11-*Gaia* sample (in gray) in comparison with the M dwarf sub-sample detected only with eROSITA during eRASS1 (in red) and the one detected with eROSITA and with reliable P_{rot} from *TESS* light curves (in green). In the highest mass bin, there are four stars with $Dist_{BJ18} > 100$ pc that we do not show to have a better visualization of the distance distribution
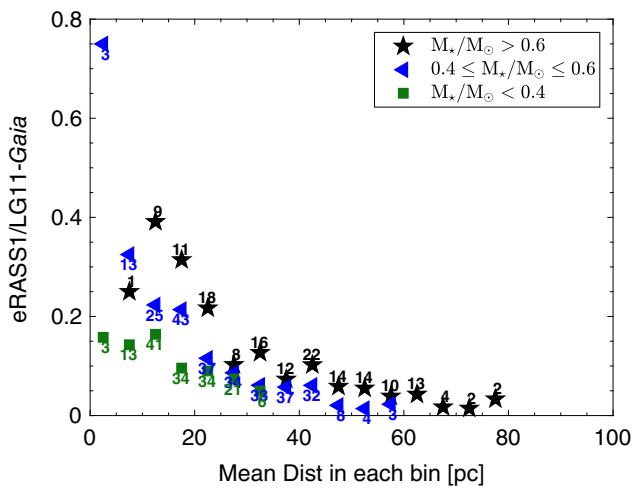
FIGURE 4 Ratio between the red and gray samples of the histograms in Figure 3, calculated for each mass bin. We indicate the number of stars in each bin for the eRASS1 detections, that is, the LG11-*Gaia*/eRASS1 sample

FIGURE 5 X-ray luminosity distribution for the highest mass bin of LG11-*Gaia* stars detected in eRASS1 compared to that of the subsample with reliable P_{rot}

To further investigate how the capability of *TESS* for detecting rotation periods depends on other parameters we show in Figure 6 a diagram of X-ray luminosity versus *TESS* magnitude[2] (T_{mag}). Stars for which we were able to derive P_{rot} values are highlighted in red. We show the rest of the eRASS1 sample with a mass color code. From this representation we see (1) that rotation periods are mostly found for stars with high L_x-level as already shown in Figure 5 and (2) that very few rotation periods are detected on optically bright stars ($T_{mag} \lesssim 9$ mag). This is surprising at first sight, as rotational modulation should be easier to identify in stars with brighter T magnitude due to the higher photometric precision.

---

[2]We have calculated T_{mag} with the conversion from *Gaia* photometry provided by Stassun et al. (2019).

We first focus on early M dwarfs (yellow and green in Figure 6). It is clear that there is a lack of optically bright ($T_{mag} \lesssim 9$ mag) stars with log L_x [erg/s] $\gtrsim 28$. The optically brightest stars sample the shortest distances. Thus, by the absence of stars in the upper left of Figure 6 we conclude that the sample is devoid of very nearby early M dwarfs in the saturated regime. This can be explained if at least for the two higher-mass bins, the unsaturated regime holds many more stars than the saturated regime (represented by the yellow and green objects at bright T_{mag} but low L_x). In fact, in the large sample of M dwarfs analyzed by McQuillan et al. (2013, 2014) and based on 3 years of *Kepler* data the period distribution shows an upper envelope that increases for decreasing masses. In particular, stars in the mass range studied in this work are largely detected in the saturated regime ($P_{rot} \lesssim 10$ d). For the lowest mass
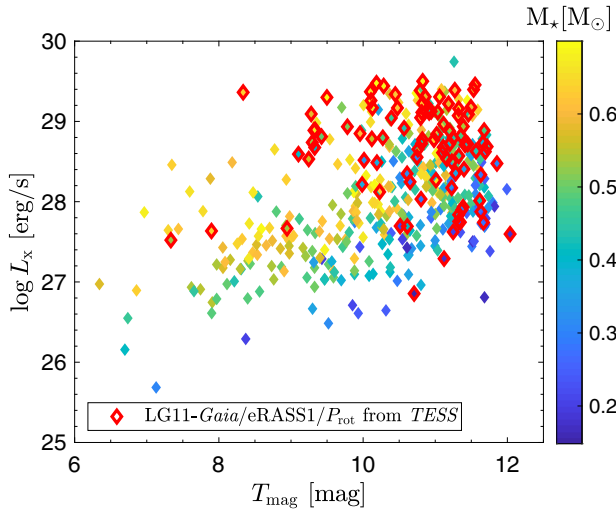
FIGURE 6 The relation between L_x and *TESS* magnitude for the LG11-*Gaia*/eRASS1 sample shown with a mass color code and the same relation for those detections with reliable P_{rot} (open red diamonds)

stars ($M_\star \leq 0.4 M_\odot$) the T magnitude distribution is similar than that of the higher-mass stars but shifted to lower L_x. However, here the absence of period detections in the optically brighter (more nearby) stars is due to the fact that these have low L_x values, that is they are unsaturated and their periods are undetectably long for *TESS*. Optically fainter—that is more distant—stars at the same (low) X-ray luminosity are entirely absent from the sample (see the void of objects in the lower right of Figure 6) because they are beyond the eRASS1 flux limit.

4 | CONCLUSIONS

We investigated the X-ray activity-rotation relation for M dwarfs combining the sample from Magaudda et al. (2020) with new X-ray data from eROSITA and photometric rotation periods extracted from *TESS* light curves. We performed a power law fit of the saturated regime in three mass bins, finding that stars with $M_\star < 0.4 M_\odot$ show a positive slope due to the paucity of mid-to-late M dwarfs with intermediate rotation periods (Newton et al. 2017). Past studies (e.g. Jeffries et al. 2011; Prosser et al. 1996) proposed a so-called "super-saturation" regime where at very fast rotation rates (and low Rossby number) the coronal activity is reduced. The rising slope that we find in the right panels of Figure 2 is driven by the lowest mass stars ($M_\star \lesssim 0.2 M_\odot$). However, we cannot ascertain whether some of them represent supersaturated downward outliers because of the absence of stars with the same mass at intermediate periods ($\approx 1 - 10$ d) mentioned above.

In the course of our investigation of sensitivity limits, we explored the mass and distance dependencies finding that: (1) at a given distance the fraction of eRASS1 detections decreases with decreasing stellar mass, a result of the mass-dependence of L_x and the eRASS1 sensitivity limit. (2) eROSITA is sensitive to detect stars with larger rotation periods that are not detectable with *TESS*, (3) for early M dwarfs the saturated regime is very poorly sampled with a very small sky volume indicating that in this mass range the majority of stars are unsaturated, that is, they are already in an evolved phase of their spin-down history consistent with *Kepler* P_{rot}-distributions.

Clearly, several observational biases mix with intrinsic distributions of X-ray activity and rotation periods. Here we have presented a first assessment of such effects that require a more detailed study in the future.

ORCID

E. Magaudda https://orcid.org/0000-0002-9107-1124

REFERENCES

Bailer-Jones, C. A. L., Rybizki, J., Fouesneau, M., Mantelet, G., & Andrae, R. 2018, *AJ*, *156*(2), 58.

Collaboration, G., Brown, A. G. A., Vallenari, A., et al. 2018, *A&A*, *616*, A1.

González-Álvarez, Micela, G., Maldonado, J., et al. 2019, *A&A*, *624*, A27. https://doi.org/10.1051/0004-6361/201834386.

Jeffries, R. D., Jackson, R. J., Briggs, K. R., Evans, P. A., & Pye, J. P. 2011, *MNRAS*, *411*(3), 2099.

Lépine, S., & Gaidos, E. 2011, *AJ*, *142*(4), 138. https://doi.org/10.1088/0004-6256/142/4/138.

Magaudda, E., Stelzer, B., Covey, K. R., Raetz, S., Matt, S. P., & Scholz, A. 2020, June, *A&A*, *638*, A20.

Magaudda, E., Stelzer, B., Raetz, S., Klutsch, A., Salvato, M., & Wolf, J. 2022, *661*, A29.

Mann, A. W., Feiden, G. A., Gaidos, E., Boyajian, T., & Braun, K. V. 2015, *ApJ*, *804*(1), 1. https://doi.org/10.1088/0004-637X/804/1/64.

Mann, A. W., Feiden, G. A., Gaidos, E., Boyajian, T., & von Braun, K. 2016, *ApJ*, *819*(1), 87. https://doi.org/10.3847/0004-637x/819/1/87.

McQuillan, A., Mazeh, T., & Aigrain, S. 2013, *ApJ*, *775*(1), L11.

McQuillan, A., Mazeh, T., & Aigrain, S. 2014, *ApJS*, *211*(2), 24.

Newton, E. R., Irwin, J., Charbonneau, D., Berlind, P., Calkins, M. L., & Mink, J. 2017, *ApJ*, *834*(1), 85.

Pallavicini, R., Golub, L., Rosner, R., Vaiana, G. S., Ayres, T., & Linsky, J. L. 1981, August, *ApJ*, *248*, 279. https://doi.org/10.1086/159152.

Pizzolato, N., Maggio, A., Micela, G., Sciortino, S., & Ventura, P. 2003, *A&A*, *397*(1), 147. https://doi.org/10.1051/0004-6361:20021560.

Predehl, P., Andritschke, R., Arefiev, V., et al. 2021, *A&A*, *647*, A1.

Prosser, C. F., Randich, S., Stauffer, J. R., Schmitt, J. H. M. M., & Simon, T. 1996, *AJ*, *112*, 1570.

Reiners, A., Schüssler, M., & Passegger, V. M. 2014, *ApJ*, *794*(2), 144. https://doi.org/10.1088/0004-637X/794/2/144.

Ricker, G. R., Winn, J. N., Vanderspek, R. et al. 2014, *Transiting Exoplanet Survey Satellite (TESS)*. In J.M. Oschmann Jacobus, M. Clampin, G. G. Fazio, et al. (Eds.), *Space Telescopes and Instrumentation 2014: Optical, Infrared, and Millimeter Wave* Vol. *9143*, p. 914320.

Stassun, K. G., Oelkers, R. J., Paegert, M., et al. 2019, *AJ*, *158*(4), 138.

Stelzer, B., Damasso, M., Scholz, A., & Matt, S. P. 2016, *MNRAS*, *463*(2), 1844. https://doi.org/10.1093/MNRAS/STW1936.

Wright, N. J., & Drake, J. J. 2016, *Nature*, *535*(7613), 526.

Wright, N. J., Drake, J. J., Mamajek, E. E., & Henry, G. W. 2011, *ApJ*, *743*(1), 48.

Wright, N. J., Newton, E. R., Williams, P. K., Drake, J. J., & Yadav, R. K. 2018, *MNRAS*, *479*(2), 2351.

AUTHOR BIOGRAPHY

E. Magaudda is a Post Doc at the Institut für Astronomie und Astrophysik Tübingen (IAAT), department of Astronomy. The current focus of her research interests is studying the stellar magnetic activity of M dwarfs through the analysis of X-ray data comined with rotation periods from optical lightcurves.

Acknowledgements

It is my pleasure and duty to thank some of the people who supported me during this chapter of my life and helped me bring it to successful completion.

Prof. Dr. Beate Stelzer welcomed me in her group giving me the chance to grow as a scientist and passing on to me in my time of greatest need one of the most important tricks in life for success: if you want to, you can. In addition to her, I would also like to thank Stefanie, with whom I worked side by side and without whom this doctoral project would not have been as complete as it ultimately turned out to be.

Prof. Dr. Steve Shore, my dear friend, who despite the distance, the pandemic and life's unexpected events never ceased to keep my passion for my studies alive in me through unique and stimulating conversations and insights.

All the people at IAAT who between chatting and grilling made lighter days that sometimes never seemed to end. In particular, I would like to thank Samu who has always encouraged me to live cheerfully, Paul who taught me the meaning and beauty of small things, Camille who gave me the strength to start again when I thought it was impossible to do so, Fabian for his patience in helping me understand the German language, and Heiko for imparting serenity and support without having to ask.

Once part of our research group and deserving of special thanks is Martina, who was the first person I met as soon as I arrived in Tübingen and who took my hand 4 years ago and has not let go since. I will never be able to repay her for all she has done for me. Along with her, I thank Giulia, Nadia, Annalisa, Carlo, Gabri, Manfredi, Francesco, Paolo & Berit for all the laughter and adventures shared over these years and for once again allowing me to have such solid points of reference that I never feel alone despite being so far away from my family. Last but not least, I want to mention my friends in Pisa who are always by my side. No matter how much this work scatters us around the world, the thought of each other is always alive within each of us.

Finally, the one who every day loses no opportunity to remind me how fundamental this world is to me. I thank you, Federico, for the love and affection

you have always shown me in constant remembrance of that promise that one day (very soon) will allow us to build that life finally side by side.

This achievement, and more generally this life, would never be as it is without my family and their always being behind me, ready to protect me and to celebrate my every success, big or small. The immense trust they have shown me every day since I left home has allowed me to be who I am today and get to this point. Always together, ready to be united in mind and heart especially when life allows no other way.